RESONANT TWO-PHOTON IONIZATION SPECTROSCOPY OF DIATOMIC TRANSITION METALS AND TRANSITION METAL CARBIDES

by

Olha Krechkivska

A dissertation submitted to the faculty of
The University of Utah
in partial fulfillment of the requirements for the degree of

Doctor of Philosophy

Department of Chemistry

The University of Utah

August 2012

The University of Utah Graduate School

STATEMENT OF DISSERTATION APPROVAL

The dissertation of **Olha Krechkivska**

has been approved by the following supervisory committee members:

Michael D. Morse	, Chair	**5/16/2012** Date Approved
Peter B. Armentrout	, Member	**5/16/2012** Date Approved
Scott L. Anderson	, Member	**5/16/2012** Date Approved
Thomas G. Richmond	, Member	**5/16/2012** Date Approved
Christoph Boehme	, Member	**5/16/2012** Date Approved

and by **Henry S. White** , Chair of the Department of **Chemistry**

and by Charles A. Wight, Dean of The Graduate School.

ABSTRACT

The optical spectrum of diatomic OsC has been investigated by means of resonant two-photon ionization spectroscopy. Spectra for six OsC isotopomers, $^{192}Os^{12}C$ (40.3 % natural abundance), $^{190}Os^{12}C$ (26.0 %), $^{189}Os^{12}C$ (16.0 %), $^{188}Os^{12}C$ (13.1%), $^{187}Os^{12}C$ (1.9 %), and $^{186}Os^{12}C$ (1.6 %), were recorded and rotationally analyzed. The ground state was found to be $X\,^3\Delta_3$, deriving from the $1\delta^3\,3\sigma^1$ electronic configuration. Four bands were found to originate from the $X\,^3\Delta_3$ ground state, giving $B_0"$=0.533 492(33) cm^{-1} and r_0''=1.672 67(5) Å for the $^{192}Os^{12}C$ isotopomer (1σ error limits).

The optical spectrum of diatomic TaC has been investigated, with transitions recorded in the range from 17 850 to 20 000 cm^{-1}. Seven bands were rotationally resolved and analyzed to obtain ground and excited state parameters, including band origins, upper and lower state rotational constants and bond lengths, Fermi contact parameter, b_F, for the ground state, and lambda doubling parameters for the excited states. The ground state of TaC was found to be $X^2\Sigma^+$, originating from the $1\sigma^2\,2\sigma^2\,1\pi^4\,3\sigma^1$ electronic configuration, giving $B_0"$=0.489683(83) cm^{-1}, $r_0"$=1.74901(15) Å, and $b_F"$=0.13120(36) cm^{-1} (1σ error limits), for $^{181}Ta^{12}C$.

Diatomic ZrFe and TiFe have been spectroscopically investigated for the first time. Band origins, excited state vibrational frequencies and anharmonicities, excited state lifetimes, the ground state vibrational interval, $\Delta G"_{1/2}$, rotational constants and

Ω values, bond lengths and rotation-vibration constants are reported for the five most abundant isotopomers of ZrFe and seven most abundant isotopomers of TiFe. The ground states of ZrFe and TiFe are assigned as nominally sextuply-bonded $^1\Sigma^+$ ($\Omega = 0^+$) states deriving from the $1\sigma^2 1\pi^4 2\sigma^2 1\delta^4$ electronic configurations.

To my grandparents

TABLE OF CONTENTS

ABSTRACT iii

LIST OF TABLES ix

LIST OF FIGURES xiii

ACKNOWLEDGMENTS xix

CHAPTERS

1. SPECTROSCOPIC STUDIES OF TRANSITION METAL DIMERS AND TRANSITION METAL CARBIDES..... 1

1.1 Evolution of spectroscopy 1
1.2 Present work 4
1.3 References 10

2. RESONANT TWO-PHOTON IONIZATION SPECTROSCOPY 13

2.1 Introduction 13
2.2 Resonant two photon ionization apparatus 14
2.3 Molecular source 17
2.4 Supersonic expansion..... 20
2.5 Resonant two-photon ionization process 23
2.6 Reflectron-type time of flight mass spectrometer..... 28
2.7 Newly assembled resonant two-photon ionization apparatus 33
2.8 Data obtained in resonant two-photon ionization experiments 34
2.8.1 Low resolution spectra 35
2.8.2 High resolution spectra 36
2.8.3 Excited state lifetime measurement 40
2.9 Analysis of vibronic spectra 40
2.9.1 Determination of ground state $\Delta G_{1/2}$..... 40
2.9.2 Determination of vibrational numbering 43
2.9.3 Vibrational analysis of the band system 45
2.10 Analysis of rotationally resolved spectra 47
2.10.1 Rotfit 47
2.10.2 Pgopher 49

2.11 References 53

3. RESONANT TWO-PHOTON IONIZATION SPECTROSCOPY OF OsC 55

3.1 Introduction 55
3.2 Experimental 57
3.3 Results 59
3.3.1 Low resolution spectrum of OsC 59
3.3.2 Rotationally resolved spectra 61
3.4 Discussion 77
3.5 Conclusion 83
3.6 References 84

4. RESONANT TWO-PHOTON IONIZATION SPECTROSCOPY OF JET COOLED TaC 88

4.1 Introduction 88
4.2 Experimental 90
4.3 Results 93
4.3.1 Vibronically resolved spectrum of $^{181}Ta^{12}C$ 93
4.3.2 Rotationally resolved spectra of $^{181}Ta^{12}C$ 95
4.4 Discussion 102
4.5 Conclusion 112
4.6 References 113

5. ZrFe, A SEXTUPLY-BONDED DIATOMIC TRANSITION METAL? 117

5.1 Introduction 117
5.2 Experimental 121
5.3 Results 122
5.3.1 Low resolution spectrum 122
5.3.2. Rotationally resolved spectra 137
5.4 Discussion 142
5.4.1 The nature of the ZrFe ground state 142
5.4.2 Strongly allowed excitations in ZrFe 143
5.4.3 The nature of the $[13.9]0^+$ state of ZrFe 147
5.5 Conclusion 148
5.6 References 149

6. ELECTRONIC SPECTROSCOPY AND ELECTRONIC STRUCTURE OF DIATOMIC TiFe 153

6.1 Introduction 153
6.2 Experimental methods 155
6.3 Experimental results 157
6.3.1 Low resolution spectrum 157
6.3.2 Rotationally resolved spectra..... 162
6.3.3 The nature of the [15.9]1 and [16.2]0^+ excited states 173
6.3.4. Intense transitions in the 20000- 21500 cm^{-1} region 176
6.4. Discussion and summary 177
6.5 References..... 179

APPENDICES

A. ROTATIONALLY RESOLVED SPECTRA, TABULATED LINE POSITIONS AND FITTED PARAMETERS OF OsC 184

B. ROTATIONALLY RESOLVED SPECTRA, TABULATED LINE POSITIONS AND FITTED PARAMETERS OF TaC 205

C. VIBRONICALLY AND ROTATIONALLY RESOLVED SPECTRA, TABULATED LINE POSITIONS AND FITTED PARAMETERS OF ZrFe..... 220

D. VIBRONICALLY AND ROTATIONALLY RESOLVED SPECTRA, TABULATED LINE POSITIONS AND FITTED PARAMETERS OF TiFe 291

LIST OF TABLES

Table

3.1 Upper state parameters of OsC: band origins (cm^{-1}), rotational constants, B′ (cm^{-1}), upper state bond lengths (Å) and lifetimes (μs)…… 62

3.2 Spectroscopic constants for the $X\,^3\Delta_3$ and $A\,^3\Sigma^-_{0+}$ states of OsC…… 63

3.3 Upper and lower state fitted parameters of $^{189}Os^{12}C$, including hyperfine effects …… 75

4.1 Ground and upper state parameters of $^{181}Ta^{12}C$, band origins, rotational constants, bond lengths, Fermi contact parameter, and lambda doubling parameters…… 103

4.2 Measures of the orbital energy difference ε(*s*)-ε(*d*) in group 5 atoms…… 107

4.3 Relativistic effects on atomic orbital energies …… 109

4.4 Ground states and bond lengths of transition metal carbides …… 111

5.1 Excited state lifetimes for some bands of ZrFe…… 130

5.2 Fitted vibrational constants for the $[13.0]0^+ \leftarrow X^1\Sigma^+$ band system of ZrFe…… 136

5.3 Results from fits of unperturbed rotationally resolved bands…… 140

6.1 Results from a vibronic fit of bands belonging to the $[15.9]^3\Pi_1 \leftarrow X^1\Sigma^+$ and the $[16.2]^3\Pi_{0+} \leftarrow X^1\Sigma^+$ band systems …… 165

6.2 Fitted ground state vibrational constants and bond length for various TiFe isotopomers …… 169

6.3 Results from the fits of bands belonging to $[15.9]^3\Pi_1$ and the $[16.2]^3\Pi_{0+}$ states of TiFe…… 171

A.1 Line Positions for the 0-0 band of the $[19.1]2 \leftarrow X\,^3\Delta_3$ electronic band system of OsC……..…… 186

A.2 Line Positions for the 1-0 band of the [19.1]2 ← $X\,^3\Delta_3$ electronic band system of OsC……. 189

A.3 Line Positions for the 0-0 band of the [20.5]3 ← $X\,^3\Delta_3$ electronic band system of OsC……. 193

A.4 Line Positions for the 0-0 band of the [21.2]2 ← $X\,^3\Delta_3$ electronic band system of OsC…… 197

A.5 Line Positions for the 0-0 band of the [20.7]1←$A\,^3\Sigma^-(0^+)$ electronic band system of OsC……..… 200

A.6 Line Positions for the 0-0 band of the [21.0]1←$A\,^3\Sigma^-(0^+)$ electronic band system of OsC……..… 203

B.1 Line positions for the [18.34] $^2\Pi_{1/2}$← $^2\Sigma^+_{1/2}$ transition of TaC……. 207

B.2 Line positions for the [18.36] $^2\Pi_{1/2}$← $^2\Sigma^+_{1/2}$ transition of TaC…… 209

B.3 Line positions for the [18.50] $^2\Pi_{1/2}$← $^2\Sigma^+_{1/2}$ transition of TaC …… 211

B.4 Line positions for the [18.52] $^2\Pi_{1/2}$← $^2\Sigma^+_{1/2}$ transition of TaC …… 213

B.5 Line positions for the [18.56] $^2\Pi_{1/2}$← $^2\Sigma^+_{1/2}$ transition of TaC……. 215

B.6 Line positions for the [19.52] $^2\Pi_{1/2}$← $^2\Sigma^+_{1/2}$ transition of TaC……. 217

B.7 Line positions for the [19.63] $^2\Pi_{1/2}$← $^2\Sigma^+_{1/2}$ transition of TaC…….…… 219

C.1 Band heads of the various ZrFe isotopomers…… 227

C.2 Vibrational fit of the [13.9] 0^+←$X^1\Sigma^+$system for ZrFe isotopomers…… 238

C.3 Calculated Franck-Condon factors for the [13.9] 0^+←$X\,^1\Sigma^+$ system of ZrFe …… 239

C.4 Fitted rotational lines of the 1-0 band of the [13.9] 0^+←$X^1\Sigma^+$system of ZrFe…… 242

C.5 Assigned rotational lines of the 2-0 band of the [13.9] 0^+←$X^1\Sigma^+$system of ZrFe…… 245

C.6 Fitted rotational lines of the 3-0 band of the

[13.9] $0^+ \leftarrow X^1\Sigma^+$system of ZrFe…… 247

C.7 Fitted rotational lines of the 4-0 band of the
[13.9] $0^+ \leftarrow X^1\Sigma^+$system of ZrFe …… 251

C.8 Assigned rotational lines of the 5-0 band of the
[13.9] $0^+ \leftarrow X^1\Sigma^+$system of ZrFe …… 255

C.9 Assigned rotational lines of the 6-0 band of the
[13.9] $0^+ \leftarrow X^1\Sigma^+$system of ZrFe …… 258

C.10 Fitted rotational lines of the 7-0 band of the
[13.9] $0^+ \leftarrow X^1\Sigma^+$system of ZrFe …… 261

C.11 Assigned rotational lines of the 8-0 band of the
[13.9] $0^+ \leftarrow X^1\Sigma^+$system of ZrFe …… 264

C.12 Assigned rotational lines of the 9-0 band of the
[13.9] $0^+ \leftarrow X^1\Sigma^+$system of ZrFe …… 267

C.13 Fitted rotational lines of the 10-0 band of the
[13.9] $0^+ \leftarrow X^1\Sigma^+$system of ZrFe …… 271

C.14 Fitted rotational lines of the 11-0 band of the
[13.9] $0^+ \leftarrow X^1\Sigma^+$system of ZrFe …… 274

C.15 Assigned rotational lines of the 18053 cm^{-1} band of ZrFe …… 277

C.16 Assigned rotational lines of the 18111 cm^{-1} band of ZrFe …… 281

C.17 Assigned rotational lines of the 18260 cm^{-1} band of ZrFe …… 284

C.18 Assigned rotational lines of the 18392 cm^{-1} band of ZrFe …… 287

C.19 Assigned rotational lines of the 18398 cm^{-1} band of ZrFe …… 288

D.1 Vibronic fit of bands belonging to the [15.9]$1 \leftarrow X^1\Sigma^+$
system of TiFe …… 303

D.2 Vibronic fit of bands belonging to the [16.2]$0^+ \leftarrow X^1\Sigma^+$
system of TiFe …… 304

D.3 Fitted rotational lines of the 1-0 band of the [15.9]$1 \leftarrow X^1\Sigma^+$
system of TiFe …… 307

D.4 Fitted rotational lines of the 2-0 band of the [15.9]$1 \leftarrow X^1\Sigma^+$

system of TiFe 310

D.5 Fitted rotational lines of the 1-0 band of the $[16.2]0^{+}\leftarrow X^{1}\Sigma^{+}$
system of TiFe 313

D.6 Fitted rotational lines of the 2-0 band of the $[16.2]0^{+}\leftarrow X^{1}\Sigma^{+}$
system of TiFe 316

D.7 Fitted rotational lines of the 3-0 band of the $[15.9]1\leftarrow X^{1}\Sigma^{+}$
system of TiFe 318

D.8 Fitted rotational lines of the 3-0 band of the $[16.2]0^{+}\leftarrow X^{1}\Sigma^{+}$
system of TiFe 322

D.9 Fitted rotational lines of the 4-0 band of the $[15.9]1\leftarrow X^{1}\Sigma^{+}$
system of TiFe 324

D.10 Fitted rotational lines of the 4-0 band of the $[16.2]0^{+}\leftarrow X^{1}\Sigma^{+}$
system of TiFe 327

D.11 Fitted rotational lines of the 5-0 band of the $[15.9]1\leftarrow X^{1}\Sigma^{+}$
system of TiFe 331

D.12 Fitted rotational lines of the 5-0 band of the $[16.2]0^{+}\leftarrow X^{1}\Sigma^{+}$
system of TiFe 336

D.13 Fitted rotational lines of the 6-0 band of the $[16.2]0^{+}\leftarrow X^{1}\Sigma^{+}$
system of TiFe 339

D.14 Fitted rotational lines of the 7-0 band of the $[16.2]0^{+}\leftarrow X^{1}\Sigma^{+}$
system of TiFe 343

D.15 Fitted rotational lines of the 8-0 band of the $[16.2]0^{+}\leftarrow X^{1}\Sigma^{+}$
system of TiFe 346

D.16 Rotational lines of the interacting 18605 and 18616
bands of $^{48}Ti^{56}Fe$ 347

D.17 Fit of B'_{v} values for levels belonging to the [15.9]1 state of TiFe 348

D.18 Fit of B'_{v} values for levels belonging to the $[16.2]0^{+}$ state of TiFe 349

LIST OF FIGURES

Figure

2.1 Schematic of the resonant two photon ionization apparatus 16

2.2 Schematic of the molecular source 18

2.3 Several ionization schemes in the R2PI experiment 26

2.4 A mass spectrum of atomic Os and OsC..... 29

2.5 Schematic of the reflectron-type time of flight mass spectrometer..... 30

2.6 A vibronic spectrum of TiFe diatomic molecule over the 16300-21400 cm^{-1} region 37

2.7 A rotationally resolved spectrum of the 7-0 band of a [16.2] $^1\Sigma^+ \leftarrow X^1\Sigma^+$, displaying different isotopic combinations of TiFe 38

2.8 A typical lifetime measurement scan 41

2.9 A portion of $^{92}Zr^{56}Fe$ low resolution spectrum..... 42

2.10 Band difference histogram plot for $^{92}Zr^{56}Fe$ 44

2.11 Determination of the vibrational assignment for [13.9]$0^+ \leftarrow X^1\Sigma$ band system of ZrFe 46

2.12 A portion of [21.2]$2 \leftarrow {}^3\Delta_3$ transition of $^{192}Os^{12}C$ and $^{189}Os^{12}C$, that covers Q branch and three P lines 48

2.13 A Pgopher simulation of [21.2]$2 \leftarrow {}^3\Delta_3$ transition of $^{189}Os^{12}C$ 50

2.14 Rotationally resolved spectrum of the [18.34]$^2\Pi_{1/2} \leftarrow {}^2\Sigma^+$ transition of TaC..... 52

3.1 Vibronically resolved resonant two-photon ionization spectrum of OsC over the range 17390-22990 cm^{-1} 60

3.2 Rotationally resolved scan over the 0-0 band of the [19.2]2← $X\,^3\Delta_3$ system of $^{192}Os^{12}C$…….…….. 64

3.3 Rotationally resolved scan over the 0-0 band of the [20.5]3← $X\,^3\Delta_3$ system of $^{192}Os^{12}C$ …….…. 66

3.4 Rotationally resolved scan over the 0-0 band of the [21.0]1← $A\,^3\Sigma^-_{0+}$ system of $^{192}Os^{12}C$ ……..…….. 68

3.5 Measured and simulated spectra of the 0-0 band of the [19.1]2← $X\,^3\Delta_3$ system of $^{189}Os^{12}C$, showing hyperfine structure ……. 76

3.6 Qualitative molecular orbital diagram of OsC ……. 78

4.1 Vibronically resolved resonant two-photon ionization spectrum of TaC over the range 17850-20000 cm^{-1}…… 94

4.2 Rotationally resolved spectrum of the [18.34] $^2\Pi_{1/2}\leftarrow{}^2\Sigma^+$ transition…… 96

4.3 Rotationally resolved spectrum of the [18.56] $^2\Pi_{1/2}\leftarrow{}^2\Sigma^+$ transition …… 97

4.4 Rotationally resolved spectrum of the [19.63] $^2\Pi_{1/2}\leftarrow{}^2\Sigma^+$ transition …… 98

4.5 Qualitative molecular orbital diagram of TaC ……. 104

5.1 Low resolution spectrum of diatomic $^{90}Zr^{56}Fe$ over the 13890 - 18870 cm^{-1} region ……. 123

5.2 Lifetime measurement for the v=10 level of the [13.9]0^+ state of ZrFe …… 127

5.3 Lifetime measurement for the 18053 cm^{-1} state of ZrFe ……. 128

5.4 Band difference histogram plot for $^{90}Zr^{56}Fe$ ……. 132

5.5 Determination of the vibrational assignment for the [13.9]$0^+\leftarrow X^1\Sigma^+$ band system of ZrFe……. 135

5.6 High resolution scan over the 3-0 transition of the [13.9]$0^+\leftarrow X^1\Sigma^+$ system of $^{90}Zr^{56}Fe$……. 138

5.7 Potential energy curves of ZrFe ……. 146

6.1 Low resolution spectrum of diatomic $^{48}Ti^{56}Fe$ ……. 158

6.2 Determination of the vibrational assignment for the

$[15.9]^3\Pi_1 \leftarrow {}^1\Sigma^+$ band system 163

6.3 Determination of the vibrational assignment for the $[16.2]^3\Pi_{0+} \leftarrow {}^1\Sigma^+$ band system 164

6.4 Rotationally resolved spectrum of the 5-0 band of the $[15.9]^3\Pi_1 \leftarrow {}^1\Sigma^+$ system, and the 4-0 band of the $[16.2]^3\Pi_{0+} \leftarrow {}^1\Sigma^+$ system..... 166

6.5 Rotationally resolved spectrum of the 7-0 band of the $[16.2]^3\Pi_{0+} \leftarrow {}^1\Sigma^+$ system..... 168

A.1 Rotationally resolved spectra of the six OsC isotopomers for the 0-0 band of the [19.1]2 $\leftarrow X\,^3\Delta_3$ electronic band system 185

A.2 Rotationally resolved spectra of the six OsC isotopomers 1-0 band of the [19.1]2 $\leftarrow X\,^3\Delta_3$ electronic band system 188

A.3 Rotationally resolved spectra of the six OsC isotopomers 0-0 band of the [20.5]3 $\leftarrow X\,^3\Delta_3$ electronic band system..... 192

A.4 Rotationally resolved spectra of the six OsC isotopomers 0-0 band of the [20.7]1$\leftarrow A\,^3\Sigma^-(0^+)$ electronic band system 195

A.5 Rotationally resolved spectra of the six OsC isotopomers 0-0 band of the[21.0]1$\leftarrow A\,^3\Sigma^-(0^+)$ electronic band system 199

A.6 Rotationally resolved spectra of the six OsC isotopomers 0-0 band of the [21.2]2 $\leftarrow X\,^3\Delta_3$ electronic band system 202

B.1 Rotationally resolved spectra of the [18.34] $^2\Pi_{1/2} \leftarrow {}^2\Sigma^+_{1/2}$ transition of TaC 206

B.2 Rotationally resolved spectra of the [18.36] $^2\Pi_{1/2} \leftarrow {}^2\Sigma^+_{1/2}$ transition of TaC..... 208

B.3 Rotationally resolved spectra of the [18.50] $^2\Pi_{1/2} \leftarrow {}^2\Sigma^+_{1/2}$ transition of TaC 210

B.4 Rotationally resolved spectra of the [18.52] $^2\Pi_{1/2} \leftarrow {}^2\Sigma^+_{1/2}$ transition of TaC 212

B.5 Rotationally resolved spectra of the [18.56] $^2\Pi_{1/2} \leftarrow {}^2\Sigma^+_{1/2}$ transition of TaC 214

B.6 Rotationally resolved spectra of the [19.52] $^2\Pi_{1/2} \leftarrow {}^2\Sigma^+_{1/2}$

transition of TaC ……..…… 216

B.7 Rotationally resolved spectra of the [19.63] $^2\Pi_{1/2} \leftarrow {}^2\Sigma^+_{1/2}$
transition of TaC……..……. 218

C.1 Spectra of the various isotopomers of ZrFe
in the 13890-14890 cm^{-1} range …… 222

C.2 Spectra of the various isotopomers of ZrFe
in the 14890-15890 cm^{-1} range …… 223

C.3 Spectra of the various isotopomers of ZrFe
in the 15890-16890 cm^{-1} range …… 224

C.4 Spectra of the various isotopomers of ZrFe
in the 16890-17890 cm^{-1} range ……. 225

C.5 Spectra of the various isotopomers of ZrFe
in the 17890-18890 cm^{-1} range ……. 226

C.6 Band difference histogram plot for $^{90}Zr^{56}Fe$ ……. 232

C.7 Band difference histogram plot for $^{91}Zr^{56}Fe$ ……. 233

C.8 Band difference histogram plot for $^{92}Zr^{56}Fe$ ……. 234

C.9 Band difference histogram plot for $^{94}Zr^{56}Fe$ ……. 235

C.10 Band difference histogram plot for $^{96}Zr^{56}Fe$…… 236

C.11 Measured vs calculated isotope shifts, $\nu(^{90}Zr^{56}Fe)$- $\nu(^{94}Zr^{56}Fe)$,
for bands belonging to the $[13.9]0^+ \leftarrow {}^1\Sigma^+$ system…… 237

C.12 Rotationally resolved spectra of the various ZrFe isotopic
combinations for the 1-0 band of the $[13.9]0^+ \leftarrow {}^1\Sigma^+$ system…… 241

C.13 Rotationally resolved spectra of the various ZrFe isotopic
combinations for the 2-0 band of the $[13.9]0^+ \leftarrow {}^1\Sigma^+$ system…… 244

C.14 Rotationally resolved spectra of the various ZrFe isotopic
combinations for the 3-0 band of the $[13.9]0^+ \leftarrow {}^1\Sigma^+$ system…… 246

C.15 Rotationally resolved spectra of the various ZrFe isotopic
combinations for the 4-0 band of the $[13.9]0^+ \leftarrow {}^1\Sigma^+$ system…… 250

C.16 Rotationally resolved spectra of the various ZrFe isotopic

combinations for the 5-0 band of the [13.9]$0^+ \leftarrow {}^1\Sigma^+$ system..... 254

C.17 Rotationally resolved spectra of the various ZrFe isotopic combinations for the 6-0 band of the [13.9]$0^+ \leftarrow {}^1\Sigma^+$ system..... 257

C.18 Rotationally resolved spectra of the various ZrFe isotopic combinations for the 7-0 band of the [13.9]$0^+ \leftarrow {}^1\Sigma^+$ system..... 260

C.19 Rotationally resolved spectra of the various ZrFe isotopic combinations for the 8-0 band of the [13.9]$0^+ \leftarrow {}^1\Sigma^+$ system..... 263

C.20 Rotationally resolved spectra of the various ZrFe isotopic combinations for the 9-0 band of the [13.9]$0^+ \leftarrow {}^1\Sigma^+$ system..... 266

C.21 Rotationally resolved spectra of the various ZrFe isotopic combinations for the 10-0 band of the [13.9]$0^+ \leftarrow {}^1\Sigma^+$ system 270

C.22 Rotationally resolved spectra of the various ZrFe isotopic combinations for the 11-0 band of the [13.9]$0^+ \leftarrow {}^1\Sigma^+$ system 273

C.23 Rotationally resolved spectra of the various ZrFe isotopic combinations of the 18053 cm^{-1} band 276

C.24 Rotationally resolved spectra of the various ZrFe isotopic combinations of the 18111 cm^{-1} band 280

C.25 Rotationally resolved spectra of the various ZrFe isotopic combinations of the 18260 cm^{-1} band 283

C.26 Rotationally resolved spectra of the various ZrFe isotopic combinations of the 18392 and 18398 cm^{-1} bands 286

C.27 Variation of $B_{v'}$ values for the [13.9]0^+ state of $^{90}Zr^{56}Fe$ as a function of v'+1/2 290

D.1 Spectra of the various isotopomers of TiFe in the 15500-16500 cm^{-1} range 293

D.2 Spectra of the various isotopomers of TiFe in the 16500-17500 cm^{-1} range 294

D.3 Spectra of the various isotopomers of TiFe in the 17500-18500 cm^{-1} range 295

D.4 Spectra of the various isotopomers of TiFe in the 18500-19400 cm^{-1} range 296

D.5 Spectra of the various isotopomers of TiFe in the 19500-20500 cm^{-1} range …… 297

D.6 Spectra of the various isotopomers of TiFe in the 20500-21500 cm^{-1} range …… 298

D.7 Spectra of the various isotopomers of TiFe in the 21500-22500 cm^{-1} range …… 299

D.8 Spectra of the various isotopomers of TiFe in the 22500-23500 cm^{-1} range …… 300

D.9 Isotope shifts in the [15.9]1-$X^1\Sigma^+$system of TiFe …… 301

D.10 Isotope shifts in the [16.2]0^+-$X^1\Sigma^+$system of TiFe …… 302

D.11 Rotationally resolved spectra of the various TiFe isotopic combinations for the 1-0 band of the [15.9]1←$X^1\Sigma^+$ system …… 306

D.12 Rotationally resolved spectra of the various TiFe isotopic combinations for the 2-0 band of the [15.9]1←$X^1\Sigma^+$ system and the 1-0 band of the [16.2]0^+←$X^1\Sigma^+$ system …… 309

D.13 Rotationally resolved spectra of the various TiFe isotopic combinations for the 3-0 band of the [15.9]1←$X^1\Sigma^+$ system and the 2-0 band of the [16.2]0^+←$X^1\Sigma^+$ system …… 315

D.14 Rotationally resolved spectra of the various TiFe isotopic combinations for the 4-0 band of the [15.9]1←$X^1\Sigma^+$ system and the 3-0 band of the [16.2]0^+←$X^1\Sigma^+$ system …… 321

D.15 Rotationally resolved spectra of the various TiFe isotopic combinations for the 5-0 band of the [15.9]1←$X^1\Sigma^+$ system and the 4-0 band of the [16.2]0^+←$X^1\Sigma^+$ system …… 326

D.16 Rotationally resolved spectra of the various TiFe isotopic combinations for the 5-0 band of the [16.2]0^+←$X^1\Sigma^+$ system…… 335

D.17 Rotationally resolved spectra of the various TiFe isotopic combinations for the 6-0 band of the [16.2]0^+←$X^1\Sigma^+$ system…… 338

D.18 Rotationally resolved spectra of the various TiFe isotopic combinations for the 7-0 band of the [16.2]0^+←$X^1\Sigma^+$ system…… 342

D.19 Rotationally resolved spectra of the various TiFe isotopic combinations for the 8-0 band of the [16.2]0^+←$X^1\Sigma^+$ system…… 345

ACKNOWLEDGMENTS

I would like to express my sincere gratitude to professor Michael D. Morse, for letting me join his research group and being a wonderful advisor and teacher throughout my years in the graduate school. Thank you for introducing me to the wonderful world of spectroscopy. I will never forget the excitement of discovering new information about molecules, being the first person to see their "fingerprints" - spectra.

I am very thankful to past and present Morse group members for creating a cheerful, friendly workplace. Special thanks goes to Dr. Ramya Nagarajan, a former Morse group member, who taught me how to operate the equipment in the laboratory. I would like to thank Maria Garcia, for her support and keen sense of humor, and Alonzo Martinez, for his help on many occasions and friendly pranks. Thank you guys for the fun times!

I would like to thank the personnel of the mechanical and electronics shops, Dennis Romney, Dale Heisler and Ron Jones for their help.

Finally I want to thank my husband, parents and grandparents for their support and believing in me.

CHAPTER 1

SPECTROSCOPIC STUDIES OF TRANSITION METAL DIMERS AND TRANSITION METAL CARBIDES

1.1 Evolution of Spectroscopy

The dispersion of light by a prism has been known to mankind since Roman times. Seneca (3 BC–65 AD) noticed that the colors produced by a prism are the same as those of the rainbow.[1] The action of a prism on a light beam was observed by Isaac Newton (1643-1727) and was called the Phenomena of Colours.[2] In one of his experiments with light, Newton displayed a 25 cm long dispersed solar spectrum on the screen, implemented by means of dark room, a small hole in a window shutter, a prism and a wall as a screen. He saw a sequence of oblong colored images of the hole and named this phenomenon the Spectrum.[2] Newton failed to notice any absorption or emission lines, probably due to poor quality of optics used. Due to this misfortune, another experimentalist, Joseph Fraunhofer (1787-1826) became the father of spectroscopy.[3] During an experiment that employed a flint-glass prism placed eight meters from a slit in the window, and a telescope placed behind the prism, he discovered that the solar spectrum was crossed by large numbers of strong and weak dark lines. Fraunhofer mapped nearly 700 dark lines in the solar spectrum, and was the first to apply spectroscopy to astronomy, recording the spectra of Sirius and other stars.[3]

The first emission spectra, discovered in the mid 19th century, were spectra of flames. It was noticed that some bright lines in emission spectra coincide with dark lines in the solar spectrum. Gustav Kirchhoff (1824-1887) linked these facts together and concluded that particular lines in the solar spectrum are due to the presence of chemical elements.[1] He discovered sodium, lithium, magnesium, chromium, iron and nickel in the solar atmosphere. Anders Ångstrom (1814-1874) identified more elements,[1] such as aluminum, calcium, strontium and barium in the solar atmosphere, and was the first to measure the wavelength of the Fraunhofer lines to six significant figures in units of 10^{-10} m,[3] a unit that is now called the Ångstrom. The development of photographic plates in 1870 provided a means of recording permanent spectra, which was an important milestone in the development of spectroscopy.

As new discoveries were made - infrared radiation in 1800 by W. Herschel,[3] ultraviolet radiation in 1803 by J. W. Ritter,[3] more and more spectra were collected, and a search for a theory to link spectra to atomic and molecular properties began. The discovery of radio waves in 1887 by H. Hertz, and their proper treatment in terms of James Clerk Maxwell's theory greatly influenced this process.[1]

For a long time experiment was ahead of theory, however, the formulations of quantum mechanics by Heisenberg, Schrödinger, Pauli, and Dirac, finally bridged the gap. In the 20th century spectroscopy has continued to advance due to major technological developments: lasers, computers, mass spectrometric techniques, detectors, supersonic nozzles, etc. Now, spectroscopy, something that started with a glass prism, sunlight and human curiosity, is rapidly developing as a science, and is utilized in countless applications in a wide variety of fields.

In this short description of the development of spectroscopy, only a few of the great scientists and their contributions were mentioned and only a few key points were stressed, but a more detailed historical analysis is unnecessary and beyond the scope and focus of this work.

Currently, a very large number of different spectroscopic techniques exist. They can be classified according to a variety of factors that complement each other: region of electromagnetic radiation employed, number of photons involved in the process, type of response generated, system under investigation, and instrumentation/detection techniques. In general, rotational excitation of a molecule requires less energy than vibrational excitation, and by far less energy than electronic excitation. Thus, pure rotational spectroscopy occurs in the microwave, millimeter and THz regions of the electromagnetic spectrum. Vibrational transitions take place in the far, mid and near infrared, so these are the boundaries of vibrational spectroscopy. Electronic transitions are found in the infrared, visible, near and far ultraviolet regions. In terms of the response of the system to electromagnetic radiation, spectroscopic techniques can be classified as based on absorption, emission or scattering methods. Detection methods are diverse as well, and include photon detection, charged particle detection, or techniques that exploit changes in the macroscopic properties of the medium with which the light wave interacts. Various spectroscopic techniques have been developed to study systems that drastically vary in size from substances in the bulk in all phases to single molecule techniques.

The resonant two-photon ionization (R2PI) spectroscopy technique employed in this dissertation uses tunable visible radiation to excite a molecule, followed by a pulse of fixed wavelength ultraviolet radiation to ionize it. The optical spectra are collected

indirectly, by detection of an ion rather than a photon. The event of ion detection is correlated with the excitation frequency, so by detecting the ions in a mass spectrometer, it is possible to collect the optical spectrum in a mass-specific manner. Molecules of interest in the Morse research group are metal dimers, diatomic metal-ligand molecules, and, infrequently, larger complexes. The output of a tunable dye laser provides a photon in the visible electromagnetic spectrum that promotes such a molecule from the ground electronic and vibrational state to an excited electronic state and either ground or excited vibrational state. Thus, in low resolution or survey scans, information about vibronic transitions is gathered. The rotational structure of these transitions is studied under high resolution, to provide spectroscopic constants for both ground and excited electronic states.

In this work, spectra of the 5d transition metal carbides, OsC and TaC, and the transition metal dimers, ZrFe and TiFe, were collected and analyzed. None of the listed molecules have been spectroscopically investigated prior to this work.

1.2 Present work

Transition metal carbides represent a class of materials that possess many desirable properties, and therefore are used in various technological applications. Due to their physical properties, such as high hardness, high melting temperatures, and high elastic modulus, transition metal carbides are used at extreme temperature and pressure, in rocket nozzles, mining tools, drill bits, etc.[4,5] Due to their optical, electronic, and magnetic properties, they are also used for optical coatings, electrical contacts, diffusion barriers and other uses.[4,5] Transition metal carbides have also been recognized for their

catalytic activity and high chemical resistance.[6] All these properties combined suggest a wide range of applications from bulk forms of transition metal carbides to nanostructures.

The first part of this work focuses on the building blocks of bulk 5d transition metal carbides, diatomic molecules, for which despite all the attractive properties, information on geometric and electronic structure remains very limited. Prior to this work, spectra for the 5d transition metal carbides were available only for WC,[7,8] IrC[9-12] and PtC.[13-19]

In this work spectra of six OsC isotopomers, $^{192}Os^{12}C$ (40.3% natural abundance), $^{190}Os^{12}C$ (26.0%), $^{189}Os^{12}C$ (16.0%), $^{188}Os^{12}C$ (13.1%), $^{187}Os^{12}C$ (1.9%), $^{186}Os^{12}C$ (1.6%) as well as $^{181}Ta^{12}C$ (98.92%), were collected and analyzed. These studies reveal the ground state term symbols and electronic configurations, band origins, rotational constants and bond lengths for ground and excited states, hyperfine constants, excited state lifetimes, and rotational line positions for OsC and TaC. In the case of OsC, the ground state was found to be $X^3\Delta_3$, deriving from the $1\delta^3 3\sigma^1$ electronic configuration, giving B_0"=0.533192(33) cm^{-1} and r_0"=1.67267(5) Å for the most abundant isotopomer, $^{192}Os^{12}C$. Along with the ground state, another low lying electronic state was found to be populated in the supersonic expansion, a $^3\Sigma^-_{0+}$ state, that derives from the $1\delta^2 3\sigma^2$ electronic configuration, giving B_0"=0.517713(91) cm^{-1} and r_0"=1.69797(15) Å for the most abundant isotopomer. The 3σ molecular orbital of OsC was confirmed by hyperfine measurements to be primarily nonbonding in character, arising from the 6*s* atomic orbital of Os. The ground state of $^{181}Ta^{12}C$ was found to be $X\ ^2\Sigma$, originating from the $1\sigma^2 2\sigma^2 1\pi^4 3\sigma^1$ electronic configuration, with B_0"=0.489683(83) cm^{-1} and r_0"=1.74901(15) Å. The ground state of $^{181}Ta^{12}C$ was found to be governed by the Hund's $b_{\beta s}$ coupling

case due to the hyperfine coupling between the magnetically active nucleus of tantalum and the singly occupied 3σ molecular orbital, which is shown to be primarily Ta 6*s* in character.

Theoretical studies have been published on TaC,[20] WC,[21] OsC,[22,23] IrC,[24] PtC,[25] and AuC^+.[26] Theoretical studies of 5d transition metal carbides are more challenging than those for the 3d and 4d series due to the increasing importance of relativistic effects (including spin-orbit coupling) and electron correlation. The growing importance of these effects in heavy molecules can be demonstrated by the example of OsC, for which the ground state was predicted to be of $^3\Sigma^-$ symmetry in two theoretical investigations, neither of which included spin-orbit effects,[22,23] but was experimentally confirmed as $^3\Delta_3$ in the present work.[27] Theoretical predictions for TaC were in agreement with the experiment,[28] both identifying a $^2\Sigma$ ground state.[20,23,29] TaC significantly differs from its congeners, VC and NbC, in having a $^2\Sigma$ ground state rather than a $^2\Delta$ ground state, however. The emergence of a different ground state in TaC is argued to result from relativistic stabilization of the 6*s*-like 3σ orbital in TaC. It is my hope that the data presented in this work will be useful in improving existing *ab initio* calculation methods for heavy atoms.

The second part of this dissertation focuses on the mixed twelve valence electron metal dimers, TiFe and ZrFe. Multiple bonding between transition metal atoms has been a topic of great interest ever since it was discovered in the 1960s in such quadruply-bonded species as $[Re_2Cl_8]^{2-}$,[30,31] $Cr_2(O_2CCH_3)_4$,[32] and $Mo_2(O_2CCH_3)_4$,[33] and in $[Tc_2Cl_8]^{3-}$.[34] In the gas phase, multiple bonding in bare transition metal dimers was first demonstrated in the 1970s in the pioneering work of Efremov, Samoilova, and Gurvich

on the 12 valence electron molecules Cr_2,[35] CrMo,[36] and Mo_2,[37] although these results were not widely recognized until subsequent laser spectroscopic work proved them to be correct.[38-43] Numerous theoretical investigations of the multiple bonding in the transition metal diatomics have been conducted since these molecules were first reported, and it is now known that the 12-electron molecules Cr_2,[44,45] Mo_2,[46] W_2,[47] CrMo,[48] CrW,[48] and MoW[48] all have closed shell $^1\Sigma_{(g)}^+$ ground states with 6 fully occupied bonding molecular orbitals in the leading configuration, making them nominally sextuply-bonded molecules. The molecules are highly multiconfigurational, however, leading to effective bond orders that are smaller than 6.[46-49]

It is interesting to consider what happens when the nuclear charge in a symmetric, multiply bonded diatomic (such as N_2) is shifted to make increasingly asymmetric but still isoelectronic molecules, such as CO, BF, or BeNe. Our intuition concerning how the bond order varies as the nuclear charge is redistributed in the 12-electron transition metal diatomics is unclear, however. How does the bond order or the bond length change as the nuclear charges in Cr_2 are made more asymmetric, moving to the isoelectronic species VMn, TiFe, ScCo, CaNi, KCu, and finally, ArZn?

We may define a parameter, ΔZ, which characterizes how far apart the groups composing the diatomic molecule lie. For the 12-electron molecules that are isoelectronic to CrMo (ΔZ=0), we have VTc and NbMn (ΔZ=2), TiRu and ZrFe (ΔZ = 4), ScRh and YCo (ΔZ=6), *etc.* Diatomic CrMo has been shown to have a closed shell, $^1\Sigma^+$ ground state with a bond length of r_0 = 1.823(1) Å,[41] while YCo also has a closed shell, $^1\Sigma^+$ ground state with r_0 = 1.983(1) Å.[50] This increase in bond length by 0.160 Å is similar to the increase of 0.164 Å that is found in moving from N_2 (r_e = 1.098 Å)[51] to BF (r_e=1.262Å),[52]

suggesting that YCo is no longer a sextuply-bonded molecule. Are the asymmetric 12-electron molecules ZrFe and TiFe ($\Delta Z=4$) more similar to the sextuply bonded CrMo ($\Delta Z=0$), or is it more like YCo ($\Delta Z=6$) in having a reduced level of bonding? To answer this question, we have undertaken studies to determine the ground electronic states of ZrFe and TiFe and measure their bond length.

This work provides the first investigation of any kind of diatomic ZrFe. The electronic configuration and term of the ZrFe ground state, the ground and excited state rotational constants and bond lengths, band origins, the excited state vibrational frequency and anharmonicity, excited state lifetimes, and the ground state vibrational interval, $\Delta G''_{1/2}$ are reported here. Spectra of six ZrFe isotopomers were recorded using the mass-resolved resonant two-photon ionization technique: $^{90}Zr^{54}Fe$ (3.0% natural abundance), $^{90}Zr^{56}Fe$ (47.2%), $^{91}Zr^{56}Fe$ (10.3%), $^{92}Zr^{56}Fe$ (15.7%), $^{94}Zr^{56}Fe$ (15.9%), and $^{96}Zr^{56}Fe$ (2.6%). For the most abundant species, $^{90}Zr^{56}Fe$ (47.2%), these values are: T_0 = 13931.9(1.2) cm^{-1}, ω'_e = 325.05(54) cm^{-1}, $\omega'_e x'_e$ = 1.589(40) cm^{-1}, and $\Delta G''_{1/2}$ = 452.2cm^{-1}. Rotationally resolved studies have revealed ground and excited state rotational constants and Ω values, bond lengths and rotation-vibration constants, giving B_0''=0.138786(30) cm^{-1} and r_0''=1.87685(20) Å for $^{90}Zr^{56}Fe$. The ground state and all observed excited states have Ω=0. Based on the short bond length, the ground state of ZrFe is assigned as a sextuply-bonded $^1\Sigma^+$ ($\Omega = 0^+$) state deriving from the $1\sigma^2 1\pi^4 2\sigma^2 1\delta^4$ electronic configuration.

The first spectroscopic investigation of diatomic TiFe is also presented in this dissertation. Spectra of the TiFe isotopomers, $^{48}Ti^{54}Fe$ (4.27% natural abundance), $^{46}Ti^{56}Fe$ (7.57%), $^{47}Ti^{56}Fe$ (6.83%), $^{48}Ti^{56}Fe$ (67.64%), $^{49}Ti^{56}Fe$ (4.96%), $^{48}Ti^{57}Fe$

(1.55%) and $^{50}Ti^{56}Fe$ (4.75%), were recorded over the 15500-23500 cm^{-1} range. Two vibrational progressions, $[15.9]1 \leftarrow X^1\Sigma^+$ and $[16.2]0^+ \leftarrow X^1\Sigma^+$ were found and analyzed. Here lower and upper limits of the ionization energy of TiFe, lower limit of the bond dissociation energy, ground and excited state rotational constants, bond lengths, Ω values, band origins, the excited state vibrational frequency and anharmonicity, excited state lifetimes, and ground state electronic configuration are reported. For the most abundant isotopomer, $^{48}Ti^{56}Fe$, T_0 =15851.95(84) cm^{-1}, ω'_e = 344.309(741) cm^{-1}, $\omega'_e x'_e$ = 2.822(104) cm^{-1}, for the $[15.9]1 \leftarrow X^1\Sigma^+$ vibrational progression, and T_0 =16183.42(502) cm^{-1}, ω'_e=349.51(322) cm^{-1}, $\omega'_e x'_e$= 5.021(352) cm^{-1}, for the $[16.2]0^+ \leftarrow X^1\Sigma^+$ vibrational progression. Both progressions originate from the same ground state, $X^1\Sigma^+$, which is formed by pairing up all 12 valence electron, in a $1\sigma^2 1\pi^4 2\sigma^2 1\delta^4$ electronic configuration. For the most abundant TiFe isotopomer, the ground state rotational constant B_0"=0.225228(31) cm^{-1}, and bond length r_0"=1.70268(12) Å.

The results of this work demonstrate striking similarities between the two 12 electron molecules, ZrFe and TiFe, and show that, just that like CrMo and Cr_2, they are best viewed as sextuply-bonded diatomic transition metals.

1.3 References

(1) Brand, J. C. D. *Lines of Light. The Sources of Dispersive Spectroscopy, 1800-1930*; Gordon and Breach Publishers, 1995.

(2) Newton, I. *Philos. Trans. R. Soc. London* **1671**, *6*, 3075.

(3) *Methods of Experimental Physics*; Williams, D., Ed.; Academic Press, 1976; Vol. 13, part A.

(4) Oyama, S. T. *in The Chemistry of Transition Metal Carbides and Nitrides*; Blackie Academic and Professional, London, 1996.

(5) Santhanam, A. T. *in The Chemistry of Transition Metal Carbides and Nitrates*; Blackie Academic and Professional, London, 1996.

(6) Ilchenko, N. I., Pyatnitsky, Yu. I., *in The Chemistry of Transition Metal Carbides and Nitrides*; Blackie Academic and Professional, London, 1996.

(7) Sickafoose, S. M.; Smith, A. W.; Morse, M. D. *J. Chem. Phys.* **2002**, *116*, 993.

(8) Li, X.; Liu, S. S.; Chen, W.; Wang, L.-S. *Journal of Chemical Physics* **1999**, *111*, 2464.

(9) Jansson, K.; Scullman, R.; Yttermo, B. *Chem. Phys. Lett.* **1969**, *4*, 188.

(10) Jansson, K.; Scullman, R. *Journal of Molecular Spectroscopy* **1970**, *36*, 248

(11) Marr, A. J.; Flores, M. E.; Steimle, T. C. *Journal of Chemical Physics* **1996**, *104*, 8183.

(12) Ma, T.; Leung, J. W. H.; Cheung, A. S. C. *Chem. Phys. Lett.* **2004**, *385*, 259.

(13) Neuhaus, H.; Scullman, R.; Yttermo, B. *Zeitschrift fur Naturforschung* **1965**, *20a*, 162.

(14) Scullman, R.; Yttermo, B. *Arkiv for Fysik* **1966**, *33*, 231.

(15) Appelblad, O.; Barrow, R. F.; Scullman, R. *Proc. Phys. Soc., London* **1967**, *91*, 260.

(16) Appelblad, O.; Nilsson, C.; Scullman, R. *Physica Scripta* **1973**, *7*, 65.

(17) Steimle, T. C.; Jung, K. Y.; Li, B.-Z. *Journal of Chemical Physics* **1995**, *102*, 5937.

(18) Steimle, T. C.; Jung, K. Y.; Li, B.-Z. *Journal of Chemical Physics* **1995**, *103*, 1767.

(19) Beaton, S. A.; Steimle, T. C. *Journal of Chemical Physics* **1999**, *111*, 10876.

(20) Majumdar, D.; Balasubramanian, K. *Chemical Physics Letters* **1998**, *284*, 273.

(21) Balasubramanian, K. *Journal of Chemical Physics* **2000**, *112*, 7425.

(22) Meloni, G.; Thomson, L. M.; Gingerich, K. A. *J. Chem. Phys.* **2001**, *115*, 4496.

(23) Wang, J., Sun, X., Wu, Z., . *J. Cluster. Sci.* **2007**, *103*, 4046.

(24) Tan, H.; Liao, M.; Balasubramanian, K. *Chemical Physics Letters* **1997**, *280*, 219.

(25) Minaev, B. F. *Physical Chemistry Chemical Physics* **2000**, *2*, 2851.

(26) Barysz, M.; Pyykko, P. *Chemical Physics Letters* **1998**, *285*, 398.

(27) Krechkivska, O., Morse, M., D.,. *J. Chem Phys* **2008**, *128*, 084314.

(28) Krechkivska, O.; Morse, M. D. *J. Chem. Phys.* **2010**, *133*, 054309/1.

(29) Heaven , M. W., Stewart, G. M., Buntine, M. A., Metha, G. F.,. *J. Phys. Chem. A* **2000**, *104*, 3308.

(30) Cotton, F. A.; Harris, C. B. *Inorg. Chem. (Washington, DC, U. S.)* **1965**, *4*, 330.

(31) Cotton, F. A.; Curtis, N. F.; Harris, C. B.; Johnson, B. F. G.; Lippard, S. J.; Mague, J. T.; Robinson, W. R.; Wood, J. S. *Science (Washington, DC, U. S.)* **1964**, *145*, 1305.

(32) Cotton, F. A.; DeBoer, B. G.; Laprade, M. D.; Pipal, J. R.; Ucko, D. A. *J. Amer. Chem. Soc.* **1970**, *92*, 2926.

(33) Lawton, D.; Mason, R. *Journal of the American Chemical Society* **1965**, *87*, 921.

(34) Cotton, F. A.; Bratton, W. K. *Journal of the American Chemical Society* **1965**, *87*, 921.

(35) Efremov, Y. M.; Samoilova, A. N.; Gurvich, L. V. *Opt. Spectrosc.* **1974**, *36*, 381.

(36) Efremov, Y. M.; Samoilova, A. N.; Gurvich, L. V. *Chemical Physics Letters* **1976**, *44*, 108.

(37) Efremov, Y. M.; Samoilova, A. N.; Kozhukhovsky, V. B.; Gurvich, L. V. *Journal of Molecular Spectroscopy* **1978**, *73*, 430.

(38) Bondybey, V. E.; English, J. H. *Chemical Physics Letters* **1982**, *94*, 443

(39) Michalopoulos, D. L.; Geusic, M. E.; Hansen, S. G.; Powers, D. E.; Smalley, R. E. *Journal of Physical Chemistry* **1982**, *86*, 3914.

(40) Riley, S. J.; Parks, E. K.; Pobo, L. G.; Wexler, S. *Journal of Chemical Physics* **1983**, *79*, 2577.

(41) Spain, E. M.; Behm, J. M.; Morse, M. D. *Chemical Physics Letters* **1991**, *179*, 411.

(42) Hopkins, J. B.; Langridge-Smith, P. R. R.; Morse, M. D.; Smalley, R. E. *Journal of Chemical Physics* **1983**, *78*, 1627.

(43) Kraus, D.; Lorenz, M.; Bondybey, V. E. *PhysChemComm* **2001**, No pp. given.

(44) Roos, B. O.; Andersson, K. *Chemical Physics Letters* **1995**, *245*, 215.

(45) Ruiperez, F.; Aquilante, F.; Ugalde, J. M.; Infante, I. *Journal of Chemical Theory and Computation* **2011**, *7*, 1640.

(46) Borin, A. C.; Gobbo, J. P.; Roos, B. O. *Chemical Physics* **2008**, *343*, 210.

(47) Borin, A. C.; Gobbo, J. P.; Roos, B. O. *Chemical Physics Letters* **2010**, *490*, 24.

(48) Ruiperez, F.; Ugalde, J. M.; Infante, I. *Inorg. Chem. (Washington, DC, U. S.)* **2011**, *50*, 9219.

(49) Roos, B. O.; Borin, A. C.; Gagliardi, L. *Angew. Chem., Int. Ed.* **2007**, *46*, 1469.

(50) Nagarajan, R.; Morse, M. D. *Journal of Chemical Physics* **2007**, *127*, 074304/1.

(51) Huber, K. P.; Herzberg, G. *Constants of Diatomic Molecules*; Van Nostrand Reinhold: New York, 1979; Vol. IV.

(52) Lovas, F. J.; Johnson, D. R. *J. Chem. Phys.* **1971**, *55*, 41.

CHAPTER 2

RESONANT TWO-PHOTON IONIZATION SPECTROSCOPY

2.1 Introduction

By means of resonant two photon ionization spectroscopy we learn about the electronic structure, and the vibrational and rotational motions of the molecules of interest. In terms of electronic structure, spectroscopic studies can tell us how the electrons are distributed among the orbitals in the ground state, how this distribution is changed upon electronic excitation, as well as the location of these excited states. Once the information about excited states is gathered in low-resolution survey scans, some of the excited vibronic states that are observed may be grouped into progressions, fitting their energies to a standard formula that provides vibrational constants and anharmonicities; these parameters provide insight into the potential energy function for the molecule in the excited state. When investigated under higher resolution, these transitions yield rotationally resolved spectra. Fitting a rotationally resolved spectrum is more complicated and sometimes quite challenging, but once successful, it provides band origins, isotope shifts, ground and excited state rotational constants for different isotopomers, hyperfine parameters for magnetically active nuclei, lambda-doubling parameters, etc. For a diatomic molecule a simple formula converts the rotational constant into bond length. The change in bond length upon excitation, along with the Ω-

values (the projection of total electronic angular momentum on the internuclear axis) of the upper and lower states, provide information about the molecular orbitals involved in a particular excitation.

The molecules of interest in the Morse research laboratory are metal dimers, metal clusters, and unsaturated metal-ligand complexes. These molecules are highly reactive and readily combine with other species to produce more stable chemical species. To probe these highly reactive species, the resonant two photon ionization spectroscopy technique has been coupled with a molecular source that employs laser ablation of a metal target disk in a stream of carrier gas followed by supersonic expansion into vacuum. This provides a means of creating the molecules of interest, cooling them in the supersonic expansion, and eliminating their further reaction to form more thermodynamically stable species. The narrow velocity distribution of the molecules in the molecular beam leads to an isolated collection of molecules in the gas phase in a collision-free environment.

2.2 Resonant Two Photon Ionization Instrument

The resonant two photon ionization apparatus consists of two vacuum chambers that serve different purposes. Molecules are created, supersonically cooled, and collimated in the first chamber, so that when they reach the second chamber they have been cooled to low temperatures, and travel in a packet with similar velocities in the axial direction, and small velocities in y and z directions. In the second chamber molecules interact with light generated by a dye laser and an ultraviolet laser. If this interaction leads to ionization, the ion is mass analyzed by reflectron time of flight mass spectrometry and detected by a microchannel plate detector. The two chambers are

separated by a 4" gate valve, to allow the user to keep the mass spectrometer under vacuum while the source chamber is serviced.

A schematic of the instrument is presented in Figure 2.1. The chamber on the left side of the schematic is the source chamber. It contains the pulsed supersonic nozzle (series 9, Parker Hannifin corporation), rotating and translating target disk mount, and molecular beam skimmer (1 cm diameter, 50° inside angle). Beginning at atmospheric pressure, the source chamber is first evacuated by a mechanical pump to about 0.03 Torr. Subsequently, the mechanical pump is used to back a VHS-10 diffusion pump, which evacuates the chamber to about 6×10^{-6} Torr. The diffusion pump is separated from the main chamber by a 10" gate valve to permit access to the chamber without waiting for the diffusion pump to cool. The experiments presented in this dissertation were conducted under conditions in which the ion gauge reading was in the range of 5-8 $\times10^{-5}$ Torr for the main chamber, for OsC and TaC, and 1-2 $\times10^{-4}$ Torr for ZrFe and TiFe.

The chamber on the right side of Figure 2.1 is the spectroscopy chamber. This chamber houses a reflectron-type time-of-flight mass spectrometer with Wiley-McLaren ion source optics[1,2] and a dual microchannel plate detector (Burle, model APD 3025 MA 12/10/12 D). In the spectroscopy chamber molecules are probed by dye laser (Lambda Physik ScanMate Pro) radiation and ionized by excimer laser (Lambda Physik COMPex) radiation about 40 ns later in time. As soon as ions are created they are accelerated up the first flight tube by the electric field. As they reach the top, they are reflected down the second flight tube, and at the end of their journey strike the microchannel plate detector. The reflectron-type time-of-flight mass spectrometer improves the mass resolution and will be discussed in detail later in this chapter.

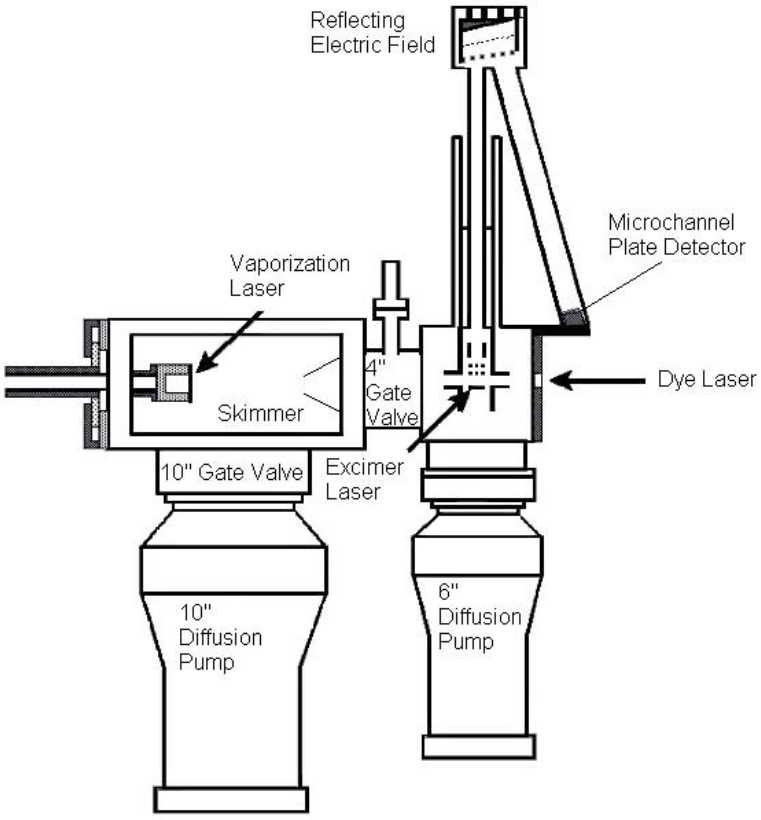

Figure 2.1. Schematic of the resonant two photon ionization instrument.

The spectroscopy chamber is evacuated by an Edwards 160 diffusion pump, backed by a Welch 1397 rotary mechanical pump. The spectroscopy chamber is kept under vacuum even when it is not in use, to prevent the microchannel plate detector from being damaged.

2.3 Molecular source

The molecules studied in the Morse laboratory, many of which are unsaturated and highly reactive metal complexes, present a certain challenge to the investigator. In order to study them one must find a way to isolate or trap these molecules, probe with laser radiation and detect the resulting signal in a timely manner. A schematic drawing of the molecular source used in the Morse laboratory is presented in Figure 2.2. It utilizes laser ablation of a metal target disk followed by supersonic expansion into vacuum to create the molecules of interest and trap them as isolated molecules in the gas phase for the duration of the experimental cycle.

A typical metal sample is a pure metal or a metal alloy disk, 2.5 cm in diameter and 2 mm thick. If the molecule of interest is a metal dimer, ultra high purity (99.98%) helium is used as the carrier gas. If the molecule of interest is a metal-ligand complex, the helium carrier gas is seeded with small percentage of a gas that provides the ligand. For example, for the investigation of OsC, helium seeded with 3% methane was used. In contrast, 0.25% methane in helium was found to be optimal for production of TaC. These studies are presented in Chapters 3 and 4 of this dissertation.

The metal sample disk is glued to a sample holder, which is rotated and translated back and forth using a mechanism that consists of a motor, a cam, and a set of gears. This

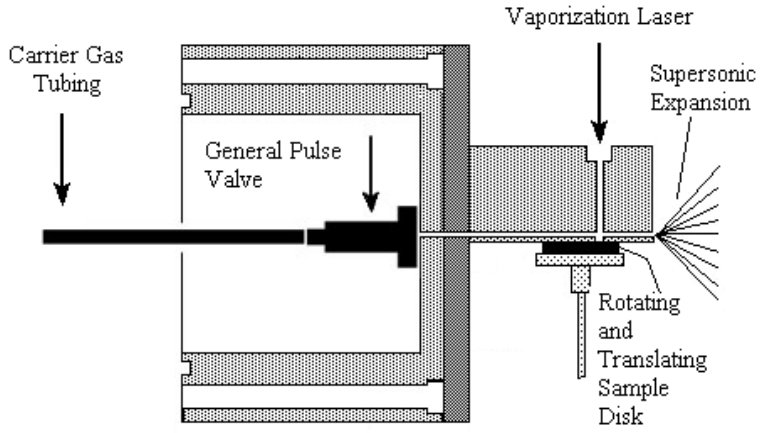

Figure 2.2. Schematic of the molecular source.

rotates and translates the sample to prevent the vaporization laser from drilling a hole through it. The assembly also pushes the sample against a stainless steel block so that the surface can be ablated without allowing gas to leak out between the sample and the block. The vaporization laser radiation is focused onto the sample using a 20" focal length lens, with the metal sample placed at the focus, so that only a small amount of a sample's surface is ablated during each experimental cycle. As the sample moves, a spiral pattern is traced out on the sample by the ablation laser due to the combined rotational and translational motion. A pulsed Nd-YAG laser (1064, 532 or 355 nm, 5 ns pulse width) is used for ablation purposes, with approximately 10 mJ/pulse measured at the vaporization block.

The vaporization block is a stainless steel block with two perpendicular narrow channels drilled through it. One channel allows the vaporization radiation to strike the sample, while the other directs the carrier gas over the sample surface. As the vaporization laser hits the metal sample, atoms, ions and electrons are boiled off the surface, creating a hot plasma.[3] The vaporization laser pulse is timed to coincide with the carrier gas pulse, so that the plasma that is created is simultaneously entrained in the carrier gas. While flowing down the expansion channel, the ablated atoms undergo collisions with each other, with the seeded reactant gas, and with the carrier gas, creating new species in the beam and destroying others. There is no fine control over what species are produced in the molecular beam. Usually atoms, oxides, and larger clusters are always present in the molecular beam. For some metal-ligand diatomic molecules or metal dimers, conditions have to be just right for them to be produced in the beam and observed in the mass spectrum. As an example, we found that specific conditions are

required to produce the TaC diatomic molecule. Using a pure Ta disk as a target and 3% methane in the helium carrier gas, no trace of TaC was found in the mass spectrum, even though Ta, TaO and Ta_2 signals were very strong. Keeping the other conditions unchanged, we decided to try a reduced concentration of methane in He, of 1%. The same species as before were present, but a small TaC peak became visible after summing 1000 experimental mass spectra, or shots. Following the same route and decreasing the methane concentration to 0.25%, a strong TaC signal was observed.

Conditions that can be varied in order to optimize molecular signal, or even try to find one are: concentration of the seeded gas in the carrier gas, backing pressure, duration of the nozzle pulse, wavelength and pulse energy of the vaporization laser, wavelength of the ionization laser, and the use of extension channels, or extenders. An extender is a metal tube, with a channel drilled through it, that is attached at the end of the vaporization block. It extends the length of the expansion channel and therefore increases the time that molecules spend in the high pressure region, allowing more time for reactions to occur. A variety of extenders, with different length and channel diameters have been employed to optimize production of the molecule of interest.

As the gas pulse and its entrained species leave the narrow channel, they undergo an expansion into the vacuum of the chamber. This is called a supersonic expansion and is discussed below.

2.4 Supersonic expansion

Usually in R2PI spectroscopy, the colder the molecules - the better. However, exceptions to this rule exist. For example, in the NbCr molecule[4] low-J rotational lines exhibit a large hyperfine splitting due to the Nb nuclear spin (I=9/2) and its large nuclear

magnetic moment.[5] The large number of hyperlines present within the low-*J* lines led to a congested spectrum that could not be resolved or assigned. It was recognized, however, that this molecule belongs to Hund's case (a_β), where the hyperfine splitting decreases with increasing rotational quantum number. As a result, warming the molecules led to an assignable rotationally resolved spectrum.[4] This was achieved by the use of a special expender that was designed to limit the amount of cooling in the supersonic expansion.

In a cold molecular beam, generally only the ground electronic state is populated. This simplifies the vibronically resolved spectrum considerably, because only transitions that originate from the ground state are present. In rare cases a very low-lying excited electronic state may be present, and transitions from this state may also be observed. Low vibrational temperatures are also typically achieved, often with only v=0 or, rarely, v=1 populated. This also simplifies the spectra, allowing vibrational features to be grouped into band systems, if perturbations among the excited states are not too severe. Finally, low rotational temperatures provide the benefit of concentrating the population in a smaller number of rotational levels, making for better signal intensities. This makes the first lines in each branch easier to identify, providing Ω-values for the ground and excited electronic states.

In the current experimental setup in the R2PI laboratory, molecules escape from a high pressure reservoir through a circular hole, with the diameter of ~2 mm, so the mean free path, λ_0, is much smaller than D, the nozzle diameter. This case is well-described by the idealized continuum model.[6] Under the adiabatic assumption and for a calorically perfect gas, the maximum velocity of the flow is

$$u_{\max} = \sqrt{\frac{2C_P T_0}{m}}, \qquad (2.1)$$

where C_p is the constant-pressure heat capacity, T_0 is the temperature of the reservoir in K, and m is the mass per mole of carrier gas. For helium that is expanding from a high pressure reservoir at room temperature, this formula provides a terminal velocity of the beam of 1.77×10^5 cm/s. Compared to the other unreactive noble gases, helium is relatively inexpensive and is not at all prone to clustering. Therefore, it is the carrier gas of choice in our R2PI experiments. An adiabatic isentropic expansion of a calorically perfect gas governed by the ideal gas law gives the following relations between the initial and final properties[6]

$$\frac{T_1}{T_0} = \left(\frac{p_1}{p_0}\right)^{(\gamma-1)/\gamma} \qquad \frac{\rho_1}{\rho_0} = \left(\frac{p_1}{p_0}\right)^{1/\gamma} \qquad \text{and} \qquad \frac{\rho_1}{\rho_0} = \left(\frac{T_1}{T_0}\right)^{1/(\gamma-1)}, \qquad (2.2)$$

where T_0, ρ_0, and p_0, are the temperature, density and pressure before the expansion, T_1, ρ_1, and p_1 are the corresponding quantities after expansion, and γ is the heat capacity ratio, c_p/c_v. As the expansion occurs, the drop in pressure causes the drop in temperature, which is very beneficial for obtaining analyzable spectra. The seemingly mysterious name of this phenomenon, supersonic expansion, comes from the fact that the expanding beam moves much faster than the local speed of sound, which depends on the local temperature. As the temperature drops during the expansion, so does the local speed of sound. It is not difficult to attain conditions where the beam velocity is a factor of 30 greater than the local speed of sound. During supersonic expansion, as the density of the expanding molecular beam decreases, and the distribution of velocities becomes more

narrow, both the collision energy and collision frequency also decrease. Low energy collisions with the carrier gas removes energy from the molecules, leading to cooling of all of the degrees of freedom. Low energy collisions are most effective, however, in cooling the motions with closely spaced quantum levels, so translations and rotations are cooled most effectively. Most of the vibrational and electronic relaxation occurs in the high density region of the expansion, or in the channel prior to expansion, where many more collisions occur, and at a higher collision energy. On the other hand, rotational and translational relaxation continues even in the low density region of the expansions. In the current experimental setup vibrational temperatures of ~ 100°K and rotational temperatures of ~ 10°K are often achieved. Translational temperatures are not generally measured, but are probably below 1°K.

2.5 Resonant two-photon ionization process

As the molecular beam leaves the vaporization channel, it undergoes the supersonic expansion and moves towards the skimmer (1 cm diameter, 50° inside angle). Molecules that have substantial velocity in the transverse directions hit the skimmer and remain in the main chamber. Having a skimmer serves two purposes: it keeps the pressure in the spectroscopy chamber lower than in the main chamber, and provides a collimated beam for the spectroscopy chamber, which is necessary due to the finite dimensions of the probe region, where the molecules are excited, ionized, and extracted by an electric field.

Resonant two photon ionization spectroscopy receives its name from the fact that two photons are used to probe the molecules, using laser pulses slightly separated in time, usually by a few tens of nanoseconds, or less. The two laser pulses are capable of

ionizing the molecule, a process that is enhanced when the first laser pulse is resonant with an electronic transition in the molecule.

The first laser pulse that interacts with the molecular beam is counterpropagated along the molecular beam axis and is provided by a Lambda Physik Scan MatePro dye laser, pumped by a Continuum Surelite II Nd:YAG laser, operating on either the second or the third harmonic, at 532 or 355 nm. The dye laser has a spectral range from 11000 to 25000 cm^{-1}, and depending on the region can provide 5-20 mJ in low resolution mode. High dye laser power is necessary while attempting to expand the spectral range by means of Raman shifting,[7] but for ordinary low resolution scans about 5 mJ is typically sufficient. The dye laser beam cross section is increased by a lens to about 1 cm^2, to maximize its overlap with the molecular and excimer beams.

The second laser pulse is fired about 40 ns after the first one, crosses the molecular beam at right angles (see Figure 2.1) and is provided by a Lambda Physik COMPex excimer laser. It can operate on three gas mixtures, KrF (248 nm, 5.0 eV), ArF (193 nm, 6.42 eV) and F_2 (157 nm, 7.9 eV). Operation on the first two mixtures is straightforward, while the F_2 emission lies in the vacuum ultraviolet and is immediately absorbed by the oxygen in the air. To prevent this from happening, a metal tube is attached between the exit port of the excimer and a window of the spectroscopy chamber. This tube is constantly flushed with nitrogen at a slow flow rate, so that the laser pulse never travels through the air and is able to reach the chamber.

The choice of the gas mixture for the excimer laser is not always straightforward. A molecule of interest can be one photon ionized by the excimer laser, causing the molecular signal to be very strong, so that no resonant enhancement can be observed.

Under this circumstance, a researcher can scan the entire spectral range of the dye laser and no transitions will be observed. Another challenge arises when the metal atom is resonant with the ionization wavelength used, as occurs when KrF (248-248.25 nm) is employed in the presence of Ta or Fe atoms, for example. In this situation the atomic signal is enormous, causing ringing of the detector signal. When this occurs, a sequence of very strong peaks is observed following the atomic peak, separated by about 1 atomic mass unit (amu), slowly decaying with increasing mass. Depending on the excimer pulse energy and the population of atoms in the molecular beam, the ringing of the signal can obscure masses lying 10 to 100 amu above the atomic mass, burying the signal of the molecule of interest if it falls in this range. This can make the experiment impossible to conduct using this ionization wavelength. To overcome this problem in my studies of the Fe-containing molecules, TiFe and ZrFe, the fifth harmonic of the Nd:YAG Brilliant B laser (5mJ/pulse, 212.8 nm) was employed for the ionization wavelength.

The ultimate goal of the R2PI process is to create ions that will be accelerated by the electric field, separated by mass and detected. However, ionization can be achieved in several different ways, and unfortunately not all of them provide useful information about the molecule. Several different ionization pathways are depicted in Figure 2.3. Figure 2.3 (a) presents the situation in which the combined energy of the dye laser and excimer photons is not enough to ionize the molecule. As a result, this excited state, even if the transition is strongly allowed, will not be seen in the spectrum. This situation is not uncommon and was observed for both OsC and TaC, where below 8.73 eV[8] and 8.68 eV,[9] respectively, no electronic transitions were observed. Although unfortunate, this fact

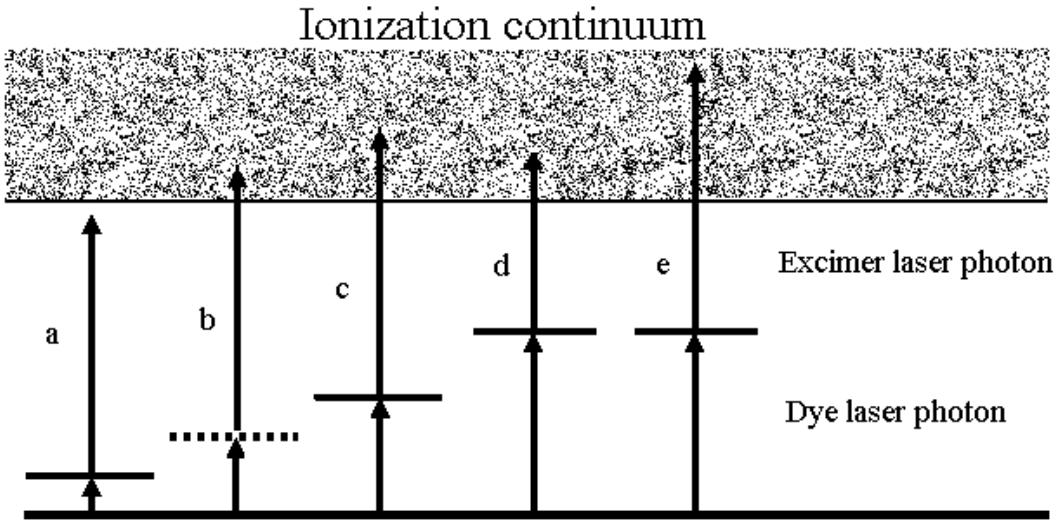

Figure 2.3 Several ionization schemes in the R2PI experiment: (a) - the first photon is absorbed through a resonant state, but even combined with the ionization laser photon, the energy is not enough to ionize the molecule, so this excited state is not seen in the spectrum; (b) - two color ionization through a virtual state; (c) - two color ionization through a resonant state; (d) - one color ionization through a resonant state, a possible scheme when the dye laser photon has energy greater than half of the ionization energy of the particular molecule; (e) - two color ionization through the same resonant state.

can provide a crude estimate of the ionization energy for these molecules. In the process shown in Figure 2.3 (b), the molecule is two photon ionized through a virtual state, which is not a real state, but rather represents weighed contributions from all the real eigenstates. The rate of two-photon ionization is proportional to[10]

$$P_{i\to f} \propto \left| \sum_j \frac{\left\langle f\left|\hat{V}\right|j\right\rangle \left\langle j\left|\hat{V}\right|i\right\rangle}{(\omega-\omega_{ji})+i\Gamma_j} \right|^2 . \qquad (2.3)$$

In this equation i, j, and f represent real eigenstates; ω_{ji} is the frequency difference between the initial state i and an intermediate state j; ω is the dye laser photon frequency, and Γ_j represents the energy width of state j due to decay processes. A molecule in the initial state, i, is promoted to the final state, f, by two interactions with the radiation field, as indicated by the presence of the transition moment operator $\hat{V}$, which occurs twice in equation (2.3). In one interaction the initial state i is carried to the intermediate state j, which is carried to the final state f via a second interaction with the field. Each possible intermediate state, j, provides a path to the final state, f. The amplitude of these various paths then interfere, either constructively or destructively, as indicated by the summation over j. Even tuned off resonance with any of the intermediate states, the rate of two photon ionization remains nonzero, contributing to a background signal. When the frequency of the dye laser, ω, is in resonance with any of the ω_{ji}, the denominator approaches zero and the rate increases quite dramatically and is dominated by one member of the summation. This is shown in Figure 2.3 (c) as a two color ionization process through a resonant state. This, of course, only occurs if the transition moment, $\left\langle j\left|\hat{V}\right|i\right\rangle$, is non-zero.

When the dye laser photon has energy greater than half of the ionization energy of the particular molecule, one color ionization through a resonant state is possible. This is depicted in Figure 2.3 (d), along with two color ionization, in Figure 2.3 (e).

An experimental mass spectrum of atomic Os and diatomic OsC is presented in Figure 2.4. The dye laser was tuned off of resonance in Figure 2.4 (a), and tuned to a resonance in Figure 2.4 (b), causing enhancement in the molecular signal.

2.6 Reflectron-type time of flight mass spectrometer

In 1973 Mamyrin *et al*[2] introduced an energy focusing device, known as a reflectron, which consists of a set of ion optics that folds the time of flight tube into two segments. Generally, a reflectron utilizes an electric field to turn the ion trajectories by almost 180°. More energetic ions penetrate deeper into the reflecting electric field compared to the less energetic ones, evening out the flight time. This lets ions of the same mass arrive at the detector nearly simultaneously, improving the resolution of the instrument. In the current experimental setup ion trajectories are turned by 162°, which allows placement of the detector off the initial ion trajectory and away from the extraction region.

A schematic diagram of the reflectron-type time of flight mass spectrometer employed in the Morse laboratory is presented in Figure 2.5. As was discussed previously, different processes by which ions are formed can exist, but resonant two photon ionization occurs in the small region where the beams from the dye laser and excimer laser overlap with the molecular beam. Ionization occurs in the small region

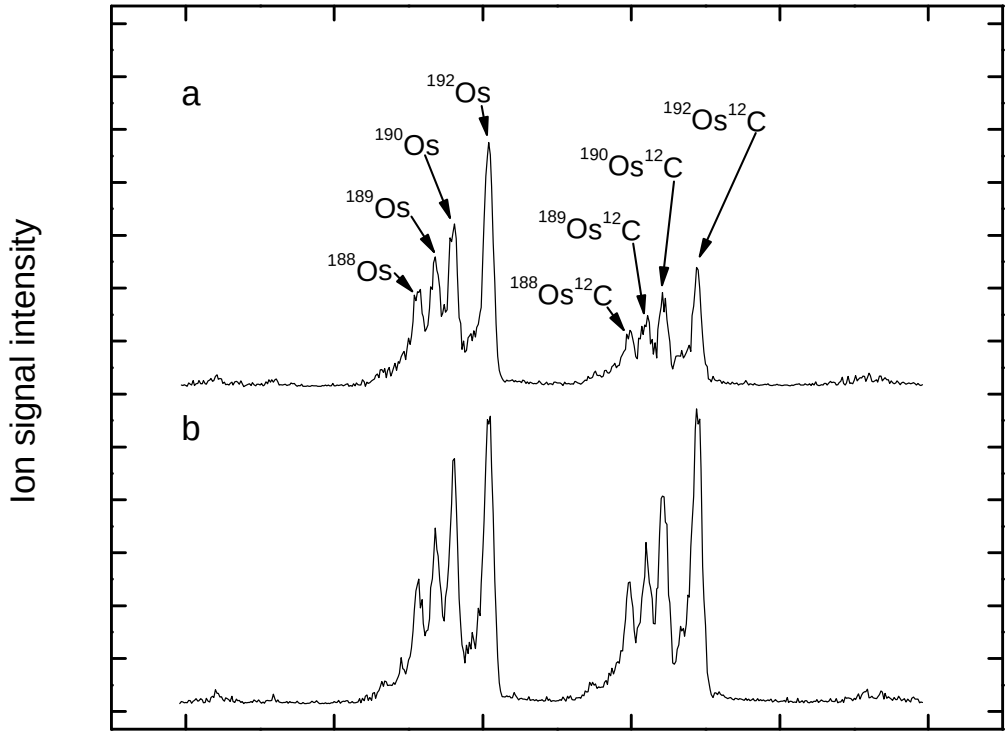

Figure 2.4 A mass spectrum of atomic Os and OsC; (a) mass spectrum was recorded with dye laser tuned away from resonance, (b) dye laser was tuned to a resonant frequency, that caused an enhancement in the OsC molecular signal.

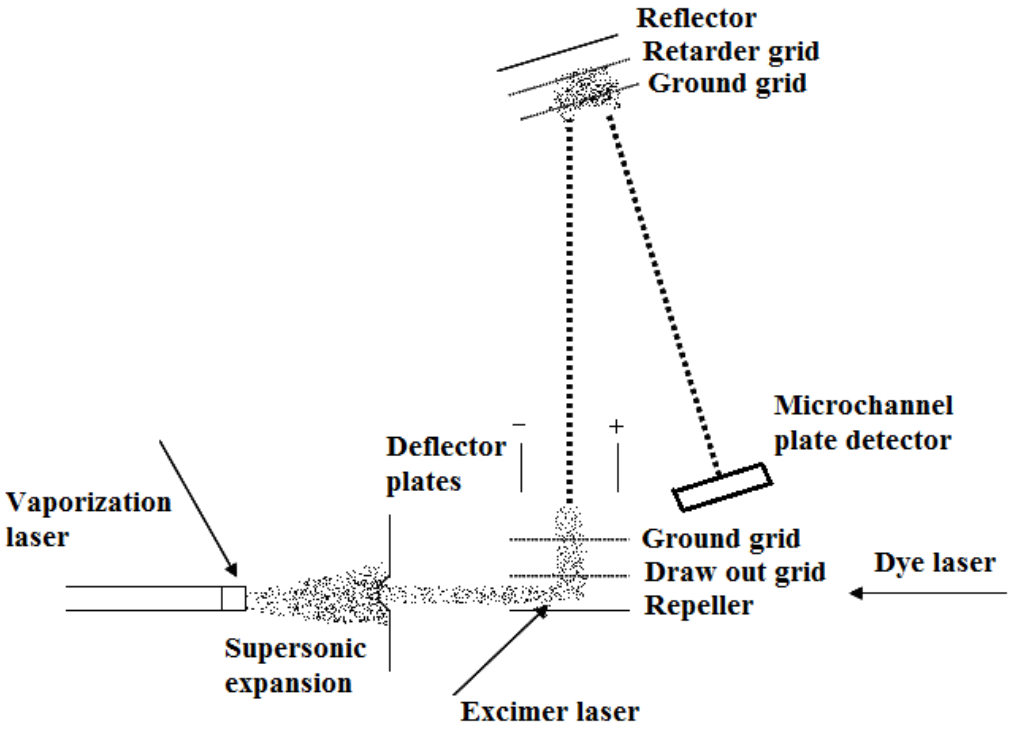

Figure 2.5. Schematic of the reflectron time of flight mass spectrometer.

between the repeller and draw-out grids, which are separated by distance s_0. A positive voltage, V_0, placed on the repeller, in combination with the smaller voltage V_1, placed on the draw-out grid, imposes an electric field, E_1, on the ionization region, given by

$$E_1 = \frac{V_0 - V_1}{s_0}. \tag{2.4}$$

This accelerates ions up to the second electrode. In the region between the draw-out grid and the ground grid, which are separated by distance s_1, the ions are further accelerated by electric field E_2, given by

$$E_2 = \frac{V_1}{s_1}. \tag{2.5}$$

The voltages V_0 and V_1 can be adjusted to bring ions of the same mass to a focus at a specific position in the flight tube, regardless of where they are produced in the ionization volume.[1] This becomes difficult to achieve, however, for long distances to the detector. If the ions are brought to a focus and then after the focus are reflected to the detector, it is possible to refocus the ions at the detector. The combination of a long path length and good ion focusing then leads to narrow peaks in the mass spectrum.

During acceleration by these electric fields, ions gain an ultimate velocity given by

$$v = \sqrt{\frac{2zeV_i}{m}}, \tag{2.6}$$

where V_i is the electrostatic potential at the location where the ion is produced, e is the electron charge, z is the ion charge, which is assumed to be unity, and m is the mass of the ion. We have never found multiply charged ions to be produced in these experiments.

As ions travel up the flight tube, they retain velocity in the direction of the molecular beam velocity, and will collide with the walls of the tube, never reaching the detector. To correct for this effect, deflector plates are placed above the extraction region. With voltage applied to the deflector plates, ions feel a transverse force that slows their forward motion so that they are able to reach the detector. Because the forward kinetic energy depends on the mass of the ion, the deflector plates must be adjusted slightly to optimize the signal of the ion of interest.

Voltages applied to the repeller, the draw-out grid, and the distances between them, s_0 and s_1, determine the focal length of the first stage of the mass spectrometer. As the ion packet travels up the first flight tube, it comes to a focus and becomes defocused again as it proceeds further up the tube. After passing through the ground grid on the reflector, the ions enter a region where they experience a retarding electric field due to the voltage applied to the retarder grid. A different electric field is experienced in the region between the retarder and the reflector. In this region the ion velocity is halted and reversed, with the ion trajectories being turned by 162°. Because the faster ions penetrate deeper into the reflecting field, they experience a longer flight time in this region and emerge later than the slower ions. In the second flight tube the faster ions catch up to the slower ones, coming to a second spatial focus. By adjusting the retarder voltage, this spatial focus is placed at the microchannel plate detector. Equation (2.5) can be re-written in terms of time t, and the distance that ions travel, L:

$$t = L\sqrt{\frac{m}{2eV}} \tag{2.7}$$

Ions with different masses will hit the detector at different times, and the time of flight spectrum is converted to a mass spectrum using equation (2.7).

As the ion packet hits the dual microchannel plate detector (Burle, model APD 3025 MA 12/10/12 D) an electron multiplication process is initiated that has a net gain of ~ 10^7. The detector is connected to a 50 Ω anode assembly to eliminate ringing of the signal.[11,12] The current produced by the microchannel plate detector is amplified and converted to a voltage by a preamplifier (Pacific Instruments- 2A50). The resulting voltage waveform is converted to a digital signal by a transient digitizer (Transiac 2001) that provides a digitized measurement every 10 ns, for a time period of 10.24 μs, therefore collecting a digitized waveform with 1024 points. Every digitized waveform corresponds to a mass spectrum, and to improve the signal to noise ratio, 30 waveforms are summed and displayed on the computer. Because of the repetition rate of the lasers, this experimental cycle is repeated at a rate of 10 Hz.

2.7 Newly assembled resonant two photon ionization apparatus

The instrument employed in ZrFe and TiFe studies is analogous to the one described earlier in this chapter, but with a few modifications. In brief, it consists of two vacuum chambers, the first one is being pumped by a Varian VHS-10 diffusion pump and backed by an Edwards E2M175 rotary mechanical pump. It houses a sample driver, an assembly that rotates and translates the sample disk, a pulsed supersonic valve (General Valves, Series 9), laser ablation assembly, and a skimmer (50° inside angle, 1.5 cm

diameter) that provides a roughly collimated molecular beam. A Q-switched Nd:YAG laser, 30-35 mJ/pulse, (1064 nm) is used for ablation of the sample.

The second chamber is pumped by a VHS-6 diffusion pump and backed by an Edwards RV12 mechanical pump. It houses a linear Wiley-McLaren[1] time-of flight mass spectrometer assembly and microchannel plate detector. The molecular beam was exposed to the output of the Nd:YAG (Continuum Surelite II) pumped tunable dye laser (Continuum ND6000), which counterpropagates along the axis of the molecular beam, and is crossed at right angles by the output of the fifth harmonic of the Nd:YAG Brilliant B laser (5mJ/pulse, 212.8 nm) about 50 ns later in time. The optical spectrum is collected mass spectrometrically; ions that are produced by the two-laser sequence are accelerated in the time-of-flight mass spectrometer and detected by a dual microchannel plate detector. The signal is amplified by a 350 MHz preamplifier (Stanford Research Systems, model SR445A) and digitized for analysis.

2.8 Data obtained in resonant two-photon ionization experiments

In resonant two photon ionization spectroscopy, optical spectra (both survey and rotationally resolved) are obtained mass-spectrometrically. Enhancement of a particular mass in the mass spectrum occurs due to a resonant absorption of a dye laser photon, and corresponds to a vibrational feature in a survey scan, or a rotational line in a high resolution scan. Therefore, before proceeding with optical scans, optimal conditions for creation of the molecule of interest are sought. Once the molecule of interest is present in the molecular beam in reasonable quantities, the ionization laser radiation is greatly reduced by quartz filters, to decrease the rate of one color ionization and therefore the baseline level. An excimer laser, operating on the ArF mixture (193 nm, 6.42 eV) was

used in the OsC and TaC studies. In the ZrFe and TiFe experiments, the 5th harmonic output (212.8 nm, 5.83 eV) of a Nd:YAG laser was employed for ionization purposes. Due to the low output energy produced by the laser at this wavelength, about 5mJ/pulse, no further attenuation was necessary.

2.8.1 Low resolution spectra

A Lambda Physik Scan MatePro dye laser, pumped by a Continuum Surelite II Nd:YAG laser was used for low (0.15 cm^{-1}) and high resolution (0.04 cm^{-1}) scans in both the OsC and the TaC studies. This laser has a spectral range from 11000 to 25000 cm^{-1}, which is divided into two regions, blue (17400-25000 cm^{-1}) and red (11000-18300 cm^{-1}), which require pumping by the third harmonic (355 nm) or second harmonic (532 nm) radiation, respectively. Depending on the dye, up to 40 nm can be scanned in the low resolution mode. Such long scans would be greatly affected by dye laser power curves, causing fluctuations in the background signal. Instead, a sequence of 10 nm scans was performed and the dye laser output was filtered down to the same energy/pulse value of about 5 mJ.

For the TiFe and ZrFe experiments a tunable dye laser (Continuum ND6000), pumped by a Continuum Surelite II Nd:YAG laser was used for both low (0.14 cm^{-1}) and high resolution (0.05 cm^{-1}) studies. For both the ZrFe and TiFe molecules, extremely weak vibrational progressions were found over the 13890-17500 cm^{-1} and 16100-19000 cm^{-1} regions, respectively. To help bring these features above the baseline noise, a high dye laser power was used, about 20-40 mJ/pulse, depending on the region.

Both dye lasers were operated on the following dyes: C 540A, C 500, C 480, C 460, C 440, and S 420 in the blue region (17400-25000 cm^{-1}); and LDS 925, LDS 867,

LDS 821, LDS 751, LDS 698, DCM, R 640, R 610, R 590, and Fl 548 in the red region (11000-18300 cm^{-1}).

Features visible in survey scans correspond to vibrational transitions within an excited electronic state. Depending on the molecule and the spectral region, survey scans can vary from those that have very few features present to very congested spectra, where no transitions may be grouped into progressions and all information is obtained from high resolution scans. Figure 2.6 displays a low resolution spectrum of diatomic TiFe over the 16300-21400 cm^{-1} region. The lower energy region displays a single vibrational progression, while the higher energy region exhibits complicated spectra with many transitions.

2.8.2 High resolution spectra

Vibronic transitions are further investigated under higher resolution to reveal their rotational structure. In high resolution studies of ZrFe and TiFe a Continuum ND6000 tunable dye laser was used (2400 lines/mm dual grating, 0.05 cm^{-1} resolution). It was discovered for ZrFe that some bands require high dye laser power (about 20 mJ/pulse) in order to record rotational spectra, with no signs of power broadening present. Others required low dye laser power (<0.1 mJ/pulse) to eliminate the effect of power broadening. This phenomenon will be discussed in section 5.3.1.2 of this dissertation. Figure 2.7 shows a rotationally resolved spectrum of the 7-0 band of the $[16.2]^3\Pi_{0+} \leftarrow X^1\Sigma^+$ band system of TiFe, for different isotopic combinations, as an illustration of a typical high resolution spectrum.

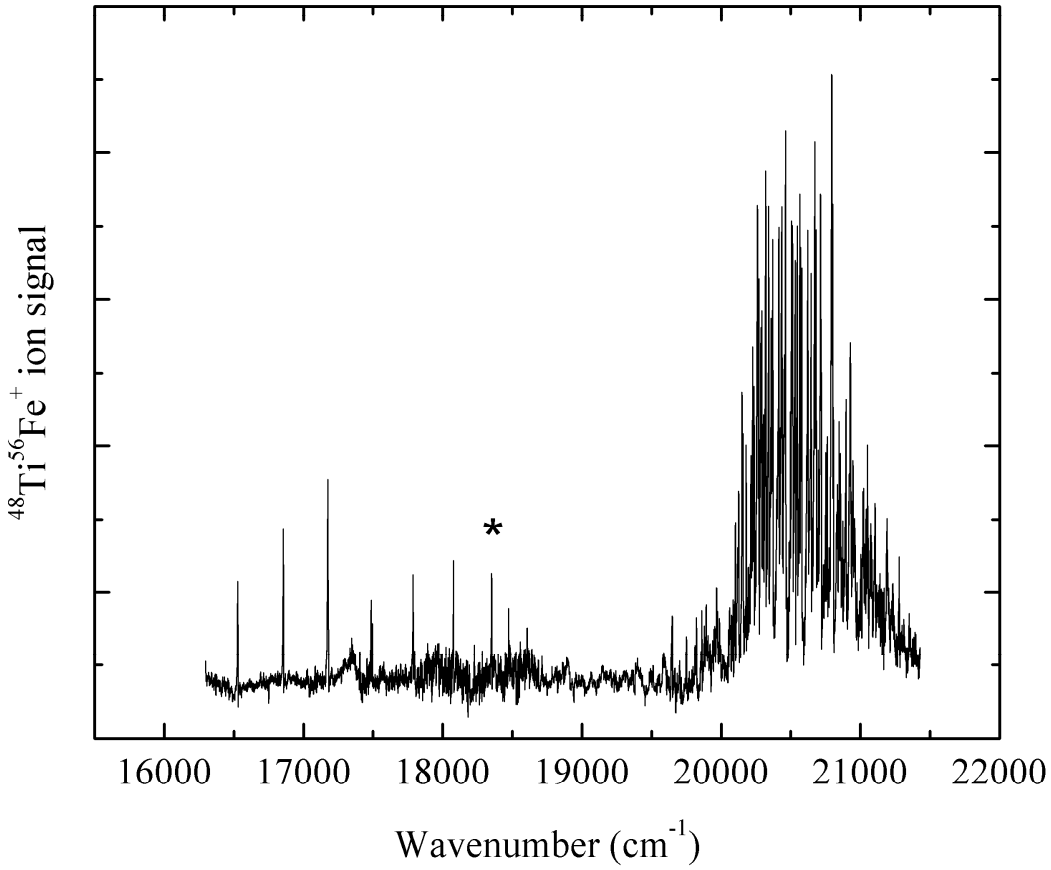

Figure 2.6. A vibronic spectrum over the 16300-21400 cm^{-1} region of TiFe diatomic molecule, as an illustration of a low resolution scan. The lower energy region displays a single vibrational progression, while the higher energy region exhibits many transitions. The feature with an asterisk is presented in Figure 2.7, scanned under high resolution.

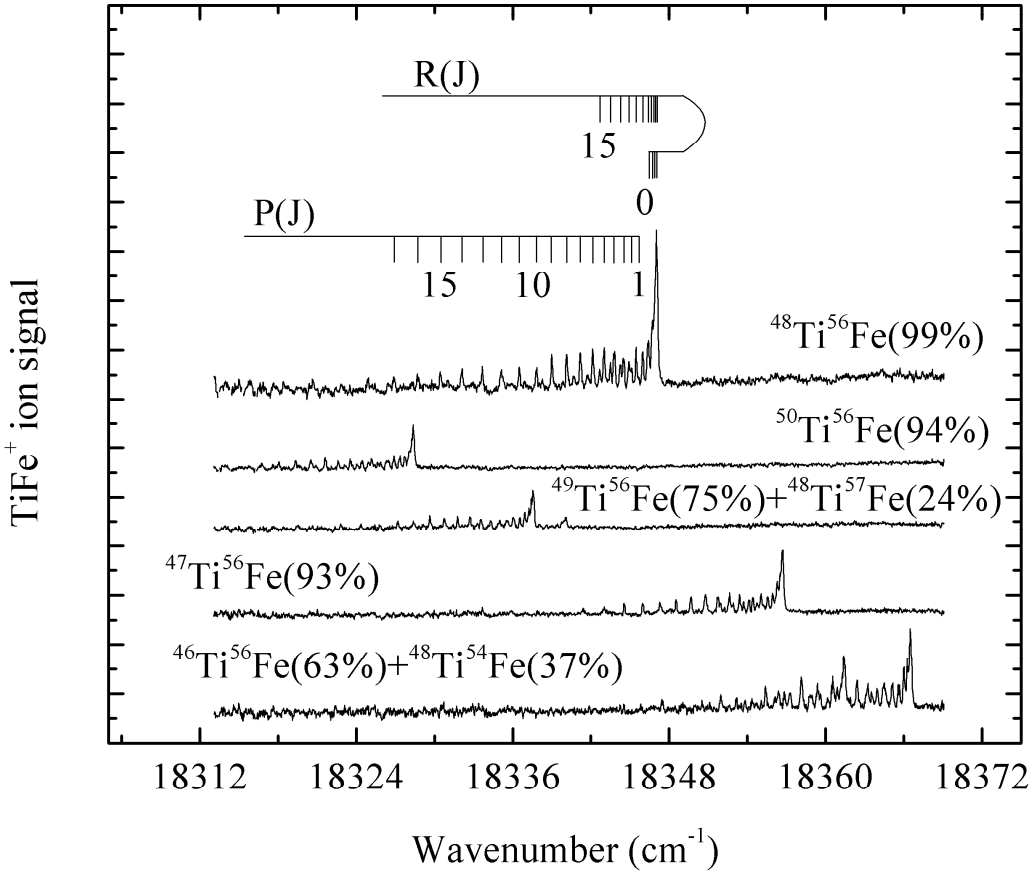

Figure 2.7. A rotationally resolved spectrum of the 7-0 band of the $[16.2]^3\Pi_{0+}\leftarrow X^1\Sigma^+$band system of TiFe, displaying different isotopic combinations.

For high resolution studies of OsC and TaC diatomic molecules, the Lambda Physik Scan MatePro tunable dye laser was used. In order to narrow its linewidth, an etalon is inserted into the oscillator cavity. This narrows the linewidth to 0.04 cm^{-1}, as compared to 0.15 cm^{-1} in low resolution mode. The oscillator cavity is then closed and evacuated to about 20 torr, after which the cavity is slowly pressurized with gas. The wavelength, λ, is fixed by the etalon and diffraction grating inside the cavity, but the index of refraction is changing during pressurization, meaning that the speed of light in this medium, c, is changing too. But, $c=\lambda \times \nu$, so the output frequency, ν, is changing as well. The gas used for pressure scanning should have a high index of refraction as compared to air, to allow a larger change in frequency to be achieved during the pressure scan, and it must be non corrosive. Sulfur hexafluoride (index of refraction n=1.000783 at 1 atm) satisfies both conditions and is used for pressure scanning in our experiments.

During a pressure scan, the pressure in the cavity is changed from about 20 torr to 800 torr, covering about 15 cm^{-1} in the blue region, and about 10 cm^{-1} in the red region. This range is scanned for 40-60 minutes, depending on the gas bleed rate. Usually three scans of the same region are collected and summed to improve the signal to noise ratio. During high resolution scans of OsC and TaC, the dye laser energy per pulse was filtered down to 1 mJ and less, to reduce or eliminate power broadening.

Simultaneously with the collection of the high resolution spectrum, about 10% of the dye laser output is reflected out of the main beam with a beam splitter and used to record etalon fringes and the absorption spectrum of a reference gas. Since the scanning rate might not be consistent throughout the scan, external etalon transmission peaks, or fringes, are used to linearize the spectrum. For calibration purposes, reference spectra of

iodine[13,14] or tellurium[15,16] are collected (for vibronic bands below and above 20000 cm^{-1}, respectively). Because the molecular beam is traveling toward the light source at a velocity of 1.77×10^5 cm/s, all measured line positions are shifted by small amount (0.10-0.12 cm^{-1}) to account for the Doppler shift.

2.8.3 Excited state lifetime measurements

Another piece of information that is obtained in the R2PI experiment about the molecule of interest, is the excited state lifetime, which is usually measured for every rotationally resolved vibronic band. For this purpose, the dye laser is set to excite a transition and the ion signal intensity is monitored as a function of the dye laser-ionization laser delay. The data are then fitted to an exponential decay curve using the Marquardt nonlinear least-squares algorithm.[17] A typical lifetime measurement is displayed in Figure 2.8, where the 18053 cm^{-1} level of ZrFe is found to have a lifetime of 145 ns. Three independent measurements of the lifetime are usually performed. The results are averaged and the standard deviation is calculated as well.

2.9 Analysis of vibronic spectra

2.9.1 Determination of ground state $\Delta G''_{1/2}$

The band difference histogram method, which proved to be successful in recent studies of ZrF and ZrCl,[18] can be used to determine the ground state vibrational interval, $\Delta G''_{1/2}$, for molecules that have complicated vibronic spectrum with many transitions. An example of such a spectrum is presented in Figure 2.9, where a 1000 cm^{-1} long portion of

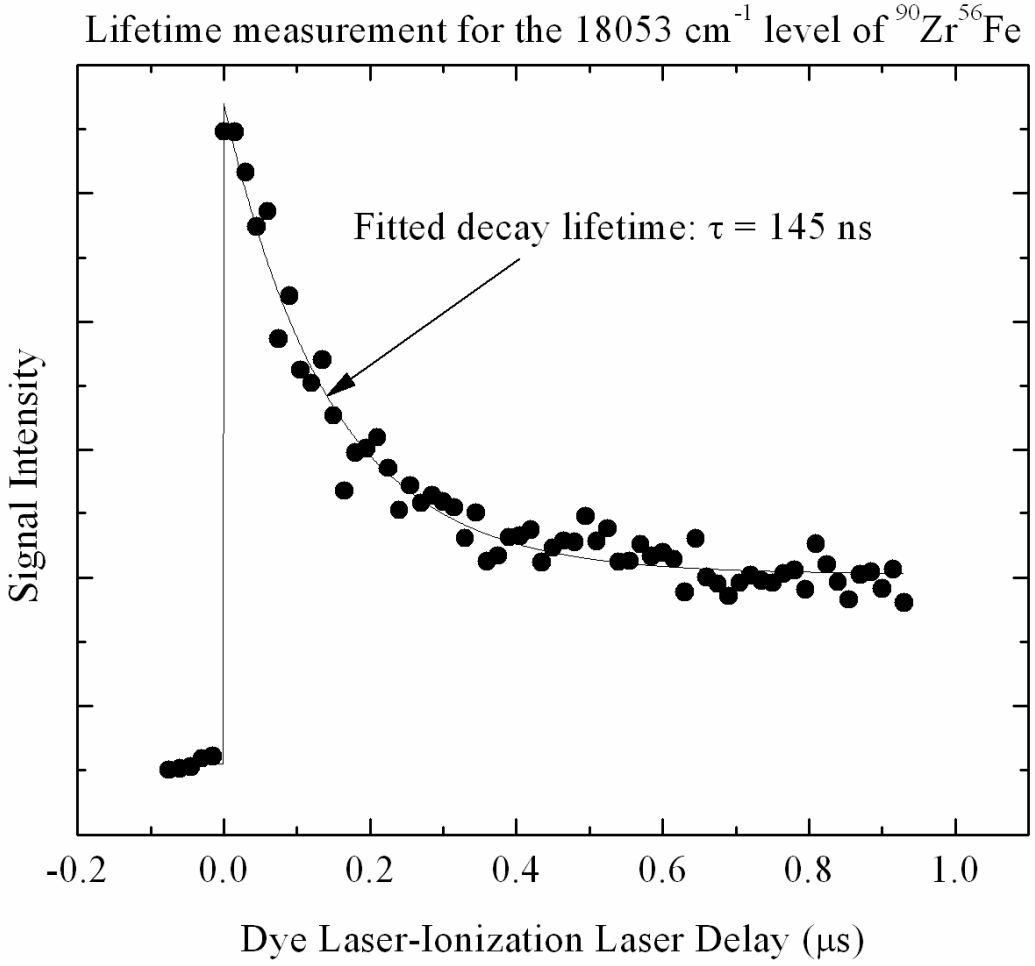

Figure 2.8 A typical excited state lifetime measurement. In this example, the decay curve returns to a higher baseline via processes that are explained in Chapter 5.

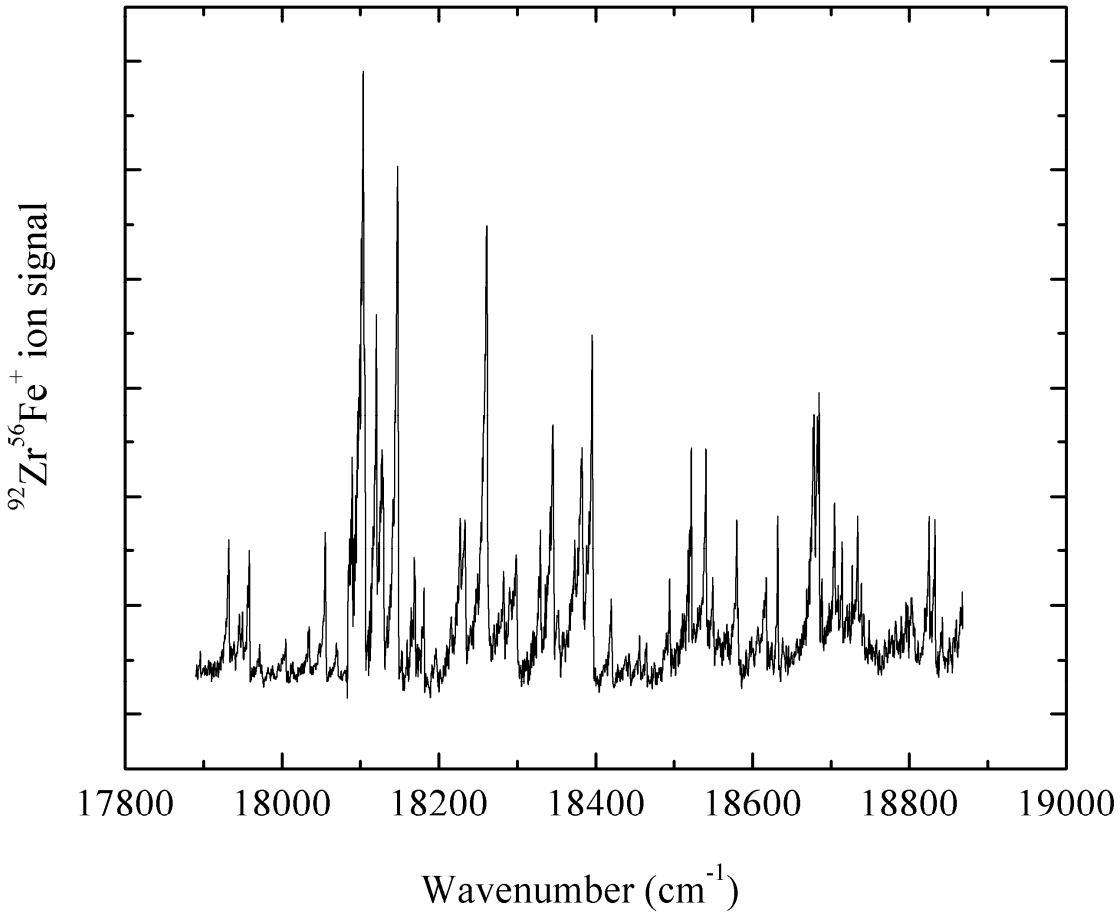

Figure 2.9 A portion of the ZrFe low resolution spectrum. Band head positions from this complicated region were used for the determination of $\Delta G''_{1/2}$ for $^{92}Zr^{56}Fe$

the $^{92}Zr^{56}Fe$ spectrum is displayed. Although the spectrum looks very congested and unassignable, it is nevertheless possible to extract an important piece of molecular information from it. To do so, the spectrum was calibrated using the observed transitions of atomic Zr and Fe, and the positions of the band heads were measured. Next, a list of the band head differences was generated by subtracting from each measured band head each of the band heads lying to lower energies. For a spectrum in which N band heads aremeasured, this leads to $(N^2 - N)/2$ band head differences. Next, each measured band difference was used to set up a Gaussian function centered on the wavenumber difference, with a width of 1 cm^{-1}. All of the $(N^2 - N)/2$ functions were then summed to give a continuous function that could be plotted over the range 200 – 800 cm^{-1}, as displayed in Figure 2.10 for $^{92}Zr^{56}Fe$. The idea is that every hot band is separated by the same amount from its corresponding cold band (ignoring the difference between band head location and band origin location), so the band differences that correspond to hot band/cold band pairs will add constructively, leading to a peak in the resulting band difference histogram plot. Application of this method to the vibronic spectra of ZrFe allowed the determination of the ground state vibrational interval for five different ZrFe isotopomers (see Chapter 5 and Appendix C of this dissertation).

2.9.2 Determination of vibrational numbering

For the molecules that display vibrational progressions in the low resolution spectrum, such as ZrFe and TiFe, the vibrational assignment is determined by the following procedure. All of the bands that belong to the progression are investigated under high resolution, therefore measured band origins and isotope shifts are known precisely.

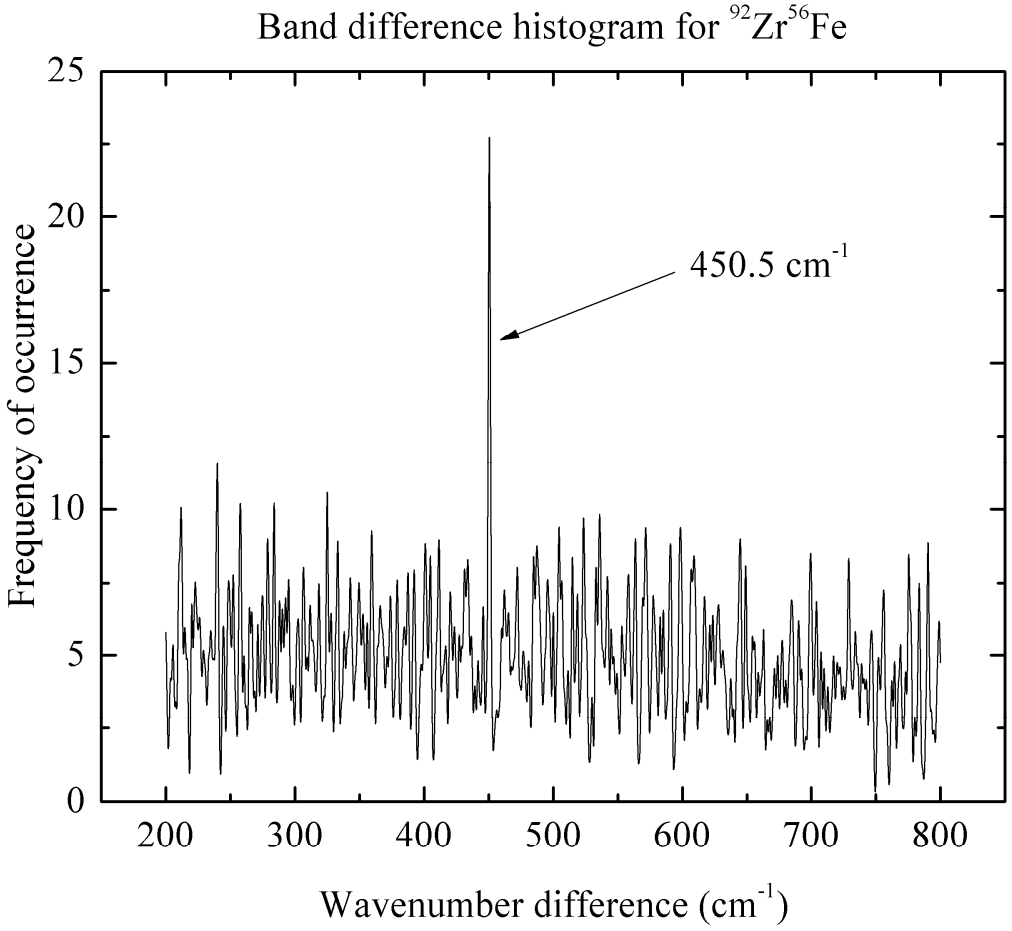

Figure 2.10 Band difference histogram plot for $^{92}Zr^{56}Fe$. A peak that appears at 450.5 cm^{-1} is assigned as $\Delta G_{1/2}$"

The isotope shift between the lighter and heavier isotopomers, $\nu_L - \nu_H$, for the *v'-0* band is related to the ground and excited state vibrational frequencies ω''_H and ω'_H and anharmonicities $\omega''_H x''_H$ and $\omega'_H x'_H$ of the heavy isotopomer according to:[19]

$$\nu_L - \nu_H = (\rho\text{-}1)[\omega_e'(v'+½) - \omega_e''(½)] - (\rho^2\text{-}1)[\omega_e' x_e'(v'+½)^2 - \omega_e'' x_e''(½)^2] \quad (2.8)$$

where ν_L is the band origin for the lighter isotopic combination, ν_H is the band origin forthe heavier isotopic combination, $\rho = \sqrt{\mu_H / \mu_L}$ is square root of the ratio between the reduced masses of the heavier and lighter isotopes, and υ' is the vibrational quantum number in the upper state.

In the case of ZrFe, the first band in the progression lies at 14250 cm^{-1}, so three different assignments were tested for it: assigning the band as the 0-0, 1-0 or 2-0 band. The upper state vibrational number, υ', was treated as a continuous parameter and predicted values for isotope shift are plotted against band origin. The measured band origins and isotope shifts are plotted as points and the curve that matches experimental points is the correctly determined vibrational numbering, see Figure 2.11.

2.9.3 Vibrational analysis of the band system

Usually all vibronic bands that belong to the vibrational progression are rotationally resolved, and provide precise measurements of band origins, $\nu_{\upsilon'-0}$, and correct vibrational numbering. Through a least-squares fit of the data to the relationship[19]

$$\nu_{\upsilon'-0} = T_0 + \omega_e'\upsilon' - \omega_e' x_e'(\upsilon'^2 + \upsilon'), \quad (2.9)$$

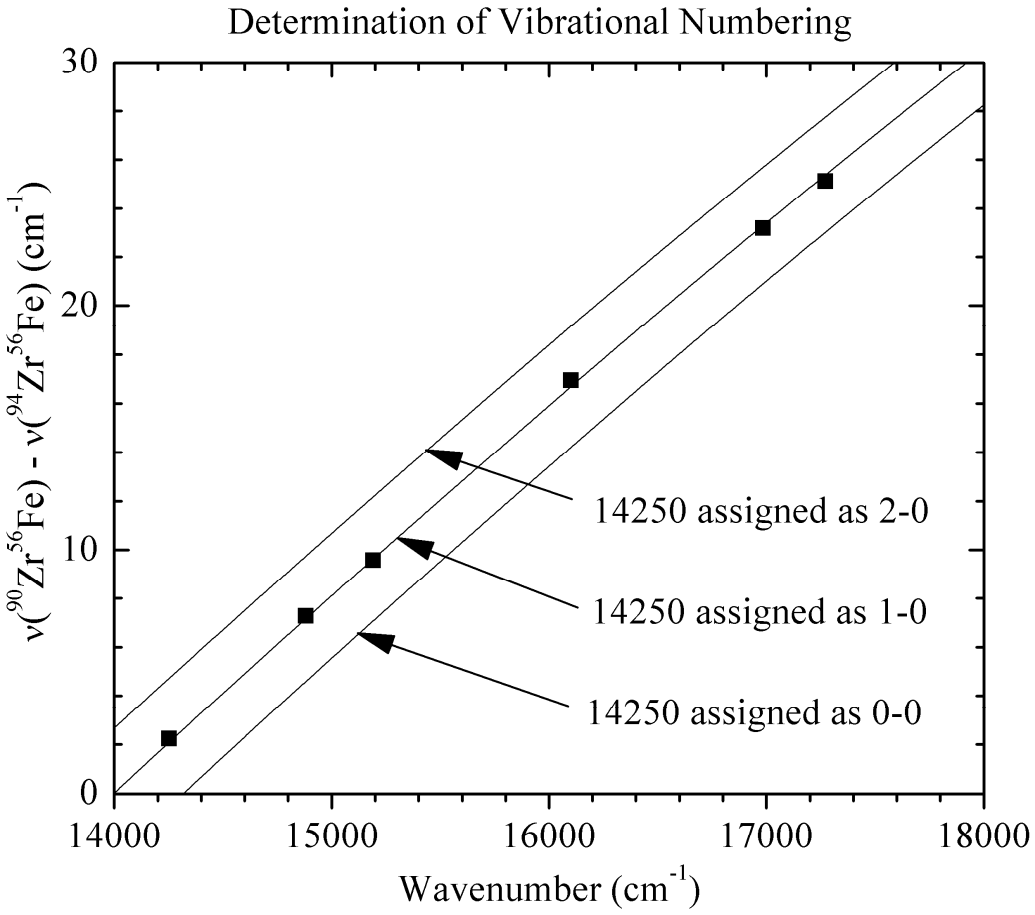

Figure 2.11. Determination of the vibrational assignment for the $[13.9]0^{+}\leftarrow X^{1}\Sigma$ band system of ZrFe. Curves represent the calculated isotope shift between the lighter and heavier isotopes of ZrFe, plotted against band frequency for three different assignments. The experimentally determined isotope shifts are plotted as small black squares against the corresponding band origins. The best agreement is obtained when the 14250 band is assigned as the 1-0 band. This progression consists of eleven members, five of which (2-0, 5-0, 6-0, 8-0, 9-0) show perturbation, and therefore excluded from the fit.

excited state spectroscopic constants, T_0, ω'_e, and $\omega_e'x_e'$ are obtained.

2.10 Analysis of rotationally resolved spectra

2.10.1 Rotfit

For fitting simple rotationally resolved spectra obtained in the R2PI experiment, a home written program called Rotfit was used. The absolute line positions obtained after calibration are fitted to the formula:[18]

$$\nu = \nu_0 + B'J'(J'+1) - B''J''(J''+1) \tag{2.10}$$

allowing upper and lower state rotational constants and Ω- values to be extracted. The $^{50}Ti^{56}Fe$, $^{49}Ti^{56}Fe$, $^{48}Ti^{57}Fe$, $^{48}Ti^{56}Fe$, $^{47}Ti^{56}Fe$, $^{46}Ti^{56}Fe$, $^{48}Ti^{54}Fe$, $^{96}Zr^{56}Fe$, $^{94}Zr^{56}Fe$, $^{92}Zr^{56}Fe$, $^{91}Zr^{56}Fe$, $^{90}Zr^{56}Fe$, $^{90}Zr^{54}Fe$,$^{192}Os^{12}C$, $^{190}Os^{12}C$, $^{188}Os^{12}C$, $^{187}Os^{12}C$, and $^{186}Os^{12}C$ isotopomers belong to Hund's case *a*, so their rotational levels are described by equation (2.10), and were fitted using the Rotfit program. The remaining OsC isotopomer, $^{189}Os^{12}C$, displayed a rather different high resolution spectrum. To illustrate this, a section of the [21.2]2←$^3\Delta_3$ band of OsC, containing the Q branch and three P lines is presented in Figure 2.12 for $^{192}Os^{12}C$ and $^{189}Os^{12}C$. The full spectrum covers 25 cm^{-1} and fine features in the $^{189}Os^{12}C$ spectrum would become too compressed to be distinguished. The ^{189}Os isotope has a nuclear spin of 3/2 and a magnetic moment of 0.6565 nuclear magnetons,[5] and therefore is subject to hyperfine interaction with the unpaired electron in the molecule. In the case of $^{189}Os^{12}C$, this additional source of angular momentum causes every rotational line being split into $2 \cdot I+1=4$ components if $J \geq 2$. Unfortunately, the

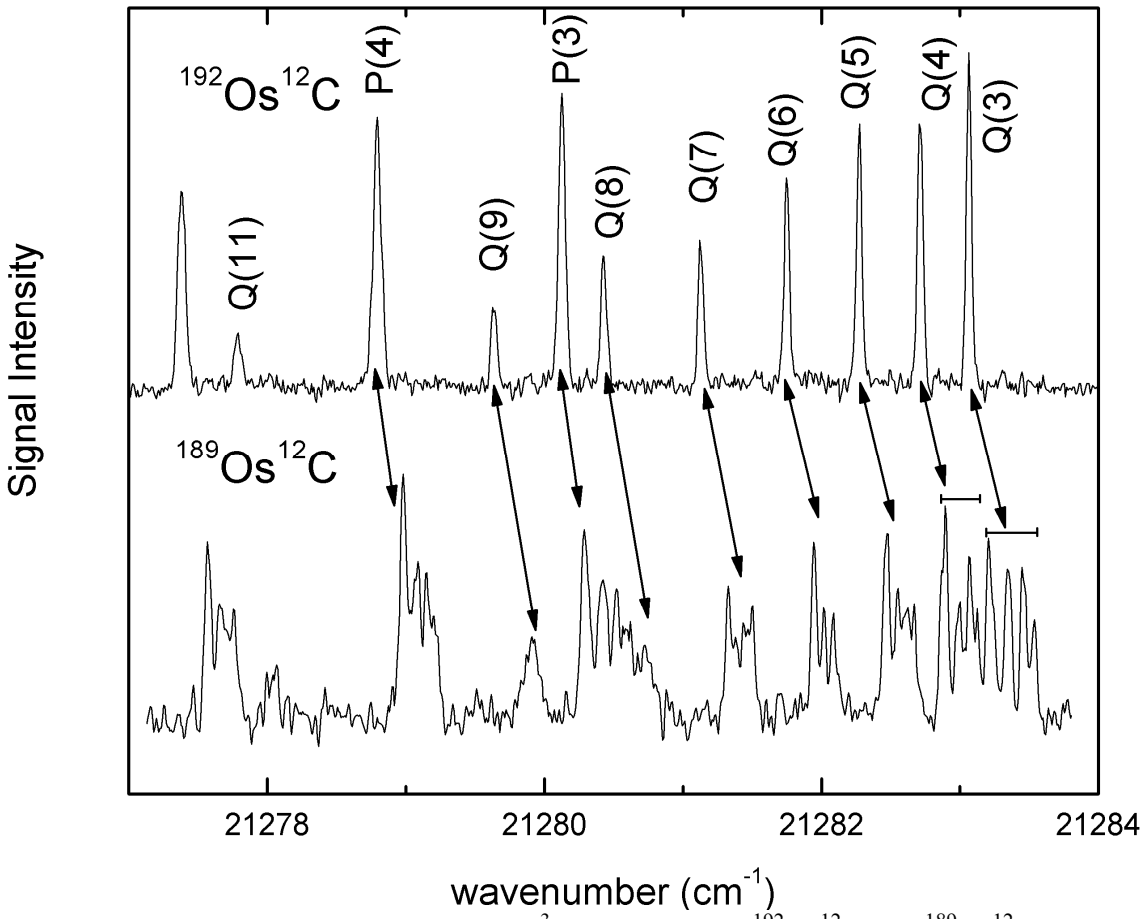

Figure 2.12. A section of the [21.2]2←$^3\Delta_3$ transition of $^{192}Os^{12}C$ and $^{189}Os^{12}C$ that displays the Q branch and three P lines. The $^{189}Os^{12}C$ isotopomer exhibits hyperfine splitting due to the magnetic interaction between ^{189}Os (I=3/2) and the unpaired electron. This results in each rotational line being split, with the separation decreasing as the rotational angular momentum number, J, increases.

analysis of hyperfine features was not implemented in the Rotfit program, so rotationally resolved spectra of $^{189}Os^{12}C$ were fitted with another program, PGopher.[20]

2.10.2 PGopher

PGopher is more difficult to use than Rotfit, but handles more complicated spectra. In a PGopher fit the user starts with a spectral simulation using guesses for the spectroscopic parameters such as band origin, temperature, linewidth, rotational constants, electronic and orbital angular momenta, nuclear spin, hyperfine parameters, lambda doubling parameters, etc, for the upper and lower states. Generally, the guessed parameters are different from the true parameters, so the simulated spectrum may look rather different from the experimental spectrum. The specified parameters have to be varied manually to get a close match between the simulated and the experimental spectra. When reasonably close agreement has been found, specific lines from the simulated spectrum are assigned to the corresponding lines in the experimental spectrum. Then the spectroscopic parameters are varied in a least-squares fit to obtain the best fit. If the error remains high it means that the assignment is wrong, and the entire process has to be reiterated to obtain the correct assignment. When the assignment is correct, an excellent fit is obtained unless the band is perturbed.

Spectra of $^{189}Os^{12}C$ were successfully fitted with PGopher. This allowed hyperfine constants, along with band origins, and ground and excited state rotational constants to be extracted. Due to the high density of spectroscopic features in the spectrum, only a small portion of the $[21.2]2 \leftarrow {}^3\Delta_3$ band of OsC is presented in Figure 2.13. In this example of Hund's case a_β coupling, each level with $J \geq 2$ is split into 4 hyperfine sublevels, with the splitting decreasing with increasing rotational number.

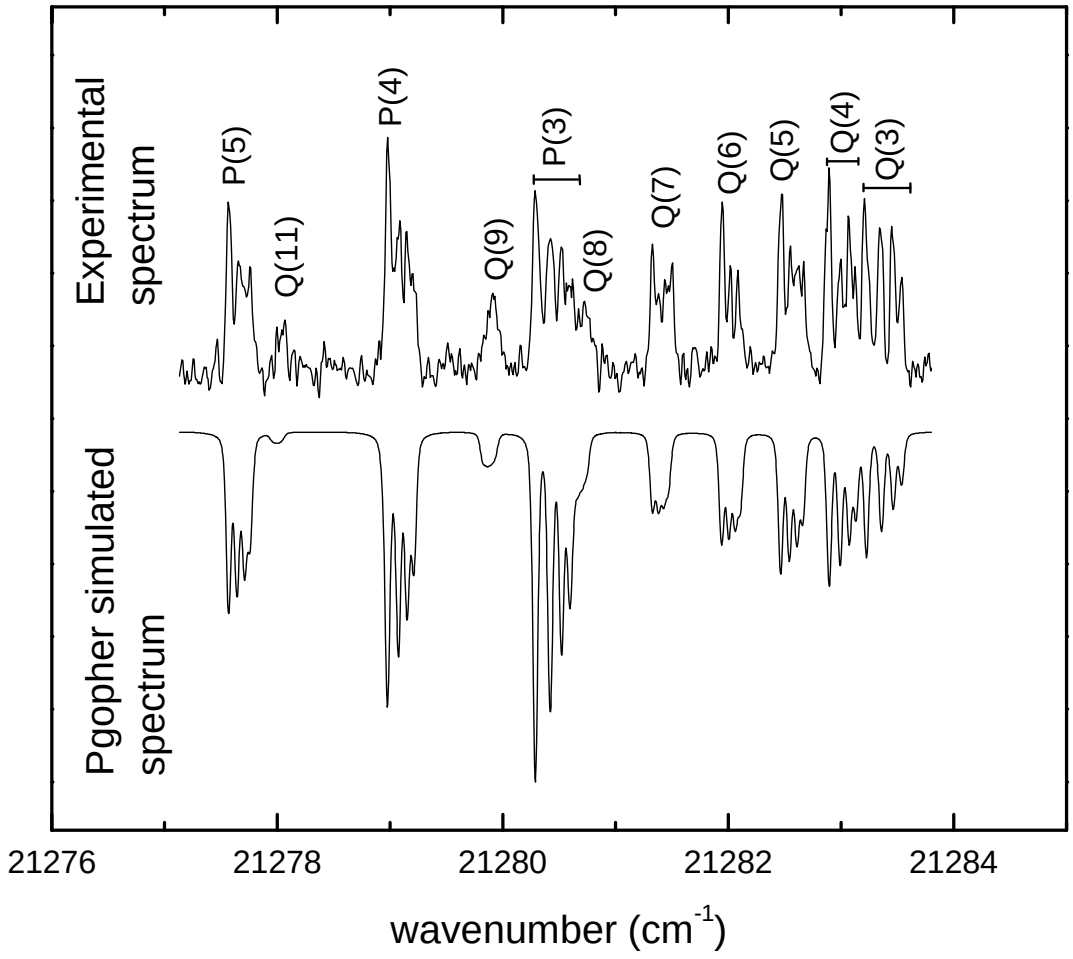

Figure 2.13. A comparison between the experimental spectrum and a PGopher simulation of the [21.2]2←$^{3}\Delta_{3}$ transition of $^{189}Os^{12}C$.

In the case of $^{181}Ta^{12}C$, there is only one Ta isotope, which has I=7/2. The ground state is a $^2\Sigma^+$ state, placing it in the Hund's case $b_{\beta S}$ coupling scheme. This leads to a quite complicated spectrum in the $^2\Pi_{1/2}\leftarrow X^2\Sigma^+$ bands observed, with eight rotational branches, four of which have band heads. In this case PGopher was a very helpful, even essential, tool in the fitting process. Seven rotationally resolved bands were successfully fitted and analyzed. The spectroscopic constants and the detailed analysis of the bands are presented in chapter 4 of this dissertation. Figure 2.14 displays the rotationally resolved spectrum of the [18.34] $^2\Pi_{1/2}\leftarrow{}^2\Sigma^+$ transition of TaC.

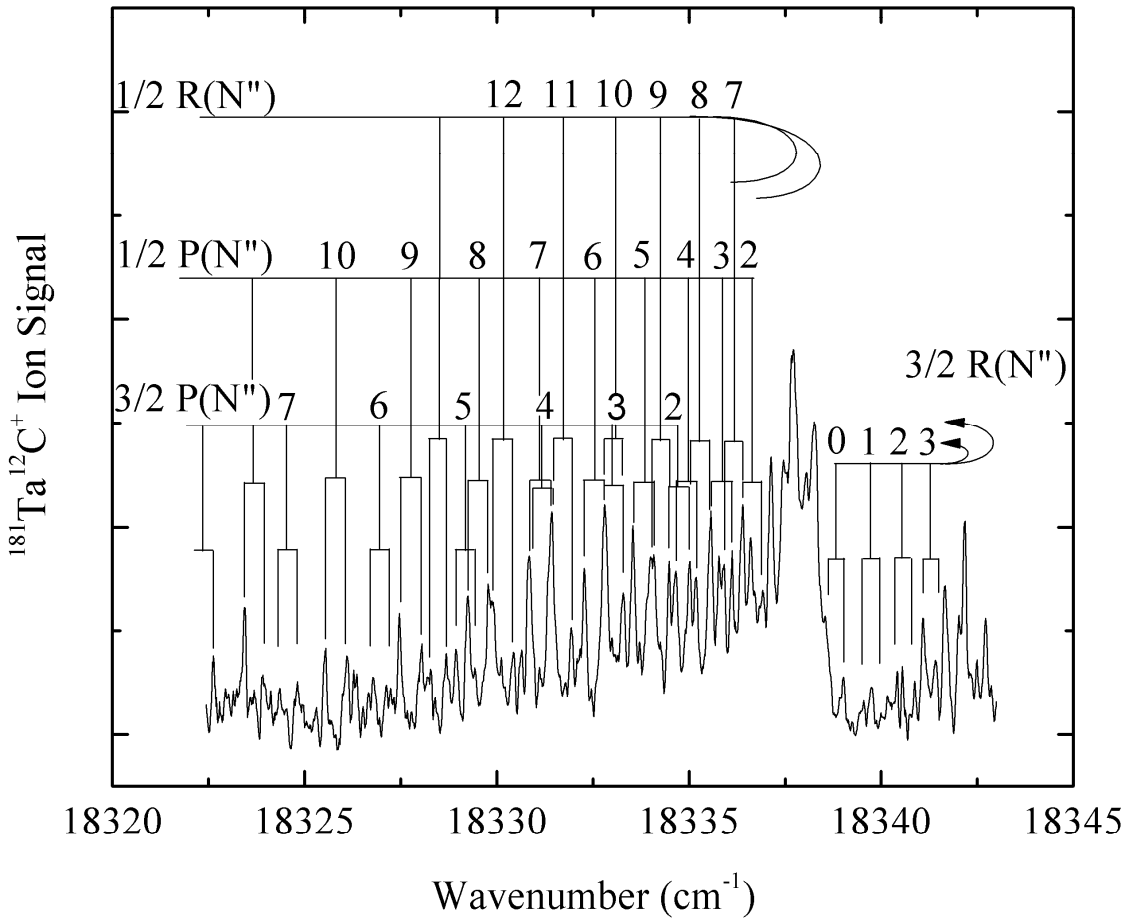

Figure 2.14. Rotationally resolved spectrum of the [18.34] $^2\Pi_{1/2}\leftarrow{}^2\Sigma^+$transition of TaC. With a $^2\Sigma$ ground state and I=7/2 nuclear spin, TaC $X^2\Sigma^+$ falls into Hund's case $b_{\beta s}$. Eight rotational branches observed, with band heads in four of them. This spectrum was successfully fitted using the PGopher program.

2.11 References

(1) Wiley, W. C.; McLaren, I. H. *Review of Scientific Instruments* **1955**, *26*, 1150

(2) Mamyrin, B. A.; Karataev, V. I.; Shmikk, D. V.; Zagulin, V. A. *Zh. Eksp. Teor. Fiz.* **1973**, *64*, 82.

(3) Ready, J. F. *Industrial Applications of Lasers*; Academic Press: New York, 1978.

(4) Sickafoose, S. M.; Langenberg, J. D.; Morse, M. D. *Journal of Physical Chemistry A* **2000**, *104*, 3521.

(5) Weltner, W., Jr. *Magnetic Atoms and Molecules*; Dover Publications, Inc.: New York, 1983.

(6) Morse, M. D. Supersonic beam sources. In *Methods of Experimental Physics: Atomic, Molecular, and Optical Physics*; Dunning, F. B., Hulet, R., Eds.; Academic Press, Inc.: Orlando, Florida, 1996; Vol. II Atoms and Molecules; pp 21.

(7) Clouthier, D. J.; Karolczak, J. *Review of Scientific Instruments* **1990**, *61*, 1607.

(8) Krechkivska, O.; Morse, M. D. *J. Chem. Phys.* **2008**, *128*, 084314/1.

(9) Krechkivska, O.; Morse, M. D. *J. Chem. Phys.* **2010***, 133*, 054309/1.

(10) Steinfeld, J. I. *Molecules and Radiation: An Introduction to Modern Molecular Spectroscopy*, Second ed.; The MIT Press: Cambridge, 1993.

(11) Wiza, J. L. *Nucl. Instrum. Meth.* **1979**, *162*, 587

(12) Beck, G. *Review of Scientific Instruments* **1979**, *47*, 849.

(13) Gerstenkorn, S.; Luc, P. *Atlas du Spectre d'Absorption de la Molécule d'Iode entre 14,800-20,000 cm^{-1}*; CNRS: Paris, 1978.

(14) Gerstenkorn, S.; Luc, P. *Revue de Physique Appliquee* **1979**, *14*, 791.

(15) Cariou, J.; Luc, P. *Atlas du Spectre d'Absorption de la Molécule Tellure, Partie 5: 21,100 - 23,800 cm^{-1}*; CNRS: Paris, 1980.

(16) Cariou, J.; Luc, P. *Atlas du Spectre d'Absorption de la Molécule de Tellure entre 18,500 - 23,800 cm^{-1}*; CNRS: Paris, 1980.

(17) Bevington, P. R. *Data Reduction and Error Analysis for the Physical Sciences*; McGraw-Hill: New York, 1969.

(18) Martinez, A.; Morse, M. D. *J. Chem. Phys.* **2011**, *135*, 024308/1.

(19) Herzberg, G. *Molecular Spectra and Molecular Structure I. Spectra of Diatomic Molecules*, 2nd ed.; Van Nostrand Reinhold: New York, 1950.

(20) Western, C. M. PGOPHER, a Program for Simulating Rotational Structure, University of Bristol, http://pgopher.chm.bris.ac.uk.

CHAPTER 3

RESONANT TWO-PHOTON IONIZATION SPECTROSCOPY OF OsC

3.1 Introduction

Recently there has been considerable interest in studying transition metal carbides due to their significance in homogeneous and heterogeneous catalysis, organometallic chemistry, and biological processes. Among the transition metal monocarbides, the 3*d* and 4*d* series have been more extensively studied than the 5*d* series, both experimentally and theoretically. Because a review of all current work on transition metal carbides is not the purpose of this article, we will concentrate on the 5*d* transition metal monocarbides.

Experimental data on the 5*d* transition metal carbides are scarce, with spectra available only for WC,[1,2] IrC,[3-6] and PtC.[7-14] Bond dissociation energies have been measured using Knudsen effusion mass spectrometry for OsC,[15,16] IrC,[17,18] and PtC,[19] and an upper bound on the bond energy of HfC has been established by this method.[20] Bond dissociation energies of the 5*d* transition metal monocarbide cations WC^+,[21] ReC^+,[22] IrC^+,[23] and PtC^+[24] have also been measured using guided ion beam techniques. Theoretical studies have been published on TaC,[25] WC,[26] OsC,[16] IrC,[27] PtC,[28] and AuC^+.[29] As compared to the 3*d* and 4*d* series, theoretical studies of the 5*d* transition metal carbides are very challenging due to the increasing importance of relativistic

effects (including spin-orbit coupling) and electron correlation.

No spectroscopic studies on diatomic OsC have been previously reported. Thermochemical measurements of the bond dissociation energy have been performed by Gingerich and co-workers using the Knudsen effusion method, thereby providing a bond energy of 6.28 ± 0.15 eV (605.6 ± 14.0 kJ/mol).[15,16] In addition, Meloni, *et al.* reported *ab initio* calculations on the S = 0, 1, 2, and 3 spin states of diatomic OsC at various levels of theory.[16] They find that the ordering of states changes significantly depending on the level of theory employed. At the highest level used in their study, the CCSD(T) level of theory, the lowest energy state was found to be $^3\Sigma^-$, arising from the $1\delta^2\,3\sigma^2$ electronic configuration. The $^3\Delta$ state arising from the $1\delta^3\,3\sigma^1$ electronic configuration was calculated to lie 0.28 eV (2220 cm^{-1}) above the $^3\Sigma^-$ state. In a more recent investigation, the B3LYP density functional theory was applied to OsC, along with the other 5*d* transition metal monocarbides.[30] Again, the $^3\Sigma^-$ state was predicted to be the ground state, with a bond length of 1.674 Å. Neither computational investigation of OsC included spin-orbit effects, however, although the authors of the B3LYP density functional study noted that the results may be different when these are considered.

Previously published experimental studies on the other group 8 transition metal carbides, FeC [31-34] and RuC [35-39] reveal their ground states to be $^3\Delta_3$ for FeC, arising from the $3\sigma^1 1\delta^3$ configuration and $^1\Sigma^+$ for RuC, arising from the $1\delta^4$ electronic configuration. The much greater importance of relativistic and spin-orbit effects in OsC make this molecule an interesting point of comparison. If the relativistic stabilization of the 6*s* orbital is sufficient, the $1\delta^2\,3\sigma^2$, $^3\Sigma^-_{0+}$ state may be the ground state, as predicted by *ab initio* calculations. If not, it is likely that the $1\delta^3\,3\sigma^1$, $^3\Delta_3$ state will emerge as the ground

level. Given the relativistic stabilization of the 6*s*-like 3σ orbital, it is unlikely that the ground state will be the $1\delta^4$, $^1\Sigma^+$ state that is the analogue of the ground state of RuC.

The spectroscopic results obtained in the present study demonstrate that the ground level of the OsC molecule is indeed the $1\delta^3\,3\sigma^1$, $^3\Delta_3$ state. Much weaker transitions arising from a state with $\Omega = 0$ are also observed, and these are assigned to the low-lying $A\,^3\Sigma^-(0^+)$ state, which remains populated in the supersonic beam.

3.2 Experimental

In this work, diatomic OsC was investigated using resonant two-photon ionization (R2PI) spectroscopy. The apparatus used in the present study has been previously described.[33] In brief, it consists of two vacuum chambers; the first of which contains the pulsed supersonic nozzle, rotating and translating target disc mount, and molecular beam skimmer (1 cm diameter, 50° inside angle), and is pumped by a VHS-10 diffusion pump, backed by a KDH-130 rotary mechanical pump. These experiments were conducted under conditions in which the ion gauge reading was in the range of 5-8 $\times 10^{-5}$ Torr and 1-2 $\times 10^{-6}$ Torr in the first and second chambers, respectively. The OsC molecules were produced by laser ablation of a 45:55 mole ratio vanadium:osmium alloy disc [Nd:YAG (yttrim aluminum garnet) laser, 355 nm, 12-15 mJ/pulse], with the laser timed to coincide with the carrier gas pulse. Helium seeded with approximately 3 % methane was used as the carrier gas. A backing pressure of 50 psig was found to be optimal for producing diatomic OsC. The OsC signal was so strong that it was possible to collect rotationally resolved spectra of the strongest vibrational transitions for the minor isotopomers ($^{187}Os^{12}C$ and $^{186}Os^{12}C$, with 1.94 % and 1.57 % natural abundance, respectively).

The second chamber is evacuated by an Edwards 160 diffusion pump, backed by a Welch 1397 rotary mechanical pump. It houses a reflectron-type time-of-flight mass spectrometer with Wiley-McLaren ion source optics.[40,41] The molecular beam was exposed to the output of a Nd:YAG-pumped tunable dye laser counterpropagating along the axis of the molecular beam, and was crossed at right angles by the output of an ArF excimer laser (193 nm) about 40 ns later in time. Molecules that absorb the dye laser radiation are then ionized by the excimer radiation, so that the ion signal of the molecule of interest may be monitored as a function of the dye laser frequency to provide the optical spectrum.

To investigate the vibronically resolved spectrum of OsC, the dye laser was scanned in low resolution mode (0.15 cm^{-1}) using an output energy of 3-7 mJ/pulse. To reveal rotational structure within the vibrational transitions, an intracavity étalon was inserted into the oscillator cavity, which was then pressure scanned with sulfur hexafluoride (SF_6), giving a resolution of 0.04 cm^{-1}. In this mode, the dye laser gave about 1 mJ of output energy, which was filtered even further to reduce power broadening. During pressure scans, the pressure in the dye laser cavity was varied from 30 to 800 Torr, allowing continuous scans of about 15 cm^{-1}. For each high resolution spectrum a reference spectrum of I_2[42,43] or Te_2[44,45] (for vibrational bands below and above 20 000 cm^{-1}, respectively) was collected for calibration purposes. As the OsC molecules were traveling toward the light source at the beam velocity of helium (1.77×10^5 cm s^{-1}), all measured line positions were shifted by a small amount (0.11- 0.12 cm^{-1}) to correct for the Doppler shift.

For each rotationally resolved vibrational transition, the excited state lifetime was measured. For this purpose, the dye laser was set to excite the transition and the ion signal intensity was monitored as a function of the dye laser- excimer delay. The data were then fitted to an exponential decay curve using the Marquardt nonlinear least-squares algorithm.[46] To provide estimates of the error in the lifetime measurement, three independent measurements of the lifetime were made, and the standard deviation among the three values is reported.

3.3 Results

3.3.1 Low resolution spectrum of OsC

The vibronically resolved spectrum of OsC, collected between 17390 and 22990 cm^{-1}, is presented in Figure 3.1. Approximately 11 vibrational bands of various intensities are observed over the spectral range 19000 to 22000 cm^{-1}, and the strongest six of these were rotationally resolved. In this region only one vibrational progression is observed, which is identified as the $[19.1]2 \leftarrow X\,^3\Delta_3$ system on the basis of rotationally resolved studies described below. Here the notation [19.1]2 refers to an $\Omega' = 2$ excited electronic state with its v = 0 level lying approximately 19.1×10^3 cm^{-1} above the ground level. The rotationally resolved bands give fitted band origins, from which the vibrational interval is deduced to be $\Delta G'_{1/2} = 953.0189 \pm 0.0022$ cm^{-1} for the most abundant isotopomer, $^{192}Os\,^{12}C$. Here and throughout this article, 1σ error limits are provided. The assignment of the two bands of this system to a common band system is supported by their similar upper state rotational constants (0.519 and 0.511 cm^{-1}), and the consistency of the measured isotope shifts with their assignment as 0-0 and 1-0 bands.

For the remaining transitions, no obvious vibrational progression could be

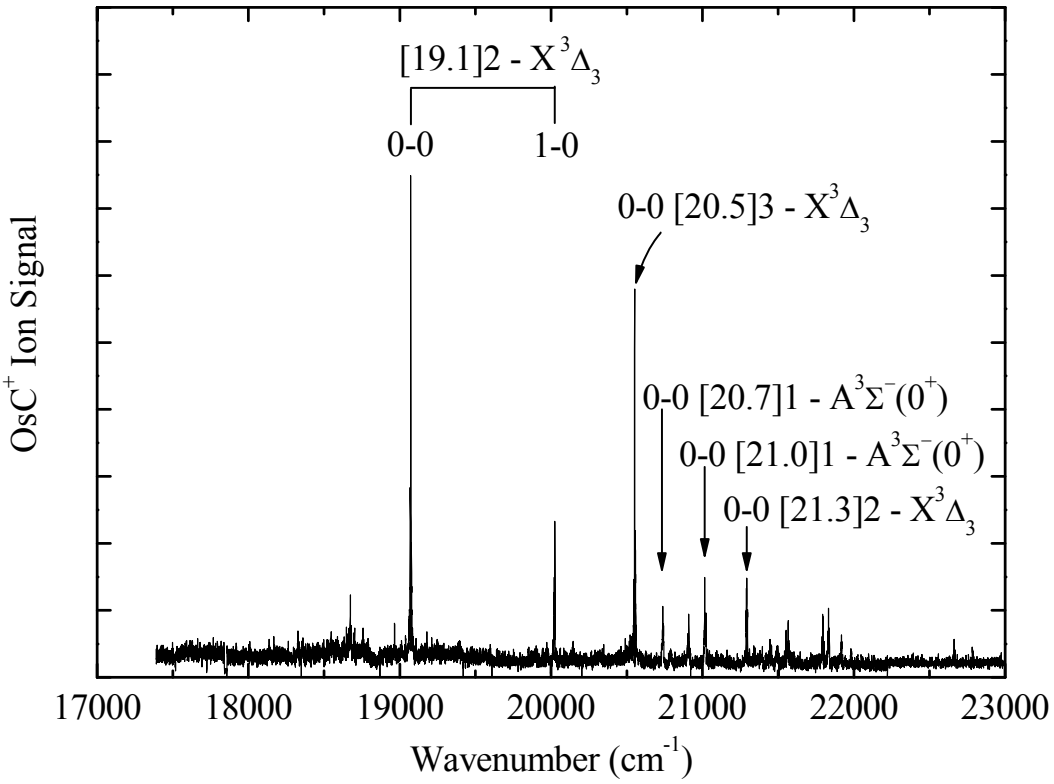

Figure 3.1. Vibronically resolved resonant two-photon ionization spectrum of OsC over the range 17390-22990 cm^{-1}.

identified, so all information about these band systems comes from the rotationally resolved work, which is described below. Excited state lifetimes, band origins, and upper state rotational constants for all of the measured bands are provided in Table 3.1. Fitted lower state rotational constants and bond lengths obtained by inversion of these data are provided in Table 3.2. In all cases, bands originating from the same lower level were used in a combined fit, so that the most precise spectroscopic parameters could be obtained.

3.3.2 Rotationally resolved spectra

3.3.2.1 The [19.1] 2 ← X $^3\Delta_3$ band system of OsC

This system consists of two strong bands, with the origin band lying near 19064 cm^{-1} and the 1-0 band near 20017 cm^{-1}; no transitions to higher vibrational levels were detected. The two upper levels have short lifetimes of 228 ± 41 and 307 ± 19 ns. Because of the strength of these transitions, and the relative ease of producing OsC in the supersonic expansion, it was possible to record rotationally resolved spectra for all of the OsC isotopomers having greater than 1% natural abundance: $^{192}Os^{12}C$ (40.3 % natural abundance), $^{190}Os^{12}C$ (26.0 %), $^{189}Os^{12}C$ (16.0 %), $^{188}Os^{12}C$ (13.1 %), $^{187}Os^{12}C$ (1.94 %), and $^{186}Os^{12}C$ (1.57 %). All rotational lines were successfully fitted to the equation

$$\nu = \nu_0 + B'J'(J'+1) - B''J''(J''+1), \qquad (3.1)$$

allowing upper and lower state rotational constants and Ω values to be extracted. Spectroscopic constants, bond lengths, and lifetimes for the 0-0 and 1-0 bands are presented in Tables 3.1 and 3.2. Figure 3.2 displays the rotationally resolved spectrum of the 0-0 band of the [19.1] 2 ←X $^3\Delta_3$ system for the most abundant isotopomer, $^{192}Os^{12}C$.

Table 3.1. Upper state parameters of OsC: band origins (cm^{-1}), rotational constants B′ (cm^{-1}), upper state bond lengths (Å) and lifetimes (μs).

Molecule		0-0 [19.1]2←$X\,^3\Delta_3$	1-0 [19.1]2←$X\,^3\Delta_3$	0-0 [20.5]3←$X\,^3\Delta_3$	0-0 [20.7]1←$A^3\Sigma_{0+}^-$	0-0 [21.0]1←$A^3\Sigma_{0+}^-$	0-0 [21.2]2←$X\,^3\Delta_3$
$^{186}Os^{12}C$	v_0	19063.9482(49)	20018.1676(19)	20543.2305(32)			21284.1693(41)
	B′	0.520993(146)	0.512105(150)	0.525856(65)			0.490873(66)
	r′	1.69423(24)	1.70886(25)	1.68637(10)			1.74543(12)
$^{187}Os^{12}C$	v_0	19063.8985(45)	20017.9177(52)	20543.1977(27)			21284.0358(31)
	B′	0.520506(125)	0.512185(211)	0.525748(102)			0.490039(203)
	r′	1.69474(20)	1.70845(35)	1.68627(16)			1.74663(36)
$^{188}Os^{12}C$	v_0	19063.8683(20)	20017.6769(13)	20543.1694(22)	20729.2670(53)	21006.2566(25)	21283.9781(27)
	B′	0.520378(44)	0.511580(40)	0.525619(30)	0.477964(286)	0.488509(227)	0.490239(35)
	r′	1.69468(7)	1.70919(7)	1.68621(5)	1.76827(53)	1.74908(41)	1.74599(6)
$^{189}Os^{12}C$	v_0	19063.8573(36)	20017.4527(48)	20543.1654(19)	20729.1636(25)	21006.2229(17)	21283.8901(22)
	B′	0.519969(79)	0.511469(90)	0.525491(81)	0.478249(136)	0.488382(116)	0.490194(131)
	r′	1.69507(13)	1.70910(15)	1.68614(13)	1.76746(25)	1.74903(21)	1.74580(23)
$^{190}Os^{12}C$	v_0	19063.7924(21)	20017.2003(18)	20543.1152(25)	20729.0462(35)	21006.1614(27)	21283.7837(13)
	B′	0.519744(45)	0.510974(47)	0.525046(43)	0.478086(193)	0.488155(182)	0.489729(47)
	r′	1.69517(7)	1.70966(8)	1.68659(7)	1.76749(36)	1.74916(33)	1.74635(8)
$^{192}Os^{12}C$	v_0	19063.7184(16)	20016.7373(15)	20543.0736(15)	20728.8359(16)	21006.0734(14)	21283.5941(13)
	B′	0.519497(34)	0.510669(33)	0.524808(34)	0.477612(84)	0.487908(77)	0.489490(31)
	r′	1.69505(6)	1.70964(6)	1.68645(6)	1.76782(16)	1.74906(14)	1.74624(6)
Lifetime (μs)		0.228(41)	0.307(19)	0.160(14)	0.496(21)	0.350(59)	0.340(16)

Table 3.2. Spectroscopic constants for the $X\,^3\Delta_3$ and $A\,^3\Sigma^-_{0+}$ states of OsC.

Molecule		$X\,^3\Delta_3$	$A\,^3\Sigma^-_{0+}$
$^{186}Os^{12}C$	B_0'' (cm^{-1})	0.534821(99)	
	r_0'' (Å)	1.67218(16)	
$^{187}Os^{12}C$	B_0'' (cm^{-1})	0.534495(104)	
	r_0'' (Å)	1.67242(16)	
$^{188}Os^{12}C$	B_0'' (cm^{-1})	0.534313(43)	0.518212(219)
	r_0'' (Å)	1.67243(7)	1.69822(36)
$^{189}Os^{12}C$	B_0'' (cm^{-1})	0.534360(63)	0.518268(121)
	r_0'' (Å)	1.67209(9)	1.69785(20)
$^{190}Os^{12}C$	B_0'' (cm^{-1})	0.533730(44)	0.517922(196)
	r_0'' (Å)	1.67282(7)	1.69815(32)
$^{192}Os^{12}C$	B_0'' (cm^{-1})	0.533492(33)	0.517713(91)
	r_0'' (Å)	1.67267(5)	1.69797(15)

.

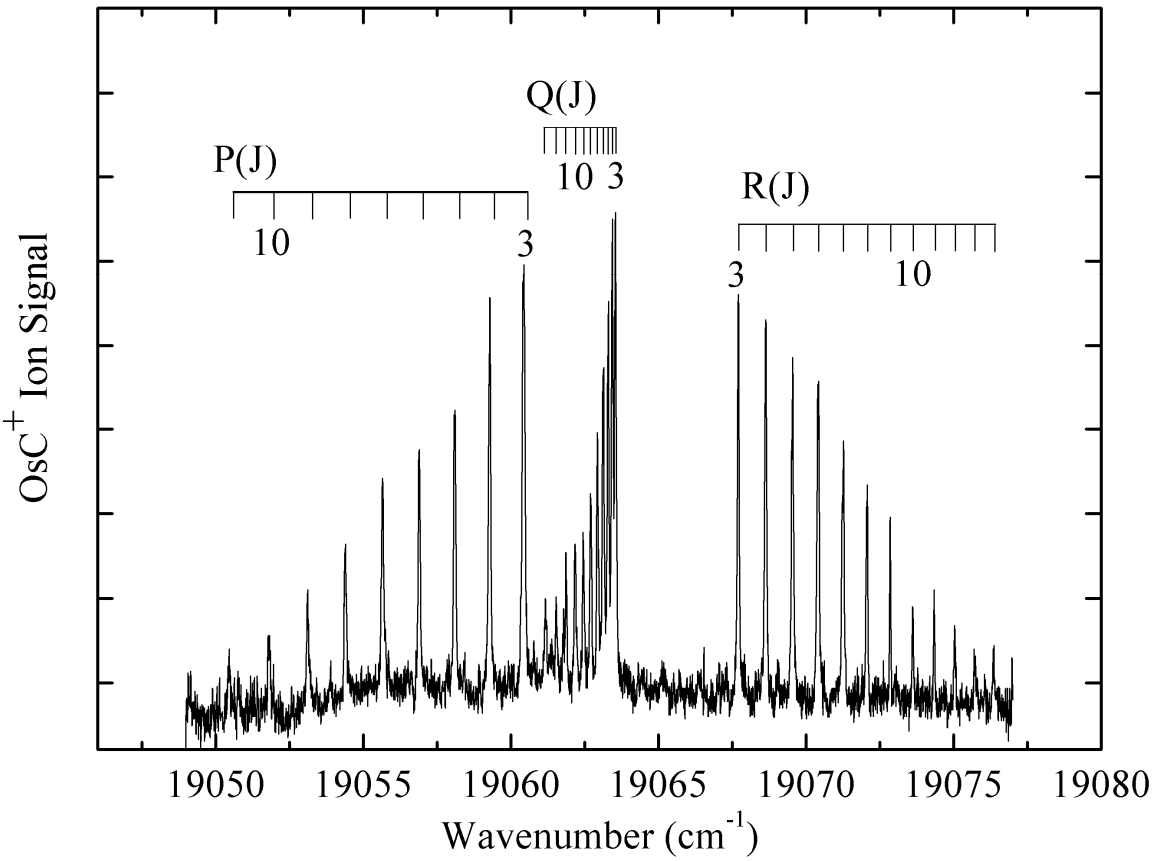

Figure 3.2 Rotationally resolved scan over the 0-0 band of the [19.2]2← $X\,^3\Delta_3$ system of $^{192}Os^{12}C$

When the spectrum was first collected, the P lines appeared much stronger than the R lines, consistent with the Hönl-London factors for a $\Delta\Omega = -1$ transition. This is not evident in the spectrum displayed in Figure 3.2, because during the scan over the R branch the dye laser intensity was increased to bring out the weaker lines. The observation of first lines of R(3), Q(3), and P(3) provides $\Omega'' = 3$, $\Omega' = 2$, confirming the Hönl-London prediction of a $\Delta\Omega = -1$ transition. As can be seen from the spectrum, the lines in the R and P branches fan out nearly symmetrically, without formation of a band head. The Q lines are closely spaced and fan out to lower energy, indicating that the bond length increases slightly upon electronic excitation. If sufficient population were present in the high J levels, a band head would eventually form in the R branch. There are large gaps between first Q line and first P and R lines, indicative of the high values of Ω in the upper and lower states. The isotope shift between the lightest ($^{186}Os^{12}C$) and the heaviest ($^{192}Os^{12}C$) isotopomers is only 0.2298 cm^{-1}, indicating that this is vibrationally a 0-0 band.

The 1-0 band possesses rotationally resolved structure very similar to that in Figure 3.2, except that Q lines fan out more rapidly to the red. The isotope shift between $^{186}Os^{12}C$ and $^{192}Os^{12}C$ was found to be 1.4303 cm^{-1}, which is consistent with the 1-0 vibrational assignment.

3.3.2.2 The [20.5] 3 $\leftarrow X\ ^3\Delta_3$ band system of OsC

A bit further to the blue, another strong transition was found near 20543 cm^{-1}, for which it was again possible to collect rotationally resolved and assignable spectra for all of the OsC isotopomers with greater than 1% natural abundance. Figure 3.3 displays the rotationally resolved spectrum of this feature for $^{192}Os^{12}C$, which we identify as the 0-0

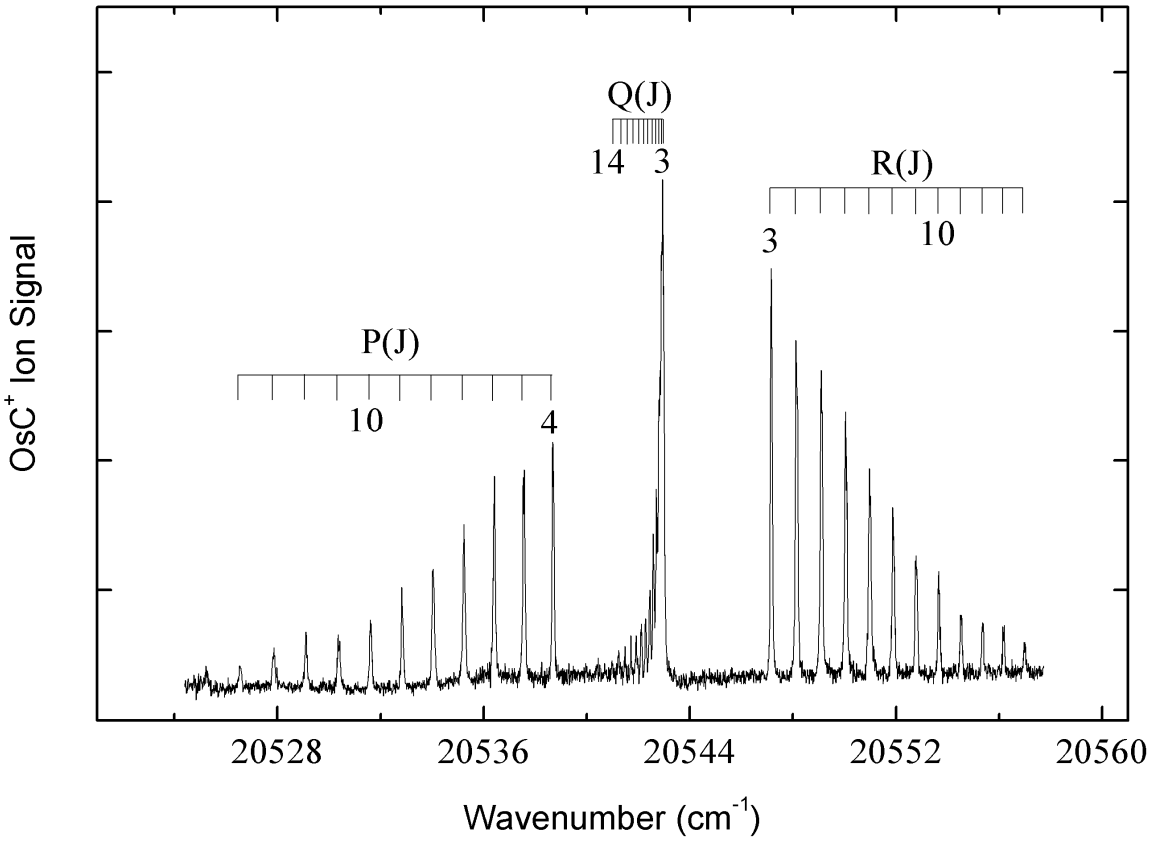

Figure 3.3. Rotationally resolved scan over the 0-0 band of the [20.5]3← $X\,^3\Delta_3$ system of $^{192}Os^{12}C$.

band of the [20.5]3 ←$X\,^3\Delta_3$ system. Again, the lines in the P and R branches fan out nearly symmetrically without formation of a band head. The large gaps between the Q branch and the first P and R lines again indicate that this transition corresponds to high Ω values. The Q lines fan out to lower energy and are very closely spaced. Assignment of the first rotational lines proved that this is an Ω′=3 ← Ω″=3 transition and originates from the same Ω″ = 3 level as the bands discussed above. The small isotope shift of 0.1569 cm^{-1} between heaviest and lightest OsC isotopomers indicates that this is a v′=0 ← v″=0 band. The bond length changes very slightly upon electronic excitation, only by 0.0138 Å, causing the 1-0 and higher members of the band system to have prohibitively small Franck-Condon factors. Thus, it should come as no surprise that only a single member of this band system is observed.

3.3.2.3. The 20729 and 21 006 cm^{-1} Ω′ = 1 ← Ω″ = 0 bands of OsC

In the vibronically resolved spectrum displayed in Figure 3.1, two weak bands are observed near 20729 and 21006 cm^{-1}. The upper states of these features have somewhat longer lifetimes than the other transitions observed in this work, but this is not sufficient to explain their weak intensity in the spectrum. Higher resolution investigations (0.04 cm^{-1}) permitted rotationally resolved spectra to be recorded and analyzed for the four isotopomers of OsC with natural abundances over 10 % for both bands. The two bands have quite similar rotational structure, so we present their analysis together, even though they are not apparently members of the same electronic band system.

The rotationally resolved spectrum of the 21006 cm^{-1} band for $^{192}Os^{12}C$ is presented in Figure 3.4. The Q lines are widely spaced and fan out to lower energy. There

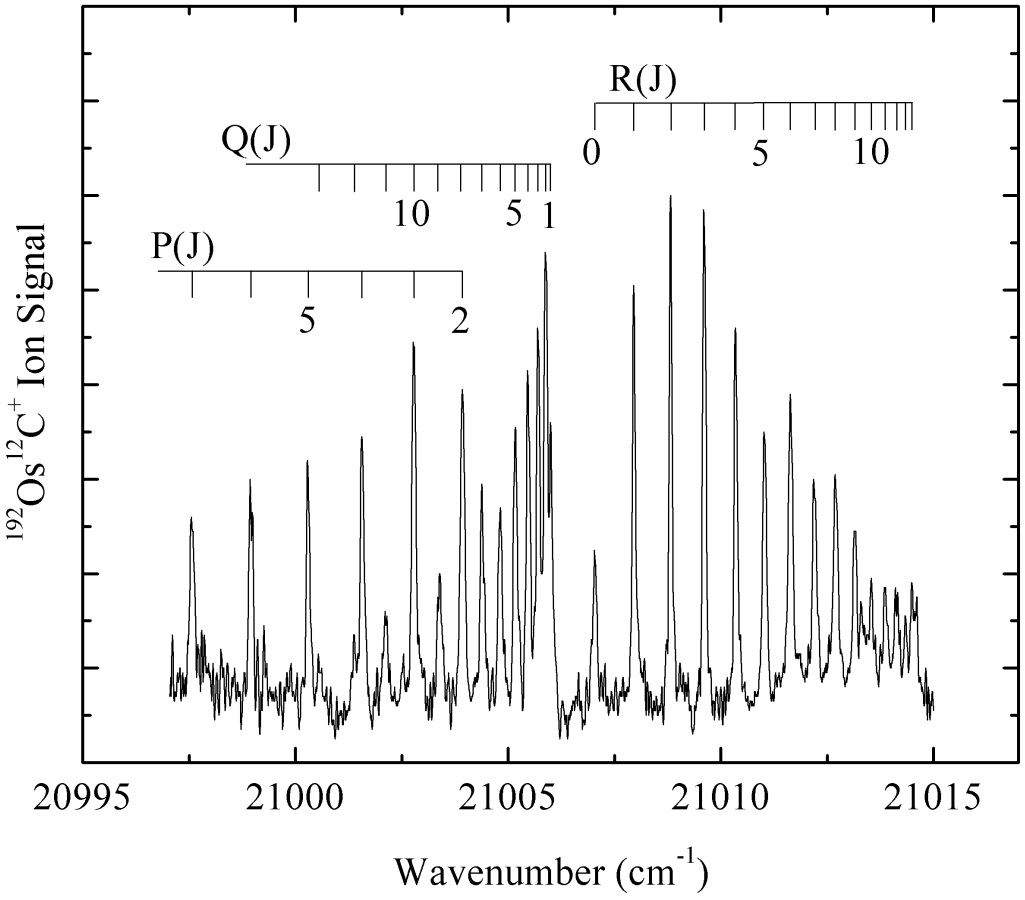

Figure 3.4. Rotationally resolved scan over the 0-0 band of the [21.0]1← $A^{3}\Sigma^{-}_{0+}$ system of $^{192}Os^{12}C$

are no gaps between the Q branch and the P and R branches, immediately demonstrating that the lower state differs from that found in the previously discussed bands. A band head is formed in the R branch, indicating a significant increase in bond length upon electronic excitation. Fitting the rotational lines using equation (3.1) provides upper and lower state rotational constants, which are given in Tables 3.1 and 3.2, respectively. For both the 20729 and 21006 cm^{-1} bands, the first lines are R(0), Q(1) and P(2), which identifies both bands as $\Omega' = 1 \leftarrow \Omega'' = 0$ transitions. The assignment of the lower state as the $A\,^3\Sigma^-_{0+}$ state is justified below in the discussion section and is based on molecular orbital arguments together with a comparison to the available *ab initio* calculations. The small isotope shift between the band origins for the $^{188}Os^{12}C$ and $^{192}Os^{12}C$ isotopomers, 0.1832 cm^{-1}, suggests that the 21006 cm^{-1} feature is vibrationally a 0-0 band. Accordingly, this feature is assigned as the 0-0 band of the $[21.0]1 \leftarrow A\,^3\Sigma^-_{0+}$ band system.

The 20729 cm^{-1} band is the weaker of the two bands, so while scanning in high resolution mode the dye laser power was increased. As a result, the rotational lines were a bit power broadened comparing to the 21006 cm^{-1} band, but it was still possible to extract useful information. The rotationally resolved spectrum is very similar to that displayed in Figure 3.4, with a band head in the R branch. Again, the first lines are found to be R(0), Q(1), and P(2), establishing the band as another $\Omega' = 1 \leftarrow \Omega'' = 0$ transition. The lower state rotational constant is the same as in the 21006 cm^{-1} band, allowing both bands to be used in a combined least squares fit. The small isotope shift between the $^{188}Os^{12}C$ and $^{192}Os^{12}C$ isotopomers, 0.4311 cm^{-1}, is about halfway between what might be expected for a 0-0 band and a 1-0 band, so that vibrational assignment of this single

feature is a bit ambiguous. For the purposes of discussion, however, we designate this feature as the 0-0 band of the [20.7]1 ← $A\,^3\Sigma^-_{0+}$ band system.

The ^{189}Os atom has nuclear spin, I = 3/2, but neither the 20729 nor the 21006 cm^{-1} band shows significant hyperfine broadening or splitting compared to the other isotopomers. No hyperfine splitting would be expected for the $A\,^3\Sigma^-_{0+}$ lower state, which is expected to belong to Hund's case (a'_β) due to the large second-order spin-orbit splitting expected in such a state, which causes $\Lambda = 0$ and $\Omega = 0$ to be good quantum numbers.[47,48] Thus, we may conclude that the hyperfine splitting in the upper states of these transitions is also negligible on the scale of our measurements. In contrast, hyperfine splitting or broadening is obvious in the ^{189}Os^{12}C isotopomer in all of the rotationally resolved spectra originating from the $X\,^3\Delta_3$ state. This is discussed in Section 3.3.2.5.

3.3.2.4. The 21284 cm^{-1} $\Omega' = 2 \leftarrow X\,^3\Delta_3$ band of OsC

The weak feature found in Figure 3.1 near 21284 cm^{-1} has also been rotationally resolved and analyzed, yielding useful data for all of the isotopomers of OsC with greater than 1% natural abundance. The rotationally resolved spectrum of this band looks very similar to that displayed in Figure 3.2, except it has more widely spaced, red-shaded Q and P lines, and more closely spaced R lines leading to an R branch band head at R(10). These facts indicate a significant lengthening of the bond upon electronic excitation. The appearance of the spectrum and subsequent rotational analysis show that this is an Ω'=2 ← Ω''=3 transition. The ν_0(^{186}Os^{12}C) - ν_0(^{192}Os^{12}C) isotope shift is rather large,

0.5752 cm^{-1}, but because there are no other observed bands with $\Omega' = 2$ that fit into a vibrational progression, we tentatively identify the band as the 0-0 vibrational band of the [21.3]2 ← $X\,^3\Delta_3$ band system.

3.3.2.5. Hyperfine structure of the rotationally resolved bands

Two of the Os isotopes, ^{187}Os (I=1/2, 1.96 % natural abundance) and ^{189}Os (I=3/2, 16.15%), have nonzero nuclear spin and are therefore subject to hyperfine interactions. The less abundant ^{187}Os isotope has a magnetic moment of 0.0643 nuclear magnetons (n.m.), while the more abundant ^{189}Os has a much larger magnetic moment of 0.6565 n.m.[49] Thus, hyperfine effects are expected to be much more readily observed in $^{189}Os^{12}C$ than in any of the other isotopomers. Indeed, hyperfine splitting and broadening are only evident in our spectra for the $^{189}Os^{12}C$ species.

Hyperfine broadening or splitting is evident in the spectra of $^{189}Os^{12}C$ for all of the bands originating from the $X\,^3\Delta_3$ level, and for none of the bands originating from the $A\ ^3\Sigma^-_{0+}$ level. Due to the huge spin-orbit parameter for the 5*d* orbitals of Os, $\zeta_{5d}(Os) \approx$ 3045 cm^{-1},[50] the $X\,^3\Delta_3$ level is expected to lie approximately 3000 cm^{-1} below the $^3\Delta_2$ level, causing both levels to conform to Hund's case (a_β). Likewise, an estimate of the shift of the $1\delta^2\,3\sigma^2$, $A\,^3\Sigma^-_{0+}$ level due to its spin-orbit perturbation by the higher-lying isoconfigurational $1\delta^2\,3\sigma^2$, $^1\Sigma^+_{0+}$ level suggests that the $A\,^3\Sigma^-_{0+}$ level is lowered in energy by 4000 to 6000 cm^{-1} due to this effect, causing it to be well separated from the corresponding $A\,^3\Sigma^-_1$ level, placing the $A\,^3\Sigma^-_{0+}$ level firmly in Hund's case (a'_β). Given the enormous spin-orbit parameter for Os, it is likely that all of the upper states found for this

molecule are also Hund's case (a) states, or spin-orbit induced mixtures of such states. Thus, hyperfine splittings in all of the states of this molecule are expected to follow the Hund's case (a_β) formula,

$$E_{hf}\left(S,\Lambda,\Sigma,\Omega,I,J,F\right)=h\Omega\left[\frac{F(F+1)-I(I+1)-J(J+1)}{2J(J+1)}\right], \tag{3.2}$$

where

$$h=a\Lambda+\left(b_F+\frac{2}{3}c\right)\Sigma, \tag{3.3}$$

$$a=2.000g_I\beta_e\beta_n\left\langle r^{-3}\right\rangle, \tag{3.4}$$

$$b_F=g_eg_I\beta_e\beta_n\left\langle r^{-3}\right\rangle, \tag{3.5}$$

and

$$c=\frac{3}{2}g_eg_I\beta_e\beta_n\left\langle 3\cos^2\theta-1\right\rangle\left\langle r^{-3}\right\rangle. \tag{3.6}$$

Here g_e = 2.0023193 is the electronic g factor;[49] $g_I \equiv \mu_I / I$ is the nuclear g factor, given by the nuclear magnetic dipole moment in nuclear magnetons divided by the nuclear spin, I; β_e is the Bohr magneton; β_n is the nuclear magneton; $|\psi(0)|^2$ is the probability density of finding the electron at the magnetic nucleus; and θ is the angle between the internuclear axis and the vector from the magnetic nucleus to the electron. In these expressions, the expectation values provide averages for a single unpaired electron. In cases in which there are more than one unpaired electron, these formulas must be

generalized to include a sum over all unpaired electrons,[48,51]

$$h = \left\langle \sum_i \left[a_i \hat{l}_{z,i} + \left(b_{F,i} + \frac{2}{3} c_i \right) \hat{s}_{z,i} \right] \right\rangle, \tag{3.7}$$

where the sum is over all electrons outside of closed shells, $\hat{l}_{z,i}$ and $\hat{s}_{z,i}$ give the projections of electronic orbital and spin angular momentum along the internuclear axis for electron i, respectively, and the parameters a_i, $b_{F\,i}$, and c_i are given by formulae (3.4)-(3.6), with the expectation values and $|\psi(0)|^2$ evaluated for electron i.

Büttgenbach has provided a detailed review of hyperfine structure in the 4*d* and 5*d* atoms,[52] including a summary of the results of fitting measured atomic hyperfine levels. For ^{189}Os, Büttgenbach listed the parameters a^{01} =0.0120 cm^{-1}, a^{12} = 0.0051 cm^{-1}, a^{10}_{5d} = -0.0042 cm^{-1}, and a^{10}_{6s} = 0.2577 cm^{-1}, as averaged values for the $5d^6 6s^2$ and $5d^7 6s^1$ configurations. These correspond to values of the *a*, b_F, and *c* parameters of a_δ = 0.0120 cm^{-1}, 2/3 c_δ = -0.0029 cm^{-1}, $b_{F,\delta}$ = -0.0042 cm^{-1}, and $b_{F,6s}$ = 0.2577 cm^{-1}.[52] Assuming the X $^3\Delta_3$ state is a pure state corresponding to the $1\delta^3\,3\sigma^1$ electronic configuration, and further assuming that the 3σ orbital has pure Os 6*s* character, these parameters combine to predict h(X $^3\Delta_3$) = 0.149 cm^{-1}. This result is completely dominated by the large value of the Fermi contact interaction for the 6*s* electron, $b_{F,6s}$, which alone contributes 0.129 cm^{-1} to the value of h.

Although the hyperfine splitting is not well resolved in any of our spectra, we have attempted to extract values of h″ and h′ for all of the bands originating from the $X^3\Delta_3$ level by fitting the spectra of the $^{189}Os^{12}C$ isotopomer using the PGOPHER program.[53] To obtain a fit, the experimental spectrum was overlaid on a simulated spectrum, and the hyperfine parameters were varied until the two spectra were similar.

Then, specific hyperlines in the experimental spectrum were assigned to the lines in the simulated spectrum, and a least-squares fit was performed. Due to the poor resolution of hyperfine structure in our experiments, the resulting fits are not as definitive as we would like, but good agreement is found among the four fitted bands for the value of h($X\,^3\Delta_3$), with values ranging between 0.1287 and 0.1428 cm^{-1}. These values are close to the value of h = 0.149 cm^{-1} that is predicted assuming that the 3σ orbital is purely Os 6*s* in character. Assuming that the only effect of admixtures of other atomic orbitals into the 3σ orbital is to reduce the contribution of $b_{F,6s}$ proportionately, these values suggest that the 3σ orbital is approximately 84% to 95% 6*s* in character. A more precise interpretation of the hyperfine interactions in this molecule will require investigation at higher resolution. Table 3.3 provides a summary of the fit results for the $^{189}Os^{12}C$ isotopomer including hyperfine interactions. Figure 3.5 presents a comparison of the measured and fitted spectra of the 0-0 band of the [19.1]2 ← $X\,^3\Delta_3$ system of $^{189}Os^{12}C$, including hyperfine effects.

3.3.2.6. The bond length of the $X\,^3\Delta$ state of OsC: correction for spin-uncoupling effects

To obtain the most accurate estimate of the ground state bond length of OsC, one must take into account the effects of the spin-uncoupling operator, which couples the observed $^3\Delta_3$ ground level to the unobserved $^3\Delta_2$ level. The spin-uncoupling operator affects the magnitude of the rotational constant, such that the measured B value of the $^3\Delta_3$ level is reduced, giving an effective B value that obeys the expression[54]

Table 3.3. Upper and lower state fitted parameters of $^{189}Os^{12}C$, including hyperfine effects.[a]

Molecule		0-0 $[19.1]2 \leftarrow X^3\Delta_3$	1-0 $[19.1]2 \leftarrow X^3\Delta_3$	0-0 $[20.5]3 \leftarrow X^3\Delta_3$	0-0 $[21.2]2 \leftarrow X^3\Delta_3$
$^{189}Os^{12}C$	v_0 (cm^{-1})	19062.737	20016.316	20543.151	21282.735
	B″ (cm^{-1})	0.5326	0.5332	0.5346	0.5346
	r″ (Å)	1.6749	1.6739	1.6717	1.6717
	h″ (cm^{-1})	0.142	0.1428	0.132	0.1287
	B′ (cm^{-1})	0.5193	0.5117	0.52441	0.4899
	r′ (Å)	1.6962	1.7087	1.6879	1.7463
	h′ (cm^{-1})	0.0148	0.0169	-0.007	0.0141

[a] obtained using the PGOPHER program (reference 54).

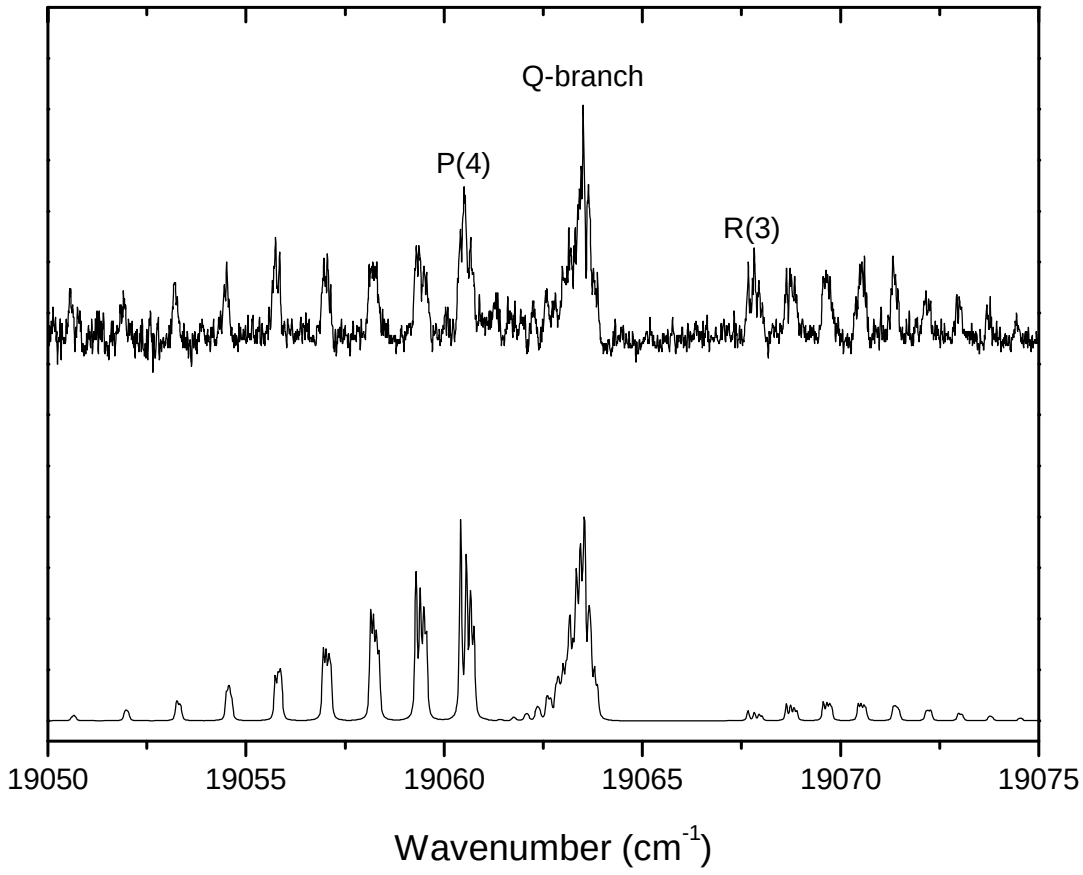

Figure 3.5. Measured (top) and simulated (bottom) spectra of the 0-0 band of the [19.1]2← $X\,^3\Delta_3$ system of $^{189}Os^{12}C$, showing hyperfine structure

$$B_{eff}(\Omega) = B_{true}\left(1 + \frac{2B_{true}\Sigma}{A\Lambda}\right). \quad (3.8)$$

For the $\delta^3\sigma^1$, $^3\Delta$ ground term of OsC, the spin-orbit parameter A may be estimated using the semiempirical method of Ishiguro and Kobori,[55] providing

$$A = -\zeta_{Os}(5d)/2, \quad (3.9)$$

where the atomic spin-orbit constant $\zeta_{Os}(5d) = 3045$ cm^{-1} is taken from the compilation of Lefebvre-Brion and Field.[50] After combining the data for all of the OsC isotopomers and correcting for the effects of spin-uncoupling, our best estimate of the OsC ground state bond length, r_0'', is 1.67214 ± 0.00028 Å (1σ error limit). The correction for the effects of the spin-uncoupling operator is minor, shortening the estimate of the bond length by only about 0.0003 Å. This is due to the small value of B, combined with the large value of A.

3.4 Discussion

In considering the possible ground and low-lying electronic states of OsC, it is useful to think about the molecular orbitals of the molecule. The valence atomic orbitals and the molecular orbitals generated from them are displayed in the qualitative molecular orbital diagram of Figure 3.6. In this diagram, the 1σ orbital of OsC is assumed to be corelike and mainly carbon 2*s* in character. The 2σ and 4σ orbitals are considered to be bonding and antibonding combinations of the Os 5*d*σ and C 2*p*σ orbitals, respectively, and the 1π and 2π orbitals are likewise considered to be bonding and antibonding combinations of the Os 5*d*π and C 2*p*π orbitals. The 3σ orbital is expected to be

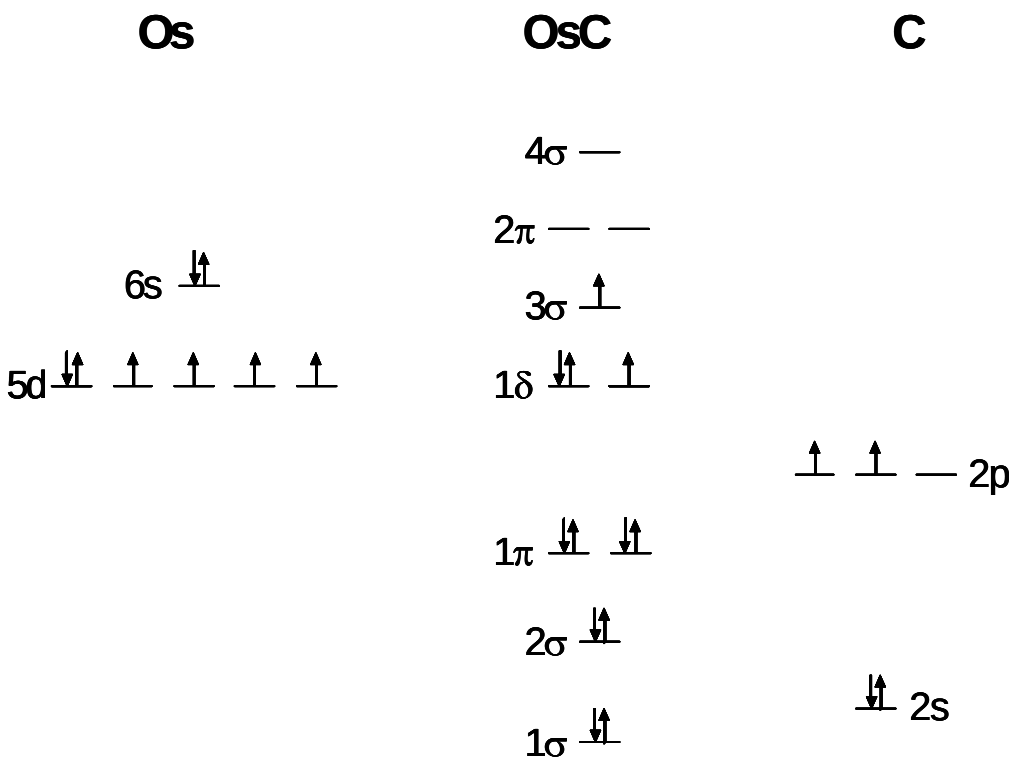

Figure 3.6 Qualitative molecular orbital diagram of OsC

primarily nonbonding in character, arising from the 6*s* orbital of Os. This is confirmed by the hyperfine measurements described in Section 3.3.2.5. The 1δ orbitals are nonbonding and almost entirely Os 5*d*δ in character. It is possible that there is significant *sp* hybridization on the carbon atom, but this possibility has no consequences for the spectroscopic results presented here and will not be discussed further.

Given that OsC has 12 valence electrons, the low-lying 1σ, 2σ, and 1π orbitals are expected to be filled in any low-lying electronic states. The real issue in this molecule concerns how the remaining four electrons fill the 1δ and 3σ orbitals. There are three configurational candidates for the ground electronic state: $1\delta^4$, giving a $^1\Sigma^+$ ground state, as in the isovalent RuC molecule,[37] $1\delta^3\,3\sigma^1$, giving a $^3\Delta_3$ ground state, as in the isovalent FeC molecule,[31-33] and $1\delta^2\,3\sigma^2$, giving a $^3\Sigma^-$ ($\Omega = 0^+$) ground state, as predicted by *ab initio* theory.[16,30] Of these possibilities, only the $^3\Delta_3$ state is consistent with the value of Ω'' obtained from the rotational analyses of the strong bands measured in this work. Therefore, $^3\Delta_3$ is established as the ground state of the OsC molecule.

The other low-lying electronic state observed in this work is a state with $\Omega'' = 0$. Although there is no experimental evidence that this state has $\Omega = 0^+$ parity, the only reasonable electronic configurations that can lead to a low-lying $\Omega = 0$ level are the $1\delta^4$, $^1\Sigma^+$ term and the $1\delta^2\,3\sigma^2$, $^3\Sigma^-$ term. To distinguish between these possibilities, it is useful to compare the bond lengths expected for the various configurations. In FeC and RuC, transfer of electrons from the δ orbital to the σ orbital leads to an increase in bond length. For example, first order configuration interaction calculations on RuC predict bond lengths of 1.642 Å (δ^4, $^1\Sigma^+$); 1.666 Å ($\delta^3\,\sigma^1$, $^3\Delta$), and 1.724 Å ($\delta^2\,\sigma^2$, $^3\Sigma^-$).[56] The increase in bond length for RuC that accompanies transfer of electrons from the δ to the σ orbital

is in agreement with the experimentally measured increase in bond length in going from the δ^4, $^1\Sigma^+$ state (1.608 Å) to the $\delta^3\sigma^1$, $^3\Delta$ state (1.635 Å).[37] Similarly, multireference configuration interaction calculations on the $\delta^3\sigma^1$, $^3\Delta$ ground state of FeC predict a shorter bond length (1.585 Å) than is predicted for the $\delta^2\sigma^2$, $^3\Sigma^-$ state (1.672 Å).[57] Finally, a CCSD(T) calculation on OsC predicts an increase in bond length of 0.02 Å when one shifts an electron from the 1δ orbital to the 3σ orbital, in going from the $1\delta^3 3\sigma^1$, $^3\Delta_3$ term (1.69 Å) to the $1\delta^2 3\sigma^2$, $^3\Sigma^-$ term (1.71 Å). Considering the measured rotational constants for OsC, and the bond lengths that they imply, the increase in bond length of 0.025 Å in going from the X $^3\Delta_3$ level to the low-lying Ω = 0 level strongly suggests that this low-lying Ω = 0 level arises from the $1\delta^2 3\sigma^2$, $^3\Sigma^-$ term. The fact that this term is predicted to be the ground term in the two published calculations lends credence to this possibility,[16,30] and therefore we assign this low-lying electronic state as the $1\delta^2 3\sigma^2$, A $^3\Sigma^-_{0+}$ level.

The *ab initio* calculations predict that the OsC ground state is the $1\delta^2 3\sigma^2$, $^3\Sigma^-$ term, with the $1\delta^3 3\sigma^1$, $^3\Delta$ term lying 2200 cm^{-1} higher in energy.[16] Adding spin-orbit effects, the $^3\Delta_3$ level is expected to be stabilized in first-order perturbation theory by an amount given by ζ_{5d}(Os), which is about 3045 cm^{-1}. The $1\delta^2 3\sigma^2$, $^3\Sigma^-_{0+}$ level is perturbed by spin-orbit interaction with the higher lying $1\delta^2 3\sigma^2$, $^1\Sigma^+_{0+}$ level, with which it has a Hamiltonian matrix element given by $\left\langle 1\delta^2 3\sigma^2, {}^3\Sigma^-_{0+} \middle| \hat{H}^{SO} \middle| 1\delta^2 3\sigma^2, {}^1\Sigma^+_{0+} \right\rangle = 2\zeta_{5d}(Os)$. For zeroth-order separations between the $^3\Sigma^-$ and $^1\Sigma^+$ terms of 0 to 5000 cm^{-1}, this results in a stabilization of the $1\delta^2 3\sigma^2$, $^3\Sigma^-_{0+}$ level by 4000 to 6000 cm^{-1}. For a zeroth-order separation that is even as large as 10 000 cm^{-1}, the $1\delta^2 3\sigma^2$, $^3\Sigma^-_{0+}$ level is still stabilized by

2880 cm^{-1}. Based on these results, it seems that spin-orbit effects will stabilize the $^3\Sigma^-_{0+}$ level even more than the $^3\Delta_3$ level. Thus, it seems that spin-orbit effects are not sufficient to reverse the predicted energetic ordering of the states to bring them into agreement with experiment. The OsC molecule represents a formidable challenge to quantum chemistry, requiring accurate treatments of electron correlation as well as relativistic effects, including spin-orbit interactions.

The upper states of the spectroscopic transitions reported here consist of the two $\Omega' = 2$ states at 19064 and 21284 cm^{-1}, an $\Omega' = 3$ state at 20543 cm^{-1}, and two $\Omega' = 1$ states at 20729 + x and 21006 + x cm^{-1}, where x represents the energy of the A $^3\Sigma^-_{0+}$ level relative to the X $^3\Delta_3$ ground level. These cannot arise from the low energy configurations of $1\delta^3\,3\sigma^1$, $1\delta^2\,3\sigma^2$, or $1\delta^4$, because all of the $\Omega = 1$, 2, or 3 levels arising from these configurations are expected to be within about 6000 cm^{-1} of the X $^3\Delta_3$ or A $^3\Sigma^-_{0+}$ levels. Thus, the upper levels involved in the measured transitions must involve either promotion of an electron from the 1π or 2σ bonding orbitals into the nonbonding 1δ and 3σ orbitals, or promotion of an electron from the nonbonding 1δ and 3σ orbitals into the antibonding 2π and 4σ orbitals. In the case of RuC, electronic states lying in the range from 12700 to 18100 cm^{-1} could be confidently assigned to the $1\delta^3\,2\pi^1$ configuration, which corresponds to the $1\delta^3\,2\pi^1$ configuration of OsC. This configuration generates two $\Omega' = 3$ levels ($^3\Phi_3$ and $^1\Phi_3$), two $\Omega = 2$ levels ($^3\Phi_2$ and $^3\Pi_2$), and two $\Omega'=1$ levels ($^1\Pi_1$ and $^3\Pi_1$), although these are expected to be very strongly mixed by spin-orbit effects due to the large spin-orbit parameter of Os. Given the stabilization of the 3σ orbital in OsC, however, it is more likely that the upper states of these transitions correspond to the $1\delta^2\,3\sigma^1\,2\pi^1$ configuration, which generates three $\Omega = 3$ levels ($^1\Phi_3$, $^3\Phi_3$, and $^5\Pi_3$), five $\Omega = 2$

levels (three $^3\Pi_2$, one $^5\Pi_2$, and one $^3\Phi_2$ level), and six $\Omega = 1$ levels (two $^1\Pi_1$, three $^3\Pi_1$, and one $^5\Pi_1$ level). Without additional information, such as might be obtained by a study of OsC in the red region of the spectrum or dispersed fluorescence studies, or by a more detailed computational investigation, it is impossible to identify either the upper state configurations or term symbols for this molecule.

Even though the spectroscopic data on the 5*d* transition metal carbides is limited to WC,[1,2] IrC,[3-5] PtC,[7,8,11,13] and now OsC, it is clear that in these molecules states in which the 6*s*-like 3σ orbital is occupied are stabilized. For example, the ground level of WC is $1\delta^1 3\sigma^1$, $^3\Delta_1$,[1] as compared to the $1\delta^2$, $^3\Sigma^-_{0+}$ ground level of MoC.[58] Similarly, the ground level of IrC is $1\delta^3 3\sigma^2$, $^2\Delta_{5/2}$,[3,4,27] as compared to the $1\delta^4\, 3\sigma^1$, $^2\Sigma^+$ ground level of RhC.[59-62] Our newly recorded data on OsC fits nicely into this trend: OsC has a $1\delta^3 3\sigma^1$, $^3\Delta_3$ ground term while RuC has a $1\delta^4$, $^1\Sigma^+$ ground term.[37] These results reflect the relativistic stabilization of the 6*s* orbital, an effect that is responsible for the yellow color of metallic gold, the fact that mercury is a liquid at room temperature, and the "inert pair effect," in which the more stable oxidation states of thallium (Tl^{1+}), lead (Pb^{2+}), and bismuth (Bi^{3+}) retain two electrons in the 6*s* orbital.[63]

3.5 Conclusion

The electronic spectrum of diatomic OsC was recorded in the range from 17390 to 22990 cm^{-1}, using resonant two-photon ionization spectroscopy. This study reveals that the ground term of OsC is $1\delta^3 3\sigma^1$, $X\,^3\Delta_3$ and that the $1\delta^2 3\sigma^2$, $A\,^3\Sigma^-_{0+}$ level lies low enough in energy to be populated in the jet-cooled molecular beam. Rotational constants and bond lengths are reported for these states, and for six excited vibronic levels of diatomic OsC.

3.6 References

(1) Sickafoose, S. M.; Smith, A. W.; Morse, M. D. *J. Chem. Phys.* **2002**, *116*, 993.

(2) Li, X.; Liu, S. S.; Chen, W.; Wang, L.-S. *J. Chem. Phys.* **1999**, *111*, 2464.

(3) Jansson, K.; Scullman, R.; Yttermo, B. *Chem. Phys. Lett.* **1969**, *4*, 188.

(4) Jansson, K.; Scullman, R. *J. Mol. Spectrosc.* **1970**, *36*, 248

(5) Marr, A. J.; Flores, M. E.; Steimle, T. C. *J. Chem. Phys.* **1996**, *104*, 8183.

(6) Ma, T.; Leung, J. W. H.; Cheung, A. S. C. *Chem. Phys. Lett.* 2004, 385, 259.

(7) Neuhaus, H.; Scullman, R.; Yttermo, B. .*Z Naturforsch.* **1965**, *20a*, 162.

(8) Scullman, R.; Yttermo, B. *Ark. Fys.* **1966**, *33*, 231.

(9) Appelblad, O.; Barrow, R. F.; Scullman, R. *Proc. Phys. Soc., London* **1967**, *91*, 260.

(10) Appelblad, O.; Nilsson, C.; Scullman, R. *Phys. Scr.* **1973**, *7*, 65.

(11) Steimle, T. C.; Jung, K. Y.; Li, B.-Z. *J. Chem. Phys.***1995**, *102*, 5937.

(12) Steimle, T. C.; Jung, K. Y.; Li, B.-Z. *J. Chem. Phys.* **1995**, *103*, 1767.

(13) Beaton, S. A.; Steimle, T. C. *J. Chem. Phys.* **1999**, *111*, 10876.

(14) Steimle, T. C.; Costen, M. L.; Hall, G. E.; Sears, T. J. *Chem. Phys. Lett.* **2000**, *319*, 363.

(15) Gingerich, K. A.; Cocke, D. L. *Inorg. Chim. Acta* **1978**, *28*, L171.

(16) Meloni, G.; Thomson, L. M.; Gingerich, K. A. *J. Chem. Phys.* **2001**, *115*, 4496.

(17) McIntyre, N. S.; Vander Auwera-Mahieu, A.; Drowart, J. *Trans. Faraday Soc.* **1968**, *64*, 3006

(18) Gupta, S. K.; Nappi, B. M.; Gingerich, K. A. *J. Phys. Chem.* **1981**, *85*, 971.

(19) Auwera-Mahieu, A. V.; Drowart, J. *Chem. Phys. Lett.* **1967**, *1*, 311.

(20) Kohl, F. J.; Stearns, C. A. *High Temp. Sci* **1974**, *6*, 284.

(21) Armentrout, P. B.; Shin, S.; Liyanage, R. *J. Phys. Chem. A* **2006**, *110*, 1242.

(22) Armentrout, M. M.; Li, F.-X.; Armentrout, P. B. *J. Phys. Chem. A* **2004**, *108*, 9660.

(23) Li, F.-X.; Zhang, X.-G.; Armentrout, P. B. *Int. J. Mass Spectrom.* **2006**, *255-256*, 279.

(24) Zhang, X.-G.; Liyanage, R.; Armentrout, P. B. *J. Am. Chem. Soc.* **2001**, *123*, 5563.

(25) Majumdar, D.; Balasubramanian, K. *Chem. Phys. Lett.* **1998**, *284*, 273.

(26) Balasubramanian, K. *J. Chem. Phys.* **2000**, *112*, 7425.

(27) Tan, H.; Liao, M.; Balasubramanian, K. *Chem. Phys. Lett.* **1997**, *280*, 219.

(28) Minaev, B. F. *Phys. Chem. Chem. Phys.* **2000**, *2*, 2851.

(29) Barysz, M.; Pyykko, P. *Chem. Phys. Lett.* **1998**, *285*, 398.

(30) Wang, J.; Sun, X.; Wu, Z. *J. J. Cluster Sci.* **2007**, *18*, 333.

(31) Balfour, W. J.; Cao, J.; Prasad, C. V. V.; Qian, C. X. *J. Chem. Phys.* **1995**, *103*, 4046.

(32) Allen, M. D.; Pesch, T. C.; Ziurys, L. M. *Astrophys. J.* **1996**, *472*, L57.

(33) Brugh, D. J.; Morse, M. D. *J. Chem. Phys.* **1997**, *107*, 9772.

(34) Aiuchi, K.; Tsuji, K.; Shibuya, K. *Chem. Phys. Lett* **1999**, *309*, 229.

(35) Scullman, R.; Thelin, B. *Phys Scr* **1971**, *3*, 19.

(36) Scullman, R.; Thelin, B. *Phys. Scr.* **1972**, *5*, 201.

(37) Langenberg, J. D.; DaBell, R. S.; Shao, L.; Dreessen, D.; Morse, M. D. *J. Chem. Phys.* **1998**, *109*, 7863.

(38) DaBell, R. S.; Meyer, R. G.; Morse, M. D. *J. Chem. Phys.* **2001**, *114*, 2938.

(39) Lindholm, N. F.; Hales, D. A.; Ober, L. A.; Morse, M. D. *J. Chem. Phys.* **2004**, *121*, 6855.

(40) Wiley, W. C.; McLaren, I. H. *Rev. Sci Instrum* **1955**, *26*, 1150

(41) Mamyrin, B. A.; Karataev, V. I.; Shmikk, D. V.; Zagulin, V. A. *Zh. Eksp. Teor. Fiz.* **1973**, *64*, 82.

(42) Gerstenkorn, S.; Luc, P. *Atlas du Spectre d'Absorption de la Molécule d'Iode entre 14,800-20,000 cm^{-1}*; CNRS: Paris, 1978.

(43) Gerstenkorn, S.; Luc, P. *Rev. Phys. Appl* **1979**, *14*, 791.

(44) Cariou, J.; Luc, P. *Atlas du Spectre d'Absorption de la Molécule Tellure, Partie 5: 21,100 - 23,800 cm^{-1}*; CNRS: Paris, 1980.

(45) Cariou, J.; Luc, P. *Atlas du Spectre d'Absorption de la Molécule de Tellure entre 18,500 - 23,800 cm^{-1}*; CNRS: Paris, 1980.

(46) Bevington, P. R. *Data Reduction and Error Analysis for the Physical Sciences*; McGraw-Hill: New York, 1969.

(47) Kopp, I.; Hougen, J. T. *Can. J. Phys* **1967**, *45*, 2581.

(48) Dunn, T. M. In *Molecular Spectroscopy:Modern Research*; Rao, K. N., Mathews, C. W., Eds.; Academic Press: New York and London, 1972; pp 231.

(49) Weltner, W., Jr. *Magnetic Atoms and Molecules*; Dover Publications, Inc.: New York, 1983.

(50) Lefebvre-Brion, H.; Field, R.; Editors *The Spectra and Dynamics of Diatomic Molecules, Revised and Enlarged Edition; Second Edition*, 2004.

(51) Townes, C. H.; Schawlow, A. L. *Microwave Spectroscopy*; Dover Publications, Inc.: New York, 1975.

(52) Büttgenbach, S. *Hyperfine Structure in 4d- and 5d-Shell Atoms*; Springer-Verlag: Berlin Heidelberg New York, 1982; Vol. 96.

(53) Western, C. M. PGOPHER, a Program for Simulating Rotational Structure, University of Bristol, http://pgopher.chm.bris.ac.uk.

(54) Herzberg, G. *Molecular Spectra and Molecular Structure I. Spectra of Diatomic Molecules*, 2nd ed.; Van Nostrand Reinhold: New York, 1950.

(55) Ishiguro, E.; Kobori, M. *J. Phys. Soc. Japan* **1967**, *22*, 263.

(56) Guo, R.; Balasubramanian, K. *J. Chem. Phys.* **2004**, *120*, 7418.

(57) Tzeli, D.; Mavridis, A. *J. Chem. Phys.* **2002**, *116*, 4901.

(58) Brugh, D. J.; Ronningen, T. J.; Morse, M. D. *J. Chem. Phys.***1998**, *109*, 7851.

(59) Lagerqvist, A.; Scullman, R. *Ark. Fys* **1966**, *32*, 475

(60) Kaving, B.; Scullman, R. *J. Mol. Spectrosc.* **1969**, *32*, 475

(61) Brom, J. M., Jr.; Graham, W. R. M.; Weltner, W., Jr. *J. Chem. Phys.* **1972**, *57*, 4116.

(62) Balfour, W. J.; Fougère, S. G.; Heuff, R. F.; Qian, C. X. W.; Zhou, C. *J. Mol. Spectrosc.* **1999**, *198*, 393.

(63) Balasubramanian, K. *J. Phys. Chem.* **1989**, *93*, 6585.

CHAPTER 4

RESONANT TWO-PHOTON IONIZATION SPECTROSCOPY OF JET COOLED TaC

4.1 Introduction

Among the transition metal carbides, TaC has the highest melting temperature of 4256 K, and other desirable physical and chemical properties, such as high hardness (1800 kg/mm^2), high elastic modulus (285 GPa), good heat and electric conductivity, and high chemical resistance and catalytic activity.[1,2] These properties suggest a wide range of applications for solid TaC, ranging from hard coatings on mining tools to new materials, including supported thin films,[3] nanoparticles,[4] *etc*. Despite these attractive properties and wide applications, information on the geometry and electronic configuration of the building blocks of bulk TaC, such as small TaC clusters, including the diatomic molecule, remains very limited. Small TaC clusters, including diatomic TaC, were first isolated in the gas phase and studied by means of Fourier transform mass spectrometry by McElvany *et al.*[5] The formation of small TaC clusters in a supersonic expansion following the reaction of tantalum and acetylene in a laser ablation source was studied by Heaven *et al.*[6]

No spectroscopic studies on diatomic TaC have been previously reported. The first computational study on the potential energy curves and spectroscopic constants of TaC

and TaC^+ was performed by Majumdar *et al*. at a variety of different levels of theory.[7] They find the ground state to be $X\ ^2\Sigma^+$, originating from the $1\sigma^2\ 2\sigma^2\ 1\pi^4\ 3\sigma^1$ electronic configuration with a bond length of r_e = 1.799 Å and a vibrational frequency of 748 cm^{-1}. The ordering of the low lying excited states changes with the level of theory employed, however. At the CASSCF-SOCI level of theory, the first and second excited states are $^4\Delta$ and $^2\Pi$, lying 0.43 and 0.48 eV above the ground state, respectively.[7] In the course of their study of the Ta_nC_m clusters, Heaven *et al.*[6] performed B3P86 density functional calculations on TaC as well as on the larger clusters. Diatomic TaC was again found to have a $^2\Sigma^+$ ground state with a bond length of 1.76 Å and a vibrational frequency of 977 cm^{-1}. Finally, in a B3LYP density functional investigation of all of the 5*d* transition metal carbides,[8] TaC was again found to have a $^2\Sigma^+$ ground state, originating from the $1\sigma^2 2\sigma^2 1\pi^4 3\sigma^1$ configuration. The bond length was predicted to be 1.735 Å, and the vibrational frequency was calculated to be 944 cm^{-1}. The first excited state was found to be $^4\Delta$, lying only 0.28 eV above the ground state.[8]

An interesting comparison can be made between TaC and other group 5 transition metal carbides. Diatomic VC and NbC have been previously studied, both experimentally and theoretically. Diatomic VC has been investigated by electron spin resonance (ESR) methods in cryogenic rare gas matrices. Its ground state has been identified as a $^2\Delta_{3/2}$ state, for which the orbital angular momentum is quenched in the cryogenic matrix.[9] A recent computational investigation of VC also predicts a $^2\Delta$ ground state, with $^4\Delta$ and $^2\Sigma^+$ as low-lying excited states, located 0.18 and 0.30 eV above the ground state, respectively.[10] A combined R2PI/LIF and density functional study of diatomic NbC also found its ground state to be $^2\Delta_{3/2}$, originating from the $1\sigma^2 2\sigma^2 1\pi^4 1\delta^1$ configuration.[11]

Low-lying excited states of $^2\Sigma^+$ and $^4\Delta$ were computed to lie 0.42 and 0.55 eV above the ground state, respectively.[11] In both VC and NbC, the low-lying $^2\Sigma^+$ and $^4\Delta$ states derive from the $1\sigma^2 2\sigma^2 1\pi^4 3\sigma^1$ and $1\sigma^2 2\sigma^1 1\pi^4 3\sigma^1 1\delta^1$ configurations, respectively.

In agreement with the computational studies, the spectroscopic results obtained in the present study demonstrate that the ground state of TaC is $^2\Sigma^+$, deriving from the $1\sigma^2 2\sigma^2 1\pi^4 3\sigma^1$ configuration. The emergence of a different ground state in TaC, demonstrates that the relativistic stabilization of the 6*s*-like 3σ molecular orbital lowers the energy of the $^2\Sigma^+$ term, as compared to the $^2\Delta$ and $^4\Delta$ terms, so $^2\Sigma^+$ emerges as the ground state.

4.2 Experimental

Diatomic TaC was investigated using resonant two-photon ionization (R2PI) spectroscopy. We will not provide a detailed description of the apparatus here, since that has been provided previously.[12] In brief, the R2PI apparatus consists of two chambers that are differentially pumped. The first chamber is pumped by a VHS-10 diffusion pump, backed by a KDH-130 rotary mechanical pump, and consists of a pulsed supersonic nozzle, a disk vaporization assembly, and a molecular beam skimmer (1 cm diameter, 50° inside angle). To produce diatomic metal-ligand molecules, output radiation from a pulsed Nd-YAG laser (532 or 355 nm) is focused onto a metal target disk, and is timed to coincide with a pulse of helium carrier gas seeded with ligand gas. In order to vaporize metal uniformly, the metal sample is attached to a mechanism that rotates and translates the sample, so that a spiral pattern is traced out on the sample by the ablation laser. The metal containing plasma that is produced flows down a narrow channel (2 mm diameter × 1.3 cm long) prior to expansion into the chamber, which is

maintained at a pressure of 4×10^{-5} Torr, as read on an ion gauge that was calibrated on air.

The second chamber is pumped by an Edwards 160 diffusion pump, backed by a Welch 1397 rotary mechanical pump, and houses a reflectron-type time-of–flight mass spectrometer (RTOFMS) with Wiley-McLaren ion source optics and a microchannel plate detector.[13,14] The molecular beam is exposed to the output of the Nd-YAG pumped tunable dye laser counterpropagating along the axis of the molecular beam, and is crossed at right angles by the output of an ArF excimer laser (193 nm) about 40 ns later in time. Molecules that absorb the dye laser radiation are then ionized by the excimer laser in a resonant two-photon ionization process. The resulting ions are separated by mass in the RTOFMS and detected with the microchannel plate detector. To provide the optical spectrum, the ion signal of the molecule of interest is recorded as a function of the dye laser frequency.

In the past, we have attempted to study diatomic TaC, but these attempts were unsuccessful due to insufficient production of diatomic TaC in the molecular beam. In the present experiment, our first attempt to produce this molecule used a Ta:C sample alloy that had a molar ratio of 9:1, along with pure helium carrier gas. Varying all possible experimental conditions, such as ablation laser energy, backing pressure, nozzle voltage and duration of the pulse, no trace of TaC was found in the mass spectrum, even though Ta, TaO, and Ta_2 signals were very strong. For our second attempt, a pure Ta metal disk was employed with helium carrier gas that was seeded with 3% CH_4. Again, the same species were present in the molecular beam, with no trace of diatomic TaC. Decreasing the concentration of methane in the carrier gas to 1%, and averaging over 1000 shots to

obtain the mass spectrum, a small peak at the mass of TaC became visible. By decreasing the concentration of CH_4 to 0.25%, a strong TaC signal was finally observed. Based on this success with TaC, we believe that using very low concentrations of methane in the helium carrier gas is the key to producing early transition metal carbides, such as LaC and HfC, in the molecular beam.

Conditions used in the present study are: a pure Ta metal target disk, in combination with helium carrier gas seeded with 0.25% methane. The ablation laser used was the third harmonic of the Nd:YAG laser, at 355 nm, 10 mJ/pulse. For ionization, an unfocused excimer laser operating on the ArF mixture (193nm) was used. A reservoir pressure of 50 psig was found to be optimal for producing diatomic TaC molecules. Spectra were collected for the $^{181}Ta^{12}C$ isotopomer (98.92% natural abundance).

To investigate the vibronic spectra of diatomic TaC, the dye laser was scanned in low resolution mode (0.15 cm^{-1}), giving an output energy of 3-10 mJ. To reveal the rotational structure of each vibronic transition, the dye laser output was narrowed using an air-spaced intracavity etalon, which was pressure scanned with sulfur hexafluoride (SF_6). This provided a resolution of about 0.04 cm^{-1} and an output energy of about 1 mJ. During pressure scans the pressure in the dye laser cavity was varied from 30 to 800 torr; this corresponded to scans over a range of about 15 cm^{-1}. For each high resolution spectrum a reference spectrum of I_2 was collected for calibration purpose.[15] As molecules were traveling towards the light source at the beam velocity of helium (1.77×10^5 cm s^{-1}) all line positions were corrected for the Doppler shift experienced by the molecules. This amounted to a small correction of about 0.1 cm^{-1} for all of the lines recorded in this study.

The measured bands were all found to originate from the same lower state, which is assumed to be the ground state. A combined fit of six analyzed bands was performed using the program PGOPHER, a freely available general purpose program for simulating and fitting rotational, vibrational, and electronic spectra.[16]

4.3 Results

4.3.1. Vibronically resolved spectrum of TaC

The vibronically resolved spectrum of TaC was collected between 17850 and 20000 cm^{-1} and is presented in Figure 4.1. Over the spectral range 18300-20000 cm^{-1}, the density of vibronic states is very high, but in the 17850-18300 cm^{-1} range it is difficult to pick the transitions out from the noise in the spectrum. A possible explanation for this change is that the combination of the dye laser photon and the ArF excimer laser photon is insufficient to ionize the TaC molecule in the region below 18300 cm^{-1}. If this is true, it would place the ionization energy of TaC at approximately IE(TaC) ≈ 8.68 eV. To establish whether or not this interpretation is correct, it would be necessary to employ a shorter ionization wavelength (perhaps the F_2 excimer laser at 157 nm) as an ionization source, and search for vibronic transitions below 18300 cm^{-1}. An alternative method would be to measure a photoionization efficiency (PIE) spectrum or to use pulsed field ionization-zero electron kinetic energy (PFI-ZEKE) spectroscopy to measure the ionization energy precisely, as has been recently done for FeC.[17]

Due to severe vibronic congestion in the low resolution spectrum, and the absence of TaC isotopomers, no definitive vibronic progressions could be identified. It was simply impossible to group the observed vibronic bands into band systems. As a result, all information about the ground and excited states of TaC is obtained from the

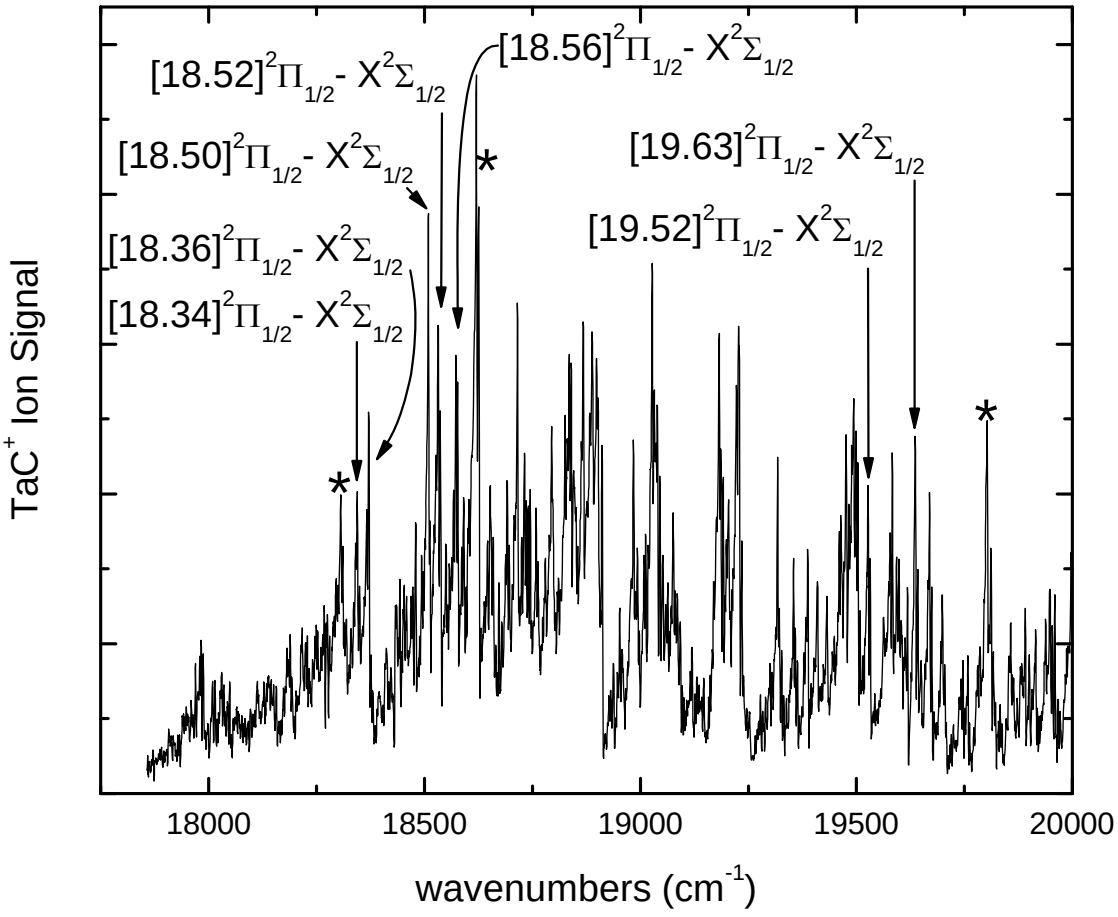

Figure 4.1 Vibronically resolved resonant two-photon ionization spectrum of TaC over the range 17850-20000 cm^{-1}. The bands labeled with asterisks consist of two or more overlapping transitions.

rotationally resolved spectra. Rotationally resolved spectra of 10 bands were collected, and 7 of these were successfully analyzed and fitted to obtain band origin positions, ground and exited state rotational constants, hyperfine parameters, and lambda doubling parameters. The remaining rotationally resolved bands that were not analyzed appeared to be single bands in the low resolution spectra, but seemed to be overlapping bands when investigated at higher resolution. These unanalyzed bands are identified with asterisks in Figure 4.1. All of the rotationally resolved and fitted spectra were found to originate from the same state, which is assumed to be the ground vibronic state of the molecule. This is the $X^2\Sigma^+$ state that is calculated to be the ground state in all of the computational studies on this molecule. The six rotationally resolved bands were analyzed, simultaneously fitted, and simulated using the PGOPHER program to obtain the most accurate ground state parameters.[16]

4.3.2. Rotationally resolved spectra of $^{181}Ta^{12}C$

The rotationally resolved spectra collected in this study for TaC are all qualitatively similar in appearance, as illustrated in Figures 4.2-4.4. In all of the spectra recorded, the band is shaded to the red, with the most intense feature corresponding to a band head. As shown most clearly in Figure 4.2, however, the band head appears to be doubled, with the two heads about 0.5 cm^{-1} apart. Additional weaker features occur to the blue of the band head in all bands that were resolved, culminating in a second band head about 4 cm^{-1} to the blue of the most intense band head. This second band head is also doubled, with a similar splitting as in the stronger band head.

These rotationally resolved spectra are too complicated to result from a Hund's case (a) – Hund's case (a) transition with large spin-orbit splitting, as would be expected if the

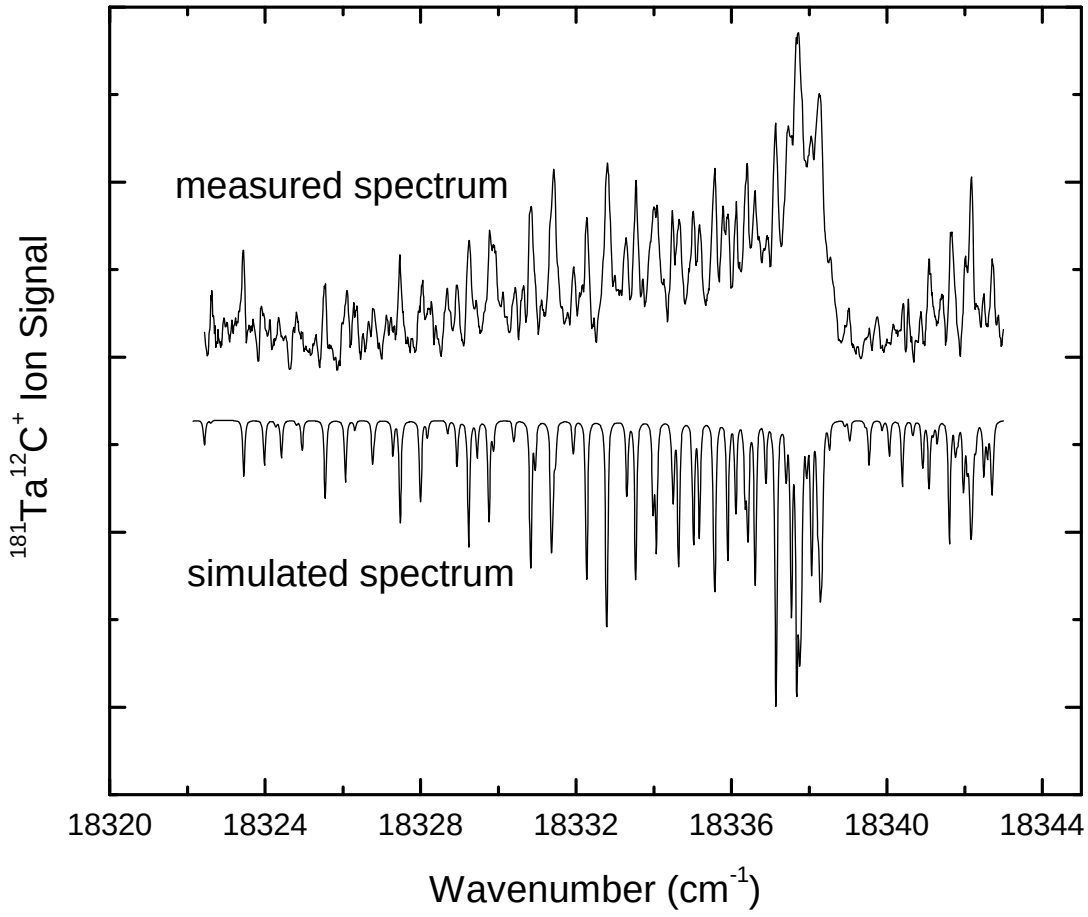

Figure 4.2 Rotationally resolved spectrum of the [18.34] $^2\Pi_{1/2}\leftarrow{}^2\Sigma^+$ transition

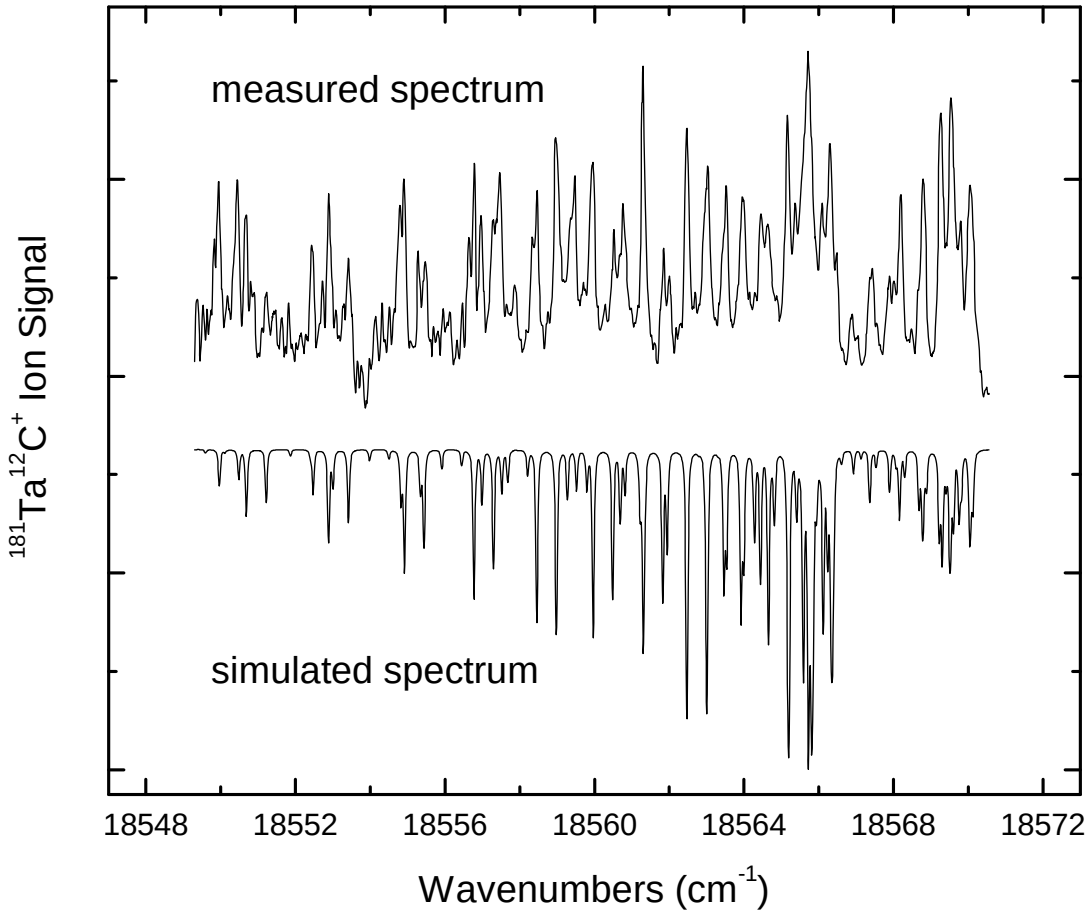

Figure 4.3. Rotationally resolved spectrum of the [18.56] $^2\Pi_{1/2}\leftarrow{}^2\Sigma^+$ transition

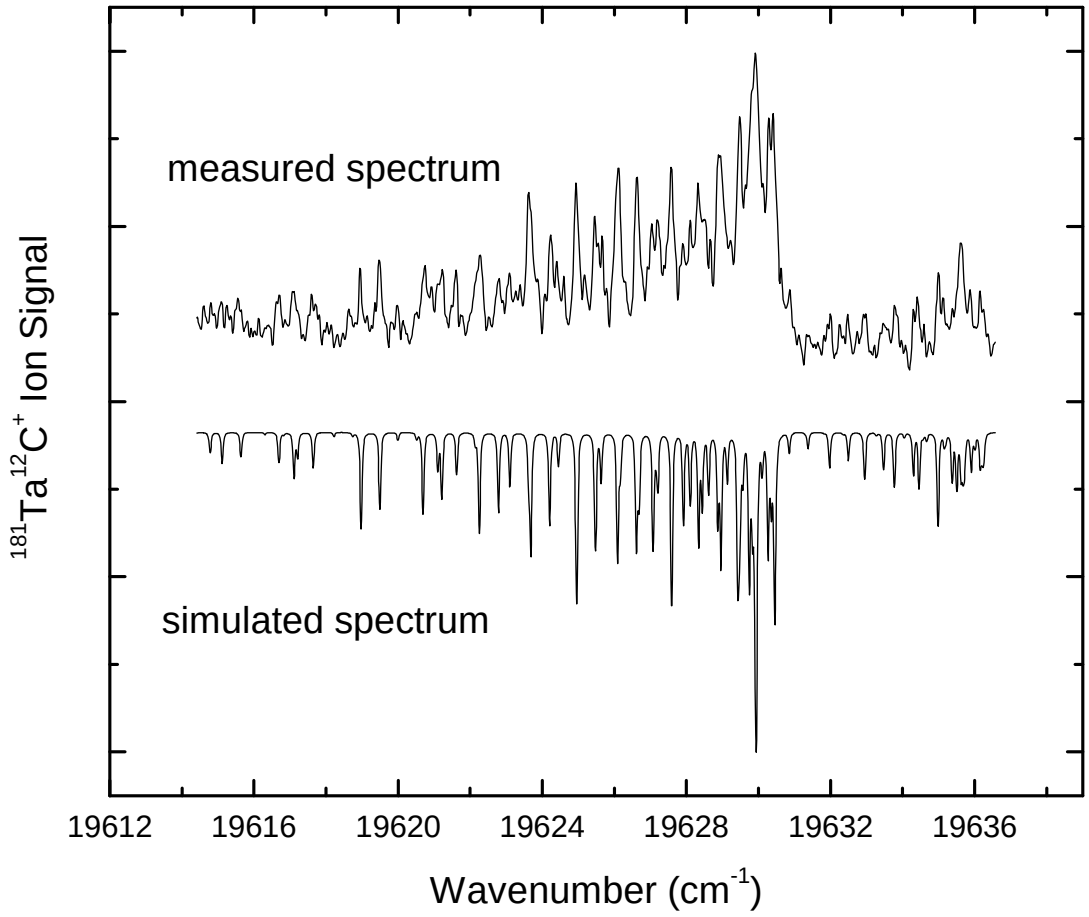

Figure 4.4. Rotationally resolved spectrum of the [19.63] $^2\Pi_{1/2}\leftarrow{}^2\Sigma^+$ transition

ground state were either the $1\sigma^2 2\sigma^2 1\pi^4 1\delta^1$, $^2\Delta$ state or the $1\sigma^2 2\sigma^1 1\pi^4 3\sigma^1 1\delta^1$, $^4\Delta$ state that are calculated to be low-lying electronic states in the molecule.[7] Thus, we focus on the $1\sigma^2 2\sigma^2 1\pi^4 3\sigma^1$, $^2\Sigma^+$ state as the likely ground state of the molecule. This state is favored by the available *ab initio* calculations[6-8] and is also able to account for the complexity of the observed spectra.

Complex spectra are expected in transitions between a Hund's case (b) $^2\Sigma^+$ ground state and a case (a) $^2\Pi_{1/2}$ or $^2\Pi_{3/2}$ upper state, with four apparent branches.[18] Because the pattern-forming quantum numbers in the upper and lower states are J′ and N″, respectively, these four branches correspond to values of J′ - N″ of 3/2, 1/2, -1/2, and -3/2. In addition, most of the transition metal molecules that have magnetically active (I>0) nuclei and $^2\Sigma^+$ ground states in which the 3σ orbital is singly-occupied, such as ScO,[19,20] YO,[21,22] LaO,[23] LaS,[24] and CoC,[25] belong to Hund's case $b_{\beta S}$.[26] In this coupling case, the magnetic hyperfine interaction, $b_F \hat{I} \cdot \hat{S}$, dominates over the spin-rotation interaction, $\gamma \hat{N} \cdot \hat{S}$, causing ***I*** and ***S*** to couple to form the resultant, ***G***. Finally, ***G*** couples with ***N*** to form the total angular momentum, ***F***.[26] The ^{181}Ta nucleus has a large nuclear spin (I = 7/2) and a rather large nuclear magnetic moment (2.35 nuclear magnetons),[27] making the $^2\Sigma^+(b_{\beta S})$ coupling case quite likely. For ^{181}TaC, I = 7/2 and S = 1/2, giving G=3, 4, with a splitting between these levels of $4b_F$. Further, if the 3σ orbital were purely Ta 6s in character, the atomic parameter $b_{F,6s}$= 0.1750 cm^{-1} for ^{181}Ta in its $5d^4 6s^1$ configuration[28] would lead to a splitting between G = 3 and 4 of 0.70 cm^{-1}. This is similar in magnitude to the doubling of all the features in the spectrum, where the observed splitting is about 0.5 cm^{-1}.

Leaving aside the question of whether the upper state is $^2\Pi_{1/2}$ or $^2\Pi_{3/2,}$ we adopt a modified version of the more commonly occurring $^2\Pi(a) - {}^2\Sigma^+(b_{\beta J})$ branch labeling scheme. In the modified scheme,[23,29,30] the $^2\Pi(a) - {}^2\Sigma^+(b_{\beta J})$ branch labels, specified by $^{\Delta N}\Delta J_{Fi' Fi''}(N'')$, are changed so that the F_i'' label is replaced by the value of G″. Thus, for a $^2\Pi_{1/2} - {}^2\Sigma^+(b_{\beta S})$ system, the eight hyperbranches are $^{O}P_{1G''}$, $^{P}P_{1G''} + {}^{P}Q_{1G''}$, $^{Q}Q_{1G''} + {}^{Q}R_{1G''}$, and $^{R}R_{1G''}$, where G″=3, 4. Likewise, for a $^2\Pi_{3/2} - {}^2\Sigma^+(b_{\beta S})$ system, the eight hyperbranches are $^{P}P_{2G''}$, $^{Q}P_{2G''} + {}^{Q}Q_{2G''}$, $^{R}Q_{2G''} + {}^{R}R_{2G''}$, and $^{S}R_{2G''}$, where G″=3, 4. The upper states of $^2\Pi_{1/2}$ or $^2\Pi_{3/2}$ may be distinguished by the first lines in the hyperbranches, with first lines (labeled by N″) of $^{O}P_{1G''}(2)$, $^{P}P_{1G''}(1) + {}^{P}Q_{1G''}(1)$, $^{Q}Q_{1G''}(0) + {}^{Q}R_{1G''}(1)$, and $^{R}R_{1G''}(0)$ for $^2\Pi_{1/2} \leftarrow {}^2\Sigma^+$ and $^{P}P_{2G''}(3)$, $^{Q}P_{2G''}(2) + {}^{Q}Q_{2G''}(2)$, $^{R}Q_{2G''}(1) + {}^{R}R_{2G''}(1)$, and $^{S}R_{2G''}(0)$ for $^2\Pi_{1/2} \leftarrow {}^2\Sigma^+$.[18]

Thus, a $^2\Pi_{3/2} \leftarrow {}^2\Sigma^+(b_{\beta S})$ transition lacks some of the lines that would be present in a $^2\Pi_{1/2} \leftarrow {}^2\Sigma^+(b_{\beta S})$ transition. An additional distinction between these two types of bands lies in the lambda-doubling of the upper $^2\Pi_\Omega$ state. In the case of $^2\Pi_{1/2}$, the lambda doubling is expected to be larger than in the $^2\Pi_{3/2}$ case, and to show a magnitude proportional to (J + 1/2).[31] In contrast, a $^2\Pi_{3/2}$ state is expected to have a much smaller lambda doubling, and a magnitude proportional to (J-1/2)(J+1/2)(J+3/2).[31] Thus, in the case of $^2\Pi_{3/2}$, the lambda doubling is expected to be unobservable in the low-J lines that are populated in our experiment, but to rapidly grow in magnitude as J increases.

None of the seven rotationally analyzed bands could be fitted to the expected structure of a $^2\Pi_{3/2}$ upper state, but all could be explained as having $^2\Pi_{1/2}$ upper states. It was necessary to include lambda doubling in the upper state in order to fit the bands, but the splitting pattern expected for the $^2\Pi_{3/2}$ was not in good agreement with the measured line positions. In addition, for many of the bands lines were observed that do not occur

for a $^2\Pi_{3/2} \leftarrow ^2\Sigma^+$ transition. Thus, we are confident that all of the upper states observed correspond to states with $\Omega = 1/2$. It is likely that these upper states are severely mixed by spin-orbit interaction so that S, Λ, and Σ may be poorly defined, but all are consistent only with $\Omega = 1/2$. Thus, upper states that are primarily $^4\Pi_{1/2}$, $^4\Pi_{-1/2}$, or $^4\Delta_{1/2}$ in character are also candidates for the upper states.

Hyperfine splitting arising in the upper states was not resolved. Likewise, the splitting of the G″ = 3 or 4 sublevels into the various F″ components was not resolved either. The bands could all be explained by including the splitting into G″-levels in the lower state and the lambda doubling in the upper state. The spin-rotation interaction could be ignored in the lower state, and the hyperfine interaction could be ignored in the upper state. The bands were therefore fitted to the $\hat{N}^2$ form of the rotational Hamiltonian given by

$$\hat{H} = B\hat{N}^2 + b_F \hat{I} \cdot \hat{S} \tag{4.1}$$

for the ground $^2\Sigma^+$ state and

$$\hat{H} = T_0 + B\hat{N}^2 + A\hat{L}_Z\hat{S}_Z + \frac{1}{2}(p+2q)\left(e^{-2i\varphi}\hat{J}_+\hat{S}_+ + e^{+2i\varphi}\hat{J}_-\hat{S}_-\right) \tag{4.2}$$

for the excited $^2\Pi_{1/2}$ states.

The simulation and fitting of the bands was performed using PGOPHER, with all six bands fitted simultaneously in order to decrease the uncertainty in the ground state constants.[16] Despite the complexity of the bands, the fact that all can be fitted with the same ground state constants makes us confident that the assignments are correct. Using this procedure, accurate values of B''_0 and b''_F have been determined for the ground state,

and B′ and (p′+2q′) have been determined for each of the upper states that were analyzed. For this system, the spin-orbit splitting, A, of the upper $^2\Pi$ states has not been determined and is expected to be very large. Therefore, A was set to 2000 cm^{-1} in all of our upper states, so that spin-uncoupling interactions between the $\Omega = 1/2$ and 3/2 components of the $^2\Pi$ states were inconsequential in the fits. As a result, the reported values of T_0 are 1000 cm^{-1} higher than the approximate subband origins. Nevertheless, we report our values in this format so that other investigators can reproduce the simulated bands using PGOPHER, if they so desire.

The electronic document also contains measured and simulated spectra for all of the rotationally resolved bands. The spectroscopic constants resulting from the simultaneous fit of all 7 bands are provided in Table 4.1, along with the vibrationally averaged bond lengths that are obtained from simple inversion of the fitted B values. The simulated spectra displayed in Figures 4.2-4.4 were all calculated assuming a temperature of 33K for the jet-cooled TaC molecules. Although this is a bit warmer than we find for many of our spectra, it seems to reproduce the measured spectra reasonably well.

4.4. Discussion

This work has determined that the ground state of TaC is $1\sigma^2 2\sigma^2 1\pi^4 3\sigma^1$, $^2\Sigma^+$. A qualitative molecular orbital diagram is displayed in Figure 4.5 to provide a basis for discussion of the bonding in this molecule. In this diagram, the 1σ orbital of TaC is assumed to be mainly 2*s* carbon in character, although some mixing with the C 2*p*σ and Ta 5*d*σ orbitals is possible. The 2σ and 4σ orbitals are the bonding and anti-bonding combinations of the Ta $5d\sigma$ and C $2p\sigma$ orbitals. The 1π and 2π orbitals are the analogous bonding and anti-bonding combinations of the Ta $5d\pi$ and C $2p\pi$ orbitals. The 1δ orbitals

Table 4.1. Ground and upper state parameters (in cm^{-1}, except bond lengths in Å) of $^{181}Ta^{12}C$, band origins, rotational constants, bond lengths, Fermi contact parameter, and lambda doubling parameters.

	ν_0[1]	B	R	b_F	p+2q
$X^2\Sigma_{1/2}$		0.489854(75)	1.74871(13)	0.13107(32)	
[18.34] $^2\Pi_{1/2}$	19336.7870(25)	0.407472(80)	1.91735(19)		0.07345(48)
[18.36] $^2\Pi_{1/2}$	19362.8778(31)	0.413287(92)	1.90382(21)		0.01545(66)
[18.50] $^2\Pi_{1/2}$	19500.3975(28)	0.405893(74)	1.92108(18)		0.21626(44)
[18.52] $^2\Pi_{1/2}$	19523.3374(30)	0.40420(11)	1.92510(26)		0.05415(73)
[18.56] $^2\Pi_{1/2}$	19564.7626(24)	0.403726(75)	1.92623(18)		0.14588(43)
[19.52] $^2\Pi_{1/2}$	20519.5941(23)	0.402792(74)	1.92846(18)		0.08667(49)
[19.63] $^2\Pi_{1/2}$	20628.9789(26)	0.417274(80)	1.89470(18)		-0.02267(59)

[1]All spectra were simulated using a large spin-orbit parameter A=2000 cm^{-1} in the upper state, therefore band origins are shifted by 1000 cm^{-1} to higher energies from their real values.

Error limits (1σ) in the fitted parameters are provided in parentheses in units of the last digit quoted.

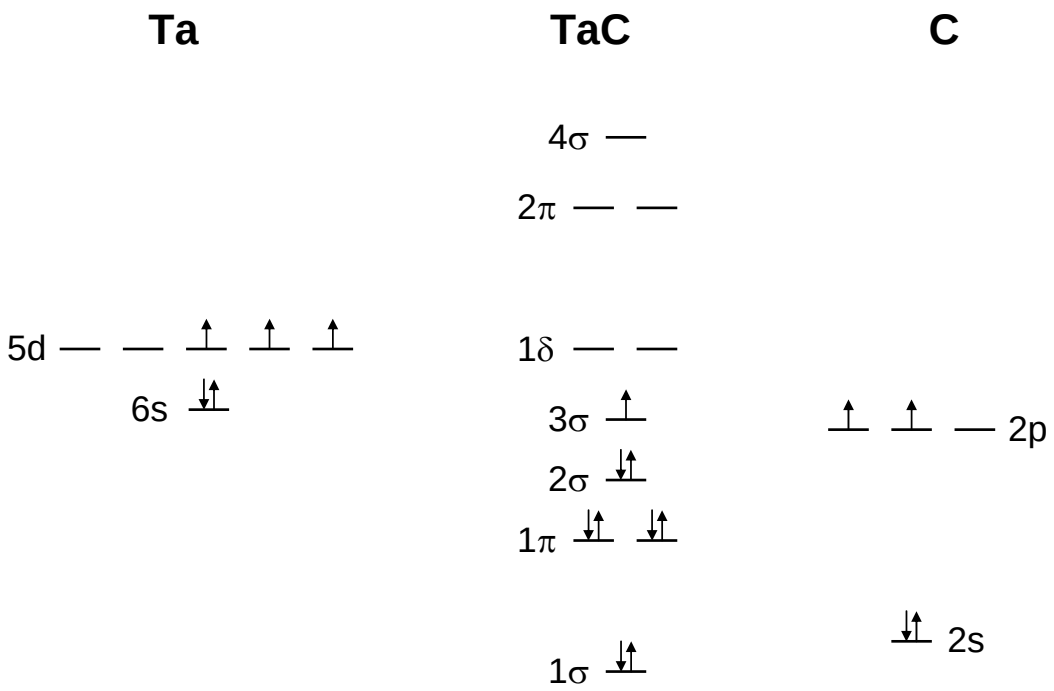

Figure 4.5. Qualitative molecular orbital diagram of TaC

are almost entirely Ta 5$d\delta$ in character and are nonbonding due to the lack of orbitals of δ symmetry on carbon. The 3σ orbital is also expected to be nonbonding and mainly Ta 6*s* in character. This is confirmed by our hyperfine measurements, which provide b_F=0.13107(32) cm^{-1}, which compares to the value $b_{F,6s}$= 0.1750 cm^{-1} for ^{181}Ta in its 5$d^4$6*s* configuration, as provided by Büttgenbach.[28] Comparison of the b_F values for TaC and atomic Ta shows that the 3σ orbital of TaC is roughly 75% Ta 6*s* in character.

The high proportion of metal n*s* character in the 3σ orbital of TaC is in agreement with hyperfine measurements in related metal carbides. Among the 3*d* series of transition metal carbides, hyperfine measurements on CoC demonstrate that the 3σ orbital has 89% Co 4*s* character.[25] In the 4*d* carbides, hyperfine studies show that this orbital has 71% 5*s* character in ZrC,[32] 83% 5*s* character in RuC,[33] and 69% 5*s* character in RhC.[34] The only other member of the 5*d* series for which hyperfine measurements are available is OsC, for which the 3σ orbital has 84-95% 6*s* character.[35] These results show that the 3σ orbital is dominated by metal n*s* character across the entire range of the transition metal carbides. Diatomic TaC is apparently no different from other transition metal carbides in this regard.

This result contrasts with the results of an *ab initio* calculation on TaC, in which the Mulliken population in the Ta 5*s*+6*s* orbitals for the X $^2\Sigma^+$ ground state is found to be 4.000.[7] This implies that there is no unpaired electron density in the tantalum 6*s* orbital, in disagreement with our result. We have considered whether there might be some alternative interpretation of our measurements that could bring theory and experiment into agreement, but this does not seem to be the case. In particular, ^{181}Ta has a large electric quadrupole moment of +3 $\times 10^{-24}$ cm^2,[27] and an e^2Qq_0 value of -0.1072 cm^{-1} has

been found in the related molecule, TaO $X^2\Delta_{3/2}$.[36] Simulation of the TaC spectrum with significant quadrupole moments included, however, leads to much more complicated spectra. The simple splitting of the ground state levels into G″=3 and G″=4 sublevels only occurs when the hyperfine interaction is dominated by the Fermi contact term. Accordingly, we are convinced that our hyperfine analysis is correct, and that the singly-occupied 3σ orbital in the TaC $X\,^2\Sigma^+$ state is dominated by tantalum 6*s* character.

In contrast to the hyperfine measurement, the measured value of the ground state bond length, r_0=1.749 Å, is in fairly good agreement with the calculated values of r_e= 1.76,[6] 1.799,[7] and 1.735 Å.[8]

Diatomic TaC differs significantly from its congeners, VC and NbC, in having a ground state of $1\sigma^2 2\sigma^2 1\pi^4 3\sigma^1$, $^2\Sigma^+$, rather than $1\sigma^2 2\sigma^2 1\pi^4 1\delta^1$, $^2\Delta$. This change in ground configuration results from the change in atomic orbital energies as one moves down the column of group 5 elements from V to Nb to Ta. The relevant atomic energy level data is provided in Table 4.2. Using known atomic energy levels,[37] the energy difference between the (n+1)*s* and n*d* orbitals, ε(*s*) – ε(*d*), may be estimated by either of two methods. In the first method, ε(*s*) – ε(*d*) is estimated as E(d^3s^2, $^4F_{3/2}$) – E(d^4s^1, $^6D_{1/2}$). This method utilizes data from the energy levels of the neutral atom, and measures the amount of energy required to excite the atom from the lowest level of the d^4s^1 configuration to the lowest level of the d^3s^2 configuration, which is negative in the cases of V and Ta. Alternatively, ε(*s*) – ε(*d*) can be estimated as the difference between the energy required to remove a *d* electron and that required to remove an *s* electron from the d^4s^1, $^6D_{1/2}$ level of the neutral atom. This energy difference is equivalent to the difference in energy between the d^3s^1, $^5F_1$ and d^4, $^5D_0$ levels of the atomic cation, which may be designated as

Table 4.2. Measures of the orbital energy difference ε(*s*)-ε(*d*) in group 5 atoms.

ε(*s*) – ε(*d*), (eV)			
Method [a]	V	Nb	Ta
$E(d^3s^2, {}^4F_{3/2}) - E(d^4s^1, {}^6D_{1/2})$	-0.262	+0.142	-1.210
$E(d^3s^1, {}^5F_1, M^+) - E(d^4, {}^5D_0, M^+)$	0.323	0.292	-1.562

[a] See text for description. Atomic energy levels taken from Reference [37].

$E(d^3s^1, {}^5F_1, M^+) - E(d^4, {}^5D_0, M^+)$. Other measures of the difference in orbital energies could be devised, but these two methods are sufficient for our purposes. The data displayed in Table 4.2 show that the while the valence *s* and *d* orbitals are similar in energy in V and Nb, the 6*s* orbital lies more than 1 eV below the 5*d* orbital in Ta. It is this dramatic stabilization in the 6*s* orbital that causes $1\sigma^2 2\sigma^2 1\pi^4 3\sigma^1$, $^2\Sigma^+$ to emerge as the ground state of TaC

A change in electronic configuration similar to that found here also occurs as one moves from the 4*d* metal carbide to the 5*d* metal carbide in other columns of the periodic table. For example, the ground term of MoC is $1\sigma^2 2\sigma^2 1\pi^4 1\delta^2$, $^3\Sigma^-$,[38] while that of WC is $1\sigma^2 2\sigma^2 1\pi^4 1\delta^1 3\sigma^1$, $^3\Delta_1$.[39] Likewise, the ground term of RuC is $1\sigma^2 2\sigma^2 1\pi^4 1\delta^4$, $^1\Sigma^+$,[33] while that of OsC is $1\sigma^2 2\sigma^2 1\pi^4 1\delta^3 3\sigma^1$, $^3\Delta_3$.[35] Among the group 9 metal carbides, RhC has a ground term of $1\sigma^2 2\sigma^2 1\pi^4 1\delta^4 3\sigma^1$, $^2\Sigma^+$,[34,40] while the ground term of IrC is $1\sigma^2 2\sigma^2 1\pi^4 1\delta^3 3\sigma^2$, $^2\Delta_{5/2}$.[41] In all of these examples, it is the stabilization of the 6*s* orbital relative to the 5*d* orbitals that lowers the energy of the 3σ orbital relative to the 1δ orbitals, causing a different ground state to emerge.

The stabilization of the 6*s* orbital relative to the 5*d* orbital is primarily a relativistic effect, as illustrated in Table 4.3, which compares the orbital energies obtained in a nonrelativistic numerical Hartree-Fock calculation to those obtained in a relativistic numerical Dirac-Fock calculation.[42] As is well-known,[43,44] relativistic effects stabilize the *s* orbitals due to their penetration close to the nucleus, where in a classical picture the kinetic energy and electron velocity become very large. The high velocity of the *s* electrons when they are close to the nucleus causes them to be the most affected by relativistic effects. The mass-velocity effect thus causes the *s* orbital to contract and drop

Table 4.3. Relativistic effects on atomic orbital energies[a]

Atom and configuration	n$d_{5/2}$ orbital	n$d_{3/2}$ orbital	(n+1)s orbital
V $3d^3\ 4s^2$	+ 2.34%	+1.87%	-0.926%
Nb $4d^4\ 5s^1$	+5.74%	+3.78%	-5.41%
Ta $5d^3\ 6s^2$	+20.15%	+15.1%	-15.60%

[a] The values provided give the percentage change in orbital energy when relativistic effects are included, as compared to the nonrelativistic treatment. Relativistic results are from numerical Dirac-Fock calculations; nonrelativistic results are from a numerical Hartree-Fock calculation (Reference 42). Results are presented separately for the j=5/2 and j=3/2 coupling of the electronic orbital angular momentum, ℓ, with the electron spin, s, for the nd electrons, because the spin-orbit interaction causes a significant difference in their energies.

in energy. Simultaneously, the nonpenetrating *d* orbitals are shielded from the nuclear charge more effectively following the relativistic *s* orbital contraction, causing them to expand and move higher in energy. The effect in Ta is quite dramatic, lowering the energy of the 6*s* orbital by 15.6% while raising the 5*d* orbital energy by 15-20%, depending on how the orbital angular momentum, *l*, is coupled to the electron spin, *s*. It is the combination of the stabilization of the 6*s* orbital and the destabilization of the 5*d* orbitals that causes the ground states of the 5*d* metal carbides often to differ from that of their 3*d* and 4*d* congeners.

Table 4.4 presents the ground state electronic configuration and term and the measured bond length for all of the experimentally known transition metal monocarbides. When no experimental data exist, computational results are provided. As expected, the contraction of the n*d* and (n+1)*s* orbitals as one moves across the periodic table generally causes the bond lengths of the transition metal carbides to shorten. A few exceptions to this general trend occur, however. Exceptions occur between the pairs CrC/MnC, CoC/NiC, MoC/TcC, RuC/RhC, RhC/PdC, and OsC/IrC. In all of these cases, the disruption of the trend of shortening bond lengths is correlated with an increase in the number of electrons in the n*s*-like 3σ orbital. Occupation of the nominally nonbonding 3σ orbital clearly causes the bond to lengthen. In essence, occupation of the more diffuse n*s*-like 3σ orbital prevents the atoms from approaching each other as closely. This is likely a Pauli repulsion effect that is mitigated by polarization of the 3σ orbital away from the carbon atom via metal n*s*-n*p* mixing.

Table 4.4. Ground states and bond lengths of transition metal carbides.

3*d* metal carbides	4*d* metal carbides	5*d* metal carbides
ScC (theory)	YC	LaC
$1\sigma^2 1\pi^3 2\sigma^2$, $^2\Pi_{3/2}$	$1\sigma^2 1\pi^3 2\sigma^1 3\sigma^1$, $^4\Pi_{5/2}$	$1\sigma^2 1\pi^4 2\sigma^1$, $^2\Sigma^+$
1.988 Å (r_e)	2.051 Å (r_0)	2.030 Å
Reference 45	Reference 46	Reference 8
TiC (theory)	ZrC	HfC (theory)
$1\sigma^2 1\pi^4 2\sigma^1 3\sigma^1$, $^3\Sigma^+$	$1\sigma^2 1\pi^4 2\sigma^1 3\sigma^1$, $^3\Sigma^+$	$1\sigma^2 1\pi^4 2\sigma^1 3\sigma^1$, $^3\Sigma^+$
1.712 Å (r_e)	1.807 Å (r_0)	1.800 Å (r_e)
Reference 47	Reference 32	Reference 8
VC (theory)	NbC	TaC
$1\sigma^2 1\pi^4\ 2\sigma^2 1\delta^1$, $^2\Delta_{3/2}$	$1\sigma^2 1\pi^4 2\sigma^2 1\delta^1$, $^2\Delta_{3/2}$	$1\sigma^2 1\pi^4 2\sigma^2 3\sigma^1$, $^2\Sigma^+$
1.636 Å (r_e)	1.700 Å (r_0)	1.749 Å (r_0)
Reference 10	Reference 11	This work
CrC	MoC	WC
$1\sigma^2 1\pi^4 2\sigma^2 1\delta^2$, $^3\Sigma^-$	$1\sigma^2 1\pi^4 2\sigma^2 1\delta^2$, $^3\Sigma^-$	$1\sigma^2 1\pi^4 2\sigma^2 1\delta^1 3\sigma^1$, $^3\Delta_1$
1.619 Å (r_0)	1.676 Å (r_0)	1.714 Å (r_0)
Reference 48	Reference 38	Reference 39
MnC (theory)	TcC (theory)	ReC (theory)
$1\sigma^2 1\pi^4 2\sigma^2 1\delta^2 3\sigma^1$, $^4\Sigma^-$	$1\sigma^2 1\pi^4 2\sigma^2 1\delta^2 3\sigma^1$, $^4\Sigma^-$	$1\sigma^2 1\pi^4 2\sigma^2 1\delta^2 3\sigma^1$, $^4\Sigma^-$
1.640 Å (r_e)	1.710 Å (r_e)	1.692 Å (r_e)
Reference 49	Reference 50	Reference 8
FeC	RuC	OsC
$1\sigma^2 1\pi^4 2\sigma^2 1\delta^3 3\sigma^1$, $^3\Delta_3$	$1\sigma^2 1\pi^4 2\sigma^2 1\delta^4$, $^1\Sigma^+$	$1\sigma^2 1\pi^4 2\sigma^2 1\delta^3 3\sigma^1$, $^3\Delta_3$
1.596 Å (r_0)	1.608 Å (r_0)	1.673 Å (r_0)
References 51,52	Reference 33	Reference 35
CoC	RhC	IrC
$1\sigma^2 1\pi^4 2\sigma^2 1\delta^4 3\sigma^1$, $^2\Sigma^+$	$1\sigma^2 1\pi^4 2\sigma^2 1\delta^4 3\sigma^1$, $^2\Sigma^+$	$1\sigma^2 1\pi^4 2\sigma^2 1\delta^3 3\sigma^2$, $^2\Delta_{5/2}$
1.561 Å (r_0)	1.616 Å (r_0)	1.686 Å (r_0)
References 25,53	Reference 54	Reference 55
NiC	PdC	PtC
$1\sigma^2 1\pi^4 2\sigma^2 1\delta^4 3\sigma^2$, $^1\Sigma^+$	$1\sigma^2 1\pi^4 2\sigma^2 1\delta^4 3\sigma^2$, $^1\Sigma^+$	$1\sigma^2 1\pi^4 2\sigma^2 1\delta^4 3\sigma^2$, $^1\Sigma^+$
1.631 Å (r_0)	1.712 Å (r_0)	1.677 Å
Reference 53,56	Reference 57	Reference 58

4.5 Conclusion

The electronic spectrum of diatomic TaC was recorded in the range from 17850 to 20000 cm^{-1}, using resonant two-photon spectroscopy. It is found that the ground state of TaC is a $^2\Sigma^+$ term that originates from the $1\sigma^2 2\sigma^2 1\pi^4 3\sigma^1$ configuration. Measured spectroscopic constants for the ground state are $B_0"$=0.489854(75) cm^{-1}, $r_0"$=1.74871(13) Å, and $b_F"$=0.13107(32) cm^{-1} (1σ error limits), for the $^{181}Ta^{12}C$ isotopomer. These results are contrasted with the ground states of the congeneric molecules VC and NbC, and it is argued that the difference in the ground configuration and term of TaC results from the relativistic stabilization of the 6*s* orbital in atomic Ta.

4.6 References

(1) Santhanam, A. T. *in The Chemistry of. Transition Metal. Carbides and Nitrides,* edited by S.T. Oyama (Blackie Academic & Professional, London) **1996**, 28.

(2) Ilchenko, N. I.; Pyatnitsky, Y. I. *in The Chemistry of. Transition Metal. Carbides and Nitrides,* edited by S.T. Oyama (Blackie Academic & Professional, London) **1996**, 311.

(3) Teghil, R.; De Bonis, A.; Galasso, A.; Villani, P.; Santagata, A. *Appl. Surf. Sci.* **2007**, *254*, 1220.

(4) Fukunaga, A.; Chu, S.; McHenry, M. E. *J. Mater. Sci. Lett.* **1999**, *18*, 431.

(5) McElvany, S. W.; Cassady, C. J. *J. Phys. Chem.* **1990**, *94*, 2057.

(6) Heaven, M. W.; Stewart, G. M.; Buntine, M. A.; Metha, G. F. *J. Phys. Chem.A* **2000**, *104*, 3308.

(7) Majumdar, D.; Balasubramanian, K. *Chem. Phys. Lett.* **1998**, *284*, 273.

(8) Wang, J.; Sun, X.; Wu, Z. *J. Cluster Sci.* **2007**, *18*, 333.

(9) Hamrick, Y. M.; Weltner, W., Jr. *J. Chem. Phys.* **1991**, *94*, 3371.

(10) Kalemos, A.; Dunning, T. H., Jr.; Mavridis, A. *J. Chem. Phys.* **2005**, *123*, 014301/1.

(11) Simard, B.; Presunka, P. I.; Loock, H. P.; Bérces, A.; Launila, O. *J. Chem. Phys.* **1997**, *107*, 307.

(12) Brugh, D. J.; Morse, M. D. *J. Chem. Phys.* **1997**, *107*, 9772.

(13) Wiley, W. C.; McLaren, I. H. *Rev. Sci. Instrum.* **1955**, *26*, 1150

(14) Mamyrin, B. A.; Karataev, V. I.; Shmikk, D. V.; Zagulin, V. A. *Zh. Eksp. Teor. Fiz.* **1973**, *64*, 82.

(15) Gerstenkorn, S.; Luc, P. *Atlas du Spectre d'Absorption de la Molécule d'Iode entre 14,800-20,000 cm^{-1}*; CNRS: Paris, 1978.

(16) Western, C. M. PGOPHER, a Program for Simulating Rotational Structure, University of Bristol, http://pgopher.chm.bris.ac.uk.

(17) Chang, Y. C.; Lam, C. S.; Reed, B.; Lau, K. C.; Liou, H. T.; Ng, C. Y. *J. Phys. Chem. A* **2009**, *113*, 4242.

(18) Herzberg, G. *Molecular Spectra and Molecular Structure I. Spectra of Diatomic Molecules*, 2nd ed.; Van Nostrand Reinhold: New York, 1950.

(19) Adams, A.; Klemperer, W.; Dunn, T. M. *Can. J. Phys.* **1968**, *46*, 2213.

(20) Stringat, R.; Athenour, C.; Femenias, J. L. *Can. J. Phys.* **1972**, *50*, 395.

(21) Steimle, T. C.; Al-Ramadin, Y. *J. Mol. Spectrosc.* **1987**, *122*, 103.

(22) Steimle, T. C.; Shirley, J. E. *J. Chem. Phys.* **1990**, *92*, 3292.

(23) Steimle, T. C.; Virgo, W. *J. Chem. Phys.* **2002**, *116*, 6012.

(24) He, S. G.; Tam, W. S.; Leung, J. W. H.; Cheung, A. S. C. *J. Chem. Phys.* **2002**, *117*, 5764.

(25) Barnes, M.; Merer, A. J.; Metha, G. F. *J. Chem. Phys.* **1995**, *103*, 8360.

(26) Dunn, T. M. In *Molecular Spectroscopy:Modern Research*; Rao, K. N., Mathews, C. W., Eds.; Academic Press: New York and London, 1972; pp 231.

(27) Weltner, W., Jr. *Magnetic Atoms and Molecules*; Dover Publications, Inc.: New York, 1983.

(28) Büttgenbach, S. *Hyperfine Structure in 4d- and 5d-Shell Atoms*; Springer-Verlag: Berlin Heidelberg New York, 1982; Vol. 96.

(29) Childs, W. J.; Steimle, T. C. *J. Chem. Phys.* **1988**, *88*, 6168.

(30) Shirley, J.; Scurlock, C.; Steimle, T. *J. Chem. Phys.* **1990**, *93*, 1568.

(31) Brown, J. M.; Merer, A. J. *J. Mol. Spectrosc.* **1979**, *74*, 488.

(32) Rixon, S. J.; Chowdhury, P. K.; Merer, A. J. *J. Mol. Spectrosc.* **2004**, *228*, 554.

(33) Langenberg, J. D.; DaBell, R. S.; Shao, L.; Dreessen, D.; Morse, M. D. *J. Chem. Phys.* **1998**, *109*, 7863.

(34) Brom, J. M., Jr.; Graham, W. R. M.; Weltner, W., Jr. *J. Chem. Phys.* **1972**, *57*, 4116.

(35) Krechkivska, O.; Morse, M. D. *J. Chem. Phys.* **2008**, *128*, 084314.

(36) Manke, K. J.; Vervoort, T. R.; Kuwata, K. T.; Varberg, T. D. *J. Chem. Phys.* **2008**, *128*, 104302/1.

(37) Moore, C. E. *Atomic Energy Levels*, Natl. Bur. Stand. U.S. Circ. No. 467 ed.; U.S. Government Printing Office: Washington, D.C., 1971.

(38) Brugh, D. J.; Ronningen, T. J.; Morse, M. D. *J. Chem. Phys.* **1998**, *109*, 7851.

(39) Sickafoose, S. M.; Smith, A. W.; Morse, M. D. *J. Chem. Phys.* **2002**, *116*, 993.

(40) Lagerqvist, A.; Scullman, R. *Ark. Fys.* **1966**, *32*, 475

(41) Jansson, K.; Scullman, R.; Yttermo, B. *Chem. Phys. Lett.* **1969**, *4*, 188.

(42) Desclaux, J. P. *At. Data Nucl. Data Tables* **1973**, *12*, 311.

(43) Pyykko, P.; Desclaux, J. P. *Acc. Chem. Res.* **1979**, *12*, 276.

(44) Balasubramanian, K. *J. Phys. Chem.* **1989**, *93*, 6585.

(45) Kalemos, A.; Mavridis, A.; Harrison, J. F. *J. Phys. Chem. A* **2001**, *105*, 755.

(46) Simard, B.; Hackett, P. A.; Balfour, W. J. *Chem. Phys. Lett.* **1994**, *230*, 103.

(47) Kalemos, A.; Mavridis, A. *J. Phys. Chem. A* **2002**, *106*, 3905.

(48) Brugh, D. J.; Morse, M. D.; Kalemos, A.; Mavridis, A. *J. Chem. Phys.* accepted for publication.

(49) Kalemos, A.; Dunning, T. H., Jr.; Mavridis, A. *J. Chem. Phys.* **2006**, *124*, 154308/1.

(50) Jackson, P.; Gadd, G. E.; Mackey, D. W.; van der Wall, H.; Willett, G. D. *J. Phys. Chem.A* **1998**, *102*, 8941.

(51) Balfour, W. J.; Cao, J.; Prasad, C. V. V.; Qian, C. X. *J. Chem. Phys.* **1995**, *103*, 4046.

(52) Allen, M. D.; Pesch, T. C.; Ziurys, L. M. *Astrophys. J.* **1996**, *472*, L57.

(53) Brewster, M. A.; Ziurys, L. M. *Astrophys. J.* **2001**, *559*, L163.

(54) Balfour, W. J.; Fougère, S. G.; Heuff, R. F.; Qian, C. X. W.; Zhou, C. *J. Mol. Spectrosc.* **1999**, *198*, 393.

(55) Marr, A. J.; Flores, M. E.; Steimle, T. C. *J. Chem. Phys.* **1996**, *104*, 8183.

(56) Brugh, D. J.; Morse, M. D. *J. Chem. Phys.* **2002**, *117*, 10703.

(57) Langenberg, J. D.; Shao, L.; Morse, M. D. *J. Chem. Phys.* **1999**, *111*, 4077.

(58) Steimle, T. C.; Jung, K. Y.; Li, B.-Z. *J. Chem. Phys.* **1995**, *102*, 5937.

CHAPTER 5

ZrFe, A SEXTUPLY-BONDED DIATOMIC TRANSITION METAL?

5.1 Introduction

Multiple bonding between transition metal atoms has been a topic of great interest ever since it was discovered in the 1960's in such quadruply-bonded species as $[Re_2Cl_8]^{2-}$,[1-2] $Cr_2(O_2CCH_3)_4$,[3] and $Mo_2(O_2CCH_3)_4$,[4] and in $[Tc_2Cl_8]^{3-}$.[5] In the gas phase, multiple bonding in bare transition metal dimers was first demonstrated in the 1970's in the pioneering work of Efremov, Samoilova, and Gurvich on the 12 valence electron molecules Cr_2,[6] CrMo,[7] and Mo_2,[8] although these results were not widely recognized until subsequent laser spectroscopic work proved them to be correct.[9-14] Numerous theoretical investigations of the multiple bonding in the transition metal diatomics have been conducted since these molecules were first reported, and it is now known that the 12-electron molecules Cr_2,[15-16] Mo_2,[17] W_2,[18] CrMo,[19] CrW,[19] and MoW[19] all have closed shell $^1\Sigma_{(g)}^+$ ground states with six fully occupied bonding molecular orbitals in the leading configuration, making them nominally sextuply-bonded molecules. The molecules are highly multiconfigurational, however, leading to effective bond orders that are smaller than 6.[17-20]

The closely related group 5 dimers, V_2,[21-24] VNb,[24-25] and Nb_2 [24, 26] have all been studied in the gas phase and have been shown to have $^3\Sigma_{(g)}^-$ ground states with a nominal bond order of 5. Likewise, the mixed group 5-6 dimers, VCr,[27] VMo,[28] NbCr,[27] and NbMo[29] have all been shown to have $^2\Delta_i$ ground states, with nominal bond orders of 5.5. In all cases, the diatomic metals have bond lengths that are far shorter than those found for the related multiply-bonded ligated transition metal compounds. A bond order of 6 is the largest that can be obtained between two transition metal atoms. Although the lanthanide and actinide dimers could in principle exhibit higher bond orders, it appears that none have bond orders higher than 5.[20]

It is interesting to consider what happens when the nuclear charge in a symmetric, multiply bonded diatomic (such as N_2) is shifted to make increasingly asymmetric but still isoelectronic molecules, such as CO, BF, or BeNe. Every chemist learns very early that N_2 and CO have triple bonds, but few would make the same claim for BF and all would claim that BeNe has a bond order of zero.[30] Our intuition concerning how the bond order varies as the nuclear charge is redistributed in the 12-electron transition metal diatomics is unclear, however. How does the bond order or the bond length change as the nuclear charges in Cr_2 are made more asymmetric, moving to the isoelectronic species VMn, TiFe, ScCo, CaNi, KCu, and finally, ArZn? Most would be happy to identify KCu as having a single bond and ArZn as being unbound, but the remaining molecules are less readily characterized.

In Chapter 6 of this manuscript, we report studies of the 12-electron molecule, TiFe, which is isoelectronic to Cr_2.[31] Here we report studies of ZrFe, which is isoelectronic to the 12-electron molecule, CrMo. We may define a parameter, ΔZ, which

characterizes how far apart the groups composing the diatomic molecule lie. For the 12-electron molecules that are isoelectronic to CrMo ($\Delta Z=0$), we have VTc and NbMn ($\Delta Z=2$), TiRu and ZrFe ($\Delta Z = 4$), ScRh and YCo ($\Delta Z=6$), *etc.* Diatomic CrMo has been shown to have a closed shell, $^1\Sigma^+$ ground state with a bond length of $r_0 = 1.823(1)$ Å,[12] while YCo also has a closed shell, $^1\Sigma^+$ ground state with $r_0 = 1.983(1)$ Å.[32] This increase in bond length by 0.160 Å is similar to the increase of 0.164 Å that is found in moving from N_2 ($r_e = 1.098$ Å)[33] to BF ($r_e = 1.262$ Å),[34] suggesting that YCo is no longer a sextuply-bonded molecule. Is the asymmetric 12-electron molecule ZrFe ($\Delta Z=4$) more similar to the sextuply bonded CrMo ($\Delta Z=0$), or is it more like YCo ($\Delta Z=6$) in having a reduced level of bonding? To answer this question, we have undertaken studies to determine the ground electronic state of ZrFe and to measure its bond length.

This work provides the first investigation of any kind of diatomic ZrFe. Here we report the electronic configuration and term of the ZrFe ground state, the ground and excited state rotational constants and bond lengths, the excited state vibrational frequency and anharmonicity, excited state lifetimes, and the ground state vibrational interval, $\Delta G''_{1/2}$. Spectra of six ZrFe isotopomers were recorded using the mass-resolved resonant two-photon ionization technique: $^{90}Zr^{54}Fe$ (3.0% natural abundance), $^{90}Zr^{56}Fe$ (47.2%), $^{91}Zr^{56}Fe$ (10.3%), $^{92}Zr^{56}Fe$ (15.7%), $^{94}Zr^{56}Fe$ (15.9%), and $^{96}Zr^{56}Fe$ (2.6%). Although a purely theoretical concept such as bond order is difficult to quantify by experimental measurements, the results of this study suggest that like CrMo, ZrFe is probably best viewed as a sextuply-bonded diatomic transition metal.

5.2 Experimental

In the present study, diatomic ZrFe was investigated by means of resonant two-photon ionization (R2PI) spectroscopy. The instrument employed is analogous to that used previously in our group,[35] with a few modifications. The source chamber is maintained at an uncorrected pressure of 2×10^{-4} torr by a 5300 L/s diffusion pump backed by a 54 L/s rotary mechanical pump. This chamber houses the sample driver, an assembly that rotates and translates the sample disk, and a pulsed supersonic nozzle (General Valve series 9). It is separated from the ionization chamber by a 1.5 cm diameter skimmer that provides a roughly collimated molecular beam. During the experimental cycle, the metal alloy sample disk (Zr:Fe 1:1 alloy, purchased from ACI Alloys) is ablated using the fundamental output (1.064 μm) of a Q-switched Nd:YAG laser, 30-35 mJ/pulse, which is timed to coincide with the maximum intensity of a helium gas pulse (180 psi backing pressure). The initially vaporized species are entrained in the helium gas pulse, and begin condensing to form clusters prior to their cooling during the supersonic expansion into vacuum.

The second chamber is maintained at a pressure of 1-2 $\times10^{-6}$ torr by a 2400 L/s diffusion pump that is backed by a 4.2 L/s mechanical pump. This chamber houses a linear Wiley-McLaren[36] time-of flight mass spectrometer assembly and microchannel plate detector. The molecular beam is exposed to the output of a Nd:YAG-pumped tunable dye laser that counterpropagates along the axis of the molecular beam and is crossed at right angles by the fifth harmonic output of a Nd:YAG laser (5mJ/pulse, 212.8 nm) about 50 ns later in time. The optical spectrum is collected mass spectrometrically: the ions that are produced by the two-laser sequence are accelerated in the time-of-flight

mass spectrometer and detected by a dual microchannel plate detector. The signal is amplified by a 350 MHz preamplifier and digitized for analysis. To provide the optical spectrum, the ion signals of the masses of interest are monitored as a function of the dye laser wavelength.

The dye laser was scanned in low resolution mode (single grating, 0.14 cm^{-1} resolution) to obtain vibronically resolved spectra of the various isotopic modifications of ZrFe. Depending on the spectral region and dyes used, the dye laser output energy varied in the range 5-40 mJ/pulse. To reveal rotational structure within each vibronic band, the dye laser was scanned in the high resolution mode (dual grating, 0.05 cm^{-1} resolution). It was discovered that some bands require a high dye laser fluence (16 mJ/cm^2) in order to record rotationally resolved spectra, with no signs of power broadening present. Others require low dye laser fluence (<0.08 mJ/cm^2) to eliminate the effects of power broadening. This phenomenon is discussed below in connection with the electronic transitions involved. Reference spectra of I_2[37-38] and etalon fringes were recorded at the same time as the rotationally resolved spectra for calibration purposes. In order to measure the lifetimes of long-lived molecular states (see below), the excitation laser is counterpropagated along the molecular beam axis. This introduces a Doppler shift into the raw spectra, because the molecules are moving toward the radiation source. Using the well-known supersonic beam velocity of helium (1.77×10^3 m/s),[39] all measured line positions are corrected for this effect, which amounts to only about 0.1 cm^{-1} for the bands reported here. A correction for the error in the I_2 atlas (-0.0056 cm^{-1}) is also made at the same time.[40]

For a few of the rotationally resolved bands, excited state lifetimes were measured. To perform this measurement, the ionization laser is fixed to fire at the time of the maximum molecular signal, and the dye laser is scanned in time. By directing the dye laser down the molecular beam axis, it is possible to excite the molecules when they are far upstream from the ionization zone, and ionize them when they get there. This allows much longer lifetimes to be probed than would be the case if the two lasers intersected the molecular beam at right angles. The lifetime curve is generated by scanning the delay between the two lasers and recording the ion signal as a function of the delay time. The delay is scanned in a randomized fashion in order to minimize the effects of fluctuations in the signal due to sample imperfections. The ion signal as a function of dye laser-ionization laser delay is then fitted to an exponential decay curve using the Marquardt nonlinear least-squares algorithm.[41]

5.3 Results

5.3.1. Low resolution spectrum

5.3.1.1 Appearance of the low resolution spectrum

The present spectroscopic study of diatomic ZrFe covers the range from 13890 cm^{-1} to 18870 cm^{-1}. As shown in Figure 5.1, the appearance of the spectrum changes drastically around 18000 cm^{-1}. Below 18000 cm^{-1}, a single vibrational progression is found, for which 11 members are observed. These transitions are extremely weak and rotational analysis was only possible using high dye laser fluences (8-30 mJ/cm^2). Despite the high laser power, no power broadening was observed. In contrast, the spectrum above 18000 cm^{-1} is very congested with many strong transitions. Rotational investigations of some of these features required the dye laser fluence to be reduced

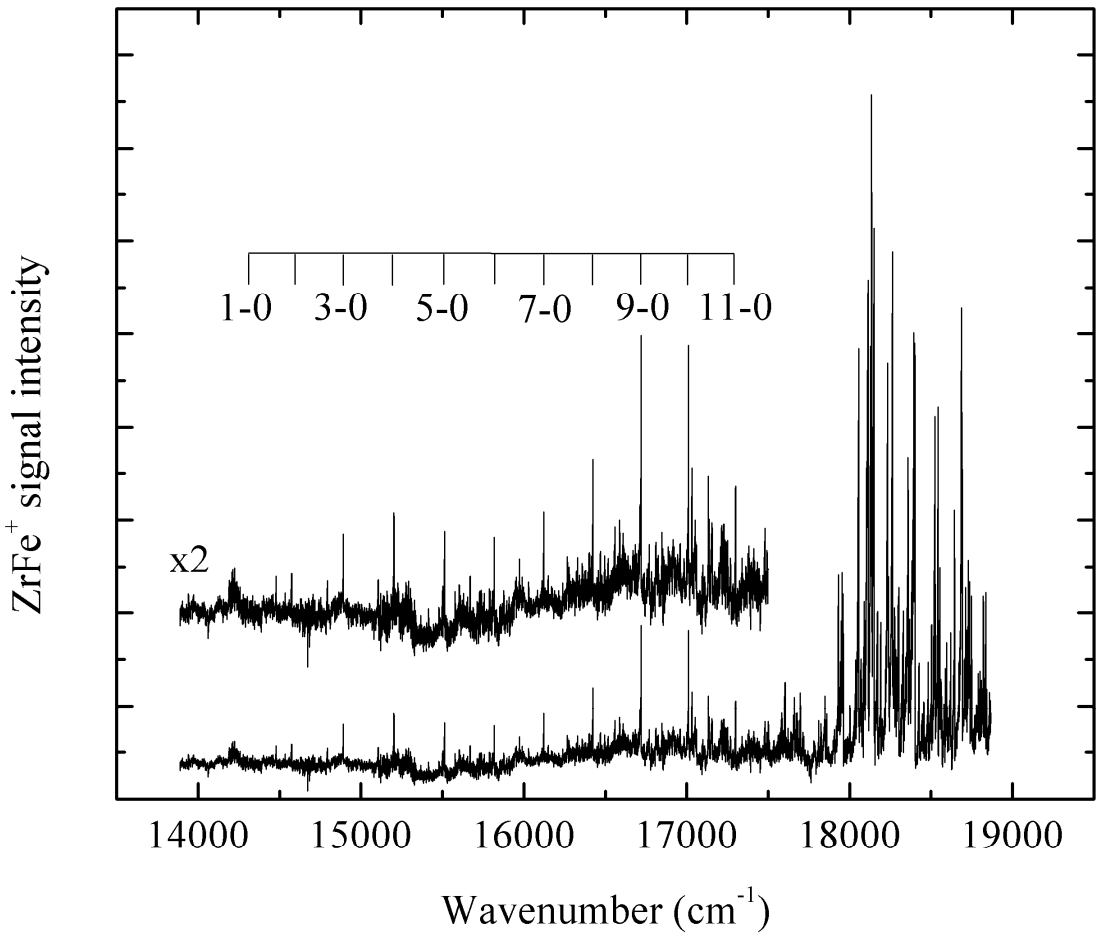

Figure 5.1. Low resolution spectrum of diatomic $^{90}Zr^{56}Fe$ over the 13890 – 18870 cm^{-1} region. The bands of the $[13.9]0^{+} \leftarrow X\ ^{1}\Sigma^{+}$ system are identified in the lower wavenumber region. The higher energy region, 18000-18870 cm^{-1}, displays a congested spectrum with much greater intensity than the low energy region.

below 0.08 mJ/cm^2, and even at that level some residual power broadening may have been present. Thus, there is a factor of at least 100 separating the oscillator strengths of the transitions in the higher and lower energy ranges. Based on these results, we believe that there are no electronically allowed transitions in the lower energy range, and that strongly allowed electronic transitions become accessible near 18000 cm^{-1}. Mixing of the states in the 13000-18000 cm^{-1} range with the strongly allowed states above 18000 cm^{-1}, probably induced by spin-orbit interactions, is the likely mechanism by which the electronically forbidden transitions gain intensity. In this connection, the relevant atomic spin-orbit parameters for the *d* orbitals have been tabulated as ζ_{3d}(Fe) = 417 cm^{-1} and ζ_{4d}(Zr) = 387 cm^{-1};[42] the parameters for the *p* orbitals have been calculated using the numerical Hartree-Fock program of Charlotte Froese Fischer to be ζ_{4p}(Fe) = 277 cm^{-1} and ζ_{5p}(Zr) = 340 cm^{-1}, although these values vary considerably with electronic configuration and term.[43] The magnitude of these values is sufficient to mix in a few percent of the strongly allowed character into the forbidden states, consistent with the observed intensities.

The observation of a resonant two-photon ionization spectrum using the 5th harmonic radiation of the Nd:YAG laser implies that the ionization energy of ZrFe lies above the 5th harmonic energy. Accordingly, IE(ZrFe) > 5.82 eV. Likewise, the observation of a band at 14252 cm^{-1} implies that this energy, added to the energy of the 5th harmonic photon, lies above the ionization limit. Accordingly, IE(ZrFe) < 7.59 eV. Together, these observations place the IE(ZrFe) in the range 5.82 eV < IE(ZrFe) < 7.59 eV.

5.3.1.2. Excited state lifetimes

To attempt to quantify the transition intensities, we have tried to measure excited state lifetimes using the time-delayed resonant two-photon ionization method described above. For most of the observed bands, the resulting excited state lifetime curves are clearly biexponential, consisting of a more rapid decay process and an extremely slow decay process. The relative amplitudes of the fast and slow components sometimes vary considerably from one isotopic combination to another, and from band to band. The slow decay process is so slow that the lifetime curve does not come close to returning to baseline within a time frame of hundreds of microseconds. Because the flight time from the expansion nozzle to the ionization region is about 480 μs, we are unable to capture a full decay curve for this process.

For a jet cooled diatomic molecule in a collision-free environment, the only realistic decay process below the dissociation and ionization thresholds is fluorescence. Even when the density of excited electronic states is large, the total density of states remains too low for true nonradiative decay. This is in contrast to the situation that can occur in some triatomic molecules, such as Al_3,[44] where the density of vibrational levels grows rapidly with increasing energy, allowing true nonradiative decay processes to occur. It is hard to believe that we could be exciting states that have fluorescence lifetimes that are several hundred microseconds long, as this would imply vanishingly small absorption oscillator strengths. A possible artifact of the time-delayed resonant two-photon ionization method, however, could explain these results. If the initially excited state fluoresces to a range of vibronic levels of the ground state, or to low-lying excited states, it could happen that a subset of the states so produced could still be ionized

at the wavelength used for ionization, in this case 212.8 nm (5.826 eV). If the states that are populated by fluorescence are themselves long-lived, as would be expected for excited vibrational levels of the ground state, a biexponential behavior with a very slow component would be expected. Fluorescence to high lying vibrational levels of the ground state would be favored by Franck-Condon factors if there were a large change in bond length upon excitation, as is found for the bands that have been rotationally resolved. In addition, ionization of the higher lying levels of the ground state produced by fluorescence would be more likely to be observed if a relatively high ionization energy were used.

Based on this possibility, we have chosen to fit the measured decay curves using a model in which the slow decay process has an infinite lifetime. This corresponds to using one baseline (A) for times in which the ionization laser fires before the dye laser and a higher baseline (B) for times in which the dye laser fires first:

$$S(t) = \begin{cases} A & if \quad t < 0 \\ B + Ce^{-t/\tau} & if \quad t \geq 0 \end{cases} \tag{5.1}$$

With this decay model, reasonable fits to the measured decay curves were obtained.

To illustrate the difference in excited state lifetimes above and below the 18000 cm^{-1} demarcation, Figures 5.2 and 5.3 provide the recorded lifetime curves for the 10-0 band of the observed progression, excited near 17009 cm^{-1} and the unclassified strong band near 18053 cm^{-1}. Both transitions exhibit the high background at long times discussed above. However, note that the delay range scanned for the 18053 cm^{-1} band is a factor of 100 smaller than that of the 10-0 band. The fitted lifetimes differ by a factor

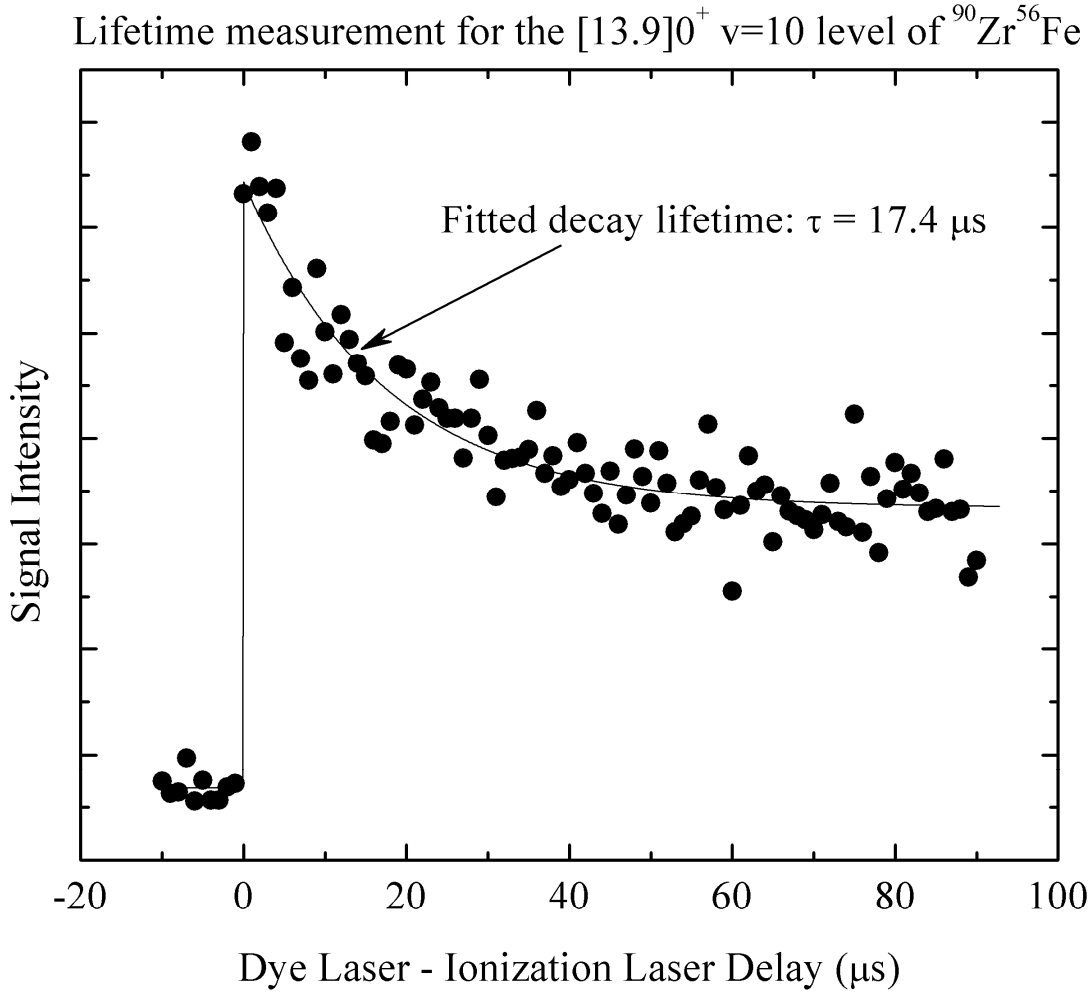

Figure 5.2. Lifetime measurement for the v=10 level of the $[13.9]0^+$ state of ZrFe.

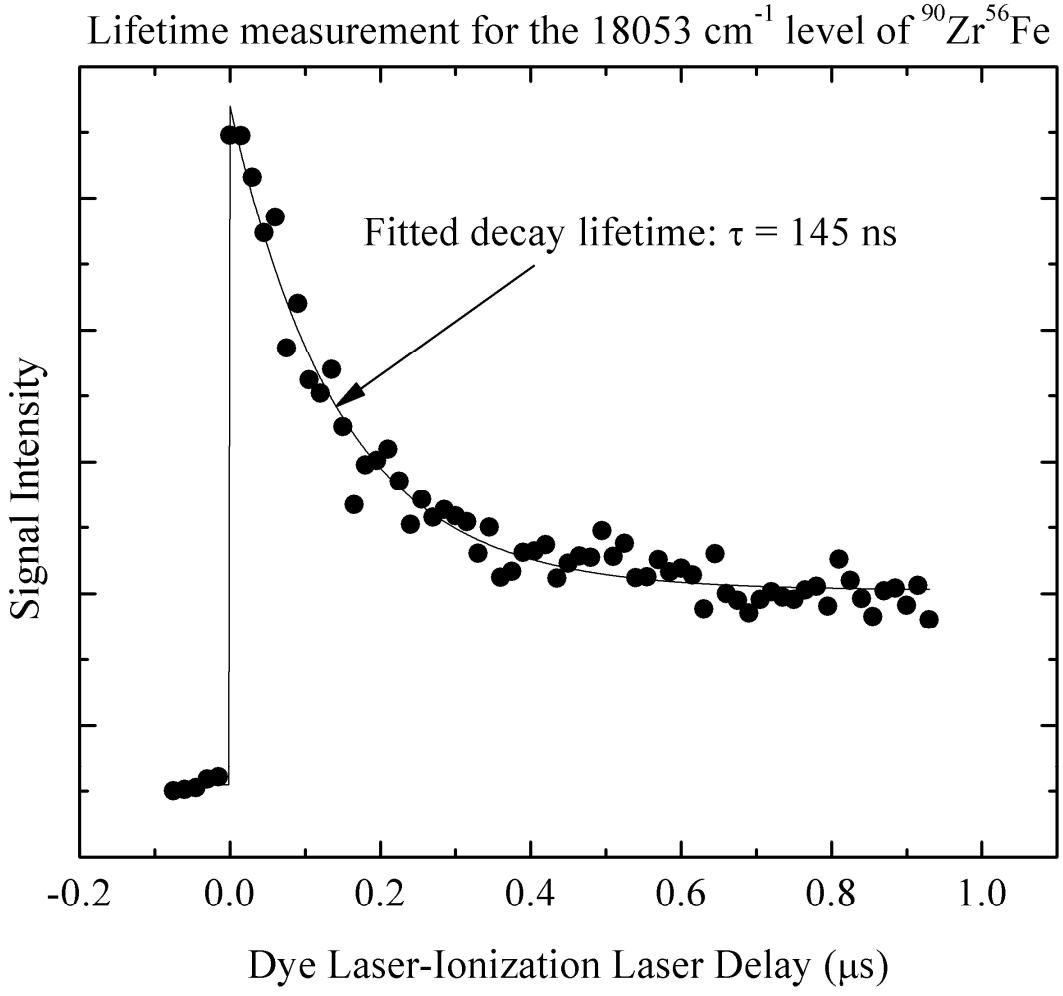

Figure 5.3. Lifetime measurement for the 18053 cm^{-1} level of ZrFe.

of 120, a value that is consistent with the different laser intensities required to rotationally resolve the transitions. Additional excited state lifetimes are listed in Table 5.1.

5.3.1.3. Determination of ground state $\Delta G_{1/2}$" for different ZrFe isotopomers

The vibronic spectrum over the 13890-18870 cm^{-1} region was collected for $^{90}Zr^{56}Fe$ (47.2% natural abundance), $^{91}Zr^{56}Fe$ (10.3%), $^{92}Zr^{56}Fe$ (15.7%), $^{94}Zr^{56}Fe$ (15.9%), and $^{96}Zr^{56}Fe$ (2.6%). For a few bands, spectra of $^{90}Zr^{54}Fe$ (3.0%) were also recorded. The low resolution spectra obtained for the minor isotopes are very similar to that exhibited in Figure 5.1 for $^{90}Zr^{56}Fe$; every isotopomer displayed a strong, congested spectrum toward the blue (18000-18870 cm^{-1}) and a single extremely weak progression in the lower energy region (13890-18000 cm^{-1}).

In order to obtain a value for the ground state vibrational interval, we employed the band difference histogram method, which proved to be successful in our recent studies of ZrF and ZrCl.[45] This method works best when the molecule has a complicated spectrum with many transitions, a condition that the ZrFe molecule meets in the higher energy region. To use the method, the spectrum was calibrated using the observed transitions of atomic Zr and Fe, and the positions of the band heads were measured. Next, a list of the band head differences was generated by subtracting from each measured band head each of the band heads lying to lower energies. For a spectrum in which N band heads are measured, this leads to $(N^2 - N)/2$ band head differences. Next, each measured band difference was used to set up a Gaussian function centered on the wavenumber difference, with a width of 1 cm^{-1}. All of the $(N^2 - N)/2$ functions were then summed to give a continuous function that could be plotted over the range

Table 5.1. Excited state lifetimes (μs) for some bands of ZrFe.[a]

Band	ν (cm^{-1})	τ($^{90}Zr^{56}Fe$)	τ($^{91}Zr^{56}Fe$)	τ($^{92}Zr^{56}Fe$)	τ($^{94}Zr^{56}Fe$)
$[13.9]0^{+}\leftarrow X^{1}\Sigma^{+}$ 2-0	14571	26.5 ± 4.5			
$[13.9]0^{+}\leftarrow X^{1}\Sigma^{+}$ 6-0	15816	30.8 ± 12.4			
$[13.9]0^{+}\leftarrow X^{1}\Sigma^{+}$ 10-0	17009	18.7 ± 2.2			
$[13.9]0^{+}\leftarrow X^{1}\Sigma^{+}$ 11-0	17297	14.0 ± 1.8			
unclassified	18053	0.141 ± 0.012	0.081 ± 0.006	0.081 ± 0.005	0.092 ± 0.008
unclassified	18260	0.136 0.011	0.169 ± 0.012	0.181 ± 0.021	0.211 ± 0.018

[a] All bands were fitted to the expression given in equation (1). Uncertainties were determined by measuring the same band three or more times, and taking the mean and standard deviation of the resulting fitted lifetimes

300 – 800 cm^{-1}, as displayed in Figure 5.4 for $^{90}Zr^{56}Fe$. The idea is that every hot band is separated by the same amount from its corresponding cold band (ignoring the difference between band head location and band origin location), so band differences that correspond to hot band/cold band pairs will add constructively, leading to a peak in the resulting band difference histogram plot. Application of this method to $^{90}Zr^{56}Fe$ leads to a peak at 452.2 cm^{-1}; the corresponding peaks for the other isotopomers are found at 451.3 cm^{-1} ($^{91}Zr^{56}Fe$); 450.5 cm^{-1} ($^{92}Zr^{56}Fe$); 448.5 cm^{-1} ($^{94}Zr^{56}Fe$); and 447.1 cm^{-1} ($^{96}Zr^{56}Fe$).

These features show the expected shift with reduced mass that is expected for $\Delta G_{1/2}$", given by $\Delta G_{1/2}"(i) = \Delta G_{1/2}"(j) \times \sqrt{\mu_j / \mu_i}$. For example, starting with $\Delta G_{1/2}"(^{90}Zr^{56}Fe) = 452.2$ cm^{-1}, the expected values for the remaining isotopomers are 451.2, 450.3, 448.5, and 446.7 cm^{-1}. These differ by only 0.2 cm^{-1} from the observed values, on average. While these could correspond to repeating excited state intervals, this is unlikely because (1) different excited states would be expected to have different vibrational frequencies, (2) anharmonicity would make intervals within a given excited state different, and (3) perturbations between states in this congested region would tend to destroy any intervals that might otherwise happen to add in phase. Thus, we conclude that $\Delta G_{1/2}"$ for ZrFe is 452.2 cm^{-1} ($^{90}Zr^{56}Fe$), 451.3 cm^{-1} ($^{91}Zr^{56}Fe$), 450.5 cm^{-1} ($^{92}Zr^{56}Fe$), 448.5 cm^{-1} ($^{94}Zr^{56}Fe$), and 447.1 cm^{-1} ($^{96}Zr^{56}Fe$). Band difference histogram plots for the minor isotopes, vibronic spectra and band head positions, rotationally resolved spectra, and fits of rotational lines are provided in appendix C of this manuscript.

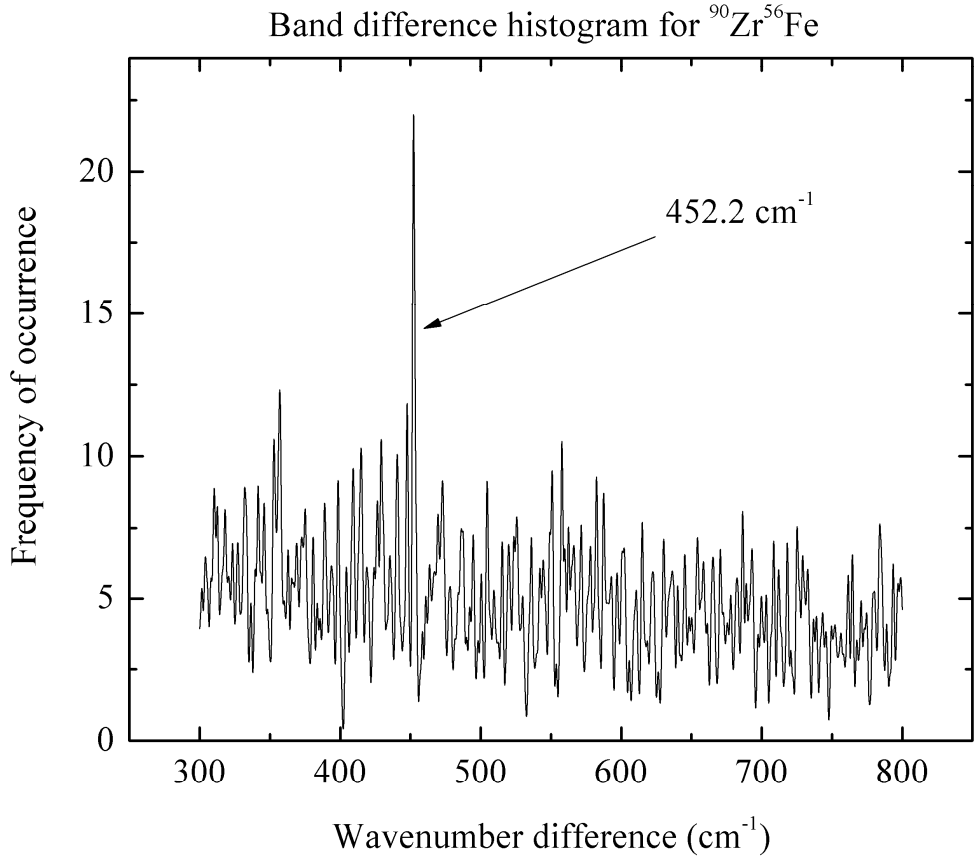

Figure 5.4. Band difference histogram plot for $^{90}Zr^{56}Fe$. A peak that appears at 452.2 cm^{-1} is assigned as $\Delta G_{1/2}$".

5.3.1.4. Vibrational numbering of the observed band system

The vibrational numbering of the progression, consisting of 11 bands in the 14200-17500 cm^{-1} range, was established through measurements of the isotope shifts. For all of the 11 bands, rotationally resolved spectra (0.05 cm^{-1}) were collected and analyzed (see below). Six of the bands were found to be relatively unperturbed, and their isotope shifts, $\nu_0(^{90}Zr^{56}Fe) - \nu_0(^{94}Zr^{56}Fe)$, were used to establish the vibrational numbering. To do so, a vibrational numbering was assumed and the six unperturbed band origins for the heavy isotopomer, $^{94}Zr^{56}Fe$ were fitted to the standard form[46]

$$\nu = T_0 + v' \omega_e' - (v'^2 + v') \omega_e' x_e'. \quad (5.2)$$

The fitted parameters, ω_e' and $\omega_e' x_e'$ were then used in the expression for the isotope shift,[44]

$$\nu(^{90}Zr^{56}Fe) - \nu(^{94}Zr^{56}Fe) =$$

$$= (\rho-1)[\omega_e'(v'+½) - \omega_e''(½)] - (\rho^2-1)[\omega_e' x_e'(v'+½)^2 - \omega_e'' x_e''(½)^2], \quad (5.3)$$

to calculate the expected isotope shift for this assignment. In addition to the fitted parameters ω_e' and $\omega_e' x_e'$ for $^{94}Zr^{56}Fe$, this expression requires ρ, which is given by $[\mu(^{94}Zr^{56}Fe)/\mu(^{90}Zr^{56}Fe)]^{1/2} = 1.00827$, as well as estimates of ω_e'' and $\omega_e'' x_e''$. For the purposes of assigning the vibrational numbering, ω_e'' was taken as equal to $\Delta G_{1/2}$" for $^{94}Zr^{56}Fe$ (448.5 cm^{-1}) and $\omega_e'' x_e''$ was taken to be zero. By treating v' as a continuous parameter, the isotope shift obtained in (5.3) could be plotted as a function of the band origin obtained from (5.2), thereby generating a continuous, nearly linear curve. This

process was repeated for several possible assignments and compared to the measured isotope shift of the unperturbed bands.

Figure 5.5 shows the results of this process. The first observed band in the progression, lying at 14255 cm^{-1}, was assigned as the 0-0, 1-0, or 2-0 band and the process described above was used to predict the isotope shift curves. Figure 5.5 shows excellent agreement with the assignment of this feature as the 1-0 band, which fixes the numbering of all the bands in the progression. Note that only the unperturbed bands give isotope shifts that lie close to the predicted curve. The perturbed 2-0, 5-0, 6-0, 8-0, and 9-0 bands are best excluded from this analysis. Our attempts to observe the 0-0 transition, predicted near 13930 cm^{-1}, were unsuccessful, probably due to small Frank-Condon overlap and relatively low dye laser energy in this region (10 mJ/pulse, LDS 750 dye). This is confirmed by calculations of the upper state RKR potential curve[47] and its Franck-Condon factors[48] with the ground state, which is modeled as a harmonic oscillator. The resulting Franck-Condon factor for the 0-0 band (0.0034) is smaller than that calculated for any of the bands that are observed, and is less than 2% of the band with the largest calculated value, the 5-0 band, which has a Franck-Condon factor of 0.185.

5.3.1.5 Vibrational analysis of the observed band system

All vibronic bands that belong to the observed band system were rotationally resolved. The band origins of the unperturbed 1-0, 3-0, 4-0, 7-0, 10-0, and 11-0 bands were the fitted to equation (5.2) to extract the vibrational constants T_0, ω_e', and $\omega_e'x_e'$ for the various isotopomers. These are listed in Table 5.2 for the four most abundant isotopomers of ZrFe.

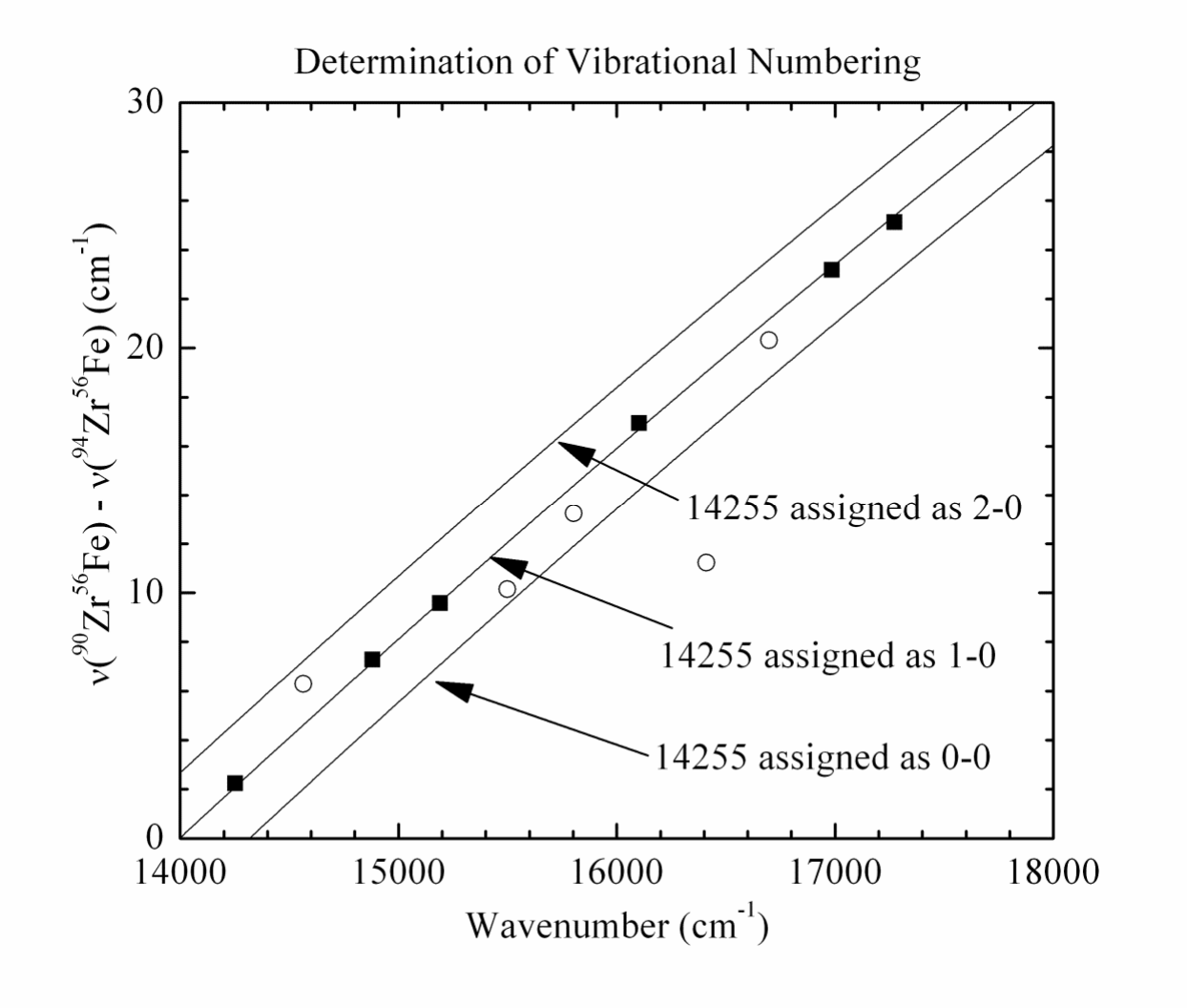

Figure 5.5. Determination of the vibrational assignment for the $[13.9]0^{+}\leftarrow X^{1}\Sigma$ band system of ZrFe. Solid lines represent the calculated isotope shift, plotted against the band origin wavenumber for three different assignments. The measured isotope shifts of the unperturbed bands are plotted as black squares; perturbed bands are plotted using open circles. The isotope shifts of the unperturbed bands are in excellent agreement with the calculated shifts when the 14255 cm^{-1} band is assigned as the 1-0 band.

Table 5.2. Fitted vibrational constants for the $[13.9]0^{+}\leftarrow X^{1}\Sigma^{+}$ band system of ZrFe.[a]

	$^{90}Zr^{56}Fe$	$^{91}Zr^{56}Fe$	$^{92}Zr^{56}Fe$	$^{94}Zr^{56}Fe$
T_0	13931.88(123)	13931.96(119)	13932.34(85)	13932.38(107)
ω'_e	325.05(54)	324.36(53)	323.51(38)	322.32(48)
$\omega'_e x'_e$	1.589(40)	1.582(39)	1.557(28)	1.556(35)

[a] All values are given in wavenumbers (cm^{-1}), with 1σ error limits in parentheses. Only the unperturbed 1-0, 3-0, 4-0, 7-0, 10-0, and 11-0 bands were used to obtain these fitted values.

5.3.2. Rotationally resolved spectra

All of the bands belonging to the observed band system were examined under high resolution (0.05 cm^{-1}). Rotational lines were recorded for the more abundant isotopomers, $^{90}Zr^{56}Fe$ (47.2%), $^{91}Zr^{56}Fe$ (10.3%), $^{92}Zr^{56}Fe$ (15.7%), $^{94}Zr^{56}Fe$ (15.9%) and $^{96}Zr^{56}Fe$ (2.6%). For a few bands, the $^{90}Zr^{54}Fe$ (3.0%) isotopomer was also recorded; for most bands, however, the much smaller reduced mass of this species gave it a large isotope shift, causing it to lie outside of the range scanned.

The bands that form the progression in the red region of the spectrum are all red shaded, displaying an R branch that rapidly forms a band head and a P branch that marches off toward the red. Despite careful examination, no Q branch is found in any of the spectra recorded for the molecule, either in the red region or in the more intense and congested blue region. This is exemplified in the spectrum of the 3-0 band that is displayed in Figure 5.6.

The lack of a Q branch immediately identifies both the upper and lower states as having $\Omega = 0$. On the basis of the short bond length obtained for the ground state (see below), comparisons to the calculated ground state of the isovalent molecule TiFe,[31, 49] and a comparison of the bond length to that of the isoelectronic $^1\Sigma^+$ molecule, CrMo, we assign the ground state as a closed-shell $^1\Sigma^+$ state. The low intensity of the band system suggests that the transition is spin-forbidden, making it impossible to identify a term symbol for the upper state, although $^3\Sigma^-(0^+)$ and $^3\Pi_{0+}$ are the most likely possibilities. The lack of any observable departure from the $B'J'(J'+1)$ form, even out to J' values as large as 31 for some bands, however, suggests that the upper state is of $^3\Pi_{0+}$ symmetry. In any case, given the assignment of the ground state as $^1\Sigma^+$, the upper state must have

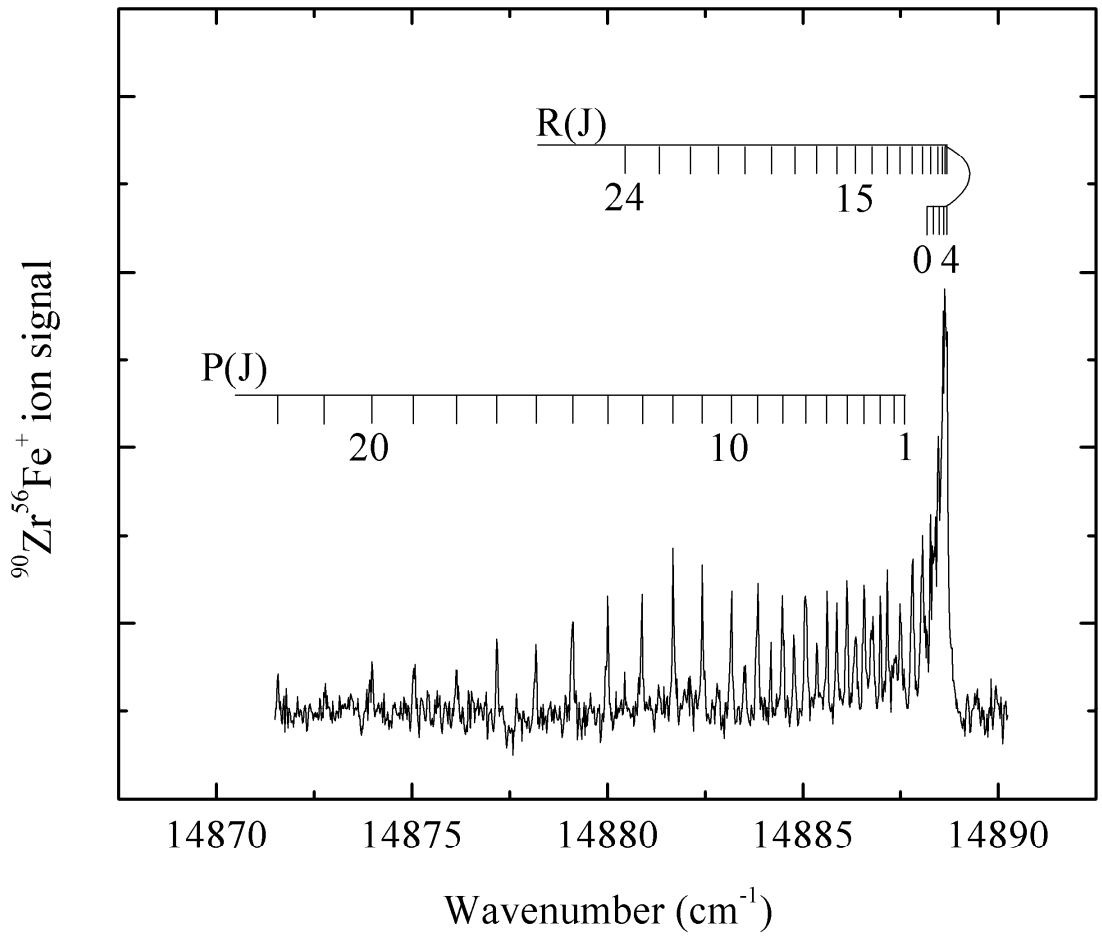

Figure 5.6. High resolution scan over the 3-0 transition of the [13.9] $0^{+}\leftarrow X^{1}\Sigma^{+}$ system of $^{90}Zr^{56}Fe$.

$\Omega=0^+$ as well. Accordingly, the upper state is designated as the $[13.9]0^+$ state, where the [13.9] designation defines the energy of the v=0 level in thousands of wavenumbers.

During the analysis of the rotationally resolved spectra, the 2-0, 5-0, 6-0, 8-0, and 9-0 bands were found to have additional features nearby, suggesting that they could be perturbed. Although many lines were assigned using combination differences involving the now known value of B_0'', often they could not be fitted to the standard expression,

$$\nu = \nu_0 + B_v'J'(J'+1) - B_0''J''(J''+1), \qquad (5.4)$$

without excessively large errors in the fit, providing further evidence of perturbations. Even for the bands that could be fitted to this form, the resulting upper state rotational constants did not have the expected smooth decrease in B_v' as a function of v'. Accordingly, these perturbed bands were excluded from the global fit of the measured rotational lines that was made to obtain the best value of the ground state rotational constant, B_0''. The unperturbed 1-0, 3-0, 4-0, 7-0, 10-0, and 11-0 bands were simultaneously fitted to the form given by (5.4), and constrained to have the same value of B_0''. These values were then inverted to obtain the vibrationally averaged bond length of the ground state, r_0'', which is also reported in Table 5.3 for the various isotopic modifications along with the values of ν_0, B_v', r_v', and B_0'' . The r_0'' bond lengths are quite similar for the various isotopomers, although they are not in agreement within the 1σ error limits. Averaging these values probably provides the best estimate of the ground state bond length, giving $r_0'' = 1.8765 \pm 0.0005$ Å.

The values of B_v' for the $v' = 1, 3, 4, 7, 10$, and 11 levels were also fitted to the expression[44]

Table 5.3 Results from fits of unperturbed rotationally resolved bands.[a]

		$^{90}Zr^{56}Fe$	$^{91}Zr^{56}Fe$	$^{92}Zr^{56}Fe$	$^{94}Zr^{56}Fe$
1-0 $[13.9]0^{+}\leftarrow X^{1}\Sigma^{+}$	ν_0	14254.1492(34)	14253.5418(32)	14252.9977(39)	14251.9054(32)
	B_v'	0.117322(28)	0.117179(45)	0.116666(46)	0.115509(48)
3-0 $[13.9]0^{+}\leftarrow X^{1}\Sigma^{+}$	ν_0	14887.9450(27)	14886.0751(34)	14884.2327(32)	14880.6580(31)
	B_v'	0.116572(25)	0.116163(34)	0.115796(39)	0.114743(38)
4-0 $[13.9]0^{+}\leftarrow X^{1}\Sigma^{+}$	ν_0	15199.3570(27)	15196.8856(27)	15194.4780(37)	15189.7750(25)
	B_v'	0.116337(27)	0.115960(40)	0.115497(41)	0.114469(48)
7-0 $[13.9]0^{+}\leftarrow X^{1}\Sigma^{+}$	ν_0	16118.8157(38)	16114.4780(52)	16110.2045(38)	16101.8612(37)
	B_v'	0.113877(28)	0.113486(48)	0.113160(39)	0.112372(48)
10-0 $[13.9]0^{+}\leftarrow X^{1}\Sigma^{+}$	ν_0	17008.3588(29)	17002.3908(40)	16996.5477(24)	16985.1813(29)
	B_v'	0.112782(27)	0.112379(33)	0.111978(37)	0.110992(39)
11- 0 $[13.9]0^{+}\leftarrow X^{1}\Sigma^{+}$	ν_0	17296.9238(30)	17290.4567(28)	17284.9923(27)	17271.7876(38)
	B_v'	0.112286(30)	0.111921(33)	0.111473(37)	0.110449(39)
	B_e'	0.118321(291)	0.118065(272)	0.117611(238)	0.116512(194)
	α_e'	0.000532(101)	0.000546(95)	0.000541(83)	0.000527(67)
	r_e'	2.0327(25)	2.0306(23)	2.0303(21)	2.0316(17)
	B_0''	0.138786(30)	0.138297(38)	0.137770(34)	0.136513(50)
	r_0''	1.87685(20)	1.87620(26)	1.87588(23)	1.87689(34)

[a] All values are given in wavenumbers (cm^{-1}), with 1σ error limits in parentheses in units of the last digits quote

$$B_v' = B_e' - (v'+1/2)\,\alpha_e' \qquad (5.5)$$

to obtain the equilibrium rotational constant B_e' and the vibration-rotation coupling constant, α_e'. The B_e' values were then inverted to obtain the equilibrium bond length of the $[13.9]0^+$ state, r_e'. Because of the extrapolation to the bottom of the well, however, the upper state bond length, r_e', is not quite as well determined as the ground state bond length, r_0''. Averaging the r_e' values obtained for the various isotopomers, we obtain $r_e' = 2.0313 \pm 0.0011$ Å as our best estimate of the bond length of the $[13.9]0^+$ state.

In addition to the members of the $[13.9]0^+ \leftarrow X^1\Sigma^+$ band system, five additional bands were examined in the congested region to the blue of 18000 cm^{-1}. These bands are much more intense than those of the $[13.9]0^+ \leftarrow X^1\Sigma^+$ band system, and are probably detectable in laser-induced fluorescence experiments owing to their short fluorescence lifetimes of 100-200 ns. Our purpose in investigating these features is to provide preliminary information that will be useful for other investigators who may be able to measure the Stark splitting of the lines, and thus to measure the dipole moment of ZrFe. All of these higher wavenumber bands displayed residual power broadening, had returning R lines overlapping with P lines at our resolution, or were perturbed, so they were excluded from the simultaneous fit. Nevertheless, figures of the rotationally resolved spectra and wavenumbers of the assigned lines are provided in the supporting data for use in Stark experiments. All of these bands again displayed only P and R lines, confirming that they also are $\Omega'=0^+ \leftarrow X^1\Sigma^+$ transitions.

5.4. Discussion

5.4.1 The nature of the ZrFe ground state

Diatomic ZrFe is isoelectronic with CrMo, but has a nuclear charge asymmetry of $\Delta Z=4$. The CrMo molecule therefore provides a useful point of comparison. Initially studied by flash photolysis of a mixture of $Cr(CO)_6$ and $Mo(CO)_6$ vapors,[7] CrMo was subsequently investigated by resonant two-photon ionization methods[12] and by cavity ringdown spectroscopy.[14] The experiments on CrMo show that the ground state is of $^1\Sigma^+$ symmetry, with a short bond length: r_e = 1.8182(15) Å, r_0 = 1.8231(10) Å.[12] Neither the vibrational frequency nor the bond energy are experimentally known, but computational values of $\Delta G_{1/2}$ of 449.4 cm^{-1} and 419 cm^{-1} and D_e of 2.09 eV and 2.63 eV have been obtained in massive multiconfigurational calculations.[19, 46] The leading configuration of CrMo is $d\sigma^2 d\pi^4 d\delta^4 s\sigma^2$, corresponding to placement of all 12 electrons in bonding orbitals, indicating a nominal bond order of 6; when CASSCF natural orbitals are used, the bonding orbital occupation is reduced to $d\sigma^{1.82}\, d\pi^{3.69}\, d\delta^{3.29}\, s\sigma^{1.90}\, s\sigma^{*0.10}\, d\pi^{*0.31}\, d\delta^{*0.71}\, d\sigma^{*0.18}$, giving a somewhat smaller effective bond order of 4.70.[19]

The ground state of ZrFe (ΔZ = 4) exhibits a high degree of similarity to that of its isoelectronic counterpart, CrMo (ΔZ=0). The bond length of ZrFe, r_0 = 1.8765(5) Å, is only 0.0534(11) Å longer than that of CrMo, similar to the 0.0306 Å increase in bond length that is found in moving from N_2 (r_e = 1.0977 Å) to CO (r_e = 1.1283 Å).[33] Likewise, the $\Delta G_{1/2}$ value measured for ZrFe converts to a vibrational force constant, neglecting anharmonicity, of 4.15 mdyne/Å. This is very similar to that obtained from computational studies of CrMo, which are 4.04 mdyne/Å or 3.51 mdyne/Å.[19, 50] Based

on the close similarity between these two molecules, we conclude that both ZrFe and CrMo probably have a sextuple bond.

In moving to the even more asymmetric 12-electron molecule, YCo ($\Delta Z = 6$), the bond length increases to $r_0 = 1.9830(8)$ Å,[32] an increase of 0.1599 Å compared to CrMo. Comparing force constants, the measured vibrational frequency of YCo, 369.8 cm^{-1},[32] converts to a force constant of 2.85 mdyne/Å, a substantial decrease relative to either CrMo or ZrFe. Thus, it appears that the bond order of YCo is significantly reduced from that of CrMo and ZrFe.

5.4.2. Strongly allowed excitations in ZrFe

Unlike CrMo, ZrFe has a high density of excited electronic states. This may be understood simply by considering the states of the separated atoms. From separated atom limits that lie within 10,000 cm^{-1} of the ground limit, 259 distinct electronic states arise for CrMo, while 2710 states arise for ZrFe.[51] Thus, it is perhaps not surprising that only one electronic transition has been discovered in CrMo, while the spectrum of ZrFe becomes very complex above 18000 cm^{-1}. Nevertheless, the two molecules exhibit strong transitions in a similar region of the spectrum – above 18000 cm^{-1} for ZrFe and near 20527 cm^{-1} for CrMo.[12] Further, in both molecules the intense bands are $\Omega = 0^+ \leftarrow X\ ^1\Sigma^+$ transitions, suggesting that they arise from analogous sources. Assuming that the ground state in both molecules is a good Hund's case (a) state, with a good term symbol of $^1\Sigma^+$ and well-defined values of S=0, Λ=0, the only allowed upper states that are consistent with $\Omega = 0^+ \leftarrow X\ ^1\Sigma^+$ transitions are also $^1\Sigma^+$ terms. Thus, we can be confident that the source of oscillator strength in both molecules is an excited $^1\Sigma^+$ state. In CrMo, this state appears to be well-isolated from other states, leading to a single electronic band

system. In ZrFe, the large density of electronic states allows forbidden states to mix with the allowed $^1\Sigma^+$ state (or states), making for a congested spectrum.

Previous work on the coinage metal dimers, Cu_2, Ag_2, Au_2, CuAg, AuAu, and AgAu, has shown that strongly allowed $^1\Sigma_{(u)}^+ \leftarrow X\,^1\Sigma_{(g)}^+$ transitions are also found in the blue region of the spectrum.[52-56] The upper states of these transitions have extremely short fluorescence lifetimes, in the range of 14-40 ns, indicative of absorption oscillator strengths of $f \approx 0.1$.[56] Diatomic CrMo, and Mo_2 exhibit similarly short lifetimes of 14 ns and 18 ns for their analogous strongly allowed $^1\Sigma_{(u)}^+ \leftarrow X\,^1\Sigma_{(g)}^+$ transitions. [12-13] All of these transitions arise from the promotion of an $s\sigma_{(g)}$ bonding electron to an $s\sigma^*(u)$ antibonding orbital. Looking at these transitions in a different light, the upper states diabatically correlate with separated ion states, such as $Cu^+ + Cu^-$ in the case of Cu_2, so that the $^1\Sigma_{(u)}^+ \leftarrow X^1\Sigma_{(g)}^+$ transition corresponds to a charge transfer transition in which an electron is transferred from one atom to the other.[56] Such transitions are extremely intense, owing to the large transition dipole moment expected. Further, although the separated ion limits typically lie 5 to 7 eV above the ground states of the separated atoms, the Coulomb attraction between the separated ions brings these electronic states down into the blue region of the spectrum when the atoms are brought to the equilibrium internuclear separation.[53-56] Thus, charge transfer transitions are likely to be tremendous sources of oscillator strength in all transition metal dimers in the blue region of the spectrum. On this basis, we believe that the source of intensity for the transitions in ZrFe above 18000 cm^{-1} is an $s\sigma^* \leftarrow s\sigma$ electronic transition that produces an excited $^1\Sigma^+$ state that diabatically correlates to the Zr^+ (d^2s^1, ^4F) + Fe^-(d^7s^2, ^4F) separated ion limit. This

separated ion limit generates four distinct $^1\Sigma^+$ states, all of which could contribute to the intensity above 18000 cm^{-1} in ZrFe.

Figure 5.7 illustrates the potential energy curves for the ground state, modeled as a harmonic oscillator, the $[13.9]0^+$ state, obtained through RKR analysis of the fitted values of ω_e', $\omega_e'x_e'$, B_e', and α_e', and the ion-pair curves, which are set up to extrapolate to the lowest separated ion limits for $Zr^+ + Fe^-$ and $Zr^- + Fe^+$, ignoring any repulsions that set in at short distance or additional attractions due to the polarization of the ions or to the formation of chemical bonds. The two ion-pair curves is given by

$$V(R) = D_e(ZrFe, X\ ^1\Sigma^+) + IE(Zr) - EA(Fe) - 116138\ cm^{-1}/R(Å) \qquad (5.6)$$

for the $Zr^+ + Fe^-$ curve and

$$V(R) = D_e(ZrFe, X\ ^1\Sigma^+) + IE(Fe) - EA(Zr) - 116138\ cm^{-1}/R(Å) \qquad (5.7)$$

for the $Zr^- + Fe^+$ curve. To plot these curves, atomic ionization energies were taken from the NIST online database[57] and electron affinities from Hotop and Lineberger.[58] The remaining parameter that is required is the bond energy, D_e. No data exist for this quantity, but using the measured bond energies for the related molecules ZrCo and ZrNi, for which $D_0(ZrCo) = 3.137(1)$ eV and $D_0(ZrNi)=2.861(1)$ eV,[59] we have estimated $D_e(ZrFe) = 3.5$ eV. This is expected to be larger than $D_0(ZrCo)$ and $D_0(ZrNi)$ because these molecules place electrons in antibonding orbitals. While there is undoubtedly some uncertainty in this value, perhaps as large as 0.5 eV, it is nevertheless clear that the ion pair states drop down into the region of the intense transitions that are observed above 18000 cm^{-1}.

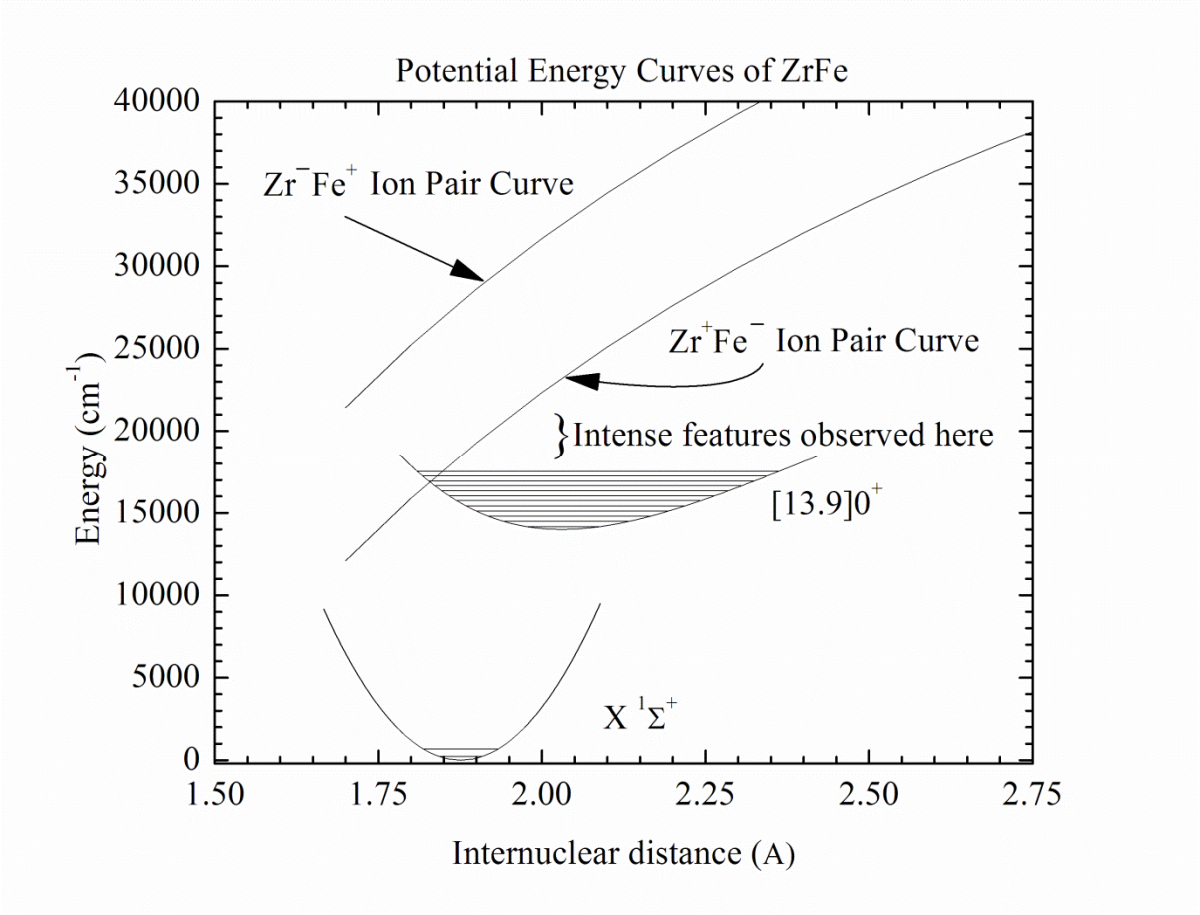

Figure 5.7. Potential energy curves of ZrFe. The ground state is modeled as harmonic, while the $[13.9]0^+$ state is shown using the RKR fitted curve. Ion pair curves are Coulomb potentials that extrapolate to the ion pair limits.

5.4.3. The nature of the $[13.9]0^+$ state of ZrFe

The exceptionally weak band system found to the red in ZrFe is also characterized by $\Omega'=0^+$. It is likely that the upper state of this system is a triplet state, which cannot undergo an allowed transition with the $^1\Sigma^+$ ground state. Nevertheless, the presence of strongly allowed transitions above 18000 cm^{-1} provides a source of oscillator strength that can be tapped into, if the triplet state can mix with the strongly allowed state. Spin-orbit coupling provides a likely mechanism for these states to mix. In view of the selection rules that govern spin-orbit mixing,[42] it is likely that the $[13.9]0^+$ state is of either $^3\Sigma_{0+}^-$ or $^3\Pi_{0+}$ symmetry. The lack of an observable deviation from the $B'J'(J'+1)$ behavior of the rotational levels suggests that the upper state is of $^3\Pi_{0+}$ symmetry.

5.5 Conclusion

Optical spectra of ZrFe have been recorded, establishing that the molecule has a $^1\Sigma^+$ ground state, with a vibration interval of $\Delta G_{1/2}'' = 452.2$ cm^{-1} for $^{90}Zr^{56}Fe$. Averaging the results obtained for the various isotopomers, the ground state bond length is found to be $r_0''=1.8765(5)$ Å. On the basis of the short bond length and a comparison to CrMo, ZrFe is best considered as having a sextuple bond. Strongly allowed transitions to the blue of 18000 cm^{-1} are assigned to a $\sigma^* \leftarrow \sigma$ electronic promotion to form a $^1\Sigma^+$ excited state that adiabatically correlates to the separated ion pair limit, $Zr^+ + Fe^-$. This charge transfer excitation provides an enormous source of oscillator strength that is transferred to other states in the region through spin-orbit and other perturbations, making for a congested spectral region. An exceptionally weak electronic transition is found to the red of the strongly allowed bands. This is thought to correspond to a spin-forbidden

excitation to a $^3\Pi_{0+}$ state, which gains intensity via spin-orbit mixing with the strongly allowed $^1\Sigma^+$ state that lies to the blue.

5.6 References

(1) Cotton, F. A.; Harris, C. B. *Inorg. Chem. (Washington, DC, United States)* **1965**, *4*, 330-333.

(2) Cotton, F. A.; Curtis, N. F.; Harris, C. B.; Johnson, B. F. G.; Lippard, S. J.; Mague, J. T.; Robinson, W. R.; Wood, J. S. *Science* **1964**, *145*, 1305-1307.

(3) Cotton, F. A.; DeBoer, B. G.; Laprade, M. D.; Pipal, J. R.; Ucko, D. A. *J. Amer. Chem. Soc.* **1970**, *92*, 2926-2927.

(4) Lawton, D.; Mason, R. *J. Am. Chem. Soc.* **1965**, *87*, 921-922.

(5) Cotton, F. A.; Bratton, W. K. *J. Am. Chem. Soc.* **1965**, *87*, 921-921.

(6) Efremov, Y. M.; Samoilova, A. N.; Gurvich, L. V. *Opt. Spectrosc.* **1974**, *36*, 381-382.

(7) Efremov, Y. M.; Samoilova, A. N.; Gurvich, L. V. *Chem. Phys. Lett.* **1976**, *44*, 108-109.

(8) Efremov, Y. M.; Samoilova, A. N.; Kozhukhovsky, V. B.; Gurvich, L. V. *J. Mol. Spectrosc.* **1978**, *73*, 430-440.

(9) Bondybey, V. E.; English, J. H. *Chem. Phys. Lett.* **1982**, *94*, 443 - 447.

(10) Michalopoulos, D. L.; Geusic, M. E.; Hansen, S. G.; Powers, D. E.; Smalley, R. E. *J. Phys. Chem.* **1982**, *86*, 3914-3916.

(11) Riley, S. J.; Parks, E. K.; Pobo, L. G.; Wexler, S. *J. Chem. Phys.* **1983**, *79*, 2577-2582.

(12) Spain, E. M.; Behm, J. M.; Morse, M. D. *Chem. Phys. Lett.* **1991**, *179*, 411-416.

(13) Hopkins, J. B.; Langridge-Smith, P. R. R.; Morse, M. D.; Smalley, R. E. *J. Chem. Phys.* **1983**, *78*, 1627-1637.

(14) Kraus, D.; Lorenz, M.; Bondybey, V. E. *PhysChemComm* **2001**, *4*, 44-48.

(15) Roos, B. O.; Andersson, K. *Chem. Phys. Lett.* **1995**, *245*, 215-223.

(16) Ruiperez, F.; Aquilante, F.; Ugalde, J. M.; Infante, I. *J. Chem. Theory Comput.* **2011**, *7*, 1640-1646.

(17) Borin, A. C.; Gobbo, J. P.; Roos, B. O. *Chem. Phys.* **2008**, *343*, 210-216.

(18) Borin, A. C.; Gobbo, J. P.; Roos, B. O. *Chem. Phys. Lett.* **2010**, *490*, 24-28.

(19) Ruiperez, F.; Ugalde, J. M.; Infante, I. *Inorg. Chem. (Washington, DC, United States)* **2011**, *50*, 9219-9229.

(20) Roos, B. O.; Borin, A. C.; Gagliardi, L. *Angew. Chem., Int. Ed.* **2007**, *46*, 1469-1472.

(21) Langridge-Smith, P. R. R.; Morse, M. D.; Hansen, G. P.; Smalley, R. E.; Merer, A. J. *J. Chem. Phys.* **1984**, *80*, 593-600.

(22) Spain, E. M.; Behm, J. M.; Morse, M. D. *J. Chem. Phys.* **1992**, *96*, 2511-2516.

(23) Spain, E. M.; Morse, M. D. *J. Phys. Chem.* **1992**, *96*, 2479-2486.

(24) James, A. M.; Kowalczyk, P.; Langlois, E.; Campbell, M. D.; Ogawa, A.; Simard, B. *J. Chem. Phys.* **1994**, *101*, 4485-4495.

(25) James, A. M.; Kowalczyk, P.; Simard, B. *Chem. Phys. Lett* **1993**, *216*, 512-518.

(26) James, A. M.; Kowalczyk, P.; Simard, B. *J. Mol. Spectrosc.* **1994**, *164*, 260-274.

(27) Sickafoose, S. M.; Langenberg, J. D.; Morse, M. D. *J. Phys. Chem. A* **2000**, *104*, 3521-3527.

(28) Nagarajan, R.; Morse, M. D. *J. Chem. Phys.* **2007**, *127*, 014311/014311-014318.

(29) Nagarajan, R.; Morse, M. D. *J. Chem. Phys.* **2007**, *127*, 164305/1-164305/6.

(30) Martinie, R. J.; Bultema, J. J.; Vander Wal, M. N.; Burkhart, B. J.; Vander Griend, D. A.; DeKock, R. L. *J. Chem. Educ.* **2011**, *88*, 1094-1097.

(31) Krechkivska, O.; Morse, M. D.; Kalemos, A.; Mavridis, A. **in preparation**.

(32) Nagarajan, R.; Morse, M. D. *J. Chem. Phys.* **2007**, *127*, 074304/1-074304/8.

(33) Huber, K. P.; Herzberg, G. *Constants of Diatomic Molecules*; Van Nostrand Reinhold: New York, 1979; Vol. IV.

(34) Lovas, F. J.; Johnson, D. R. *J. Chem. Phys.* **1971**, *55*, 41-44.

(35) Brugh, D. J.; Morse, M. D. *J. Chem. Phys.* **1997**, *107*, 9772-9782

(36) Wiley, W. C.; McLaren, I. H. *Rev. Sci. Instrum.* **1955**, *26*, 1150 - 1157.

(37) Gerstenkorn, S.; Luc, P. *Atlas du Spectre d'Absorption de la Molécule d'Iode entre 14,800-20,000 cm^{-1}*; CNRS: Paris, 1978.

(38) Gerstenkorn, S.; Luc, P. *Atlas du Spectre d'Absorption de la Molécule d'Iode entre 14,000-15,600 cm^{-1}*; CNRS: Paris, 1978.

(39) Morse, M. D. Supersonic beam sources. In *Methods of Experimental Physics: Atomic, Molecular, and Optical Physics*; Dunning, F. B., Hulet, R., Eds.; Academic Press, Inc.: Orlando, Florida, 1996; Vol. II Atoms and Molecules; pp 21-47.

(40) Gerstenkorn, S.; Luc, P. *Rev. Phys. Appl,* **1979**, *14*, 791-794.

(41) Bevington, P. R. *Data Reduction and Error Analysis for the Physical Sciences*; McGraw-Hill: New York, 1969.

(42) Lefebvre-Brion, H.; Field, R. W. *The Spectra and Dynamics of Diatomic Molecules*; Elsevier: Amsterdam, 2004.

(43) Fischer, C. F. *The Hartree-Fock Method for Atoms*; John Wiley & Sons: New York, 1977.

(44) Fu, Z.; Lemire, G. W.; Hamrick, Y. M.; Taylor, S.; Shui, J.-C.; Morse, M. D. *J. Chem. Phys.* **1988**, *88*, 3524-3531.

(45) Martinez, A.; Morse, M. D. *J. Chem. Phys.* **2011**, *135*, 024308/1-024308/10.

(46) Herzberg, G. *Molecular Spectra and Molecular Structure I. Spectra of Diatomic Molecules*, 2nd ed.; Van Nostrand Reinhold: New York, 1950.

(47) LeRoy, R. J. *University of Waterloo Chemical Physics Research Report, CP-425* **1992**, http://leroy.uwaterloo.ca/programs/.

(48) LeRoy, R. J. *University of Waterloo Chemical Physics Research Report CP-663* **2007**, http://leroy.uwaterloo.ca/programs/.

(49) Gutsev, G. L.; Mochena, M. D.; Jena, P.; Bauschlicher, C. W., Jr.; Partridge, H., III. *J. Chem. Phys.* **2004**, *121*, 6785-6797.

(50) Angeli, C.; Cavallini, A.; Cimiraglia, R. *J. Chem. Phys.* **2007**, *127*, 074306/1-074306/7.

(51) Moore, C. E. *Atomic Energy Levels*, Natl. Bur. Stand. U.S. Circ. No. 467 ed.; U.S. Government Printing Office: Washington, D.C., 1971.

(52) Bondybey, V. E.; Schwartz, G. P.; English, J. H. *J. Chem. Phys.* **1983**, *78*, 11-15.

(53) Bishea, G. A.; Marak, N.; Morse, M. D. *J. Chem. Phys.* **1991**, *95*, 5618-5629.

(54) Bishea, G. A.; Morse, M. D. *J. Chem. Phys.* **1991**, *95*, 5646-5659.

(55) Bishea, G. A.; Pinegar, J. C.; Morse, M. D. *J. Chem. Phys.* **1991**, *95*, 5630-5645.

(56) Morse, M. D. Chemical bonding in the late transition metals: The nickel and copper group dimers. In *Adv. Metal Semicond. Clusters*; Duncan, M. A., Ed.; JAI Press: Greenwich, Conn., 1993; Vol. 1; pp 83-121.

(57) Martin, W. C.; Musgrove, A.; Kotochigova, S.; Sansonetti, J. E. *Ground Levels and Ionization Energies for the Neutral Atoms* **2011**, *http://www.nist.gov/pml/data/ion_energy.cfm*.

(58) Hotop, H.; Lineberger, W. C. *J. Phys. Chem. Ref. Data* **1985**, *14*, 731-750.

(59) Arrington, C. A.; Blume, T.; Morse, M. D.; Doverstål, M.; Sassenberg, U. *J. Phys. Chem.* **1994**, *98*, 1398-1406.

CHAPTER 6

ELECTRONIC SPECTROSCOPY AND ELECTRONIC STRUCTURE OF DIATOMIC TiFe

6.1 Introduction

Among the diatomic transition metals, Cr_2 occupies a position of particular prominence because of early controversies concerning its ground state potential curve, especially as regards the bond length. With ground state atoms having configurations of $3d^5\ 4s^1$, ^7S, it is possible in principle to spin-pair all 12 valence electrons in Cr_2, placing them in $s\sigma_g$, $d\sigma_g$, $d\pi_u$, and $d\delta_g$ bonding orbitals to form a tightly bound diatomic molecule with a nominal sextuple bond. This intriguing possibility has sparked a large experimental and computational effort.

On the experimental side, the first spectrum of Cr_2 was obtained in 1974 in a transient absorption study of the products formed in a flash photolysis experiment on gaseous $Cr(CO)_6$.[1] The spectrum was assigned to a $^1\Sigma_u^+ \leftarrow X\ ^1\Sigma_g^+$ transition in diatomic Cr_2, for which a bond length of 1.71 Å found. However, the possibility that the carrier of the spectrum might be linear CrO_2 or CrC_2 was not rigorously excluded. Subsequently, the molecule was investigated by matrix isolation absorption and emission[2-4] and Raman spectroscopy,[5-7] and by laser-induced fluorescence[8,9] and resonant two-photon ionization spectroscopy[10] in jet-cooled molecular beams. While these results have shown that the $^1\Sigma_g^+$ ground state of Cr_2 has a short bond length with $r_e = 1.6788$ Å,[8] details of the shape

of the potential energy surface did not emerge until the photoelectron spectrum of mass-selected Cr_2^- was measured in 1991, revealing a broad shelf at longer internuclear separations where the d-orbital bonds have been broken, followed by a further rise to the dissociation limit as the s-orbital bond is broken.[11]

Computational chemistry has found Cr_2 to be very challenging, owing to the large exchange effects that result from the small size of the $3d^5$ subshell and the high degree of electron correlation in the molecule. An early MCSCF calculation found Cr_2 to have a bond length of 3.06 Å dominated by s-orbital bonding,[12] while a subsequent calculation on the isovalent Mo_2 found a double minimum, in which the molecule could exist in either a long-bonded form dominated by s-orbital bonding or as a short-bonded form in a deeper d-bonded well.[13] This led to speculation that Cr_2 might exhibit a double-minimum potential curve in the ground state, prompting the photoelectron study mentioned above. As a result of the computational difficulties inherent in a study of Cr_2, it has become a standard test molecule for all newly-developed electronic structure methods.[14-53]

It is interesting to consider how the electronic structure of Cr_2 may change, as one proceeds along an isoelectronic sequence that redistributes charge from one nucleus to the other. We may define our position on this isoelectronic sequence in terms of the nuclear charge asymmetry, defined by $\Delta Z = |Z_A - Z_B|$. It is now known that Cr_2 ($\Delta Z = 0$) has a very short bond with a high degree of multiple bonding character. How does this change in moving to VMn (ΔZ=2), TiFe (ΔZ=4), ScCo (ΔZ=6), CaNi (ΔZ=8), KCu (ΔZ=10), and ArZn (ΔZ=12)? Does the bond strength decrease and the bond length increase smoothly as one moves along this sequence, or are there break points where the nature of the bonding changes abruptly? Among the multiply bonded p-block molecules,

N_2 (ΔZ=0, r_e = 1.0977 Å, ω_e = 2358.6 cm^{-1})[54] and CO (ΔZ=2, r_e = 1.1283 Å, ω_e = 2169.8 cm^{-1})[54] are uniformly considered to have triple bonds that are well-described by the simple Lewis dot structures, :N≡N: and :C≡O: . It is harder to justify that BF (ΔZ=4, r_e = 1.2626 Å, ω_e = 1402.1 cm^{-1})[54] has the corresponding triply bonded structure, :B≡F:, in part due to the high positive charge that this requires on the fluorine atom. By the time one reaches BeNe, no chemist would describe this species as having a triply-bonded :Be≡Ne: structure. The lack of corresponding data on the transition metal species has prompted this investigation of diatomic TiFe. No previous spectroscopic data exist for this molecule, and only one computational study has been previously reported.[55] In order to rectify this situation, and learn how the electronic structure is modified as the nuclear charge is made more asymmetric in these 12-electron molecules, we have undertaken spectroscopic and computational studies of diatomic TiFe. A previous study of the isovalent molecule, ZrFe, has already been reported.[56]

6.2 Experimental methods

In the present study, diatomic TiFe was investigated by means of resonant two-photon ionization spectroscopy (R2PI). The instrument employed in this work is identical to that used in our recent investigation of the isovalent ZrFe molecule,[56] and is therefore only briefly described. Diatomic TiFe is produced by focusing the fundamental radiation from a Q-switched Nd:YAG laser (1064 nm, 25-30 mJ/pulse) onto a Ti:Fe 1:1 alloy (ACI Alloys) in the throat of a pulsed supersonic expansion of helium (180-200 psi backing pressure). The alloy sample is in the form of a disk that is rotated and translated to prevent the drilling of a deep hole into the sample, thereby maintaining a nearly constant TiFe concentration in the resulting molecular beam. After supersonic expansion

into the source chamber, the molecular beam passes through a skimmer (50° inside angle, 1.5 cm diameter) that provides a roughly collimated beam in the second chamber, which is the ionization region of a linear time-of-flight mass spectrometer.

In the second chamber, the molecular beam is exposed to unfocussed radiation emitted by a Nd:YAG pumped dye laser that is counterpropagated along the molecular beam axis. After a few tens of nanoseconds, the 5^{th} harmonic output of a Nd:YAG laser (212.8 nm, 5-6 mJ/pulse) is directed across the molecular beam axis at right angles. Neither wavelength is capable of ionizing the molecule in a one-photon process, but the absorption of one dye laser photon and one 5^{th} harmonic photon can ionize the molecule. The net result is that when the dye laser is resonant with a transition, the molecule is carried to the excited state, where absorption of the 5^{th} harmonic radiation leads to efficient ionization. The resulting ions are accelerated in a two-stage Wiley-McLaren ion extraction assembly[57] and travel up a flight tube to a microchannel plate. The output signal is then preamplified (350 MHz) and digitized for processing in a personal computer. By recording the signal for specific masses of interest as a function of the dye laser wavenumber, the spectra for those species are obtained. After collecting the spectrum of TiFe using the 5^{th} harmonic of the Nd:YAG laser (212.8 nm, 5.83 eV) for ionization, portions of the spectrum were scanned a second time using the 4^{th} harmonic (266 nm, 4.66 eV) for ionization, with the goal of comparing the two scans to place limits on the ionization energy of the TiFe molecule.

To reveal the rotational structure of the observed vibronic bands, the dye laser was scanned in high resolution mode (dual grating, 0.05 cm^{-1} resolution) over the various members of the two band systems that were identified. At the same time, a portion of the

dye laser output radiation was sent through a cell containing gaseous I_2; another portion was sent through a 0.22 cm^{-1} free spectral range étalon. The transmitted intensities were recorded and were used to provide an absolute calibration of the spectrum using the precisely known wavenumbers of the iodine lines that are listed in the I_2 atlas of Gerstenkorn and Luc.[58] Because in our instrument the TiFe molecules travel at the beam velocity of helium (1.77×10^5 cm/s)[59] toward the dye laser, a small correction for the Doppler shift experienced by the molecules was required. At the same time, a correction for the error in the I_2 atlas (-0.0056 cm^{-1}) was also made.[60] Together, these corrections amounted to less than 0.11 cm^{-1} for all of the bands reported here.

For a few of the rotationally resolved bands, excited state lifetimes were measured. To do so, the ionization laser was fired at the time of greatest TiFe signal intensity, and the dye laser was scanned in time. The measured ion signal as a function of delay time was then fitted to an exponential decay curve using the Marquardt nonlinear least-squares algorithm.[61]

6.3 Experimental results

6.3.1. Low resolution spectrum

The present spectroscopic study of TiFe covers the range from 15 500 cm^{-1} to 23 500 cm^{-1}. This range can be divided into three sections that display qualitatively different spectra. The low energy region, 15 500-19 500 cm^{-1}, contains only two extremely weak, partially overlapping band systems; the mid-energy region, 19 500-21 500 cm^{-1}, contains a large number of intense bands, and the high energy region, 21 500-23 500 cm^{-1}, contains a high density of somewhat weaker transitions. This is illustrated in Figure 6.1, which displays the low resolution spectrum for the most abundant

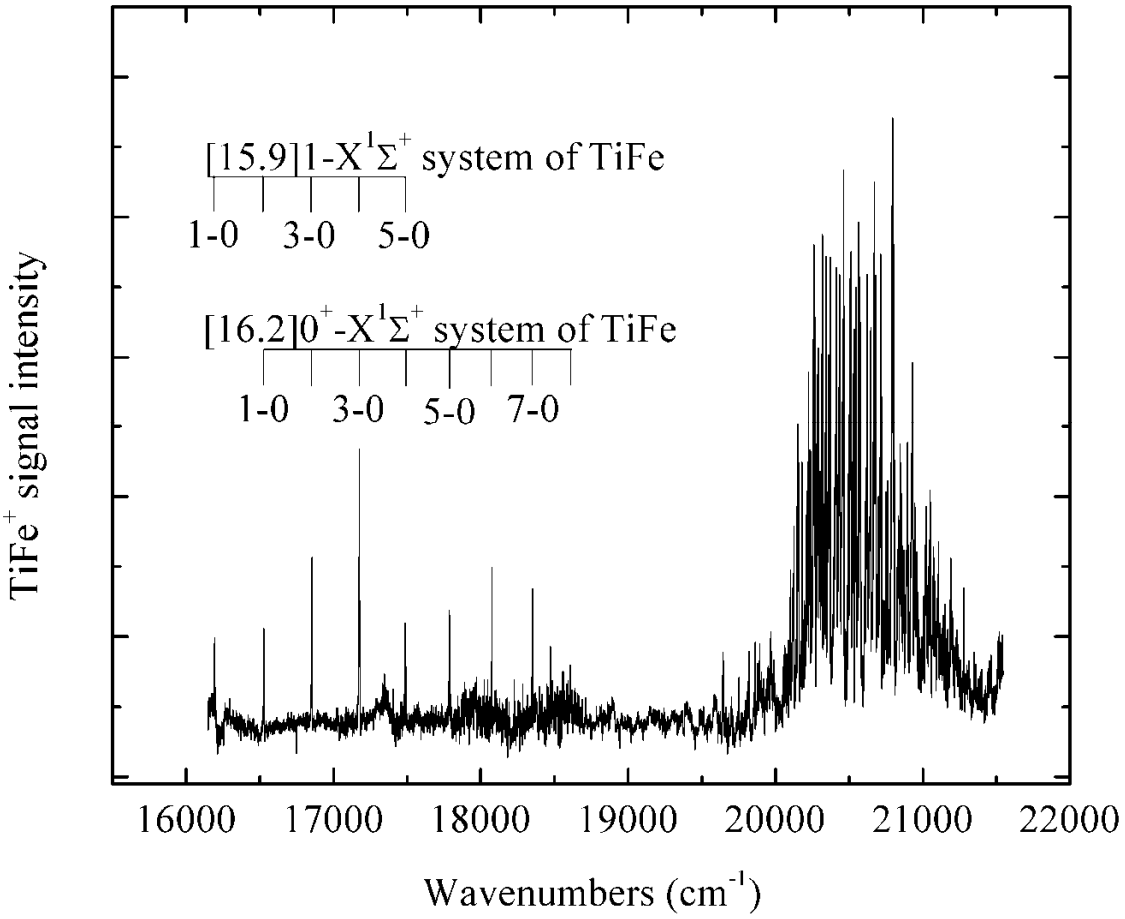

Figure 6.1. Low resolution spectrum of diatomic $^{48}Ti^{56}Fe$ over the 16 000-21 500 cm^{-1} region. A lower energy region, 16000-19500 cm^{-1}, displays what appears to be a single progression, which under higher resolution is revealed to be two partially overlapping progressions. A higher energy region, 19 500-21 500 cm^{-1}, displays a high density of much stronger transitions.

isotopomer, $^{48}Ti^{56}Fe$ (67.7% natural abundance), over the 16 000 - 21 500 cm^{-1} range. Spectra for all of the isotopomers that are present in greater than 1% natural abundance were recorded over the entire scanned range. These include $^{48}Ti^{54}Fe$ (4.3%), $^{46}Ti^{56}Fe$ (7.3%), $^{47}T^{i56}Fe$ (6.7%), $^{48}Ti^{56}Fe$ (67.7%), $^{49}T^{56}Fe$ (5.0%), $^{48}Ti^{57}Fe$ (1.6%), and $^{50}Ti^{56}Fe$ (5.0%). Vibronically and rotationally resolved spectra, tables of line assignments, and fitted parameters are provided in Appendix D of this manuscript.

The low resolution spectrum of TiFe is remarkably similar to the spectrum of the isovalent molecule, ZrFe, which was recently investigated in our group.[56] Both species have extremely weak vibronic progressions in the 16 000-19 000 cm^{-1} range (14 000-17 500 cm^{-1} in ZrFe), followed by a highly congested region of intense transitions at higher energies. For both molecules, high dye laser fluences (8-30 mJ/cm^2) were used for rotational studies of the band systems, and no power broadening was observed. Similarly, the lifetimes of the upper states of the weak band system were found to lie in the range of 14-31 μs for ZrFe, while our studies of the 18 072 and 18 346 cm^{-1} bands of $^{48}Ti^{56}Fe$ reveal excited state lifetimes of 23 ± 4 and 26 ± 6 μs. The long excited state lifetimes and the lack of power broadening in these spectra demonstrate that the transitions are very weak indeed. These observations provide strong evidence that the bands correspond to spin-forbidden transitions, a possibility that is further supported by computational studies that are reported below. The observation of strong transitions above 20 000 cm^{-1} also suggests that the upper states of the spin-forbidden transitions borrow intensity from these higher-lying, strongly allowed states by mixing that is induced by spin-orbit interactions. In this context, we note that the orbital spin-orbit parameters are given by $\zeta_{3d}(Ti) = 123$ cm^{-1} and $\zeta_{3d}(Fe) = 417$ cm^{-1}.[62] These values are

large enough to allow admixtures of a few percent of the strongly allowed character into the spin-forbidden states, consistent with the long lifetimes and low susceptibility to power broadening that are observed.

Following the initial survey of the spectrum that was undertaken using the fifth harmonic of the Nd:YAG laser (212.8 nm) for ionization, portions of the spectrum were rescanned using the fourth harmonic, 266 nm, for ionization in order to bracket the ionization energy of the molecule. The lowest energy transition that could be observed with the 266 nm (4.661 eV) radiation lies at 20 178 cm^{-1} (2.502 eV), placing the ionization energy below 7.16 eV. It was found that the 5-0 band of the $[16.2]0^+ \leftarrow X^1\Sigma^+$ system, which lies at 17 788 cm^{-1} (2.205 eV) could not be observed using 266 nm radiation for ionization, thereby placing the ionization energy of TiFe above 6.86 eV. On this basis, the ionization energy of TiFe is thought to lie in the range 6.86 eV < IE(TiFe) < 7.16 eV. This is similar to the ionization energy of the isoelectronic molecule, Cr_2, which has been established as 6.999(1) eV.[63]

In a large number of diatomic transition metals, predissociation is found to set in abruptly as soon as the energy exceeds the energy of the lowest separated atom limit, particularly when a large density of electronic states is present.[64-69] Given the large density of states evident toward higher energies in Figure 6.1, scans were conducted to higher wavenumbers in the hope of finding a predissociation threshold. Despite scanning slightly beyond 23 500 cm^{-1}, no predissociation threshold was found. On this basis, we believe that the bond energy of TiFe is greater than the wavenumber of the last observed band, placing D_0(TiFe) above 2.91 eV.

A vibrational progression consisting of eight bands was found in the survey scan over the 16 000-19 000 cm^{-1} region. Higher resolution (0.05 cm^{-1}) studies, however, revealed that four members of the apparent progression consisted of two closely spaced bands of different upper state electronic symmetry. One band had P, Q and R branches, with first lines of R(0), Q(1) and P(2); the second band displayed only P and R branches, with first lines of R(0) and P(1). Accordingly, what was on first glance only a single band system was instead assigned to two systems that were eventually labeled as the $[15.9]1 \leftarrow X^1\Sigma^+$ and $[16.2]0^+ \leftarrow X^1\Sigma^+$ systems. The detailed rotational analysis and the reasoning behind this assignment are presented below.

For all of the bands belonging to the two band systems, rotationally resolved spectra were collected and analyzed, allowing band origins and isotope shifts to be precisely measured. These values were then used to establish the vibrational numbering of the bands. By assuming a vibrational numbering and fitting the band origins of the heavier isotopomer to the standard formula,[70]

$$\nu = T_0 + v' \omega_e' - (v'^2 + v') \omega_e' x_e', \tag{6.1}$$

the fitted parameters ω_e' and $\omega_e' x_e'$ could be used to calculate the predicted isotope shift using the formula[70]

$$\nu_L - \nu_H = (\rho-1)[\omega_e'(v'+½) - \omega_e''(½)] - (\rho^2-1)[\omega_e' x_e'(v'+½)^2 - \omega_e'' x_e''(½)^2] \tag{6.2}$$

For TiFe, the heavy isotopomer (ν_H) was chosen to be $^{50}Ti^{56}Fe$ because of the lack of other observable isotopic combinations at mass 106. The light isotopomer (ν_L) was chosen as $^{48}Ti^{56}Fe$ due to its high abundance, combined with the lack of other observable isotopomers at mass 104. For these species, the dimensionless parameter, ρ, is given as

$\rho = \sqrt{\mu_H / \mu_L} = 1.01670$. By treating equations (6.1) and (6.2) as functions of a continuous parameter, ν′, it was possible to plot the predicted isotope shift, ν(^{48}Ti^{56}Fe) – ν(^{50}Ti^{56}Fe), as a function of the band frequency, ν, for various assignments of the bands. The resulting curves were then compared to the measured isotope shift and band origin values to identify the correct vibrational numbering. To do so, the ground state vibrational frequency, ω_e'' was taken as 534 cm^{-1} and the anharmonicity, $\omega_e''x_e''$ was neglected, as its effect on the isotope shift is minimal.

The resulting plots are unequivocal. Figure 6.2 shows the isotope shift *vs.* transition wavenumber plot for the [15.9]1 ← $X^1\Sigma^+$ band system, which establishes that the first observed band, found near 16 191 cm^{-1} in ^{48}Ti^{56}Fe, is the 1-0 band. Likewise, Figure 6.3 demonstrates that the first observed band of the [16.2] 0^+ ← $X\ ^1\Sigma^+$ system, found near 16 525 cm^{-1} in ^{48}Ti^{56}Fe, is also the 1-0 band.

Fitting all vibronic bands that belong to the same band system to equation (6.1), then gives the values of T_0, ω_e', and $\omega_e'x_e'$ for the various isotopomers. The resulting fitted vibrational constants for the [15.9]1←$X^1\Sigma^+$ and [16.2]0^+←$X^1\Sigma^+$ band systems are presented in Table 6.1.

6.3.2. Rotationally resolved spectra

All of the bands that were found in survey scans (0.14 cm^{-1} resolution) in the 16 000-19 000 cm^{-1} region were subsequently investigated in high resolution (0.05 cm^{-1}). At this higher resolution, four features, located near 16 525, 16 849, 17 168 and 17 480 cm^{-1}, were found to consist of two bands within a few wavenumbers of each other. This is illustrated in Figure 6.4, which displays the rotationally resolved spectrum near

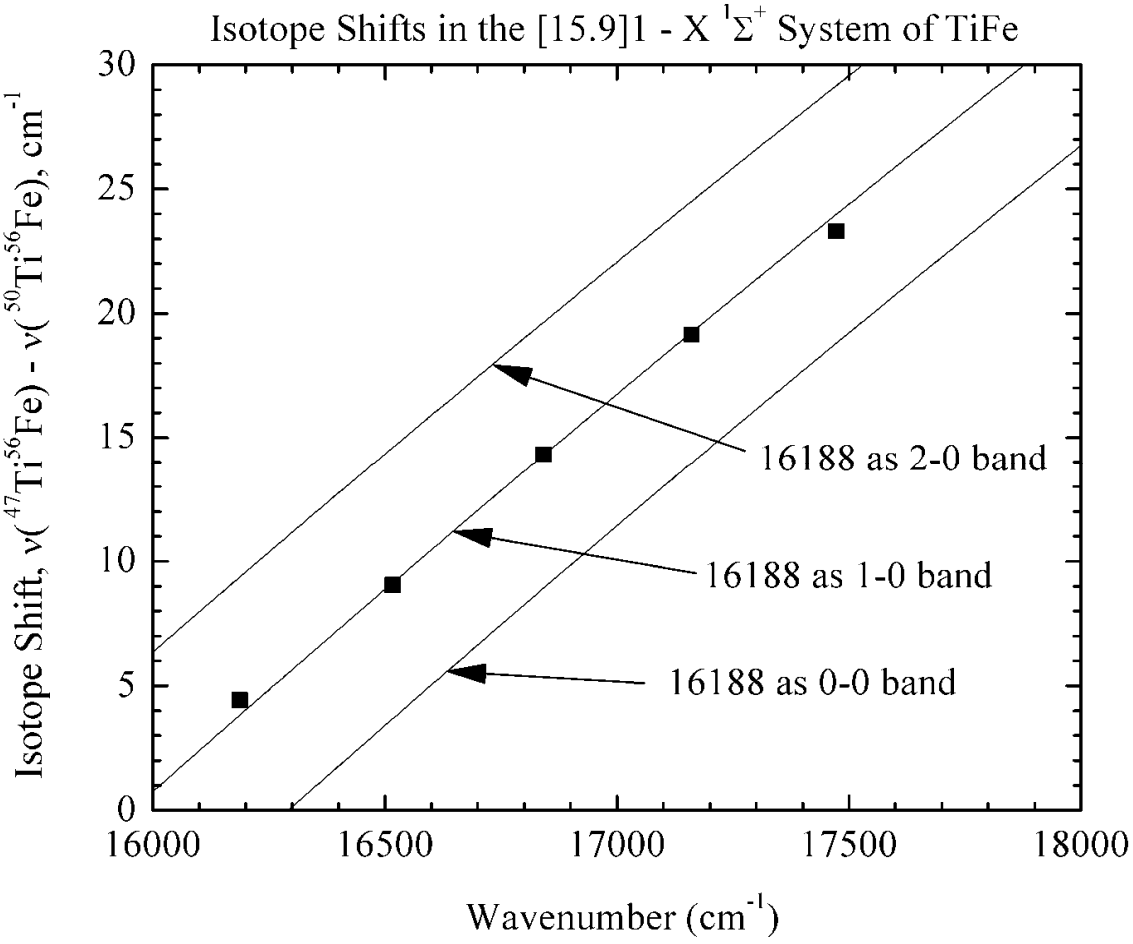

Figure 6.2. Determination of the vibrational assignment for the $[15.9]^3\Pi_1 \leftarrow {}^1\Sigma^+$ band system. Solid lines provide the calculated isotope shift, plotted against the band origin wavenumber for three different assignments. The measured isotope shifts are plotted as black squares and are in excellent agreement with the calculated shifts, when the 16188 cm^{-1} band is assigned as the 1-0 band.

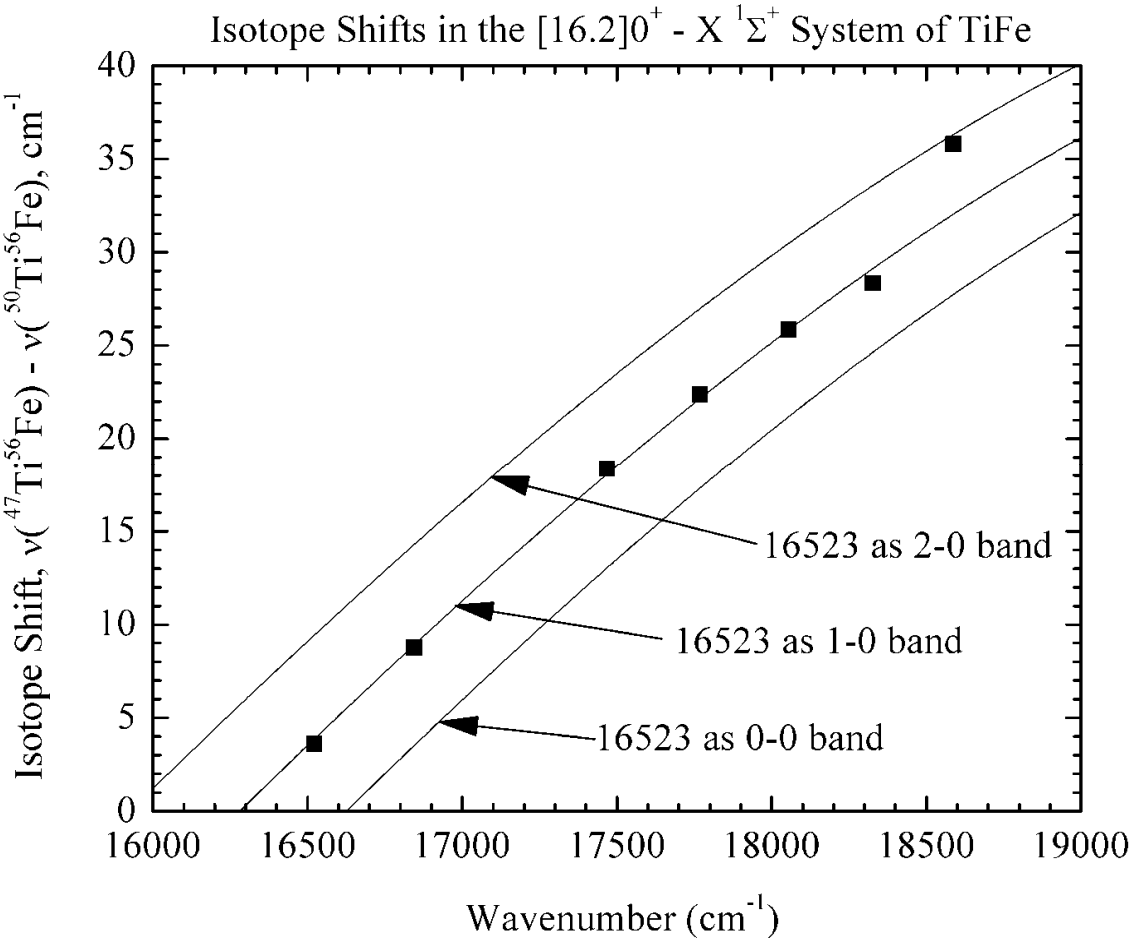

Figure 6.3. Determination of the vibrational assignment for the $[16.2]^3\Pi_{0^+} \leftarrow {}^1\Sigma^+$ band system. Solid curves provide the calculated isotope shift, plotted against the band origin wavenumber for three different assignments. The measured isotope shifts are plotted as black squares and are in excellent agreement with the calculated shifts, when the 16523 cm^{-1} band is assigned as the 1-0 band.

Table 6.1. Results from a vibronic fit of bands belonging to the $[15.9]^3\Pi_1 \leftarrow X\ ^1\Sigma^+$ and the $[16.2]^3\Pi_{0^+} \leftarrow X\ ^1\Sigma^+$ band systems of TiFe

	$^{46}Ti^{56}Fe$	$^{48}Ti^{54}Fe$	$^{47}Ti^{56}Fe$	$^{48}Ti^{56}Fe$	$^{49}Ti^{56}Fe$	$^{50}Ti^{56}Fe$
Fitted spectroscopic constants for the $[15.9]^3\Pi_1 \leftarrow X\ ^1\Sigma^+$ band system[a]						
T_0 (cm^{-1})	15849.67(64)		15851.54(89)	15851.95(84)	15852.39(51)	15852.54(32)
ω_e' (cm^{-1})	349.175(589)		346.156(784)	344.309(741)	342.471(459)	340.683(287)
$\omega_e'x_e'$ (cm^{-1})	3.000(85)		2.841(110)	2.822(104)	2.808(63)	2.743(40)
k_e' (mdyn/Å)	1.812		1.802	1.803	1.804	1.804
Fitted spectroscopic constants for the $[16.2]^3\Pi_{0^+} \leftarrow X\ ^1\Sigma^+$ band system						
T_0 (cm^{-1})	16179.51(461)	16182.00(522)	16180.71(442)	16183.42(502)	16180.41(500)	16181.54(476)
ω_e' (cm^{-1})	355.99(260)	352.98(3351)	353.39(249)	349.51(322)	351.59(288)	349.20(274)
$\omega_e'x_e'$ (cm^{-1})	5.443(255)	5.170(366)	5.315(244)	5.021(352)	5.466(286)	5.347(272)
k_e' (mdyn/Å)	1.884	1.895	1.874	1.900	1.879	1.922

[a]Error limits (1σ) for the resulting fitted spectroscopic constants are provided in units of the last digit quoted

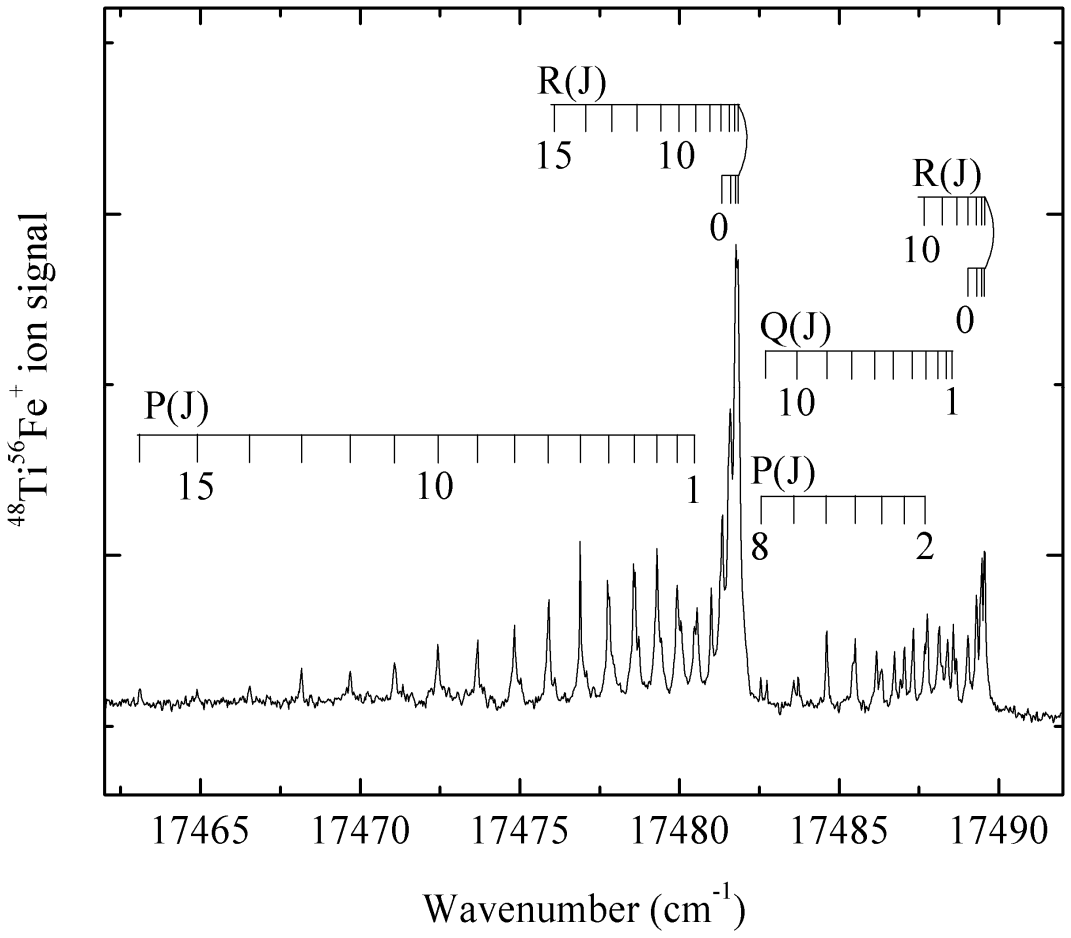

Figure 6.4. Rotationally resolved spectrum of the 5-0 band of the $[15.9]^3\Pi_1$-$X^1\Sigma^+$ system (on the right), and the 4-0 band of the $[16.2]^3\Pi_{0^+}$-$X^1\Sigma^+$ system (on the left).

17 480 cm^{-1} for the most abundant isotopomer, $^{48}Ti^{56}Fe$. Above 17 480 cm^{-1}, the observed features consisted of only a single band, as displayed in Figure 6.5. All of the features that were found to contain pairs of bands were similar to that shown in Figure 6.4, with both bands red shaded, displaying R branch band heads at low values of J and a series of P lines marching off to lower wavenumbers. In fact, all of the observed bands, even those which appeared as single features, were red shaded, indicating an increase in bond length upon electronic excitation.

For the features that turned out to consist of pairs of bands, one of the bands had only R and P branches with first lines of R(0) and P(1) while the second band had R, Q, and P branches with first lines of R(0), Q(1), and P(2). These first lines demonstrate that the Ω values for the band systems are $\Omega'=0 \leftarrow \Omega''=0$ for the bands containing only R and P lines, and $\Omega'=1 \leftarrow \Omega''=0$ for the bands with all three branches. Further analysis demonstrated that all of the bands originate from the same lower state. Accordingly, the bands were fit to the standard form

$$\nu(J' \leftarrow J'') = \nu_0 + B'J'(J' + 1) - B''J''(J'' + 1), \tag{6.3}$$

with B″ constrained to be the same for all bands belonging to the same isotopomer. This procedure provides the most accurate values of B″ and the various $B_{v'}$ values as well. For the most abundant $^{48}Ti^{56}Fe$ isotopomer the values of B″ and r_0'' were found to be 0.225 228(31) cm^{-1} and 1.702 68(12) Å respectively (1σ error limits given in parentheses). Fitted ground state spectroscopic constants for the remaining TiFe isotopomers are presented in Table 6.2. Combining the results for all of the masses for which only a single isotopomer was observed ($^{47}Ti^{56}Fe$, $^{48}Ti^{56}Fe$, and $^{50}Ti^{56}Fe$), we obtain our best estimate of the ground state bond length to be r_0''= 1.7024(3) Å.

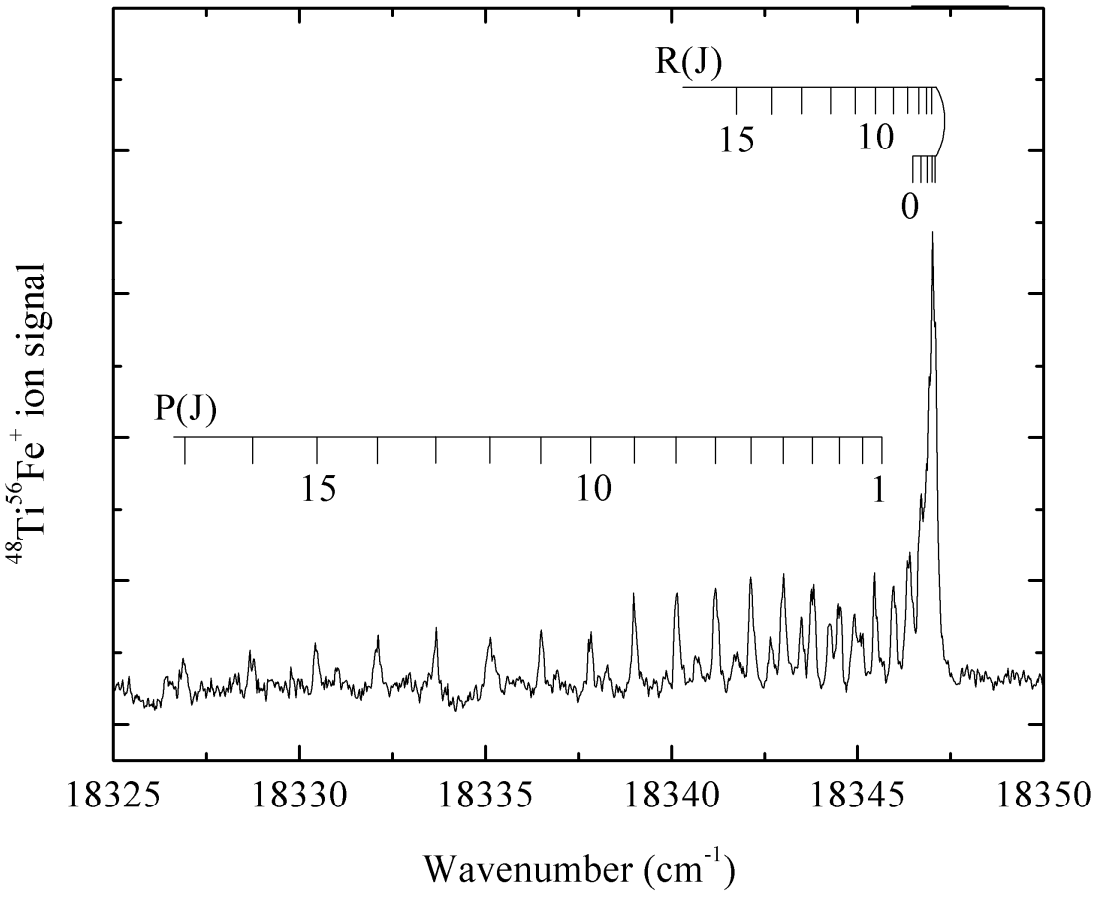

Figure 6.5. Rotationally resolved spectrum of the 7-0 band of the $[16.2]^3\Pi_0^+$-$X^1\Sigma^+$ system.

Table 6.2.Fitted ground state vibrational constants and bond length for various TiFe isotopomers obtained in a combined fit of allrotationally resolved bands[a]

	$^{46}Ti^{56}Fe$	$^{48}Ti^{54}Fe$	$^{47}Ti^{56}Fe$	$^{48}Ti^{56}Fe$	$^{49}Ti^{56}Fe$	$^{50}Ti^{56}Fe$
B_0'' (cm^{-1})	0.230619(56)	0.229557(86)	0.227903(41)	0.225228(31)	0.222829(51)	0.220525(56)
r_0'' (Å)	1.70222(21)	1.70088(32)	1.70230(15)	1.70268(12)	1.70238(19)	1.70212(22)

[a]Errors (1σ) are provided for all fitted spectroscopic constants in parentheses following the reported value, in units of the last digit
quoted

This bond length is similar to that of the isoelectronic Cr_2 molecule ($r_0'' = 1.6858$ Å)[8], suggesting that the Ω=0 ground state of TiFe is also a closed-shell, $^1\Sigma^+$ state. This is supported by a density functional calculation that provides a calculated bond length of 1.67 Å for the predicted $^1\Sigma^+$ ground state.[55] Based on the good agreement between theory and experiment, we assign the ground state as $X^1\Sigma^+$. This implies that the upper state of the [16.2]0 system has $\Omega=0^+$, since transitions from a $^1\Sigma^+(\Omega=0^+)$ state to a state with $\Omega=0^-$ are forbidden.

Excluding bands that were obviously perturbed, the fitted values of B'_v for the bands belonging to $[15.9]1\leftarrow X^1\Sigma^+$ and $[16.2]0^+\leftarrow X^1\Sigma^+$ band systems were fitted to the expression,

$$B_v' = B_e' - \alpha_e' (v + ½), \tag{6.4}$$

to determine the constants B_e' and α_e' for these two band systems. Values of B_v', B_e', r_e', and α_e' for the different isotopic modifications of TiFe are presented in Table 6.3. In the table, the value of α_e calculated from the Pekeris relationship,

$$\alpha_e = [6(\omega_e x_e B_e^3)^{1/2} - 6B_e^2]/\omega_e \tag{6.5}$$

is also provided. The Pekeris values of α_e are in poor agreement with the fitted results, providing additional evidence that the observed states are perturbed. Inverting the values of B_e' to obtain r_e', and combining the results for the masses having only a single observable isotopomer, we obtain our best estimates of the equilibrium bond lengths of the upper states as $r_e'([15.9]1) = 1.8857(36)$ Å and $r_e'([16.2]0^+) = 1.8839(22)$ Å.

Table.6.3 Results from the fits of bands belonging to $[15.9]^3\Pi_1$ and $[16.2]^3\Pi_{0^+}$ states of TiFe[a]

Vibrational level	B_v' ($^{46}Ti^{56}Fe$)	B_v' ($^{48}Ti^{54}Fe$)	B_v' ($^{47}Ti^{56}Fe$)	B_v' ($^{48}Ti^{56}Fe$)	B_v' ($^{49}Ti^{56}Fe$)	B_v' ($^{50}Ti^{56}Fe$)
$[15.9]^3\Pi_1$ state of TiFe						
1	0.18772(21)		0.18399(-38)	0.18248(-5)	0.18246(-1)	0.17496[b]
2			0.18436(50)	0.18214(20)	0.18026(1)	0.178323(20)
3	0.18549(-32)		0.18352(17)	0.18125(-10)	0.17801(-1)	0.177405(-41)
4	0.18474(-21)		0.18255(-30)	0.18056(-20)		0.176610(20)
5	0.18442(32)		0.18236(2)	0.18033(15)	0.17816[b]	0.17917[b]
Fitted spectroscopic constants for the $[15.9]^3\Pi_1$ state of TiFe						
B_e' (cm^{-1})	0.18878(58)		0.18513(55)	0.18341(26)	0.18581(3)	0.18044(14)
r_e' (Å)	1.8970(29)		1.8887(28)	1.8868(13)	1.8643(2)	1.8817(7)
α_e' (cm^{-1})	0.000850(282)		0.000508(276)	0.000589(132)	0.002226(18)	0.000856(75)
α_e' (Pekeris)[c]	0.001829		0.001733	0.001713	0.001747	0.001662
$[16.2]^3\Pi_{0^+}$ state of TiFe						
1	0.18716(9)	0.18615(0)	0.18499(0)	0.18261(-9)	0.18078(9)	0.17885(6)
2	0.18630(-10)	0.18533(0)	0.18412(-2)	0.18183(18)	0.17998(-14)	0.17819(-10)
3	0.18569(-6)	0.18451(0)	0.18329(1)	0.18050(-9)		
4	0.18516(8)	0.18453[b]	0.18309[b]	0.18108[b]	0.17901(4)	0.17732(3)
5	0.18588[b]	0.18439[b]	0.18364[b]	0.18144[b]	0.17948[b]	0.17756[b]
6	0.18702[b]	0.18701[b]	0.18481[b]	0.18254[b]	0.18051[b]	0.17862[b]
7	0.18354[b]	0.18488[b]	0.18417[b]	0.18283[b]	0.18162[b]	0.17967[b]
8	0.18715[b]		0.18120[b]		0.17624[b]	0.17841[b]

Table 6.3 continued

Fitted spectroscopic constants for the $[16.2]^3\Pi_{0^+}$ state of TiFe						
B_e' (cm^{-1})	0.18806(20)	0.18739(0)	0.18625(4)	0.18429(48)	0.18155(28)	0.17954(19)
r_e' (Å)	1.8850(2)	1.8826(0)	1.8831(2)	1.8823(25)	1.8860(15)	1.8864(10)
α_e' (cm^{-1})	0.000660(107)	0.000822(4)	0.000847(27)	0.001056(292)	0.000576(154)	0.000499(108)
α_e' (Pekeris)[c]	0.002611	0.002538	0.002560	0.002433	0.002539	0.002452

[a] Residuals in the fit of the B_v' values are provided in parentheses following each entry, in units of 0.00001 cm^{-1}. Error limits (1σ) for the resulting fitted spectroscopic constants are provided in units of the last digit quoted.
[b] Omitted from the fit, because the B_v' value showed evidence of perturbations, specifically, a failure of the B_v' values to decrease with increasing v′.
[c] The value of α_e calculated from the Pekeris relationship, $\alpha_e = [6(\omega_e x_e B_e^3)^{1/2} - 6B_e^2]/\omega_e$, should be close to the fitted value if the bands are unperturbed and follow a Morse potential reasonably closely. The failure of the calculated values to match the fitted values shows that the levels are either perturbed or follow a potential that differs significantly from the Morse potential.

6.3.3. The nature of the [15.9]1 and [16.2]0^+ excited states

The similar bond lengths in the [15.9]1 and [16.2]0^+ states, along with the similar vibrational frequencies of 344.3(7) and 349.5(3.2) cm^{-1}, respectively, suggest that the two states may be spin-orbit components of the same Hund's case (a) state. If so, the Hund's case (a) state must be inverted, with the bottom of the $\Omega=1$ well lying about 329.4 cm^{-1} below the bottom of the $\Omega=0^+$ well.

The weak intensity of the observed band systems suggests that they are electronically forbidden, presumably gaining intensity through spin-orbit mixing with the intense upper states that lie further to the blue. Although the Hund's case (a) state responsible for both the [15.9]1 and [16.2]0^+ states could be either a $^3\Sigma^-$ or a $^3\Pi$ state, a $^3\Sigma^-$ state would undergo spin-orbit splitting only in the second order of perturbation theory, leading to a small splitting, and generally the $\Omega=0^+$ component would be expected to lie lower in energy. Also, some departure from the $B'J'(J'+1)$ formula would be expected at higher J values, due to spin-uncoupling interactions between the $^3\Sigma^-(0^+)$ and $^3\Sigma^-(1)$ components. Thus, it is likely that the observed [15.9]1 and [16.2]0^+ states are components of an inverted $^3\Pi$ state.

Given that the leading contribution to the $^1\Sigma^+$ ground state is a $1\sigma^2\ 2\sigma^2\ 1\pi^4\ 1\delta^4$ configuration (see below), $^3\Pi$ states can be generated by one-electron promotions of a 1σ or 2σ electron to the 2π orbital, a 1δ electron to the 2π orbital, a 1π electron to the 2δ orbital, or a 1π electron to the 3σ or 4σ orbital. In terms of the partially occupied orbitals, these lead to $1\sigma^1 2\pi^1$, $2\sigma^1 2\pi^1$, $1\delta^3 2\pi^1$, $1\pi^3 2\delta^1$, $1\pi^3 3\sigma^1$ and $1\pi^3 4\sigma^1$ configurations. The first of these, $1\sigma^1 2\pi^1$ or $2\sigma^1 2\pi^1$, has the orbital that is responsible for the spin-orbit splitting (2π) less than half-full, so the resulting $^3\Pi$ state would be regular, not inverted. These

configurations may be excluded from further consideration. The last two configurations move an electron from a strongly bonding 1π orbital to a strongly antibonding 3σ or 4σ orbital, and would not be expected to arise at such a low energy. The remaining two configurations, $1\delta^3 2\pi^1$ and $1\pi^3 2\delta^1$, have an orbital that is more than half-full (favoring an inverted $^3\Pi$ state) and another orbital that is less than half-full (favoring a regular $^3\Pi$ state). Thus, more detailed consideration is required to decide which of these could be consistent with the data.

To consider the spin-orbit splitting expected for the $1\delta^3 2\pi^1$, $^3\Pi$ and $1\pi^3 2\delta^1$, $^3\Pi$ states, we note that the spin-orbit operator can be expressed as an effective one-electron operator given by[71,72]

$$\hat{H}^{SO} = \sum_{i\alpha} \hat{a}_{i\alpha} \hat{l}_{i\alpha} \cdot \hat{s}_i \tag{6.6}$$

where the sum is over all electrons, *i*, and nuclei, α. Here $\hat{a}_{i\alpha}$ is an operator that depends only on the radial distance of electron *i* from nucleus α; $\hat{l}_{i\alpha}$ is the orbital angular momentum operator for electron *i* measured about nucleus α; and $\hat{s}_i$ is the spin angular momentum of electron *i*. In the first-order perturbation treatment of the spin-orbit interaction of a $^3\Pi$ state, the spin-orbit energy is given by $E^{SO} = A\Lambda\Sigma$, where Λ and Σ are the projections of L and S on the internuclear axis, respectively, and A is the spin-orbit constant for the state in question. As a result, E^{SO} vanishes for a $^3\Pi_1$ state (Λ=1, Σ=0), but the $^3\Pi_0$ component (Λ=1, Σ=-1) has a nonzero spin-orbit energy (-A) given by

$$E^{SO}(^3\Pi_0) = -A = \left\langle {}^3\Pi_0 \middle| \hat{H}^{SO} \middle| {}^3\Pi_0 \right\rangle \tag{6.7}$$

Treating the $^3\Pi_0$ states as single Slater determinants, and applying the Slater-Condon rules for the evaluation of one-electron operators,[72] it is possible to express the spin-orbit energies in terms of the parameters $a_\delta \equiv \left\langle \delta \left| \sum_\alpha \hat{a}_\alpha \right| \delta \right\rangle$ and $a_\pi \equiv \left\langle \pi \left| \sum_\alpha \hat{a}_\alpha \right| \pi \right\rangle$ as[62]

$$E^{SO}(1\delta^3 2\pi^1, {}^3\Pi_0) = a_\delta + \tfrac{1}{2}\, a_\pi \tag{6.8}$$

and

$$E^{SO}(1\pi^3 2\delta^1, {}^3\Pi_0) = -a_\delta - \tfrac{1}{2}\, a_\pi. \tag{6.9}$$

For a π orbital that is expressed as $|\pi\rangle = c_1\,|3d\pi(\mathrm{Ti})\rangle + c_2\,|3d\pi(\mathrm{Fe})\rangle$, a_π is given by

$$a_\pi = |c_1|^2 \zeta_{3d}(\mathrm{Ti}) + |c_2|^2 \zeta_{3d}(\mathrm{Fe}). \tag{6.10}$$

Similarly, for a δ orbital that is expressed as $|\delta\rangle = c_1'\,|3d\delta(\mathrm{Ti})\rangle + c_2'\,|3d\delta(\mathrm{Fe})\rangle$, a_δ is given by

$$a_\delta = |c_1'|^2 \zeta_{3d}(\mathrm{Ti}) + |c_2'|^2 \zeta_{3d}(\mathrm{Fe}). \tag{6.11}$$

If we estimate that the π and δ orbitals have equal contributions on the two atoms, then we expect $a_\pi = a_\delta = \tfrac{1}{2}[\zeta_{3d}(\mathrm{Ti}) + \zeta_{3d}(\mathrm{Fe})] = 270\ \mathrm{cm}^{-1}$. Thus, equations (6.8) and (6.9) predict that the $1\delta^3 2\pi^1$, $^3\Pi$ state will be inverted, with a $^3\Pi_0 - {}^3\Pi_1$ energy difference of about 405 cm^{-1}, while the $1\pi^3 2\delta^1$, $^3\Pi$ state will be regular, with a $^3\Pi_0 - {}^3\Pi_1$ energy difference of about -405 cm^{-1}. The experimentally measured separation of $^3\Pi_0 - {}^3\Pi_1 = 329.4\ \mathrm{cm}^{-1}$ strongly suggests that the excited state is a $^3\Pi$ state deriving from a $1\delta^3 2\pi^1$ configuration. The difference between the measured spin-orbit splitting (329.4 cm^{-1}) and that calculated by this method (405 cm^{-1}) can be explained by unequal contributions from the two atoms to the molecular orbitals, by

configurational mixing with other states, or by second-order spin-orbit effects due to interactions with other nearby states that can shift the $^3\Pi_{0^+}$ level relative to the $^3\Pi_1$ level. Even so, the fact that the $1\delta^3 2\pi^1$ configuration is the only one that produces an inverted $^3\Pi$ state provides strong evidence that this assignment is correct

6.3.4. Intense transitions in the 20 000 – 21 500 cm^{-1} region

In the 20 000 – 21 500 range, TiFe displays a high density of vibronic transitions that are notable for their high intensity. In this regard, TiFe is reminiscent of the coinage metal dimers, Cu_2,[73] CuAg,[74] CuAu,[75] AgAu,[76] and Au_2,[76] and the group 6 dimers CrMo[77] and Mo_2,[78] all of which exhibit similarly intense transitions in the blue region (19 300 – 25 900 cm^{-1}) that have short fluorescence state lifetimes (τ = 14-40 ns) and large absorption oscillator strengths (f = 0.08 – 0.24). In the case of the coinage metal dimers, we have previously argued that ion pair states arising from the $M^+ + M'^-$ separated ion limit are found in this energy range as a result of the long-range attraction of the ions,[74-76,79] which, ignoring polarization effects, bond formation, and short-range repulsions, have potential energy curves given by

$$V(R) = D_e(M\text{-}M', X\ ^1\Sigma^+) + IE(M) - EA(M') - 116138\ cm^{-1}/R(Å). \qquad (6.12)$$

In the case of Au_2, *ab initio* calculations clearly identify the B 0_u^+ state (τ = 18 ns, f = 0.13)[76] as correlating diabatically to the $Au^+ + Au^-$ separated ion limit.[80] Further, transitions from the covalent ground state to these ion-pair states are charge transfer transitions that have large transition dipole moments. Thus, for the coinage metal dimers and by extension the group 6 dimers, ion pair states provide a source of considerable

oscillator strength that is shared with other states of the appropriate symmetry through state mixing via configuration interaction and spin-orbit interaction.

There is no reason why these ion-pair states should be limited to the coinage metal or group 6 dimers. In fact, this mechanism is expected to provide an important source of oscillator strength in the blue region of the spectrum for all of the transition metal diatomics, owing to the similarity of ionization energies and electron affinities for these species. In the case of TiFe, if we estimate the bond energy to be 3 eV and employ IE(Ti) = 6.828 eV[81] and EA(Fe) = 0.163 eV,[82] equation (12) predicts that the lowest ion pair states should lie in the vicinity of 20 000 cm^{-1} at R = 2.0 Å, quite close to the energy where intense transitions begin. The same mechanism has been invoked to explain the intense transitions in ZrFe that occur in a similar spectral region.[56]

6.4. Discussion and summary

Diatomic TiFe ($\Delta Z=4$) has been experimentally investigated for the first time, and is found to have a strongly bound $^1\Sigma^+$ ground state arising from a leading configuration of $1\sigma^2\ 2\sigma^2\ 1\pi^4\ 1\delta^4$, with $r_0 = 1.7024(3)$ Å. This is very similar to the nominally sextuply-bonded isoelectronic molecule, Cr_2, for which $r_0 = 1.6858$ Å.[8] These similar molecules may be contrasted with the isoelectronic molecule, ScCo ($\Delta Z=6$), which is generated from TiFe by shifting one proton from the Ti nucleus to the Fe nucleus. In ScCo, a $^1\Sigma^+$ ground state is also found, but the bond length is increased to 1.8121(10) Å,[83] indicating a significant change in the nature of the bonding. This is probably a move from a more covalent bonding mechanism to one with greater ionic character.

The $\Omega = 0^+$ and 1 levels of a $^3\Pi_i$ excited state arising from the $1\sigma^2\ 2\sigma^2\ 1\pi^4\ 1\delta^3\ 2\pi^1$ configuration have been identified in the experiments. Given the huge density of states

present in this molecule, it is remarkable that this state results from a nearly pure electronic configuration, as do the calculated states that arise from the $1\sigma^2\ 2\sigma^2\ 1\pi^4\ 1\delta^3\ 2\delta^1$ configuration. As might be expected when the antibonding 2π orbital is populated, there is a significant increase in bond length when moving from the ground state to this $^3\Pi$ state, which has $r_e \approx 1.885$ Å and $\omega_e \approx 346.9\ cm^{-1}$, averaged over the $\Omega = 0^+$ and 1 components.

Further to the blue (20 000-21 500 cm^{-1}) a congested region of the spectrum is found in which there is a large number of much more intense transitions. It is argued that ion-pair states corresponding to $Ti^+ + Fe^-$ provide the oscillator strength for transitions in this region, and that this oscillator strength is shared with other nearby states through state mixing induced by configuration interaction and spin-orbit mixing.

6.5 References

(1) Efremov, Y. M.; Samoilova, A. N.; Gurvich, L. V. *Opt. Spectrosc.* **1974**, *36*, 381.

(2) Kuendig, E. P.; Moskovits, M.; Ozin, G. A. *Nature (London)* **1975**, *254*, 503.

(3) Klotzbuecher, W. E.; Ozin, G. A. *J. Am. Chem. Soc.* **1978**, *100*, 2262.

(4) Pellin, M. J.; Gruen, D. M. *J. Chem. Phys.* **1983**, *79*, 5887.

(5) DiLella, D. P.; Limm, W.; Lipson, R. H.; Moskovits, M.; Taylor, K. V. *J. Chem. Phys.* **1982**, *77*, 5263.

(6) Moskovits, M.; Limm, W.; Mejean, T. *J. Phys. Chem.* **1985**, *89*, 3886.

(7) Moskovits, M.; Limm, W.; Mejean, T. *J. Chem. Phys.* **1985**, *82*, 4875.

(8) Bondybey, V. E.; English, J. H. *Chemical Physics Letters* **1982**, *94*, 443

(9) Riley, S. J.; Parks, E. K.; Pobo, L. G.; Wexler, S. *Journal of Chemical Physics* **1983**, *79*, 2577.

(10) Michalopoulos, D. L.; Geusic, M. E.; Hansen, S. G.; Powers, D. E.; Smalley, R. E. *Journal of Physical Chemistry* **1982**, *86*, 3914.

(11) Casey, S. M.; Villalta, P. W.; Bengali, A. A.; Cheng, C. L.; Dick, J. P.; Fenn, P. T.; Leopold, D. G. *J. Am. Chem. Soc.* **1991**, *113*, 6688.

(12) Goodgame, M. M.; Goddard, W. A., III. *Journal of Physical Chemistry* **1981**, *85*, 215.

(13) Goodgame, M. M.; Goddard, W. A., III. *Phys. Rev. Lett.* **1982**, *48*, 135.

(14) Atha, P. M.; Hillier, I. H. *Mol. Phys.* **1982**, *45*, 285.

(15) Bernholc, J.; Holzwarth, N. A. W. *Phys. Rev. Lett.* **1983**, *50*, 1451.

(16) Kok, R. A.; Hall, M. B. *Journal of Physical Chemistry* **1983**, *87*, 715.

(17) Walch, S. P.; Bauschlicher, C. W., Jr.; Roos, B. O.; Nelin, C. J. *Chem. Phys. Lett.* **1983**, *103*, 175.

(18) Delley, B.; Freeman, A. J.; Ellis, D. E. *Phys. Rev. Lett.* **1983**, *50*, 488.

(19) McLean, A. D.; Liu, B. *Chem. Phys. Lett.* **1983**, *101*, 144.

(20) Baykara, N. A.; McMaster, B. N.; Salahub, D. R. *Mol. Phys.* **1984**, *52*, 891.

(21) Delley, B. *Phys. Rev. Lett.* **1985**, *55*, 2090.

(22) Das, G. P.; Jaffe, R. L. *Chemical Physics Letters* **1984**, *109*, 206.

(23) Goodgame, M. M.; Goddard, W. A., III. *Phys. Rev. Lett.* **1985**, *54*, 661.

(24) Radzio, E.; Andzelem, J.; Salahub, D. R. *J. Comput. Chem.* **1985**, *6*, 533.

(25) Richman, K. W.; McCullough, E. A., Jr. *J. Chem. Phys.* **1987**, *87*, 5050.

(26) Miyoshi, E.; Sakai, Y. *J. Comput. Chem.* **1988**, *9*, 719.

(27) Scuseria, G. E.; Schaefer, H. F., III. *Chemical Physics Letters* **1990**, *174*, 501.

(28) Scuseria, G. E. *J. Chem. Phys.* **1991**, *94*, 442.

(29) Andersson, K.; Roos, B. O.; Malmqvist, P. A.; Widmark, P. O. *Chemical Physics Letters* **1994**, *230*, 391.

(30) Bauschlicher, C. W., Jr.; Partridge, H. *Chem. Phys. Lett.* **1994**, *231*, 277.

(31) Visscher, L.; DeRaedt, H.; Nieuwpoort, W. C. *Chemical Physics Letters* **1994**, *227*, 327.

(32) Andersson, K. *Chemical Physics Letters* **1995**, *237*, 212.

(33) Edgecombe, K. E.; Becke, A. D. *Chemical Physics Letters* **1995**, *244*, 427.

(34) Roos, B. O.; Andersson, K. *Chemical Physics Letters* **1995**, *245*, 215.

(35) Panas, I. *Molecular Physics* **1996**, *89*, 239.

(36) Stoll, H.; Werner, H.-J. *Molecular Physics* **1996**, *88*, 793.

(37) Dachsel, H.; Harrison, R. J.; Dixon, D. A. *Journal of Physical Chemistry A* **1999**, *103*, 152.

(38) Thomas, E. J.; Murray, J. S.; O'Connor, C. J.; Politzer, P. *J. Mol. Struct. THEOCHEM* **1999**, *487*, 177.

(39) Barden, C. J.; Rienstra-Kiracofe, J. C.; Schaefer, H. F., III. *J. Chem. Phys.* **2000**, *113*, 690.

(40) Yanagisawa, S.; Tsuneda, T.; Hirao, K. *Journal of Chemical Physics* **2000**, *112*, 545.

(41) Desmarais, N.; Reuse, F. A.; Khanna, S. N. *J. Chem. Phys.* **2000**, *112*, 5576.

(42) Boudreaux, E. A.; Baxter, E. *International Journal of Quantum Chemistry* **2001**, *85*, 509.

(43) Gutsev, G. L.; Bauschlicher, C. W. *Journal of Physical Chemistry A* **2003**, *107*, 4755.

(44) Valiev, M.; Bylaska, E. J.; Weare, J. H. *J. Chem. Phys.* **2003**, *119*, 5955.

(45) Boudreaux, E. A.; Baxter, E. *International Journal of Quantum Chemistry* **2004**, *100*, 1170.

(46) Celani, P.; Stoll, H.; Werner, H. J.; Knowles, P. J. *Molecular Physics* **2004**, *102*, 2369.

(47) Rajchel, L.; Zuchowski, P. S.; Klos, J.; Szczesniak, M. M.; Chalasinski, G. *J. Chem. Phys.* **2007**, *127*, 244302/1.

(48) Brynda, M.; Gagliardi, L.; Roos, B. O. *Chemical Physics Letters* **2009**, *471*, 1.

(49) Kitagawa, Y.; Nakanishi, Y.; Saito, T.; Kawakami, T.; Okumura, M.; Yamaguchi, K. *International Journal of Quantum Chemistry* **2009**, *109*, 3315.

(50) Mueller, T. *Journal of Physical Chemistry A* **2009**, *113*, 12729.

(51) Kurashige, Y.; Yanai, T. *J. Chem. Phys.* **2011**, *135*, 094104/1.

(52) Ruiperez, F.; Aquilante, F.; Ugalde, J. M.; Infante, I. *J. Chem. Theory Comput.* **2011**, *7*, 1640.

(53) Hongo, K.; Maezono, R. *International Journal of Quantum Chemistry* **2012**, *112*, 1243.

(54) Huber, K. P.; Herzberg, G. *Constants of Diatomic Molecules*; Van Nostrand Reinhold: New York, 1979; Vol. IV.

(55) Gutsev, G. L.; Mochena, M. D.; Jena, P.; Bauschlicher, C. W., Jr.; Partridge, H., III. *Journal of Chemical Physics* **2004**, *121*, 6785.

(56) Krechkivska, O.; Morse, M. D. *J. Phys. Chem. A* **accepted**.

(57) Wiley, W. C.; McLaren, I. H. *Review of Scientific Instruments* **1955**, *26*, 1150

(58) Gerstenkorn, S.; Luc, P. *Atlas du Spectre d'Absorption de la Molécule d'Iode entre 14,800-20,000 cm^{-1}*; CNRS: Paris, 1978.

(59) Morse, M. D. Supersonic beam sources. In *Methods of Experimental Physics: Atomic, Molecular, and Optical Physics*; Dunning, F. B., Hulet, R., Eds.; Academic Press, Inc.: Orlando, Florida, 1996; Vol. II Atoms and Molecules; pp 21.

(60) Gerstenkorn, S.; Luc, P. *Revue de Physique Appliquee* **1979**, *14*, 791.

(61) Bevington, P. R. *Data Reduction and Error Analysis for the Physical Sciences*; McGraw-Hill: New York, 1969.

(62) Lefebvre-Brion, H.; Field, R. W. *The Spectra and Dynamics of Diatomic Molecules*; Elsevier: Amsterdam, 2004.

(63) Simard, B.; Lebeault-Dorget, M.-A.; Marijnissen, A.; ter Meulen, J. J. *Journal of Chemical Physics* **1998**, *108*, 9668.

(64) Russon, L. M.; Heidecke, S. A.; Birke, M. K.; Conceicao, J.; Morse, M. D.; Armentrout, P. B. *Journal of Chemical Physics* **1994**, *100*, 4747.

(65) Arrington, C. A.; Blume, T.; Morse, M. D.; Doverstål, M.; Sassenberg, U. *Journal of Physical Chemistry* **1994**, *98*, 1398.

(66) Russon, L. M.; Heidecke, S. A.; Birke, M. K.; Conceicao, J.; Armentrout, P. B.; Morse, M. D. *Chemical Physics Letters* **1993**, *204*, 235.

(67) Behm, J. M.; Arrington, C. A.; Morse, M. D. *Journal of Chemical Physics* **1993**, *99*, 6409.

(68) Spain, E. M.; Morse, M. D. *Journal of Physical Chemistry* **1992**, *96*, 2479.

(69) Taylor, S.; Spain, E. M.; Morse, M. D. *Journal of Chemical Physics* **1990**, *92*, 2698.

(70) Herzberg, G. *Molecular Spectra and Molecular Structure I. Spectra of Diatomic Molecules*, 2nd ed.; Van Nostrand Reinhold: New York, 1950.

(71) Veseth, L. *Theor. Chim. Acta* **1970**, *18*, 368.

(72) Simons, J.; Nichols, J. *Quantum Mechanics in Chemistry*, 1997.

(73) Bondybey, V. E.; Schwartz, G. P.; English, J. H. *J. Chem. Phys.* **1983**, *78*, 11.

(74) Bishea, G. A.; Marak, N.; Morse, M. D. *Journal of Chemical Physics* **1991**, *95*, 5618.

(75) Bishea, G. A.; Pinegar, J. C.; Morse, M. D. *Journal of Chemical Physics* **1991**, *95*, 5630.

(76) Bishea, G. A.; Morse, M. D. *Journal of Chemical Physics* **1991**, *95*, 5646.

(77) Spain, E. M.; Behm, J. M.; Morse, M. D. *Chemical Physics Letters* **1991**, *179*, 411.

(78) Hopkins, J. B.; Langridge-Smith, P. R. R.; Morse, M. D.; Smalley, R. E. *Journal of Chemical Physics* **1983**, *78*, 1627.

(79) Morse, M. D. Chemical bonding in the late transition metals: The nickel and copper group dimers. In *Advances in Metal and Semiconductor Clusters*; Duncan, M. A., Ed.; JAI Press: Greenwich, Conn., 1993; Vol. 1; pp 83.

(80) Ermler, W. C.; Lee, Y. S.; Pitzer, K. S. *J. Chem. Phys.* **1979**, *70*, 293.

(81) Sohl, J. E.; Zhu, Y.; Knight, R. D. *Journal of the Optical Society of America B* **1990**, *7*, 9.

(82) Hotop, H.; Lineberger, W. C. *Journal of Physical and Chemical Reference Data* **1985**, *14*, 731.

(83) Nagarajan, R.; Morse, M. D. *Journal of Chemical Physics* **2007**, *127*, 074304/1.

APPENDIX A

ROTATIONALLY RESOLVED SPECTRA, TABULATED LINE POSITIONS AND FITTED PARAMETERS OF OsC

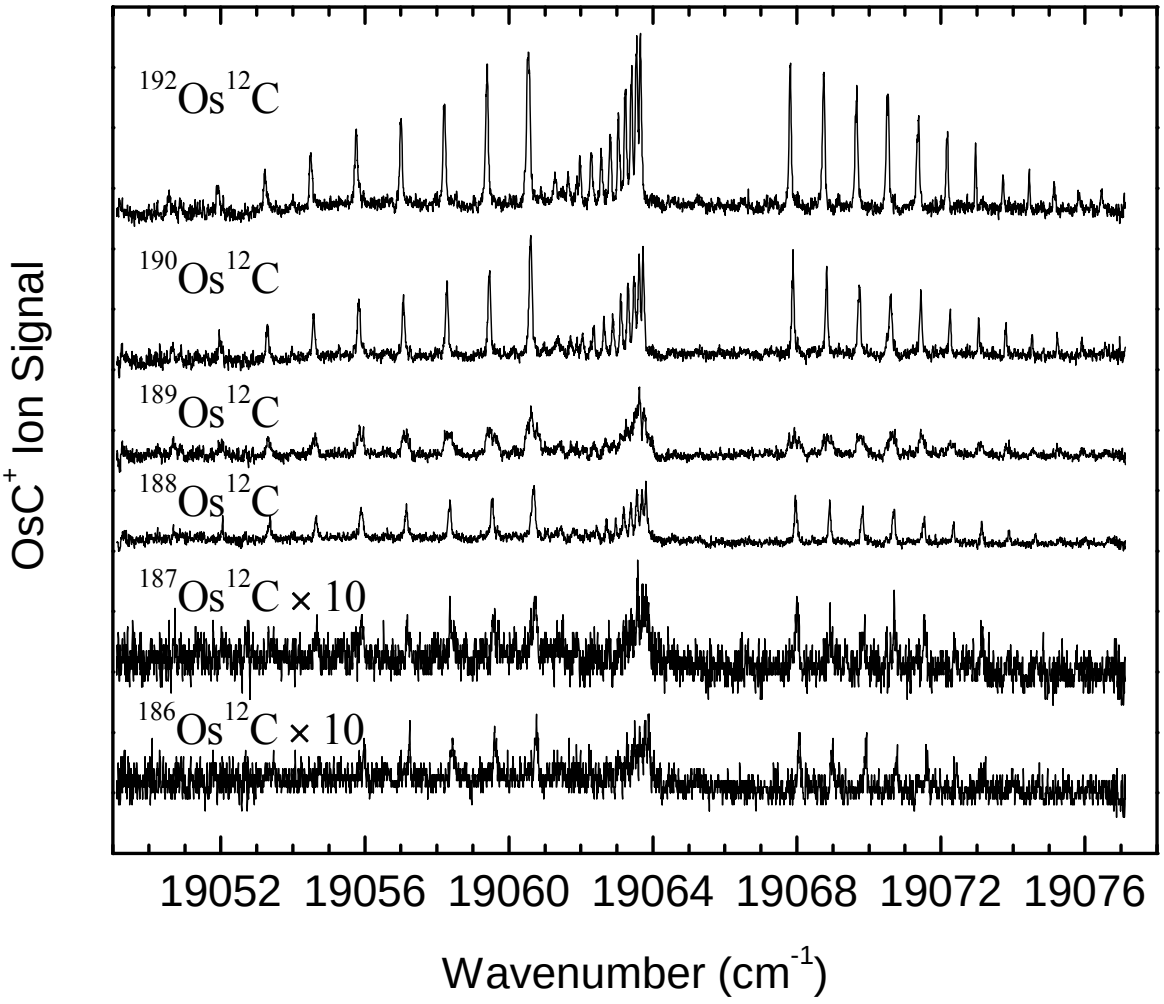

Figure A.1. Rotationally resolved spectra of the six OsC isotopomers for the 0-0 band of the [19.1]2 ← $X\,^3\Delta_3$ electronic band system

Table A.1

Line Positions for the 0-0 band of the [19.1]2 ← $X\,^3\Delta_3$ electronic band system of OsC [a]

Line	$^{186}Os^{12}C$	$^{187}Os^{12}C$	$^{188}Os^{12}C$	$^{189}Os^{12}C$	$^{190}Os^{12}C$	$^{192}Os^{12}C$
P(3)	19060.653(3)	19060.624(-16)	19060.577(2)	19060.568(-3)	19060.497(9)	19060.431(2)
P(4)	19059.505(-1)	19059.465(-10)	19059.425(2)	19059.412(-2)	19059.349(6)	19059.283(-1)
P(5)	19058.306(17)	19058.259(15)	19058.248(-2)	19058.222(4)	19058.172(4)	19058.099(4)
P(6)	19057.129(-14)	19057.068(-3)	19057.046(-7)	19057.019(-6)	19056.966(2)	19056.897(0)
P(7)	19055.873(7)	19055.833(-5)	19055.797(6)	19055.777(-5)	19055.731(2)	19055.655(7)
P(8)		19054.565(-2)	19054.537(2)	19054.512(-11)	19054.471(-2)	19054.392(7)
P(9)			19053.255(-8)	19053.208(-6)	19053.183(-4)	19053.114(-6)
P(10)			19051.928(0)		19051.852(7)	19051.791(-2)
P(11)						19050.449(-7)
Q(3)	19063.777(5)		19063.694(7)		19063.618(7)	19063.542(9)
Q(4)	19063.674(-2)	19063.611(8)	19063.585(4)		19063.513(0)	19063.436(2)
Q(5)	19063.530(4)	19063.470(9)	19063.447(3)		19063.375(-2)	19063.295(4)
Q(6)	19063.377(-10)		19063.284(-1)		19063.204(1)	19063.127(3)
Q(7)	19063.181(-8)		19063.084(4)		19063.004(5)	19062.935(0)
Q(8)			19062.862(3)		19062.779(7)	19062.710(1)
Q(9)			19062.608(6)		19062.535(-1)	19062.455(4)
Q(10)			19062.328(8)		19062.244(10)	19062.179(0)
Q(11)			19062.026(3)		19061.939(7)	19061.870(1)
Q(12)					19061.605(6)	19061.536(0)

Table A.1 continued

Q(13)						19061.176(-5)
R(3)	19067.955(-4)	19067.893(2)	19067.856(8)	19067.836(8)	19067.784(-1)	19067.707(-1)
R(4)	19068.878(3)	19068.809(15)	19068.802(-8)	19068.757(13)	19068.718(-8)	19068.635(-1)
R(5)	19069.805(-20)	19069.729(-4)	19069.704(-9)	19069.663(2)	19069.624(-14)	19069.540(-7)
R(6)	19070.656(5)	19070.595(3)	19070.580(-12)	19070.529(4)	19070.496(-15)	19070.413(-9)
R(7)	19071.497(13)	19071.453(-10)	19071.416(-3)	19071.369(2)	19071.333(-8)	19071.249(-2)
R(8)	19072.330(1)	19072.266(-6)	19072.239(-7)	19072.187(-6)	19072.144(-3)	19072.068(-6)
R(9)		19073.043(6)	19073.024(-3)	19072.970(-9)	19072.937(-8)	19072.853(-4)
R(10)			19073.785(-1)	19073.700(14)	19073.694(-5)	19073.617(-9)
R(11)			19074.516(2)		19074.421(-1)	19074.345(-6)
R(12)					19075.127(-3)	19075.036(6)
R(13)					19075.797(3)	19075.713(4)
R(14)						19076.354(11)
Fitted Spectroscopic Constants:						
v_0 (cm^{-1})	19063.9482(49)	19063.8985(45)	19063.8683(20)	19063.8573(36)	19063.7924(21)	19063.7184(16)
B' (cm^{-1})	0.520993(146)	0.520506(125)	0.520378(44)	0.519969(79)	0.519744(45)	0.519497(34)
r′ (Å)	1.69423(24)	1.69474(20)	1.69468(7)	1.69507(13)	1.69517(7)	1.69505(6)
B" (cm^{-1})	0.534821(98)	0.534502(96)	0.534313(42)	0.534360(62)	0.533730(43)	0.533492(33)
r″ (Å)	1.67218(15)	1.67241(15)	1.67243(7)	1.67209(97)	1.67282(7)	1.67267(5)

[a] Following each measured line position, the residual in the least-squares fit (fitted value - measured value) is provided in parentheses, in units of 0.001 cm^{-1}. In the list of fitted spectroscopic constants, 1σ error limits are provided in units of the last digits quoted in the specified parameter. Conversion of rotational constants to bond lengths has been performed without any corrections due to S-uncoupling or other heterogeneous perturbations.

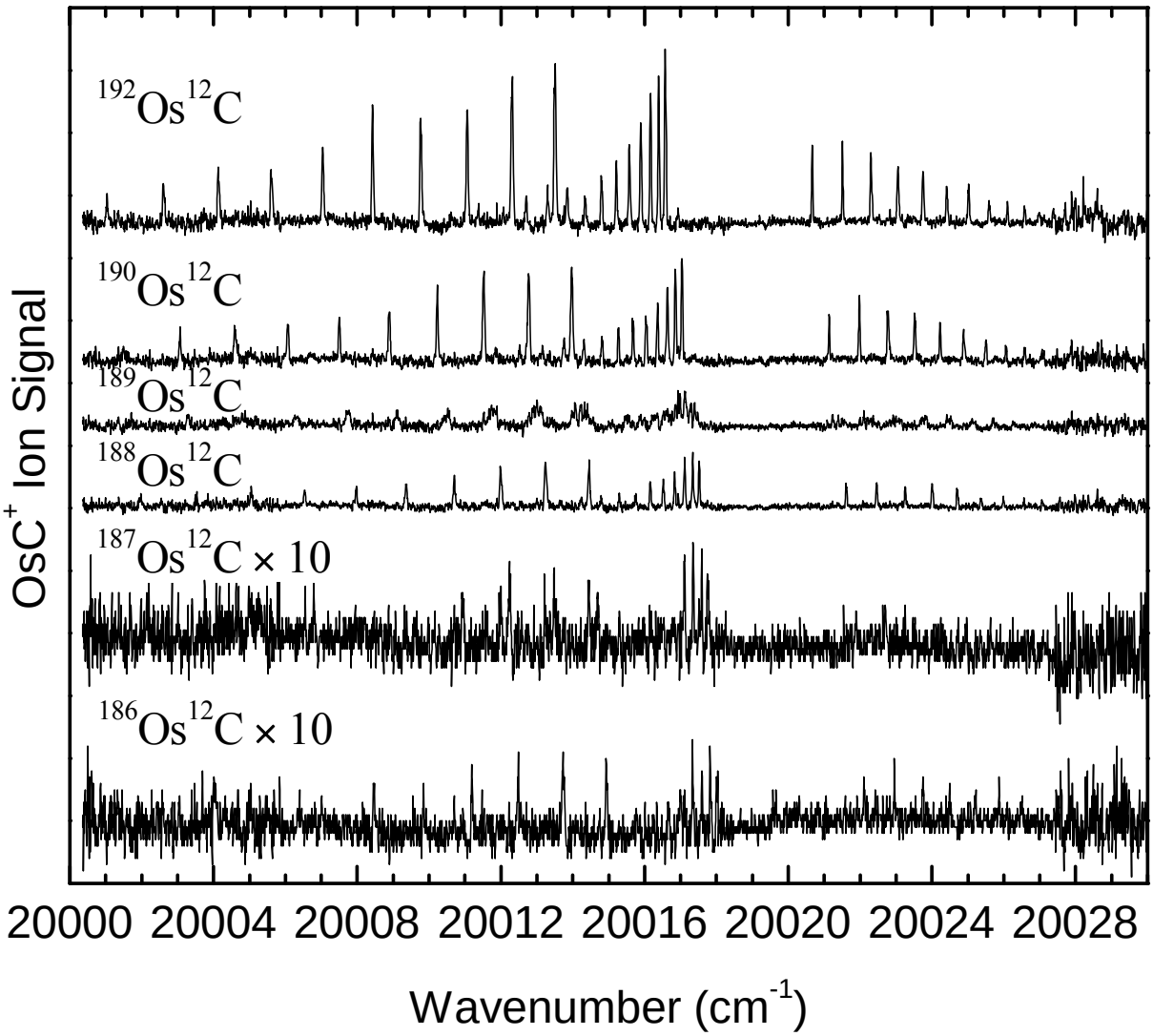

Figure A.2. Rotationally resolved spectra of the six OsC isotopomers 1-0 band of the [19.1]2 ← $X\,^3\Delta_3$ electronic band system.

Table A.2

Line Positions for the 1-0 band of the [19.1]2 ← $X\,^3\Delta_3$ electronic band system of OsC [a]

Line	$^{186}Os^{12}C$	$^{187}Os^{12}C$	$^{188}Os^{12}C$	$^{189}Os^{12}C$	$^{190}Os^{12}C$	$^{192}Os^{12}C$
P(3)	20014.824(-2)	20014.576(0)	20014.334(0)	20014.113(-3)	20013.854(8)	20013.392(8)
P(4)	20013.618(-2)	20013.372(2)	20013.129(1)	20012.893(10)	20012.656(1)	20012.193(2)
P(5)	20012.363(2)	20012.116(10)	20011.879(0)	20011.654(-3)	20011.403(5)	20010.944(2)
P(6)	20011.071(-3)	20010.826(8)	20010.582(2)	20010.356(-2)	20010.109(4)	20009.652(-1)
P(7)	20009.726(0)		20009.244(-3)	20008.994(17)	20008.772(1)	20008.310(0)
P(8)	20008.344(-6)		20007.855(0)	20007.609(12)	20007.387(0)	20006.922(2)
P(9)			20006.422(0)	20006.173(13)	20005.950(5)	20005.490(1)
P(10)			20004.939(6)		20004.481(-3)	20004.019(-5)
P(11)			20003.411(11)		20002.948(7)	20002.492(-2)
P(12)			20001.854(-1)			20000.918(3)
Q(3)	20017.897(-2)	20017.657(-7)	20017.403(1)		20016.922(5)	20016.459(4)
Q(4)	20017.706(7)	20017.473(-1)	20017.223(-1)		20016.738(7)	20016.275(6)
Q(5)	20017.479(7)	20017.237(11)	20016.998(-3)		20016.514(4)	20016.048(4)
Q(6)	20017.213(1)	20016.982(-1)	20016.718(4)		20016.245(-1)	20015.777(2)
Q(7)			20016.401(3)		20015.929(-3)	20015.454(5)
Q(8)			20016.041(-1)		20015.560(2)	20015.093(1)
Q(9)			20015.632(-1)		20015.156(-3)	20014.686(-3)
Q(10)			20015.176(1)		20014.699(-2)	20014.226(1)
Q(11)			20014.679(-3)		20014.194(2)	20013.725(0)

Table A.2 continued

Q(12)			20014.126(5)		20013.641(9)	20013.186(-9)
Q(13)					20013.046(13)	20012.586(-3)
Q(14)					20012.416(6)	
Q(15)					20011.739(0)	
R(3)	20021.997(-5)	20021.763(-15)	20021.495(2)	20021.278(-8)	20021.022(-7)	20020.548(1)
R(4)	20022.836(-2)	20022.591(2)	20022.341(-3)	20022.115(-5)	20021.860(-5)	20021.392(-4)
R(5)	20023.630(1)	20023.404(-9)	20023.135(-1)	20022.915(-12)	20022.658(-8)	20022.180(0)
R(6)	20024.383(0)	20024.151(0)	20023.889(-4)	20023.658(-7)	20023.403(-5)	20022.934(-6)
R(7)	20025.085(4)		20024.590(-1)	20024.359(-5)	20024.105(-3)	20023.634(-4)
R(8)	20025.752(-2)		20025.248(1)	20025.013(-2)	20024.767(-7)	20024.294(-8)
R(9)			20025.869(-7)	20025.627(-5)	20025.384(-12)	20024.900(-3)
R(10)			20026.443(-12)		20025.942(-3)	20025.472(-10)
R(11)			20026.948(6)		20026.467(-7)	20025.985(-4)
R(12)			20027.437(-5)		20026.944(-8)	20026.458(-4)
R(13)			20027.862(2)			20026.869(13)
R(14)						20027.260(4)
R(15)						20027.593(8)

Table A.2 continued

Fitted Spectroscopic Constants:						
v_0 (cm^{-1})	20018.1676(19)	20017.9177(52)	20017.6769(13)	20017.4527(48)	20017.2003(18)	20016.7373(15)
B' (cm^{-1})	0.512105(150)	0.512185(211)	0.511580(40)	0.511469(90)	0.510974(47)	0.510669(33)
r′ (Å)	1.70886(25)	1.70845(35)	1.70919(7)	1.70910(15)	1.70966(8)	1.70964(6)
B" (cm^{-1})	0.534821(98)	0.534502(96)	0.534313(42)	0.534360(62)	0.533730(43)	0.533492(33)
r″ (Å)	1.67218(15)	1.67241(15)	1.67243(7)	1.67209(97)	1.67282(7)	1.67267(5)

[a] Following each measured line position, the residual in the least-squares fit (fitted value - measured value) is provided in parentheses, in units of 0.001 cm^{-1}. In the list of fitted spectroscopic constants, 1σ error limits are provided in units of the last digits quoted in the specified parameter. Conversion of rotational constants to bond lengths has been performed without any corrections due to S-uncoupling or other heterogeneous perturbations.

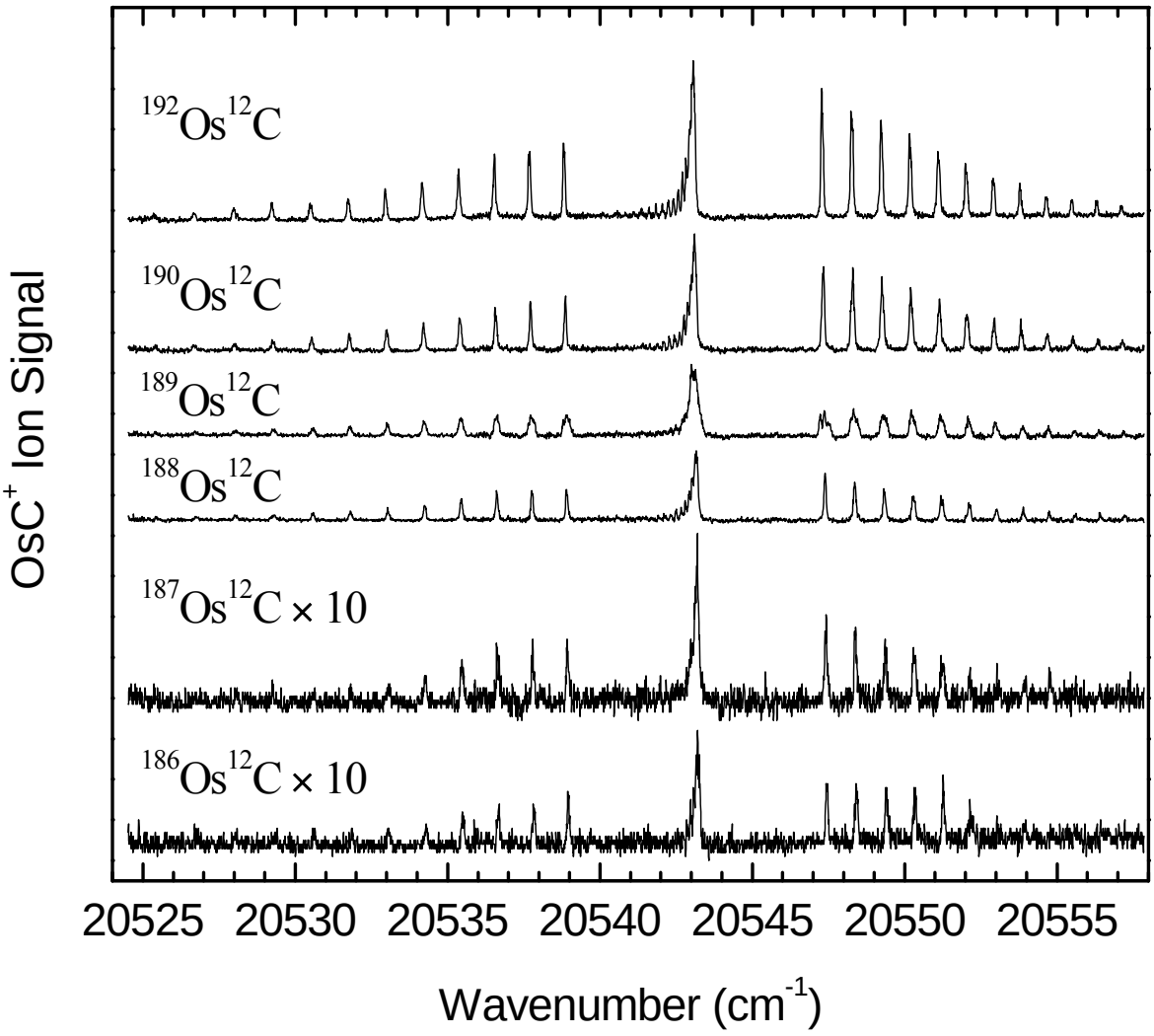

Figure A.3. Rotationally resolved spectra of the six OsC isotopomers 0-0 band of the [20.5]3 ← $X\,^3\Delta_3$ electronic band system.

Table A.3

Line Positions for the 0-0 band of the [20.5]3 ← $X\,^3\Delta_3$ electronic band system of OsC [a]

Line	$^{186}Os^{12}C$	$^{187}Os^{12}C$	$^{188}Os^{12}C$	$^{189}Os^{12}C$	$^{190}Os^{12}C$	$^{192}Os^{12}C$
P(4)	20538.841(4)	20538.815(1)	20538.794(-4)	20538.789(-5)	20538.744(-2)	20538.701(0)
P(5)	20537.706(-3)	20537.681(-3)	20537.647(6)	20537.643(1)	20537.605(0)	20537.567(-2)
P(6)	20536.542(2)	20536.529(-8)	20536.500(-3)	20536.488(-1)	20536.453(-3)	20536.415(-4)
P(7)	20535.378(-11)	20535.353(-6)	20535.327(-3)	20535.316(-4)	20535.289(-11)	20535.239(1)
P(8)	20534.172(0)	20534.146(9)	20534.134(0)	20534.118(1)	20534.088(2)	20534.045(6)
P(9)	20532.945(13)	20532.946(0)	20532.924(2)	20532.909(-1)	20532.886(-3)	20532.844(2)
P(10)	20531.729(-2)	20531.721(-1)	20531.693(8)	20531.683(-3)	20531.659(0)	20531.617(5)
P(11)	20530.478(0)	20530.480(-4)	20530.458(0)	20530.444(-10)	20530.424(-6)	20530.390(-9)
P(12)			20529.206(-7)	20529.175(-5)	20529.165(-5)	20529.113(10)
P(13)			20527.938(-16)		20527.883(1)	20527.853(-5)
P(14)			20526.636(-9)		20526.609(-18)	20526.564(-8)
P(15)			20525.323(-8)		20525.283(-3)	
Q(3)			20543.068(-3)			20542.963(7)
Q(4)	20543.044(7)		20543.008(-13)		20542.943(-1)	
Q(5)	20542.965(-3)		20542.916(-8)		20542.853(2)	20542.815(-2)
Q(6)	20542.856(-2)		20542.803(2)		20542.765(-14)	20542.705(3)
Q(7)	20542.729(-1)		20542.684(-2)		20542.638(-9)	20542.587(0)
Q(8)			20542.537(7)		20542.499(-9)	20542.448(0)

Table A.3 continued

Q(9)			20542.376(11)		20542.338(-5)	20542.292(0)
Q(10)			20542.208(6)		20542.161(-1)	20542.123(-5)
Q(11)			20542.016(6)		20541.975(-6)	20541.925(3)
Q(12)			20541.809(4)		20541.769(-8)	20541.718(1)
Q(13)					20541.527(8)	20541.494(-1)
Q(14)						20541.237(13)
Q(15)						20540.988(1)
R(3)	20547.323(7)	20547.294(5)	20547.268(2)	20547.269(-6)	20547.205(7)	20547.167(1)
R(4)	20548.307(3)	20548.273(7)	20548.244(8)	20548.238(5)	20548.182(10)	20548.151(-3)
R(5)	20549.286(-15)	20549.246(-2)	20549.219(-3)	20549.201(4)	20549.146(10)	20549.109(2)
R(6)	20550.216(0)	20550.195(-4)	20550.165(-2)	20550.146(4)	20550.085(16)	20550.059(-3)
R(7)	20551.145(-3)	20551.124(-4)	20551.094(-1)	20551.070(6)	20551.022(7)	20550.988(-4)
R(8)	20552.048(3)	20552.019(12)	20552.006(-2)	20551.983(2)	20551.930(11)	20551.896(-2)
R(9)		20552.927(-2)	20552.902(-2)	20552.874(3)	20552.825(9)	20552.792(-4)
R(10)		20553.803(-2)	20553.768(9)	20553.745(6)	20553.709(2)	20553.662(2)
R(11)		20554.659(2)	20554.625(11)	20554.601(6)	20554.566(4)	20554.524(-1)
R(12)			20555.479(0)	20555.447(-2)	20555.403(9)	20555.369(-5)
R(13)			20556.290(14)	20556.263(2)	20556.231(5)	20556.180(7)
R(14)			20557.123(-10)	20557.072(-4)	20557.038(5)	20557.000(-6)

Table A.3 continued

Fitted Spectroscopic Constants:						
v_0 (cm^{-1})	20543.2305(32)	20543.1977(27)	20543.1694(22)	20543.1654(19)	20543.1152(25)	20543.0736(15)
B' (cm^{-1})	0.525856(65)	0.525748(102)	0.525619(30)	0.525491(81)	0.525046(43)	0.524808(34)
r′ (Å)	1.68637(10)	1.68627(16)	1.68621(5)	1.68614(13)	1.68659(7)	1.68645(6)
B" (cm^{-1})	0.534821(98)	0.534502(96)	0.534313(42)	0.534360(62)	0.533730(43)	0.533492(33)
r″ (Å)	1.67218(15)	1.67241(15)	1.67243(7)	1.67209(97)	1.67282(7)	1.67267(5)

[a] Following each measured line position, the residual in the least-squares fit (fitted value - measured value) is provided in parentheses, in units of 0.001 cm^{-1}. In the list of fitted spectroscopic constants, 1σ error limits are provided in units of the last digits quoted in the specified parameter. Conversion of rotational constants to bond lengths has been performed without any corrections due to S-uncoupling or other heterogeneous perturbations.

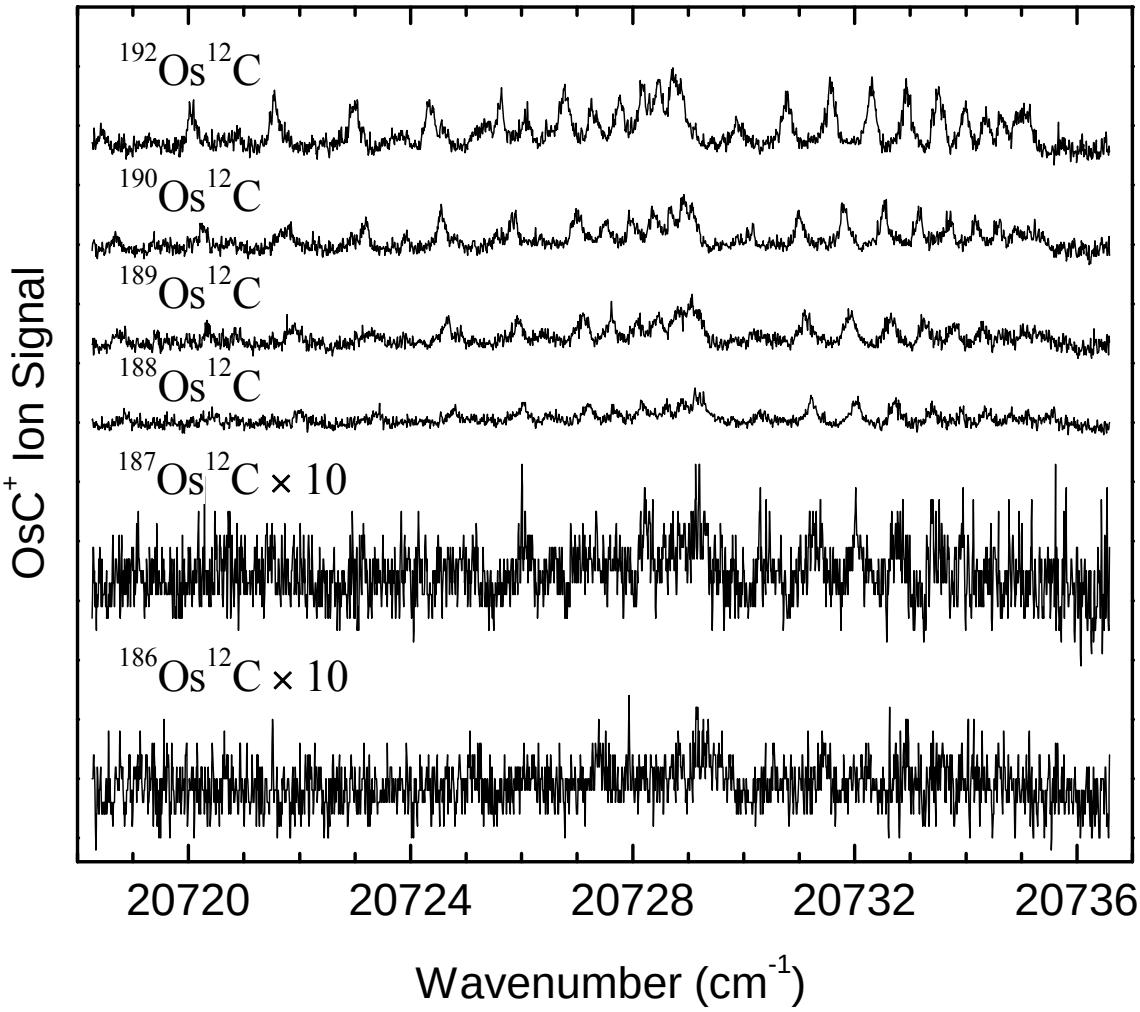

Figure A.4. Rotationally resolved spectra of the six OsC isotopomers 0-0 band of the [20.7]1←$A\,^3\Sigma^-(0^+)$ electronic band system.

Table A.4

Line Positions for the 0-0 band of the [21.2]2 ← $X\,^3\Delta_3$ electronic band system of OsC [a]

Line	$^{186}Os^{12}C$	$^{187}Os^{12}C$	$^{188}Os^{12}C$	$^{189}Os^{12}C$	$^{190}Os^{12}C$	$^{192}Os^{12}C$
P(3)	21280.706(-10)	21280.558(4)	21280.513(-5)	21280.419(0)	21280.322(-5)	21280.127(2)
P(4)	21279.355(8)	21279.228(-2)	21279.172(2)	21279.077(8)	21278.986(0)	21278.796(2)
P(5)	21277.943(-1)	21277.803(-1)	21277.757(-3)	21277.659(4)	21277.565(2)	21277.379(0)
P(6)	21276.438(-5)	21276.285(3)	21276.246(-2)	21276.157(-5)	21276.057(2)	21275.876(-4)
P(7)	21274.842(-6)		21274.652(-6)	21274.552(2)	21274.464(0)	21274.283(-6)
P(8)	21273.148(3)		21272.968(-7)	21272.864(3)	21272.780(0)	21272.595(-1)
P(9)			21271.169(18)	21271.088(4)	21271.016(-7)	21270.821(2)
P(10)			21269.308(17)	21269.227(1)	21269.145(4)	21268.975(-11)
P(11)				21267.275(1)	21267.199(2)	21267.017(1)
Q(3)	21283.639(3)	21283.509(-7)	21283.445(4)		21283.252(3)	21283.062(4)
Q(4)	21283.292(-1)	21283.140(7)	21283.094(3)		21282.899(5)	21282.713(1)
Q(5)	21282.849(2)	21282.704(-2)	21282.659(-3)		21282.464(-1)	21282.274(0)
Q(6)	21282.327(-3)	21282.173(-5)	21282.131(-4)		21281.934(1)	21281.749(-3)
Q(7)	21281.695(14)	21281.544(2)	21281.508(2)		21281.314(6)	21281.128(2)
Q(8)	21280.996(9)		21280.810(-5)		21280.621(-5)	21280.426(0)
Q(9)	21280.227(-13)		21280.017(-5)		21279.829(-5)	21279.634(0)
Q(11)			21278.170(-9)		21277.977(-1)	21277.786(0)
Q(12)					21276.913(7)	21276.732(-2)
Q(13)					21275.778(-2)	21275.582(4)

Table A.4 continued

R(3)	21287.372(-1)	21287.286(-5)	21287.176(-2)	21286.986(-4)	
R(4)	21287.997(2)	21287.911(-2)	21287.801(0)	21287.611(-2)	
R(5)	21288.535(4)	21288.453(-5)	21288.341(0)	21288.146(2)	
R(6)	21288.981(9)	21288.904(-6)	21288.794(-2)	21288.599(0)	
R(7)	21289.360(-7)	21289.260(0)	21289.147(8)	21288.952(9)	
R(8)	21289.633(-3)		21289.437(-7)	21289.233(3)	
R(9)	21289.818(-2)		21289.619(0)	21289.428(-5)	
R(10)	21289.912(3)		21289.718(-1)	21289.528(-5)	
R(13)				21289.286(5)	
R(14)				21289.030(8)	
R(15)				21288.688(9)	
R(16)				21288.270(-1)	
R(17)				21287.764(-13)	

Fitted Spectroscopic Constants**:**						
v_0 (cm^{-1})	21284.1693(41)	21284.0358(31)	21283.9781(27)	21283.8901(22)	21283.7837(13)	21283.5941(13)
B' (cm^{-1})	0.490873(66)	0.490039(203)	0.490239(35)	0.490194(131)	0.489729(47)	0.489490(31)
r′ (Å)	1.74543(12)	1.74663(36)	1.74599(6)	1.74580(23)	1.74635(8)	1.74624(6)
B" (cm^{-1})	0.534821(98)	0.534502(96)	0.534313(42)	0.534360(62)	0.533730(43)	0.533492(33)
r″ (Å)	1.67218(15)	1.67241(15)	1.67243(7)	1.67209(97)	1.67282(7)	1.67267(5)

[a] Following each measured line position, the residual in the least-squares fit (fitted value - measured value) is provided in parentheses, in units of 0.001 cm^{-1}. In the list of fitted spectroscopic constants, 1σ error limits are provided in units of the last digits quoted in the specified parameter. Conversion of rotational constants to bond lengths has been performed without any corrections due to S-uncoupling or other heterogeneous perturbations

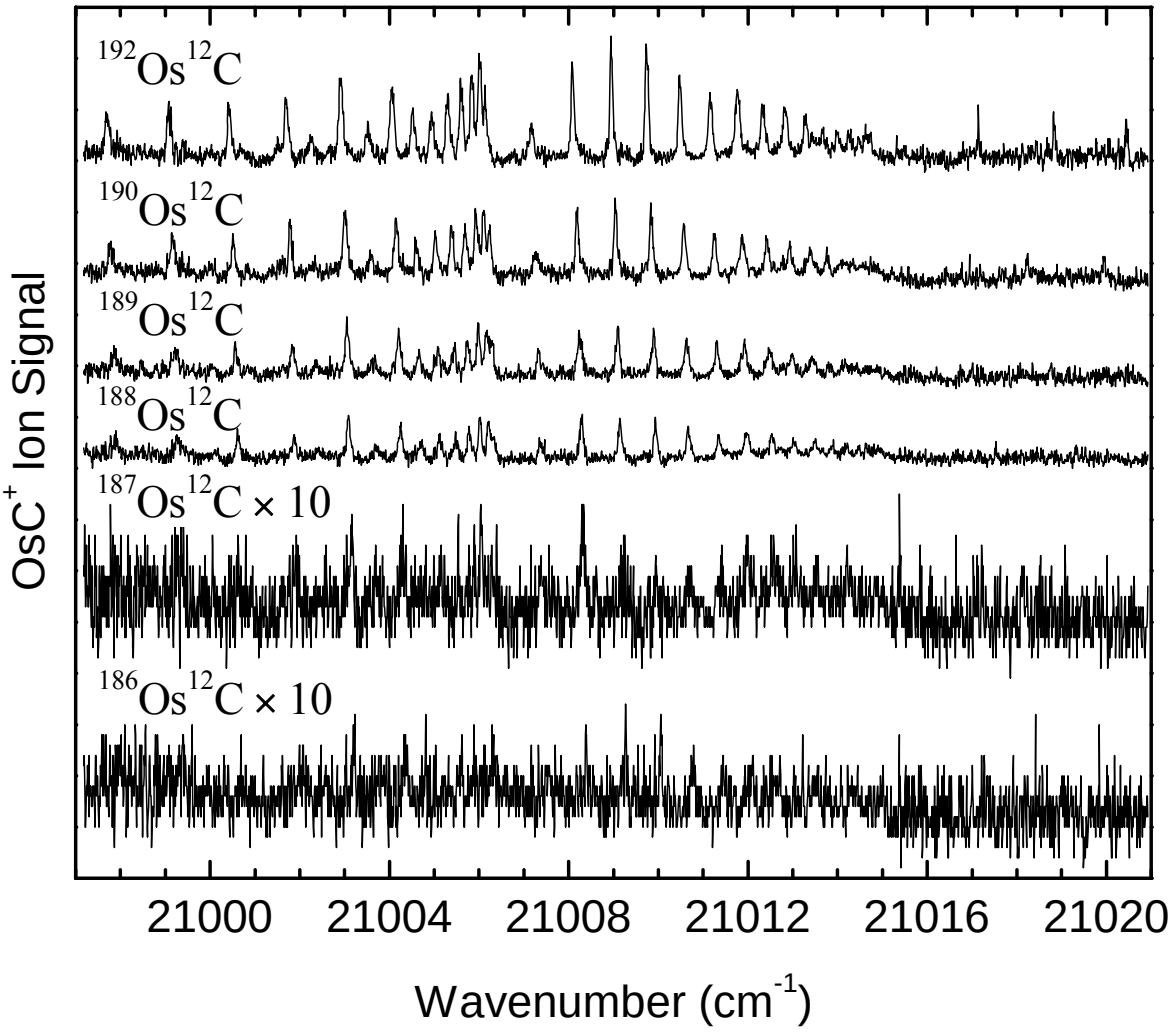

Figure A.5. Rotationally resolved spectra of the six OsC isotopomers 0-0 band of the [21.0]1←$A\,^3\Sigma^-(0^+)$ electronic band system.

Table A.5.

Line Positions for the 0-0 band of the [20.7]1←A $^3\Sigma^-(0^+)$ electronic band system of OsC[a]

Line	$^{188}Os^{12}C$	$^{189}Os^{12}C$	$^{190}Os^{12}C$	$^{192}Os^{12}C$
P(2)	20727.112(1)	20727.004(6)	20726.894(1)	20726.678(7)
P(3)	20725.926(-10)	20725.818(-5)	20725.700(-1)	20725.488(1)
P(4)	20724.653(-15)	20724.534(3)	20724.432(-7)	20724.214(-1)
P(5)	20723.282(-2)	20723.179(2)	20723.074(-4)	20722.850(6)
P(6)	20721.869(-28)	20721.751(-7)	20721.653(-17)	20721.420(0)
P(7)			20720.147(-25)	20719.909(-5)
Q(1)			20728.955(12)	20728.751(5)
Q(2)		20728.921(2)	20728.802(5)	20728.603(-8)
Q(3)	20728.789(-5)	20728.686(-2)	20728.569(0)	20728.349(6)
Q(4)	20728.462(0)	20728.356(8)	20728.252(-2)	20728.038(-4)
Q(5)	20728.059(0)	20727.972(-9)	20727.852(-1)	20727.640(-7)
Q(6)		20727.490(-8)	20727.390(-16)	20727.148(4)
Q(8)				20725.940(8)
Q(9)				20725.222(5)
R(0)	20730.208(15)		20730.004(-1)	20729.788(3)
R(1)	20731.096(2)	20731.002(-5)	20730.870(9)	20730.665(1)
R(2)	20731.885(8)	20731.792(1)	20731.665(10)	20731.464(-3)
R(3)	20732.589(19)	20732.510(0)	20732.386(7)	20732.178(-2)
R(4)	20733.240(2)	20733.144(2)	20733.028(3)	20732.814(-4)
R(5)	20733.793(2)	20733.695(7)	20733.583(5)	20733.367(-3)
R(6)	20734.260(8)	20734.173(5)	20734.067(-1)	20733.844(-6)
R(7)			20734.447(18)	20734.236(-4)
R(8)			20734.777(7)	20734.545(1)
Fitted Spectroscopic Constants**:**				
v_0 (cm^{-1})	20729.2670(53)	20729.1636(25)	20729.0462(35)	20728.8359(16)
B' (cm^{-1})	0.477964(286)	0.478249(136)	0.478086(193)	0.477612(84)
r′ (Å)	1.76827(53)	1.76746(25)	1.76749(36)	1.76782(16)
B" (cm^{-1})	0.518212(216)	0.518268(119)	0.517922(193)	0.517713(90)
r″ (Å)	1.69822(35)	1.69785(20)	1.69815(32)	1.69797(15)

[a] Following each measured line position, the residual in the least-squares fit (fitted value - measured value) is provided in parentheses, in units of 0.001 cm^{-1}. In the list of fitted spectroscopic constants, 1σ error limits are provided in units of the last digits quoted in

Table A.5 continued

the specified parameter. Conversion of rotational constants to bond lengths has been performed without any corrections due to S-uncoupling or other heterogeneous perturbations

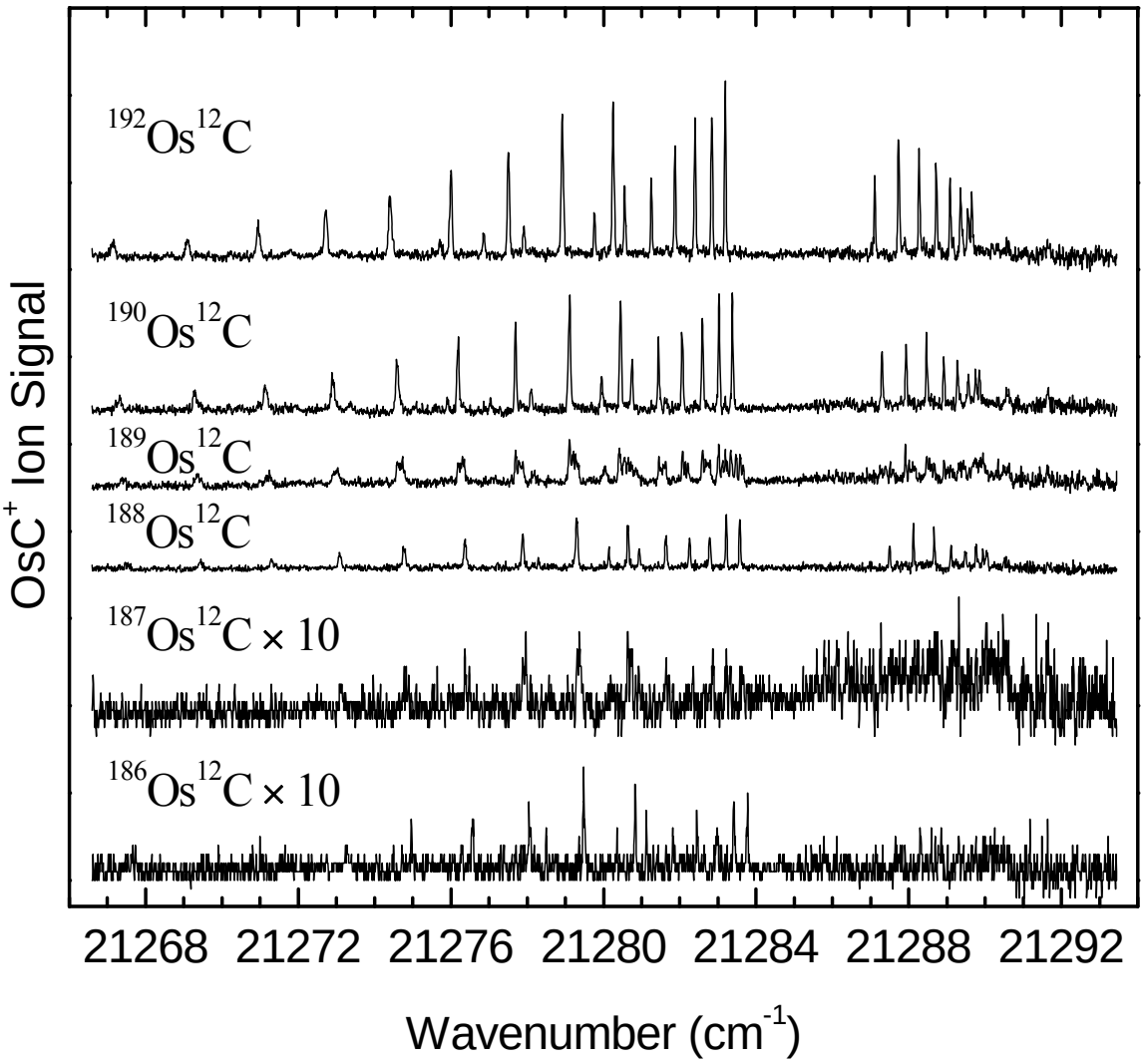

Figure A.6. Rotationally resolved spectra of the six OsC isotopomers 0-0 band of the [21.3]2←$X\,^3\Delta_3$ electronic band system.

Table A.6

Line Positions for the 0-0 band of the [21.0]1←A $^3\Sigma^-(0^+)$ electronic band system of OsC [a]

Line	$^{188}Os^{12}C$	$^{189}Os^{12}C$	$^{190}Os^{12}C$	$^{192}Os^{12}C$
P(2)	21004.127(-3)	21004.087(3)	21004.027(3)	21003.933(10)
P(3)	21002.963(6)	21002.930(4)	21002.879(-4)	21002.791(-3)
P(4)	21001.748(7)	21001.717(1)	21001.662(-1)	21001.582(-8)
P(5)	21000.482(-1)	21000.435(7)	21000.384(3)	21000.303(-3)
P(6)	20999.135(12)	20999.108(-1)	20999.038(16)	20998.967(0)
P(7)	20997.746(8)	20997.713(-1)	20997.640(20)	20997.583(-9)
Q(1)	21006.192(5)	21006.160(3)	21006.109(-7)	21006.007(7)
Q(2)	21006.091(-13)	21006.053(-9)	21005.981(2)	21005.892(2)
Q(3)	21005.901(-1)	21005.859(5)	21005.808(-4)	21005.716(0)
Q(4)	21005.654(8)	21005.622(3)	21005.561(5)	21005.486(-9)
Q(5)	21005.358(8)	21005.332(-6)	21005.266(3)	21005.178(2)
Q(6)	21004.998(11)	21004.968(-1)	21004.903(8)	21004.820(1)
Q(7)	21004.582(11)	21004.541(8)	21004.481(14)	21004.401(4)
Q(8)				21003.933(-6)
Q(9)	21003.580(3)		21003.470(12)	21003.395(-4)
Q(10)				21002.791(4)
Q(11)				21002.134(6)
R(0)	21007.242(-8)	21007.207(-7)	21007.146(-8)	21007.044(5)
R(1)	21008.165(-14)	21008.116(0)	21008.064(-9)	21007.962(3)
R(2)	21009.021(-12)	21008.978(-4)	21008.924(-13)	21008.827(-5)
R(3)	21009.811(-3)	21009.775(-4)	21009.714(-5)	21009.622(-3)
R(4)	21010.544(4)	21010.509(0)	21010.447(1)	21010.354(2)
R(5)	21011.228(-1)	21011.180(7)	21011.131(-5)	21011.039(-4)
R(6)	21011.860(-12)	21011.807(-2)	21011.754(-8)	21011.643(9)
R(7)	21012.416(-7)	21012.366(-3)	21012.307(-2)	21012.209(2)
R(8)	21012.906(5)	21012.865(-3)	21012.805(0)	21012.703(7)
R(9)	21013.365(-12)		21013.254(-9)	21013.153(-4)
R(10)	21013.739(-2)		21013.639(-13)	21013.535(-6)
R(11)				21013.848(1)
R(12)				21014.109(1)

Table A.6 Continued

Fitted Spectroscopic Constants:				
v_0 (cm^{-1})	21006.2566(25)	21006.2229(17)	21006.1614(27)	21006.0734(14)
B' (cm^{-1})	0.488509(227)	0.488382(116)	0.488155(182)	0.487908(77)
r′ (Å)	1.74908(41)	1.74903(21)	1.74916(33)	1.74906(14)
B" (cm^{-1})	0.518212(216)	0.518268(119)	0.517922(193)	0.517713(90)
r″ (Å)	1.69822(35)	1.69785(20)	1.69815(32)	1.69797(15)

[a] Following each measured line position, the residual in the least-squares fit (fitted value - measured value) is provided in parentheses, in units of 0.001 cm^{-1}. In the list of fitted spectroscopic constants, 1σ error limits are provided in units of the last digits quoted in the specified parameter. Conversion of rotational constants to bond lengths has been performed without any corrections due to S-uncoupling or other heterogeneous perturbations

APPENDIX B

ROTATIONALLY RESOLVED AND SIMULATED SPECTRA, TABULATED LINE POSITIONS AND FITTED PARAMETERS OF TaC

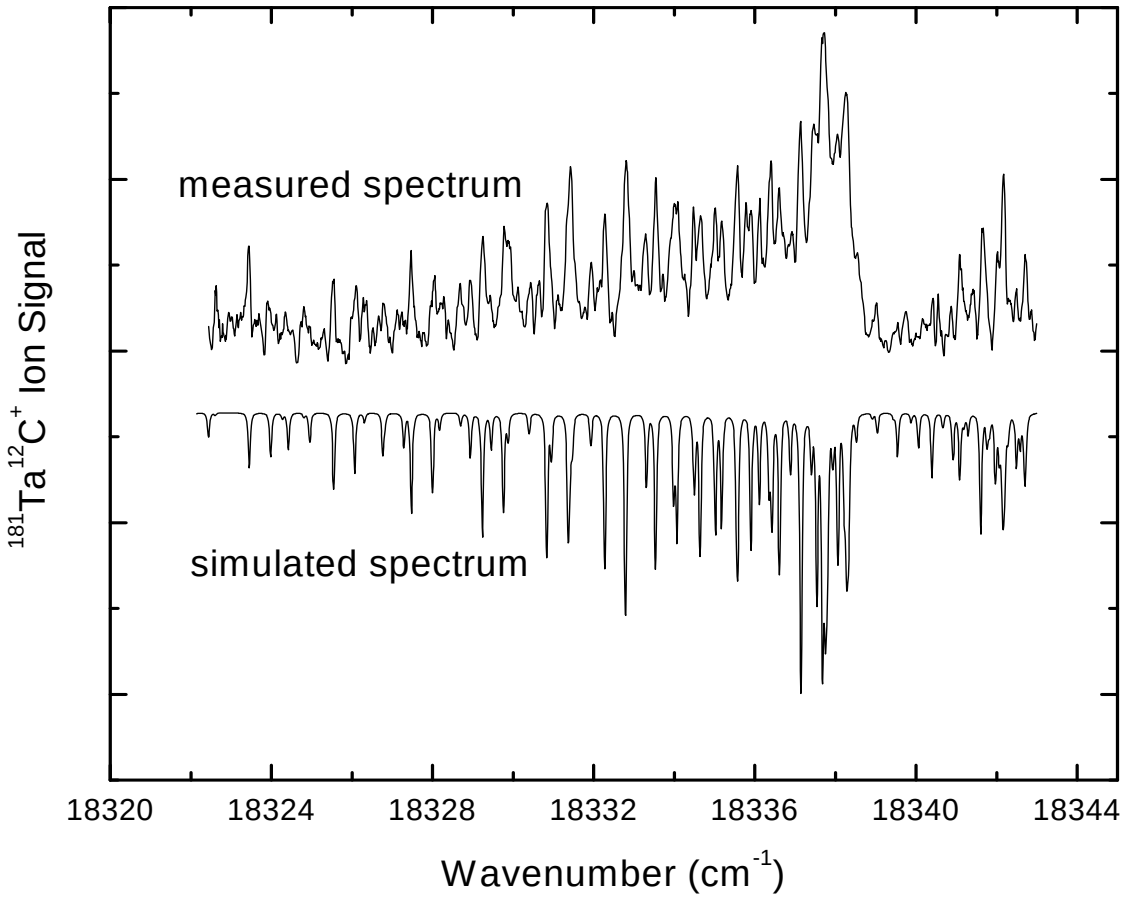

Figure B.1. Rotationally resolved spectra of the [18.34] $^2\Pi_{1/2} \leftarrow {}^2\Sigma^+_{1/2}$ transition of TaC

Table B.1

Line positions for the [18.34] $^2\Pi_{1/2} \leftarrow {}^2\Sigma^+_{1/2}$ transition of TaC.[a]

Rotational line[b]	Observed line	Rotational line	Observed line
$^{O}P_{13}(2)$	18335.003(9)	$^{P}P_{13}(8)+^{P}Q_{13}(8)$	18328.043(44)
$^{O}P_{14}(2)$	18334.471(1)	$^{P}P_{14}(8)+^{P}Q_{14}(8)$	18327.464(-11)
$^{O}P_{13}(3)$	18333.280(-34)	$^{P}P_{13}(9)+^{P}Q_{13}(9)$	18326.100(30)
$^{O}P_{14}(4)$	18330.910(-35)	$^{P}P_{14}(9)+^{P}Q_{14}(9)$	18325.537(-9)
$^{O}P_{13}(5)$	18329.432(-27)	$^{P}P_{13}(10)+^{P}Q_{13}(10)$	18323.925(-52)
$^{O}P_{14}(5)$	18328.942(7)	$^{P}P_{14}(10)+^{P}Q_{14}(10)$	18323.440(-13)
$^{O}P_{13}(6)$	18327.229(-55)	$^{Q}R_{14}(6)+^{Q}Q_{14}(6)$	18336.602(-8)
$^{O}P_{14}(6)$	18326.786(26)	$^{Q}R_{14}(7)+^{Q}Q_{14}(7)$	18335.900(0)
$^{P}P_{13}(1)+^{P}Q_{13}(1)$	18336.924(44)	$^{Q}R_{13}(8)+^{Q}Q_{13}(8)$	18335.552(3)
$^{P}P_{14}(1)+^{P}Q_{14}(1)$	18336.366(10)	$^{Q}R_{13}(9)+^{Q}Q_{13}(9)$	18334.468(-41)
$^{P}P_{13}(2)+^{P}Q_{13}(2)$	18336.120(14)	$^{Q}R_{14}(9)+^{Q}Q_{14}(9)$	18334.014(30)
$^{P}P_{14}(2)+^{P}Q_{14}(2)$	18335.581(-1)	$^{Q}R_{13}(11)+^{Q}Q_{13}(11)$	18331.941(8)
$^{P}P_{13}(3)+^{P}Q_{13}(3)$	18335.178(11)	$^{Q}R_{13}(12)+^{Q}Q_{13}(12)$	18330.423(25)
$^{P}P_{14}(3)+^{P}Q_{14}(3)$	18334.650(7)	$^{Q}R_{14}(12)+^{Q}Q_{14}(12)$	18329.887(13)
$^{P}P_{13}(4)+^{P}Q_{13}(4)$	18334.087(23)	$^{Q}R_{13}(13)+^{Q}Q_{13}(13)$	18328.683(-15)
$^{P}P_{14}(4)+^{P}Q_{14}(4)$	18333.546(7)	$^{R}R_{14}(0)$	18338.545(24)
$^{P}P_{13}(5)+^{P}Q_{13}(5)$	18332.808(13)	$^{R}R_{13}(0)$	18339.015(-31)
$^{P}P_{14}(5)+^{P}Q_{14}(5)$	18332.278(7)	$^{R}R_{14}(1)$	18339.548(6)
$^{P}P_{13}(6)+^{P}Q_{13}(6)$	18331.379(18)	$^{R}R_{14}(2)$	18340.416(19)
$^{P}P_{14}(6)+^{P}Q_{14}(6)$	18330.838(1)	$^{R}R_{13}(2)$	18340.871(-51)
$^{P}P_{13}(7)+^{P}Q_{13}(7)$	18329.790(27)	$^{R}R_{14}(3)$	18341.085(-3)
$^{P}P_{14}(7)+^{P}Q_{14}(7)$	18329.246(8)	$^{R}R_{13}(3)$	18341.625(13)

[a] All numerical values are given in wave numbers (cm^{-1}). Residuals in the fit are given in parentheses in units of $0.001 cm^{-1}$.

[b] Branches are labeled using a modified version of the more commonly occurring $^2\Pi(a) - {}^2\Sigma^+(b_{\beta J})$ branch labeling scheme. In the modified scheme, the $^2\Pi(a) - {}^2\Sigma^+(b_{\beta J})$ branch labels, specified by $^{\Delta N}\Delta J_{Fi' Fi''}(N'')$, are changed so that the F_i'' label is replaced by the value of G″. Thus, for this $^2\Pi_{1/2} - {}^2\Sigma^+(b_{\beta S})$ system, the eight hyperbranches are $^{O}P_{1G''}$, $^{P}P_{1G''} + {}^{P}Q_{1G''}$, $^{Q}Q_{1G''} + {}^{Q}R_{1G''}$, and $^{R}R_{1G''}$, where G″=3, 4.

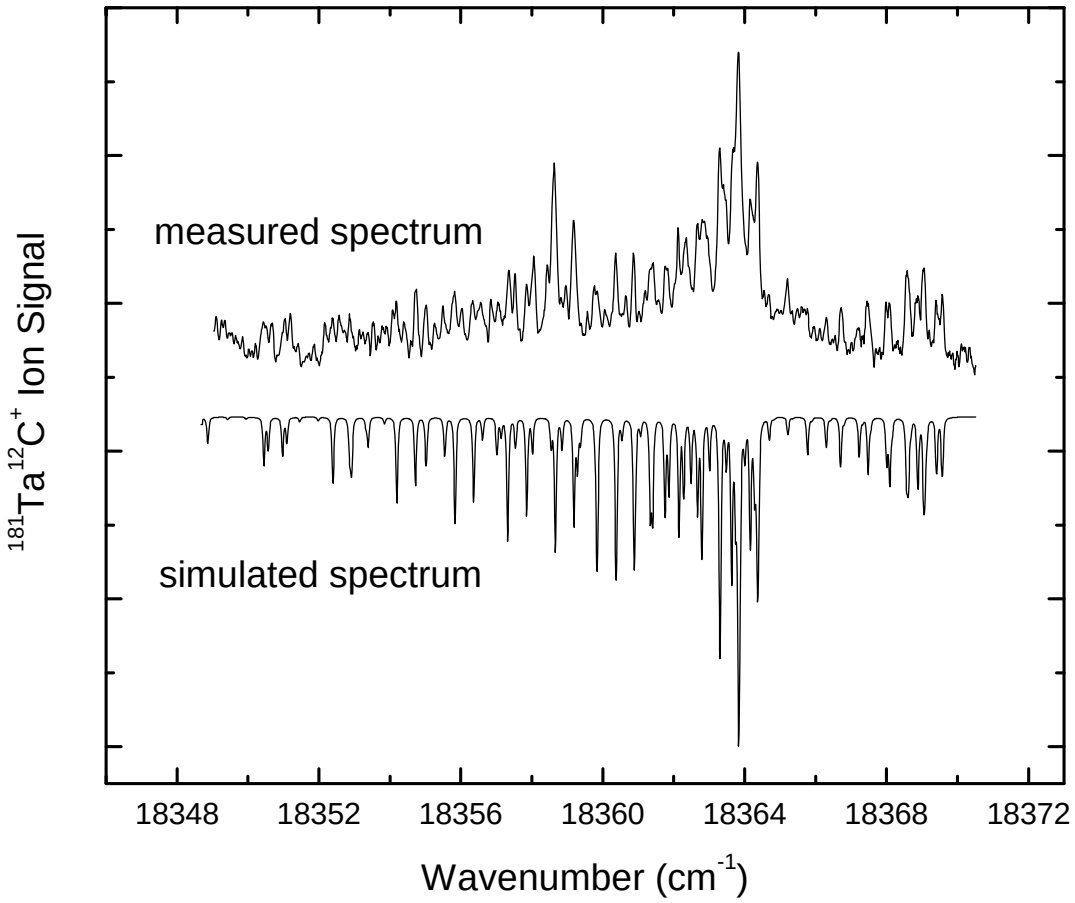

Figure B.2. Rotationally resolved spectra of the [18.36] $^2\Pi_{1/2} \leftarrow {}^2\Sigma^+_{1/2}$ transition of TaC.

Table B.2

Line positions for the [18.36] $^2\Pi_{1/2} \leftarrow {}^2\Sigma^+_{1/2}$ transition of TaC.[a]

Rotational line[b]	Observed line	Rotational line	Observed line
$^{O}P_{13}(4)$	18357.531(0)	$^{Q}R_{13}(7)+{}^{Q}Q_{13}(7)$	18362.673(12)
$^{O}P_{14}(4)$	18357.053(46)	$^{Q}R_{14}(7)+{}^{Q}Q_{14}(7)$	18362.122(-15)
$^{O}P_{13}(5)$	18355.499(-34)	$^{Q}R_{13}(8)+{}^{Q}Q_{13}(8)$	18361.837(-19)
$^{O}P_{14}(5)$	18355.013(5)	$^{R}R_{14}(0)$	18364.672(-27)
$^{P}P_{13}(1)+{}^{P}Q_{13}(1)$	18363.022(10)	$^{R}R_{13}(0)$	18365.206(-17)
$^{P}P_{14}(2)+{}^{P}Q_{14}(2)$	18361.765(5)	$^{R}R_{14}(1)$	18365.762(-16)
$^{P}P_{13}(3)+{}^{P}Q_{13}(3)$	18361.413(10)	$^{R}R_{13}(1)$	18366.306(4)
$^{P}P_{14}(3)+{}^{P}Q_{14}(3)$	18360.872(-7)	$^{R}R_{14}(2)$	18366.715(12)
$^{P}P_{13}(4)+{}^{P}Q_{13}(4)$	18360.362(-7)	$^{R}R_{13}(2)$	18367.202(-25)
$^{P}P_{14}(4)+{}^{P}Q_{14}(4)$	18359.844(-1)	$^{R}R_{14}(3)$	18367.460(-15)
$^{P}P_{13}(5)+{}^{P}Q_{13}(5)$	18359.180(-2)	$^{R}R_{13}(3)$	18367.992(-7)
$^{P}P_{14}(5)+{}^{P}Q_{14}(5)$	18358.629(-29)	$^{R}R_{14}(4)$	18368.083(-11)
$^{P}P_{13}(6)+{}^{P}Q_{13}(6)$	18357.855(14)	$^{R}R_{13}(5)$	18369.061(-22)
$^{P}P_{14}(6)+{}^{P}Q_{14}(6)$	18357.354(37)	$^{R}R_{14}(6)$	18368.861(-10)
$^{P}P_{13}(7)+{}^{P}Q_{13}(7)$	18356.331(-16)	$^{R}R_{13}(6)$	18369.396(1)
$^{P}P_{14}(7)+{}^{P}Q_{14}(7)$	18355.811(-12)	$^{R}R_{13}(7)$	18369.571(17)
$^{P}P_{13}(8)+{}^{P}Q_{13}(8)$	18354.731(31)	$^{R}R_{13}(8)$	18369.571(12)
$^{P}P_{14}(8)+{}^{P}Q_{14}(8)$	18354.181(6)		

[a] All numerical values are given in wave numbers (cm^{-1}). Residuals in the fit are given in parentheses in units of $0.001 cm^{-1}$.

[b] Branches are labeled using a modified version of the more commonly occurring $^2\Pi(a) - {}^2\Sigma^+(b_{\beta J})$ branch labeling scheme. In the modified scheme, the $^2\Pi(a) - {}^2\Sigma^+(b_{\beta J})$ branch labels, specified by $^{\Delta N}\Delta J_{Fi' Fi''}(N'')$, are changed so that the F_i'' label is replaced by the value of G''. Thus, for this $^2\Pi_{1/2} - {}^2\Sigma^+(b_{\beta S})$ system, the eight hyperbranches are $^{O}P_{1G''}$, $^{P}P_{1G''} + {}^{P}Q_{1G''}$, $^{Q}Q_{1G''} + {}^{Q}R_{1G''}$, and $^{R}R_{1G''}$, where $G''=3, 4$.

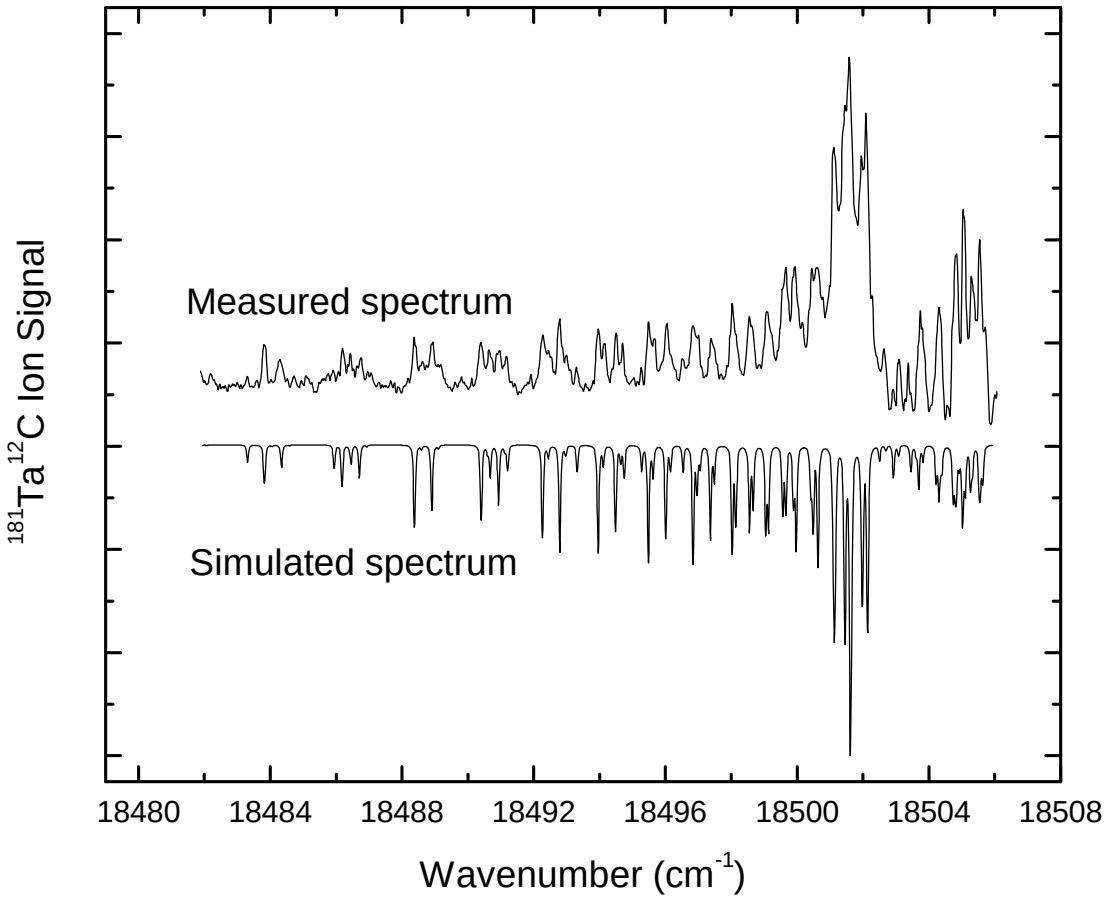

Figure B.3. Rotationally resolved spectra of the [18.50] $^2\Pi_{1/2} \leftarrow {}^2\Sigma^+_{1/2}$ transition of TaC.

Table B.3

Line positions for the [18.50] $^2\Pi_{1/2} \leftarrow {}^2\Sigma^+_{1/2}$ transition of TaC.[a]

Rotational line[b]	Observed line	Rotational line	Observed line
$^{O}P_{14}(3)$	18496.523(-12)	$^{P}P_{13}(8)+^{P}Q_{13}(8)$	18490.958(22)
$^{O}P_{13}(4)$	18495.266(-12)	$^{P}P_{14}(8)+^{P}Q_{14}(8)$	18490.396(-15)
$^{O}P_{13}(5)$	18493.290(-38)	$^{P}P_{13}(9)+^{P}Q_{13}(9)$	18488.895(-14)
$^{O}P_{14}(6)$	18490.706(20)	$^{P}P_{14}(9)+^{P}Q_{14}(9)$	18488.369(-16)
$^{O}P_{13}(8)$	18486.434(-37)	$^{P}P_{13}(10)+^{P}Q_{13}(10)$	18486.753(39)
$^{O}P_{14}(8)$	18485.911(-35)	$^{P}P_{14}(10)+^{P}Q_{14}(10)$	18486.195(5)
$^{O}P_{14}(9)$	18483.305(-19)	$^{P}P_{13}(11)+^{P}Q_{13}(11)$	18484.289(-62)
$^{P}P_{14}(1)+^{P}Q_{14}(1)$	18499.870(-22)	$^{P}P_{14}(11)+^{P}Q_{14}(11)$	18483.825(-2)
$^{P}P_{13}(2)+^{P}Q_{13}(2)$	18499.556(-10)	$^{Q}R_{13}(11)+^{Q}Q_{13}(11)$	18496.152(-20)
$^{P}P_{14}(2)+^{P}Q_{14}(2)$	18499.086(44)	$^{Q}R_{14}(11)+^{Q}Q_{14}(11)$	18495.671(23)
$^{P}P_{13}(3)+^{P}Q_{13}(3)$	18498.550(2)	$^{Q}R_{13}(12)+^{Q}Q_{13}(12)$	18494.699(30)
$^{P}P_{14}(3)+^{P}Q_{14}(3)$	18498.029(5)	$^{Q}R_{14}(12)+^{Q}Q_{14}(12)$	18494.148(4)
$^{P}P_{13}(4)+^{P}Q_{13}(4)$	18497.383(21)	$^{Q}R_{13}(13)+^{Q}Q_{13}(13)$	18492.987(-11)
$^{P}P_{14}(4)+^{P}Q_{14}(4)$	18496.841(4)	$^{Q}R_{14}(13)+^{Q}Q_{14}(13)$	18492.451(-22)
$^{P}P_{13}(5)+^{P}Q_{13}(5)$	18496.042(35)	$^{Q}R_{13}(14)+^{Q}Q_{13}(14)$	18491.175(17)
$^{P}P_{14}(5)+^{P}Q_{14}(5)$	18495.491(8)	$^{Q}R_{14}(14)+^{Q}Q_{14}(14)$	18490.641(7)
$^{P}P_{13}(6)+^{P}Q_{13}(6)$	18494.503(18)	$^{Q}R_{13}(15)+^{Q}Q_{13}(15)$	18489.172(21)
$^{P}P_{14}(6)+^{P}Q_{14}(6)$	18493.966(5)	$^{Q}R_{14}(15)+^{Q}Q_{14}(15)$	18488.623(-4)
$^{P}P_{13}(7)+^{P}Q_{13}(7)$	18492.787(-7)	$^{Q}R_{13}(16)+^{Q}Q_{13}(16)$	18486.960(-15)
$^{P}P_{14}(7)+^{P}Q_{14}(7)$	18492.278(8)		

[a] All numerical values are given in wave numbers (cm^{-1}). Residuals in the fit are given in parentheses in units of $0.001 cm^{-1}$.

[b] Branches are labeled using a modified version of the more commonly occurring $^2\Pi(a) - {}^2\Sigma^+(b_{\beta J})$ branch labeling scheme. In the modified scheme, the $^2\Pi(a) - {}^2\Sigma^+(b_{\beta J})$ branch labels, specified by $^{\Delta N}\Delta J_{Fi' Fi''}(N'')$, are changed so that the F_i'' label is replaced by the value of G″. Thus, for this $^2\Pi_{1/2} - {}^2\Sigma^+(b_{\beta S})$ system, the eight hyperbranches are $^{O}P_{1G''}$, $^{P}P_{1G''} + {}^{P}Q_{1G''}$, $^{Q}Q_{1G''} + {}^{Q}R_{1G''}$, and $^{R}R_{1G''}$, where G″=3, 4.

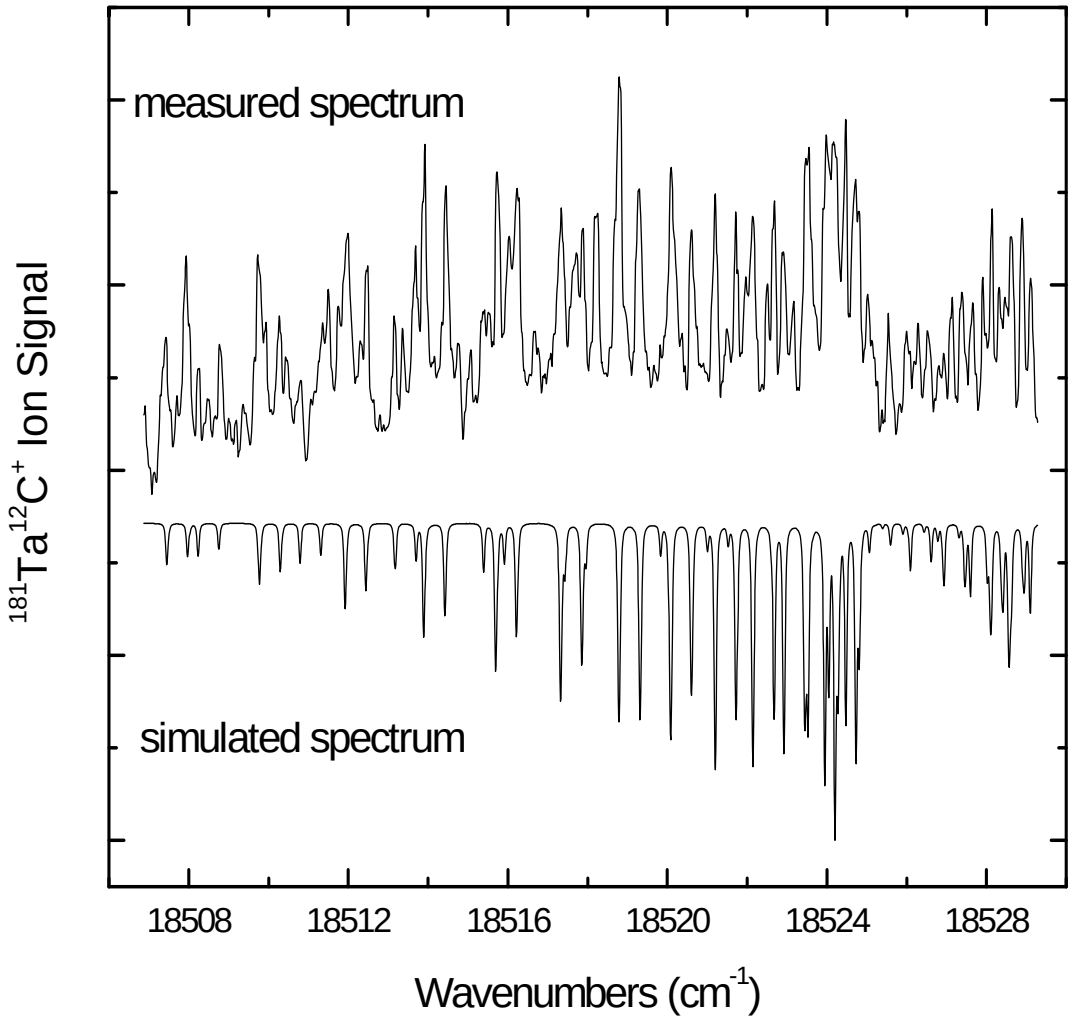

Figure B.4. Rotationally resolved spectra of the [18.52] $^{2}\Pi_{1/2} \leftarrow {}^{2}\Sigma^{+}_{1/2}$ transition of TaC.

Table B.4

Line positions for the [18.52] $^2\Pi_{1/2} \leftarrow {}^2\Sigma^+_{1/2}$ transition of TaC.[a]

Rotational line[b]	Observed line	Rotational line	Observed line
$^{O}P_{14}(5)$	18515.394(3)	$^{P}P_{13}(8)+^{P}Q_{13}(8)$	18514.444(30)
$^{O}P_{13}(6)$	18513.681(-20)	$^{P}P_{14}(8)+^{P}Q_{14}(8)$	18513.912(22)
$^{O}P_{14}(6)$	18513.159(-18)	$^{P}P_{13}(9)+^{P}Q_{13}(9)$	18512.463(23)
$^{O}P_{13}(7)$	18511.356(41)	$^{P}P_{14}(9)+^{P}Q_{14}(9)$	18511.972(57)
$^{O}P_{14}(7)$	18510.797(6)	$^{P}P_{13}(10)+^{P}Q_{13}(10)$	18510.263(-31)
$^{O}P_{13}(8)$	18508.789(31)	$^{P}P_{14}(10)+^{P}Q_{14}(10)$	18509.747(-23)
$^{O}P_{14}(8)$	18508.245(11)	$^{P}P_{13}(11)+^{P}Q_{13}(11)$	18507.931(-46)
$^{P}P_{13}(2)+^{P}Q_{13}(2)$	18522.685(25)	$^{P}P_{14}(11)+^{P}Q_{14}(11)$	18507.416(-36)
$^{P}P_{14}(2)+^{P}Q_{14}(2)$	18522.144(9)	$^{R}R_{14}(0)$	18525.026(-49)
$^{P}P_{13}(3)+^{P}Q_{13}(3)$	18521.717(3)	$^{R}R_{13}(0)$	18525.540(-59)
$^{P}P_{14}(3)+^{P}Q_{14}(3)$	18521.200(10)	$^{R}R_{14}(1)$	18526.017(-72)
$^{P}P_{13}(4)+^{P}Q_{13}(4)$	18520.601(4)	$^{R}R_{13}(1)$	18526.542(-71)
$^{P}P_{14}(4)+^{P}Q_{14}(4)$	18520.097(24)	$^{R}R_{14}(2)$	18526.932(1)
$^{P}P_{13}(6)+^{P}Q_{13}(6)$	18517.878(29)	$^{R}R_{13}(2)$	18527.388(-67)
$^{P}P_{14}(6)+^{P}Q_{14}(6)$	18517.343(19)	$^{R}R_{14}(3)$	18527.655(53)
$^{P}P_{13}(7)+^{P}Q_{13}(7)$	18516.245(28)		
$^{P}P_{14}(7)+^{P}Q_{14}(7)$	18515.732(39)		

[a] All numerical values are given in wave numbers (cm^{-1}). Residuals in the fit are given in parentheses in units of $0.001 cm^{-1}$.

[b] Branches are labeled using a modified version of the more commonly occurring $^2\Pi(a) - {}^2\Sigma^+(b_{\beta J})$ branch labeling scheme. In the modified scheme, the $^2\Pi(a) - {}^2\Sigma^+(b_{\beta J})$ branch labels, specified by $^{\Delta N}\Delta J_{Fi' Fi''}(N'')$, are changed so that the F_i'' label is replaced by the value of G''. Thus, for this $^2\Pi_{1/2} - {}^2\Sigma^+(b_{\beta S})$ system, the eight hyperbranches are $^{O}P_{1G''}$, $^{P}P_{1G''} + {}^{P}Q_{1G''}$, $^{Q}Q_{1G''} + {}^{Q}R_{1G''}$, and $^{R}R_{1G''}$, where G''=3, 4.

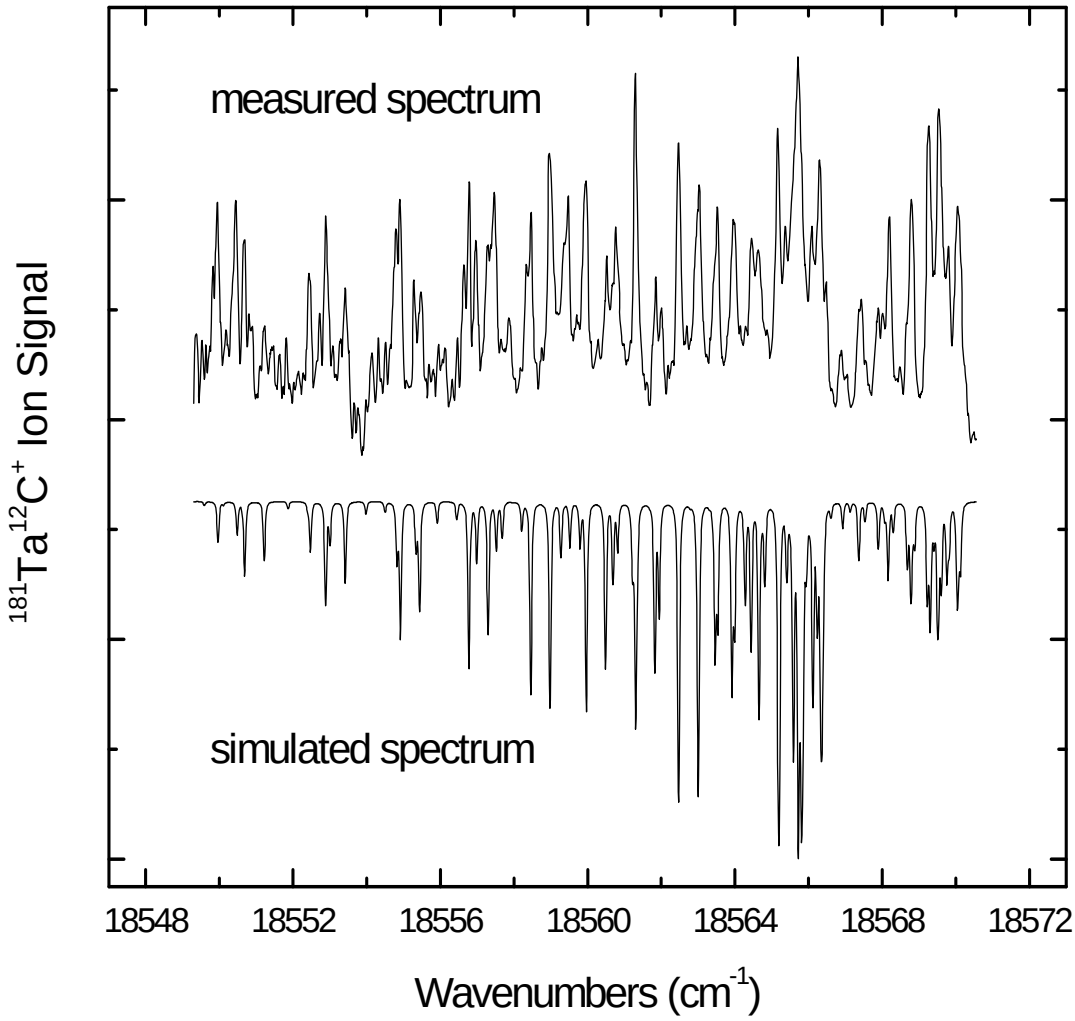

Figure B.5. Rotationally resolved spectra of the [18.56] $^2\Pi_{1/2} \leftarrow {}^2\Sigma^+_{1/2}$ transition of TaC.

Table B.5.

Line positions for the [18.56] $^2\Pi_{1/2} \leftarrow {}^2\Sigma^+_{1/2}$ transition of TaC.[a]

Rotational line[b]	Observed line	Rotational line	Observed line
$^{O}P_{14}(3)$	18560.764(-55)	$^{P}P_{13}(8)+^{P}Q_{13}(8)$	18555.474(32)
$^{O}P_{13}(4)$	18559.469(-47)	$^{P}P_{14}(8)+^{P}Q_{14}(8)$	18554.906(-12)
$^{O}P_{13}(5)$	18557.464(-52)	$^{P}P_{13}(9)+^{P}Q_{13}(9)$	18553.416(3)
$^{O}P_{14}(5)$	18556.959(-32)	$^{P}P_{14}(9)+^{P}Q_{14}(9)$	18552.896(7)
$^{O}P_{13}(6)$	18555.284(-59)	$^{P}P_{13}(10)+^{P}Q_{13}(10)$	18551.215(2)
$^{O}P_{14}(6)$	18554.796(-23)	$^{P}P_{14}(10)+^{P}Q_{14}(10)$	18550.672(-17)
$^{O}P_{14}(7)$	18552.443(-31)	$^{P}P_{13}(11)+^{P}Q_{13}(11)$	18548.829(-11)
$^{O}P_{13}(8)$	18550.445(-36)	$^{P}P_{14}(11)+^{P}Q_{14}(11)$	18548.270(-45)
$^{O}P_{14}(8)$	18549.940(-17)	$^{Q}R_{13}(7)+^{Q}Q_{13}(7)$	18564.455(9)
$^{O}P_{14}(9)$	18547.331(64)	$^{Q}R_{14}(7)+^{Q}Q_{14}(7)$	18563.921(-1)
$^{P}P_{13}(1)+^{P}Q_{13}(1)$	18564.871(59)	$^{Q}R_{13}(13)+^{Q}Q_{13}(13)$	18556.467(24)
$^{P}P_{14}(1)+^{P}Q_{14}(1)$	18564.294(6)	$^{Q}R_{14}(13)+^{Q}Q_{14}(13)$	18555.953(34)
$^{P}P_{13}(2)+^{P}Q_{13}(2)$	18563.989(-2)	$^{Q}R_{13}(14)+^{Q}Q_{13}(14)$	18554.515(9)
$^{P}P_{14}(2)+^{P}Q_{14}(2)$	18563.522(55)	$^{Q}R_{14}(15)+^{Q}Q_{14}(15)$	18551.818(-54)
$^{P}P_{13}(4)+^{P}Q_{13}(4)$	18561.854(23)	$^{R}R_{14}(0)$	18566.476(70)
$^{P}P_{14}(4)+^{P}Q_{14}(4)$	18561.296(-11)	$^{R}R_{13}(0)$	18566.892(-38)
$^{P}P_{13}(5)+^{P}Q_{13}(5)$	18560.523(31)	$^{R}R_{14}(1)$	18567.427(56)
$^{P}P_{14}(5)+^{P}Q_{14}(5)$	18559.966(-2)	$^{R}R_{13}(1)$	18567.900(4)
$^{P}P_{13}(6)+^{P}Q_{13}(6)$	18559.014(33)	$^{R}R_{14}(2)$	18568.192(27)
$^{P}P_{14}(6)+^{P}Q_{14}(6)$	18558.461(4)	$^{R}R_{13}(2)$	18568.732(43)
$^{P}P_{13}(7)+^{P}Q_{13}(7)$	18557.289(-9)	$^{R}R_{14}(3)$	18568.798(13)
$^{P}P_{14}(7)+^{P}Q_{14}(7)$	18556.786(13)	$^{R}R_{14}(4)$	18569.235(1)

[a] All numerical values are given in wave numbers (cm^{-1}). Residuals in the fit are given in parentheses in units of $0.001 cm^{-1}$.

[b] Branches are labeled using a modified version of the more commonly occurring $^2\Pi(a) - {}^2\Sigma^+(b_{\beta J})$ branch labeling scheme. In the modified scheme, the $^2\Pi(a) - {}^2\Sigma^+(b_{\beta J})$ branch labels, specified by $^{\Delta N}\Delta J_{Fi' Fi''}(N'')$, are changed so that the F_i'' label is replaced by the value of G″. Thus, for this $^2\Pi_{1/2} - {}^2\Sigma^+(b_{\beta S})$ system, the eight hyperbranches are $^{O}P_{1G''}$, $^{P}P_{1G''} + {}^{P}Q_{1G''}$, $^{Q}Q_{1G''} + {}^{Q}R_{1G''}$, and $^{R}R_{1G''}$, where G″=3, 4.

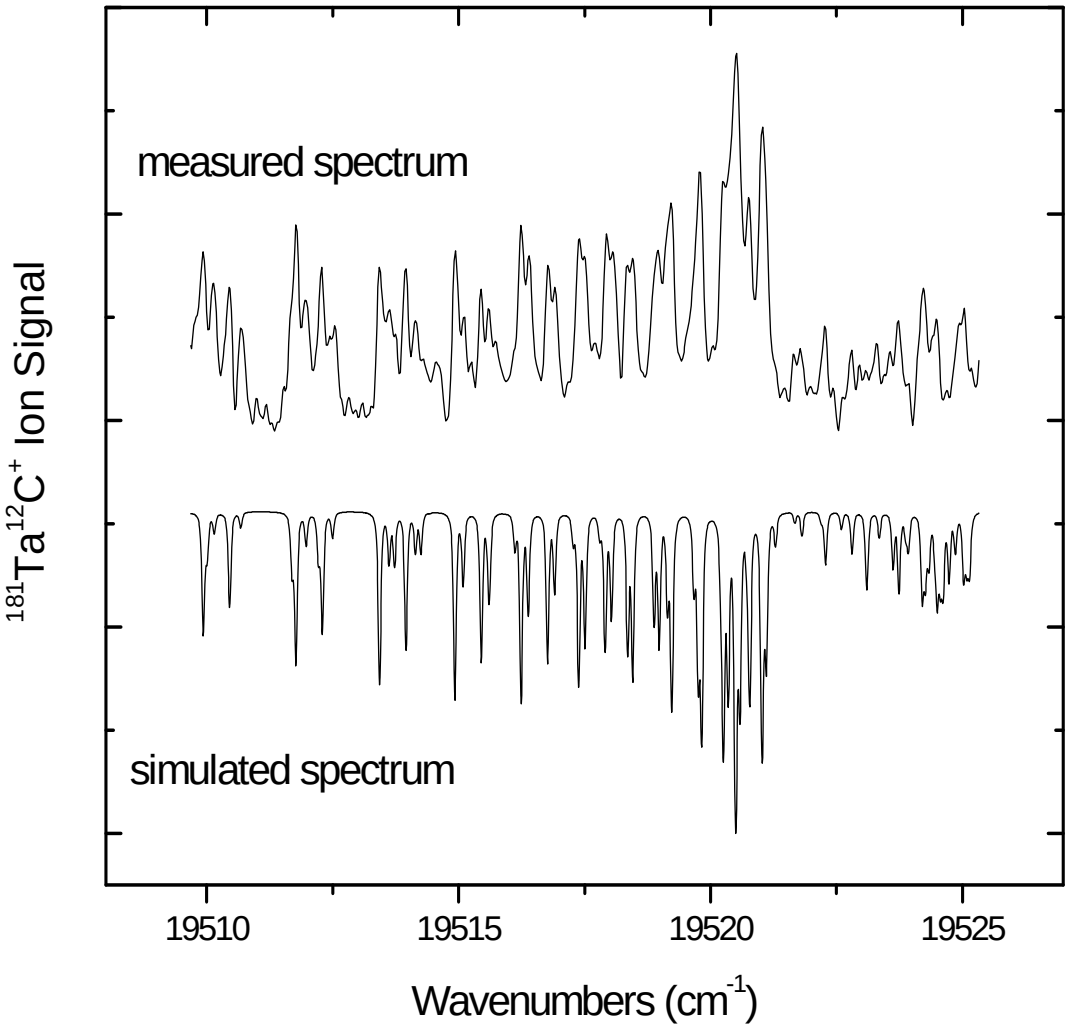

Figure B.6. Rotationally resolved spectra of the [19.52] $^2\Pi_{1/2} \leftarrow {}^2\Sigma^+_{1/2}$ transition of TaC

Table B.6

Line positions for the [19.52] $^2\Pi_{1/2} \leftarrow {}^2\Sigma^+_{1/2}$ transition of TaC.[a]

Rotational line[b]	Observed line	Rotational line	Observed line
$^{O}P_{13}(4)$	19514.294(45)	$^{Q}R_{13}(7)+{}^{Q}Q_{13}(7)$	19518.951(-29)
$^{O}P_{14}(4)$	19513.758(33)	$^{Q}R_{14}(7)+{}^{Q}Q_{14}(7)$	19518.461(5)
$^{O}P_{14}(5)$	19511.649(-40)	$^{Q}R_{13}(8)+{}^{Q}Q_{13}(8)$	19518.061(29)
$^{P}P_{13}(1)+{}^{P}Q_{13}(1)$	19519.652(-20)	$^{Q}R_{14}(8)+{}^{Q}Q_{14}(8)$	19517.500(-8)
$^{P}P_{14}(1)+{}^{P}Q_{14}(1)$	19519.137(-10)	$^{Q}R_{13}(9)+{}^{Q}Q_{13}(9)$	19516.911(2)
$^{P}P_{13}(2)+{}^{P}Q_{13}(2)$	19518.877(0)	$^{Q}R_{14}(9)+{}^{Q}Q_{14}(9)$	19516.400(15)
$^{P}P_{14}(2)+{}^{P}Q_{14}(2)$	19518.353(0)	$^{Q}R_{14}(10)+{}^{Q}Q_{14}(10)$	19515.107(19)
$^{P}P_{13}(3)+{}^{P}Q_{13}(3)$	19517.941(33)	$^{Q}R_{13}(11)+{}^{Q}Q_{13}(11)$	19514.153(12)
$^{P}P_{14}(3)+{}^{P}Q_{14}(3)$	19517.392(8)	$^{Q}R_{14}(11)+{}^{Q}Q_{14}(11)$	19513.645(28)
$^{P}P_{13}(4)+{}^{P}Q_{13}(4)$	19516.784(19)	$^{Q}R_{13}(12)+{}^{Q}Q_{13}(12)$	19512.467(-29)
$^{P}P_{14}(4)+{}^{P}Q_{14}(4)$	19516.239(-2)	$^{Q}R_{14}(12)+{}^{Q}Q_{14}(12)$	19511.959(-13)
$^{P}P_{13}(5)+{}^{P}Q_{13}(5)$	19515.445(-2)	$^{Q}R_{13}(13)+{}^{Q}Q_{13}(13)$	19510.698(22)
$^{P}P_{14}(5)+{}^{P}Q_{14}(5)$	19514.934(11)	$^{Q}R_{14}(13)+{}^{Q}Q_{14}(13)$	19510.131(-21)
$^{P}P_{13}(6)+{}^{P}Q_{13}(6)$	19513.948(-8)	$^{R}R_{14}(0)$	19521.287(-5)
$^{P}P_{14}(6)+{}^{P}Q_{14}(6)$	19513.421(-10)	$^{R}R_{13}(0)$	19521.762(-54)
$^{P}P_{13}(7)+{}^{P}Q_{13}(7)$	19512.280(-10)	$^{R}R_{14}(1)$	19522.273(-9)
$^{P}P_{14}(7)+{}^{P}Q_{14}(7)$	19511.780(15)	$^{R}R_{13}(1)$	19522.804(-3)
$^{P}P_{13}(8)+{}^{P}Q_{13}(8)$	19510.456(7)	$^{R}R_{14}(3)$	19523.728(-12)
$^{P}P_{14}(8)+{}^{P}Q_{14}(8)$	19509.940(15)	$^{R}R_{13}(3)$	19524.274(9)
$^{Q}R_{13}(4)+{}^{Q}Q_{13}(4)$	19520.762(-17)	$^{R}R_{14}(4)$	19524.209(1)
$^{Q}R_{14}(4)+{}^{Q}Q_{14}(4)$	19520.243(-12)	$^{R}R_{13}(5)$	19524.492(-10)
$^{Q}R_{13}(6)+{}^{Q}Q_{13}(6)$	19519.750(-4)	$^{R}R_{14}(12)$	19521.652(-23)
$^{Q}R_{14}(6)+{}^{Q}Q_{14}(6)$	19519.216(-14)		

[a] All numerical values are given in wave numbers (cm^{-1}). Residuals in the fit are given in parentheses in units of $0.001 cm^{-1}$.

[b] Branches are labeled using a modified version of the more commonly occurring $^2\Pi(a) - {}^2\Sigma^+(b_{\beta J})$ branch labeling scheme. In the modified scheme, the $^2\Pi(a) - {}^2\Sigma^+(b_{\beta J})$ branch labels, specified by $^{\Delta N}\Delta J_{Fi' Fi''}(N'')$, are changed so that the F_i'' label is replaced by the value of G″. Thus, for this $^2\Pi_{1/2} - {}^2\Sigma^+(b_{\beta S})$ system, the eight hyperbranches are $^{O}P_{1G''}$, $^{P}P_{1G''} + {}^{P}Q_{1G''}$, $^{Q}Q_{1G''} + {}^{Q}R_{1G''}$, and $^{R}R_{1G''}$, where G″=3, 4.

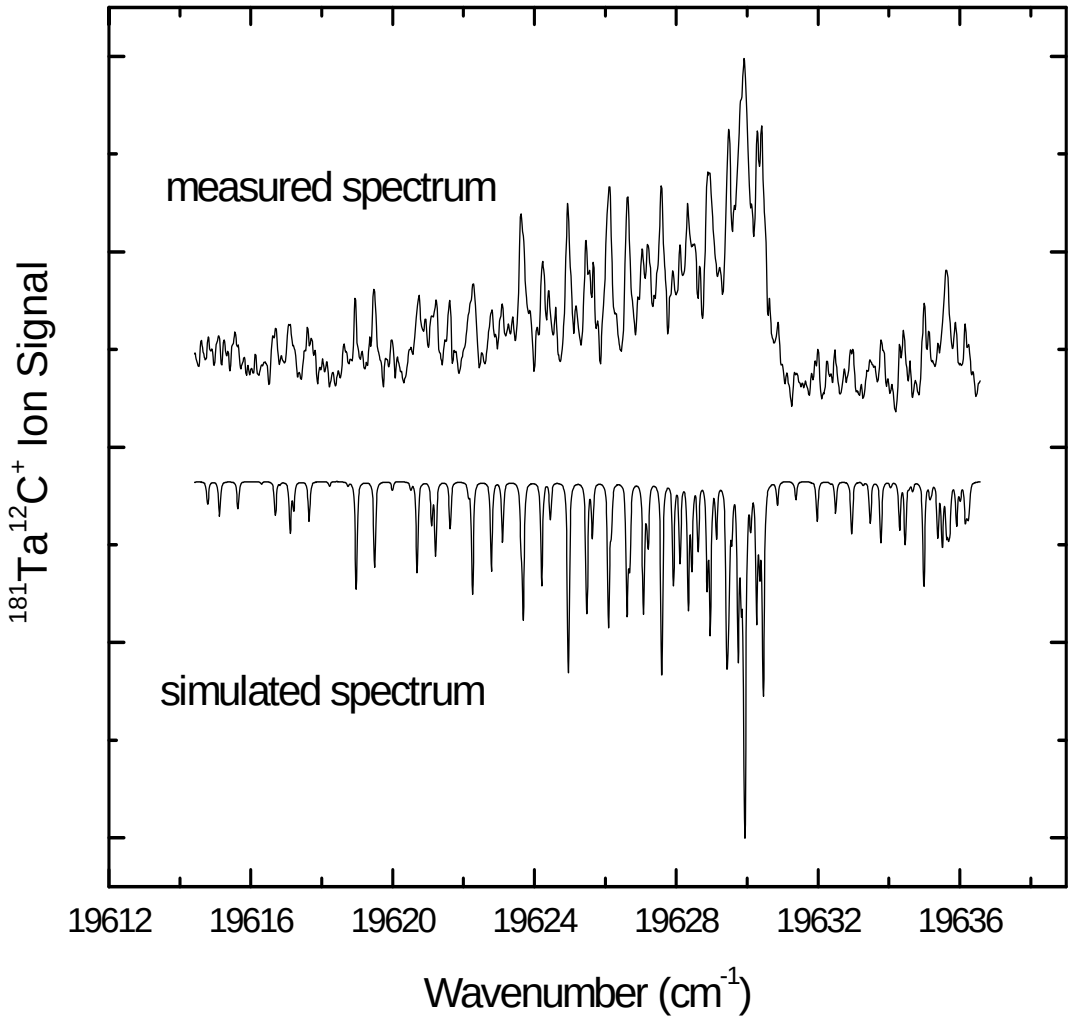

Figure B.7. Rotationally resolved spectra of the [19.63] $^2\Pi_{1/2} \leftarrow {}^2\Sigma^+_{1/2}$ transition of TaC.

Table B.7.

Line positions for the [19.63] $^2\Pi_{1/2} \leftarrow {}^2\Sigma^+_{1/2}$ transition of TaC.[a]

Rotational line[b]	Observed line	Rotational line	Observed line
$^{O}P_{13}(4)$	19623.613(-2)	$^{P}P_{13}(9)+{}^{P}Q_{13}(9)$	19619.477(-22)
$^{O}P_{14}(4)$	19623.091(1)	$^{P}P_{14}(9)+{}^{P}Q_{14}(9)$	19618.945(-29)
$^{O}P_{13}(5)$	19621.602(-23)	$^{Q}R_{14}(6)+{}^{Q}Q_{14}(6)$	19628.946(-10)
$^{O}P_{14}(5)$	19621.129(28)	$^{Q}R_{13}(7)+{}^{Q}Q_{13}(7)$	19628.890(21)
$^{O}P_{13}(6)$	19619.477(-13)	$^{Q}R_{13}(8)+{}^{Q}Q_{13}(8)$	19628.105(-7)
$^{P}P_{14}(1)+{}^{P}Q_{14}(1)$	19628.666(50)	$^{Q}R_{13}(9)+{}^{Q}Q_{13}(9)$	19627.209(1)
$^{P}P_{13}(2)+{}^{P}Q_{13}(2)$	19628.474(31)	$^{Q}R_{14}(11)+{}^{Q}Q_{14}(11)$	19624.402(-43)
$^{P}P_{14}(2)+{}^{P}Q_{14}(2)$	19627.901(-18)	$^{Q}R_{13}(13)+{}^{Q}Q_{13}(13)$	19622.177(29)
$^{P}P_{13}(3)+{}^{P}Q_{13}(3)$	19627.580(-22)	$^{Q}R_{13}(14)+{}^{Q}Q_{13}(14)$	19620.514(-5)
$^{P}P_{14}(3)+{}^{P}Q_{14}(3)$	19627.039(-38)	$^{Q}R_{14}(14)+{}^{Q}Q_{14}(14)$	19619.978(-17)
$^{P}P_{13}(4)+{}^{P}Q_{13}(4)$	19626.628(14)	$^{R}R_{14}(0)$	19630.877(19)
$P_{14}(4)+{}^{P}Q_{14}(4)$	19626.066(-24)	$^{R}R_{13}(0)$	19631.403(20)
$^{P}P_{13}(5)+{}^{P}Q_{13}(5)$	19625.540(58)	$^{R}R_{14}(1)$	19632.003(27)
$^{P}P_{14}(5)+{}^{P}Q_{14}(5)$	19624.940(-18)	$^{R}R_{13}(1)$	19632.474(-26)
$^{P}P_{13}(6)+{}^{P}Q_{13}(6)$	19624.234(30)	$^{R}R_{14}(2)$	19632.986(38)
$^{P}P_{14}(6)+{}^{P}Q_{14}(6)$	19623.639(-41)	$^{R}R_{13}(2)$	19633.457(-15)
$^{P}P_{13}(7)+{}^{P}Q_{13}(7)$	19622.797(16)	$^{R}R_{14}(3)$	19633.778(3)
$^{P}P_{14}(7)+{}^{P}Q_{14}(7)$	19622.286(29)	$^{R}R_{13}(3)$	19634.306(7)
$^{P}P_{13}(8)+{}^{P}Q_{13}(8)$	19621.219(7)	$^{R}R_{14}(4)$	19634.413(-44)
$^{P}P_{14}(8)+{}^{P}Q_{14}(8)$	19620.743(55)		

[a] All numerical values are given in wave numbers (cm^{-1}). Residuals in the fit are given in parentheses in units of $0.001 cm^{-1}$.

[b] Branches are labeled using a modified version of the more commonly occurring $^2\Pi(a) - {}^2\Sigma^+(b_{\beta J})$ branch labeling scheme. In the modified scheme, the $^2\Pi(a) - {}^2\Sigma^+(b_{\beta J})$ branch labels, specified by $^{\Delta N}\Delta J_{Fi' Fi''}(N'')$, are changed so that the F_i'' label is replaced by the value of G″. Thus, for this $^2\Pi_{1/2} - {}^2\Sigma^+(b_{\beta S})$ system, the eight hyperbranches are $^{O}P_{1G''}$, $^{P}P_{1G''} + {}^{P}Q_{1G''}$, $^{Q}Q_{1G''} + {}^{Q}R_{1G''}$, and $^{R}R_{1G''}$, where G″=3, 4.

APPENDIX C

ROTATIONALLY RESOLVED SPECTRA, TABULATED LINE POSITIONS AND FITTED PARAMETERS OF ZrFe

C.1 Vibronically resolved spectra of ZrFe

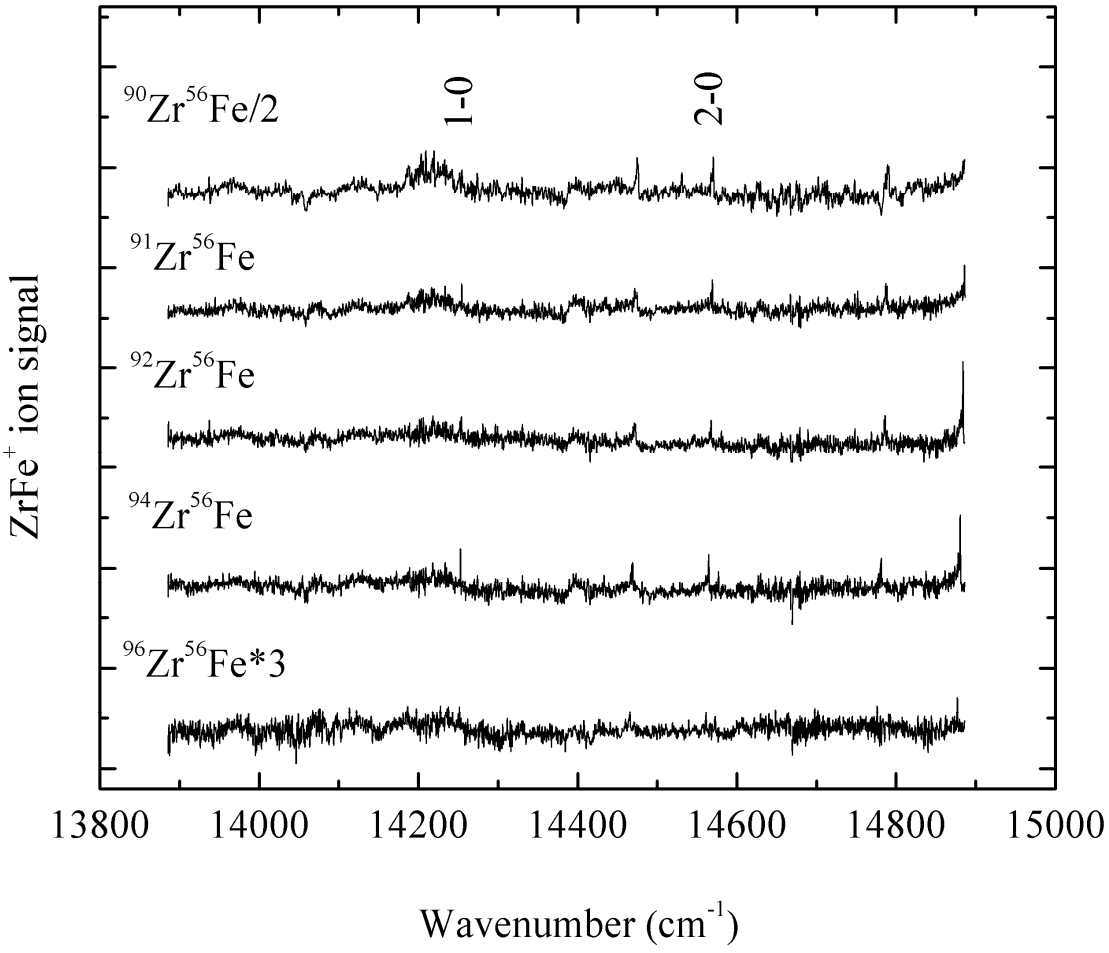

Figure C.1. Spectra of the various isotopomers of ZrFe in the 13890 - 14890 cm^{-1} range.

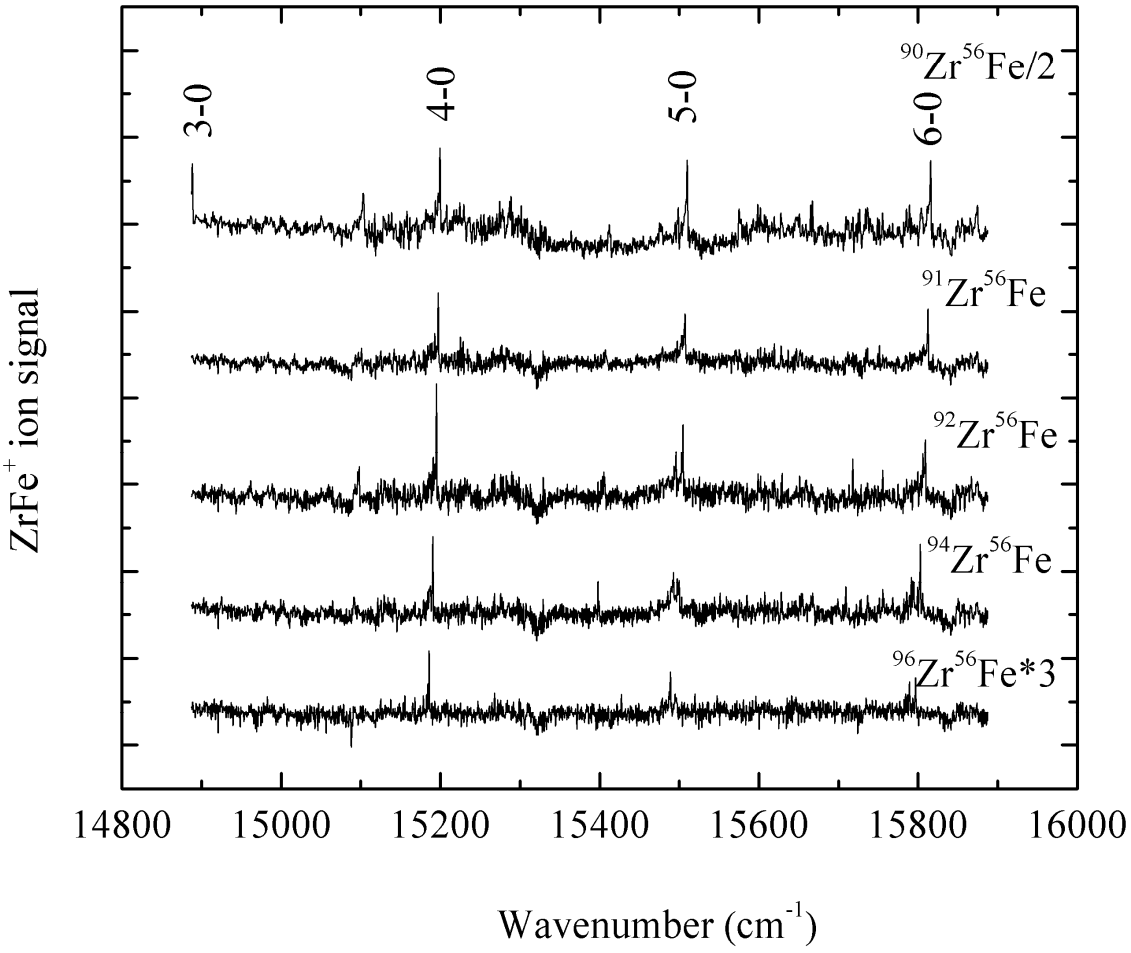

Figure C.2. Spectra of the various isotopomers of ZrFe in the 14890 - 15890 cm^{-1} range.

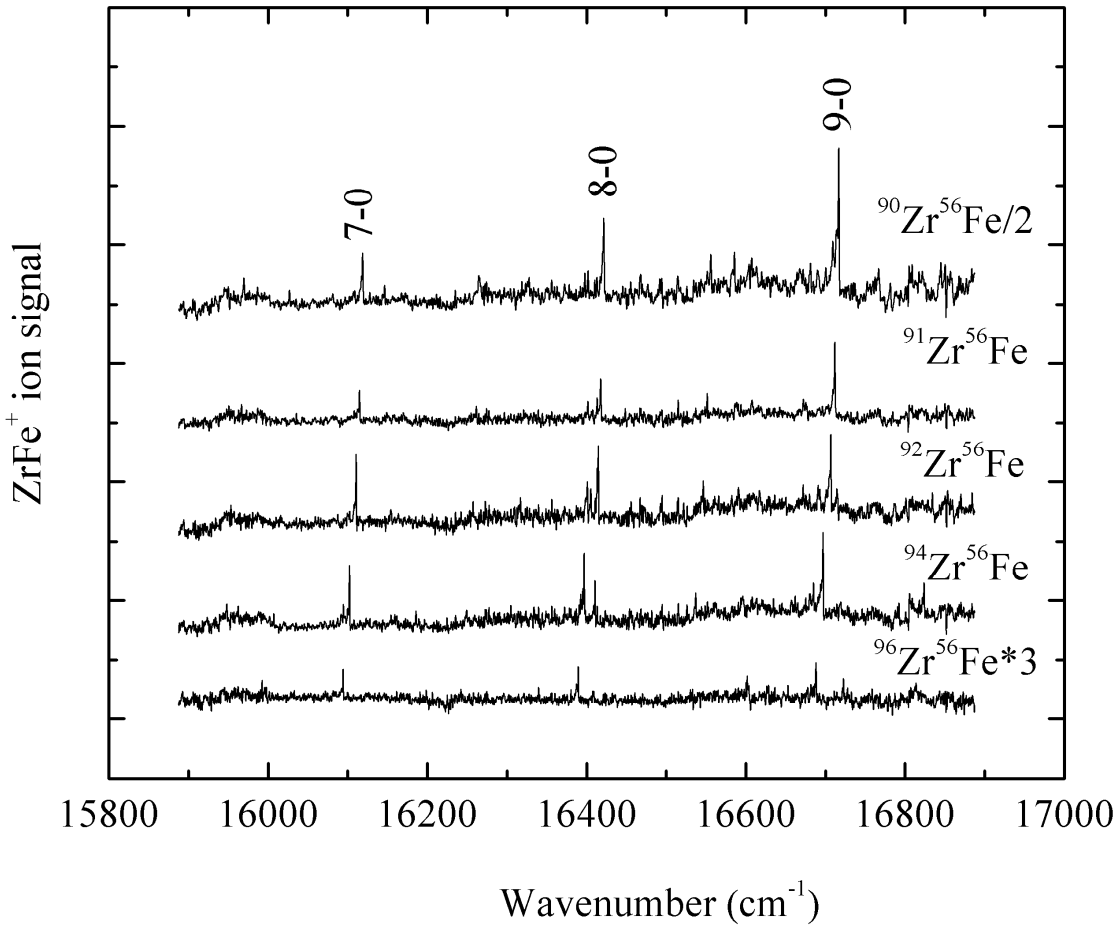

Figure C.3. Spectra of the various isotopomers of ZrFe in the 15890 - 16890 cm^{-1} range.

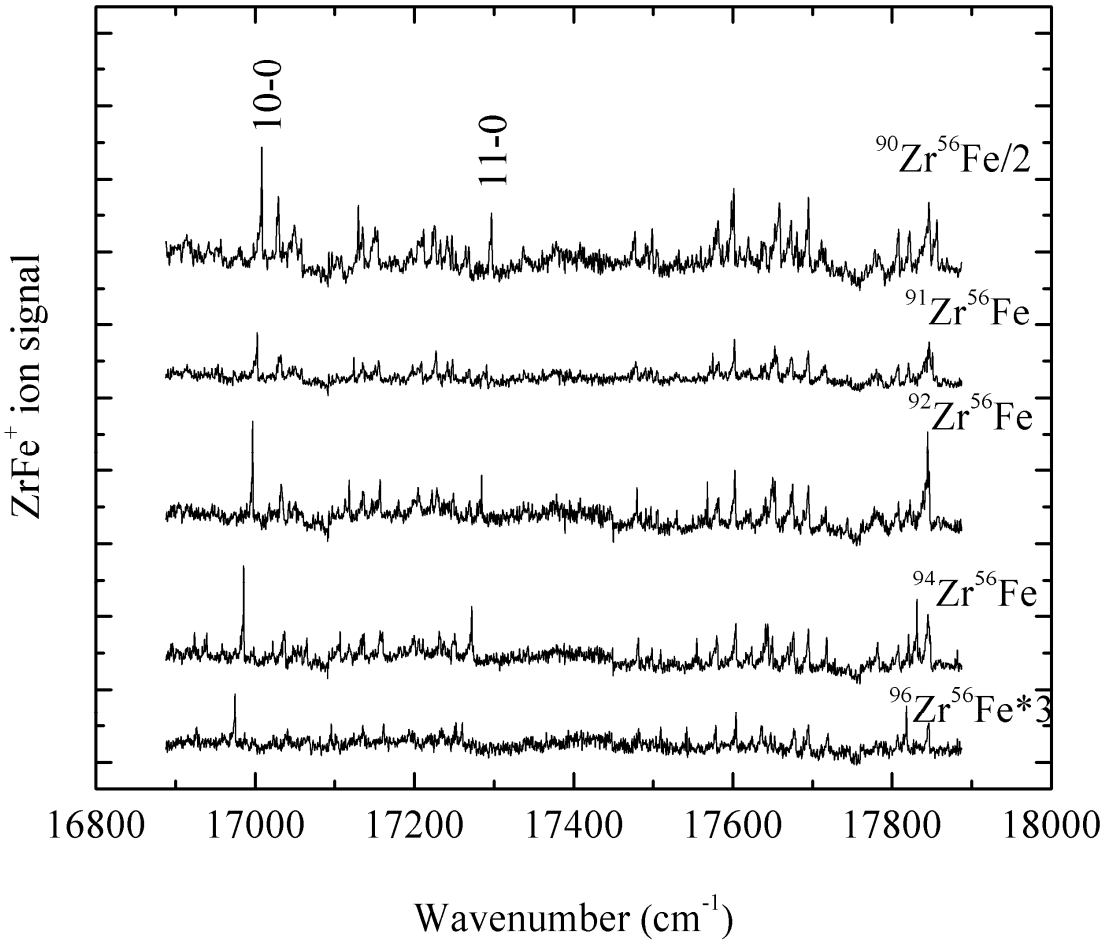

Figure C.4. Spectra of the various isotopomers of ZrFe in the 16890 - 17890 cm^{-1} range.

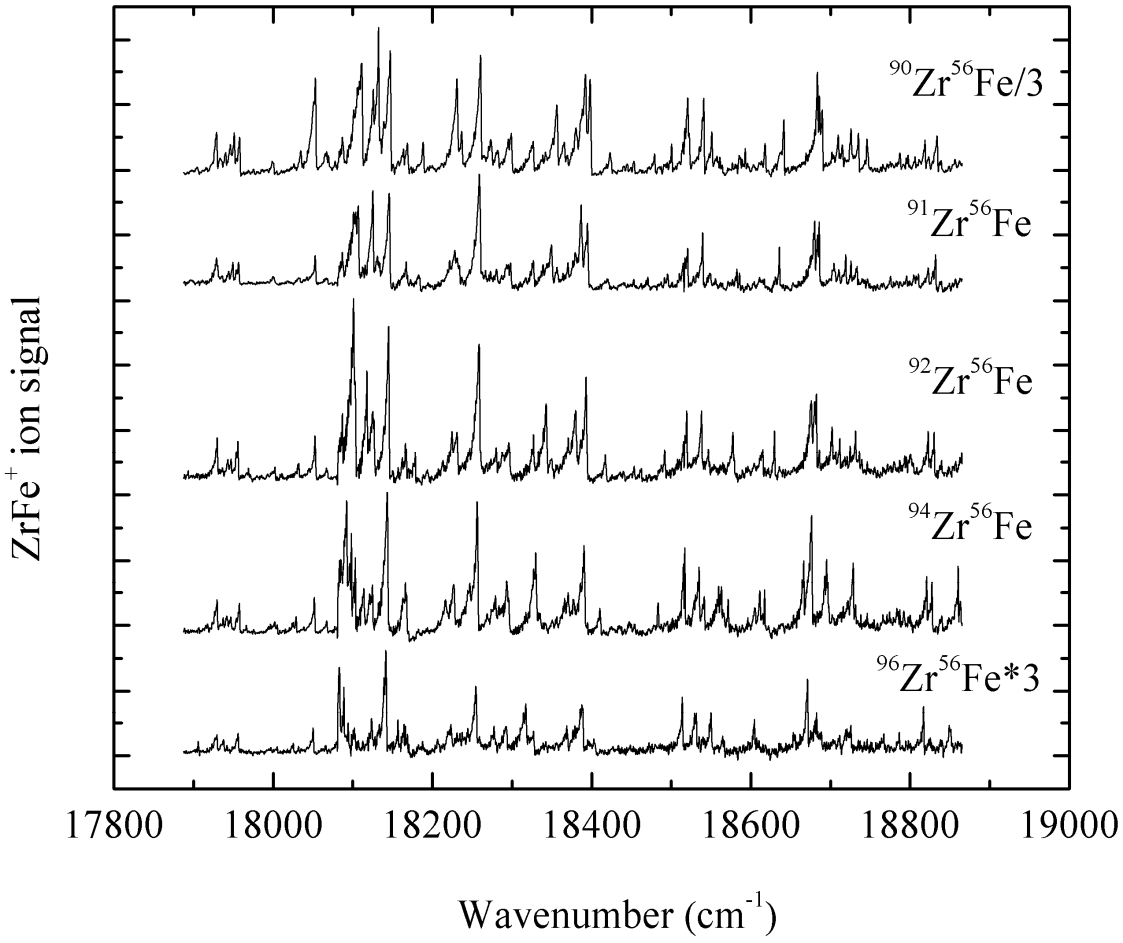

Figure C.5. Spectra of the various isotopomers of ZrFe in the 17890 - 18890 cm^{-1} range.

Table C.1

Band heads of the various ZrFe isotopomers.

$^{90}Zr^{56}Fe$	$^{91}Zr^{56}Fe$	$^{92}Zr^{56}Fe$	$^{94}Zr^{56}Fe$	$^{96}Zr^{56}Fe$	comment
			18860.9	18851.7	
18840.0	18840.2		18840.5		
18835.0	18832.6	18830.7	18828.3		
	18823.8	18823.1	18821.6	18817.6	
18819.7					
	18811.2				
			18793.4		
18807.1					
18798.1					
	18796.6				
18788.4					
				18787.1	
	18776.2				
				18767.6	
18747.9		18746.8			
		18736.7			
			18732.1		
18736.1	18734.2	18732.1	18729.3	18726.1	
18727.0	18726.6	18725.2			
	18719.9				
18716.0					
		18712.3			
				18711.9	
	18711.8				
18710.8	18706.9	18702.7			
			18697.0		
				18689.4	
		18686.7			
				18683.1	
18690.8	18686.8	18682.8	18677.2	18672.1	
18684.8	18681.1	18676.8	18667.0	18656.1	
18642.4	18636.5	18630.6	18617.9	18605.0	
18619.2	18617.6	18615.7	18612.3		
			18606.4		
18593.9	18586.3	18579.7	18572.3	18567.0	
18588.0	18583.1	18578.3			
			18563.7		
				18550.7	

Table C.1 continued

18552.2	18549.9	18547.4	18542.3	18536.3	
18542.0	18540.3	18539.1	18535.9	18532.0	
	18528.8				
				18524.6	
18523.7	18521.4	18520.2	18517.7	18514.7	
18521.8					
18501.6	18496.8	18492.5	18484.3		
18480.1					
	18471.3				
		18463.0			
			18455.0		
18454.5					
		18454.0			
	18453.8				
18446.1					
18441.9					
			18438.2		
18425.7	18422.2	18418.4	18411.8	18404.8	
18399.7	18395.7	18393.9	18391.5	18389.7	[18.40] rotationally resolved
18393.7	18388.9	18380.7			[18.39] rotationally resolved
18383.0	18371.2				
			18371.1		
				18370.4	
			18367.5		
				18357.5	
18367.0	18358.1				
				18343.0	
				18340.1	
18357.9	18351.0	18344.1	18330.7	18318.2	
18327.6	18327.7	18327.6		18327.7	
18300.4	18299.1	18297.7	18296.5	18294.1	
18283.9	18281.7	18281.2	18279.9	18278.6	
18275.4					
18261.9	18260.6	18259.7	18257.3	18255.6	[18.26] rotationally resolved
18237.9	18234.4	18231.9	18228.0	18224.7	
18232.2		18225.6			
			18217.4		
		18214.1			
		18195.5			
				18169.2	
				18164.7	

Table C.1 continued

18189.7	18184.9	18179.2	18168.2	18157.4	
18169.4	18168.0	18167.7			
18164.8					
18148.4	18147.0	18146.1	18144.2	18142.7	
		18127.2	18125.3	18124.6	
			18114.5	18103.6	
18133.4	18126.1	18118.4	18103.6		
				18094.7	
18126.6					
			18098.8	18089.4	
18112.7	18108.1	18103.9	18093.1	18084.2	[18.11] rotationally resolved
18089.2	18088.1	18087.5			
18070.5	18069.0	18069.0	18068.0	18067.1	
18054.3	18053.6	18053.7	18052.6	18050.9	[18.05] rotationally resolved
			18039.1		
				18032.6	
18036.4	18034.2	18032.7	18029.6	18025.8	
18027.1					
18001.7	18001.7	18002.7	18005.7	18005.8	
			18002.6		
		17969.5			
			17967.1		
17959.1	17957.5	17956.4	17958.3	17956.5	
17954.2					
17952.1	17950.0	17947.7			
			17947.4		
				17938.3	
	17944.9				
17941.6					
			17937.7		
17930.2	17931.1	17930.3	17930.2	17929.9	
				17906.8	
		17893.8			
17863.6					
17857.5	17851.5				
17848.7	17847.6	17847.3	17848.4	17847.1	
		17839.6			
			17831.8		
17823.3	17822.2	17823.2	17821.5	17818.5	
17809.2	17809.0	17808.7	17808.4	17807.6	
	17788.7				

Table C.1 continued

			17783.8		
	17781.2				
		17763.9			
		17744.8			
17717.5	17718.1	17717.5	17718.8	17720.2	
17712.8					
17696.6	17696.0	17695.7	17696.3	17695.8	
		17689.9			
				17689.6	
17681.6					
17674.7	17675.6	17676.9	17677.3	17679.2	
				17653.1	
17660.5	17656.5	17653.6	17650.4	17648.3	
			17645.1		
		17641.8			
	17642.1				
17641.3					
				17637.4	
		17622.8	17624.1	17625.0	
17602.6	17603.1	17603.4	17604.3	17604.7	
17584.3	17583.3	17582.6	17581.3	17579.4	
	17575.4				
		17568.6			
			17555.3		
		17530.3			
			17509.7		
	17506.4	17506.3			
17500.2	17499.0	17497.4	17499.3		
17478.2	17480.5	17480.1	17481.9		
			17343.6		
17297.9	17291.2	17284.8	17272.5	17260.7	[13.9] 11-0
	17270.0	17270.1			
17248.4	17248.9	17249.7	17252.8	17253.2	
	17242.4				
17233.5					
			17233.2		
	17228.5				
17227.3					
		17222.7			
17212.4					
	17209.7				

Table C.1 continued

			17206.5		
		17205.3			
			17201.6		
	17198.7				
			17188.8		
			17183.9		
17154.9	17156.4	17157.5	17160.7	17162.3	
		17147.0			
17136.9	17137.2	17137.2	17137.3	17137.2	
17130.6	17124.6	17118.7	17107.3	17096.1	
			17065.6		
17059.2	17059.4		17058.7		
	17051.8				
	17043.7				
17030.4	17033.5	17035.1	17038.0	17041.2	
			17022.4		
			16998.8		
		16997.5	16986.0	16975.1	[13.9] 10-0
				16987.3	
			16959.5		
			16939.8		
				16927.1	
			16924.7		
			16824.3		
			16792.7		
		16715.7			
		16707.2	16697.6		[13.9] 9-0
			16685.4		
		16546.9	16537.8		
			16526.7		
		16515.7	16515.7		
	16494.9	16495.1	16495.1		
		16415.2	16411.0		[13.9] 8-0
		16406.0			
		16401.5			
			16397.4		
	16262.0				

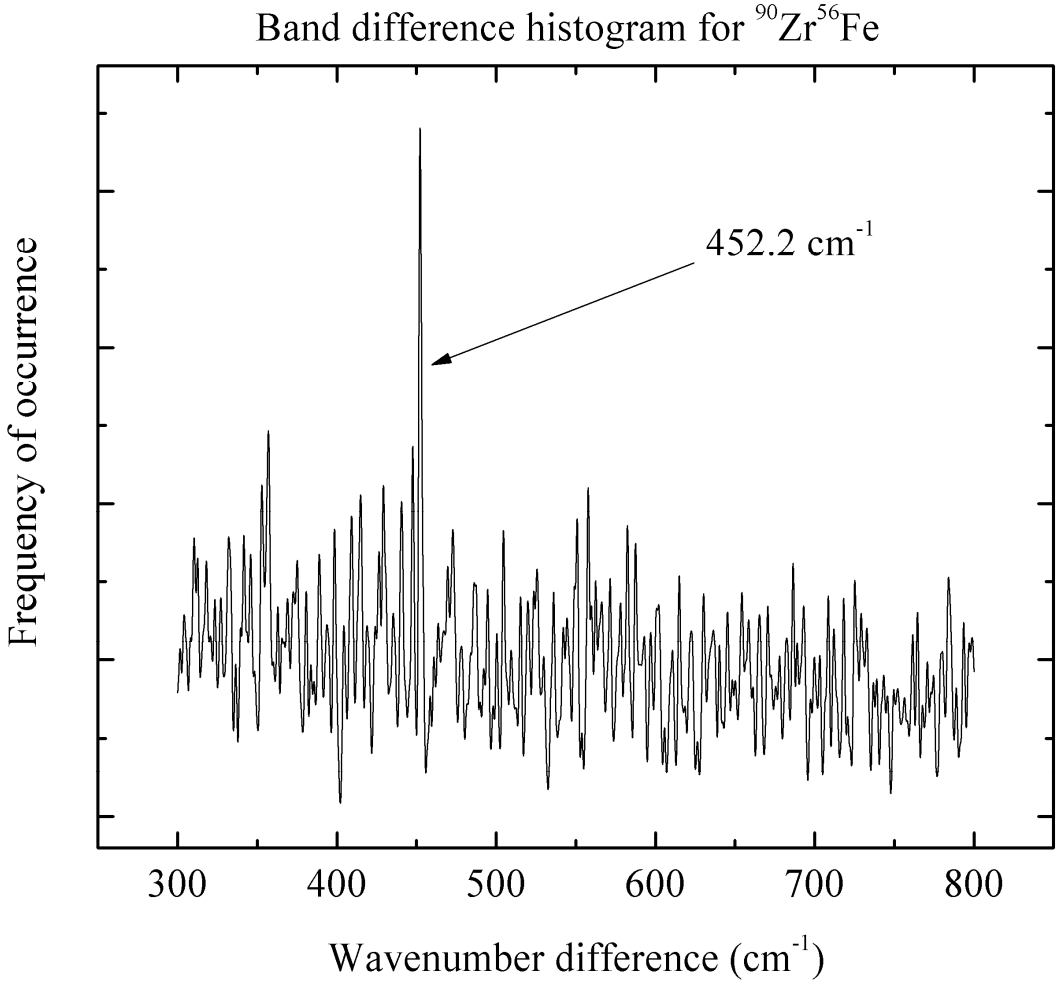

Figure C.6. Band difference histogram plot for $^{90}Zr^{56}Fe$, showing the peak at 452.2 cm^{-1} that corresponds to the ground state value of $\Delta G''_{1/2}$.

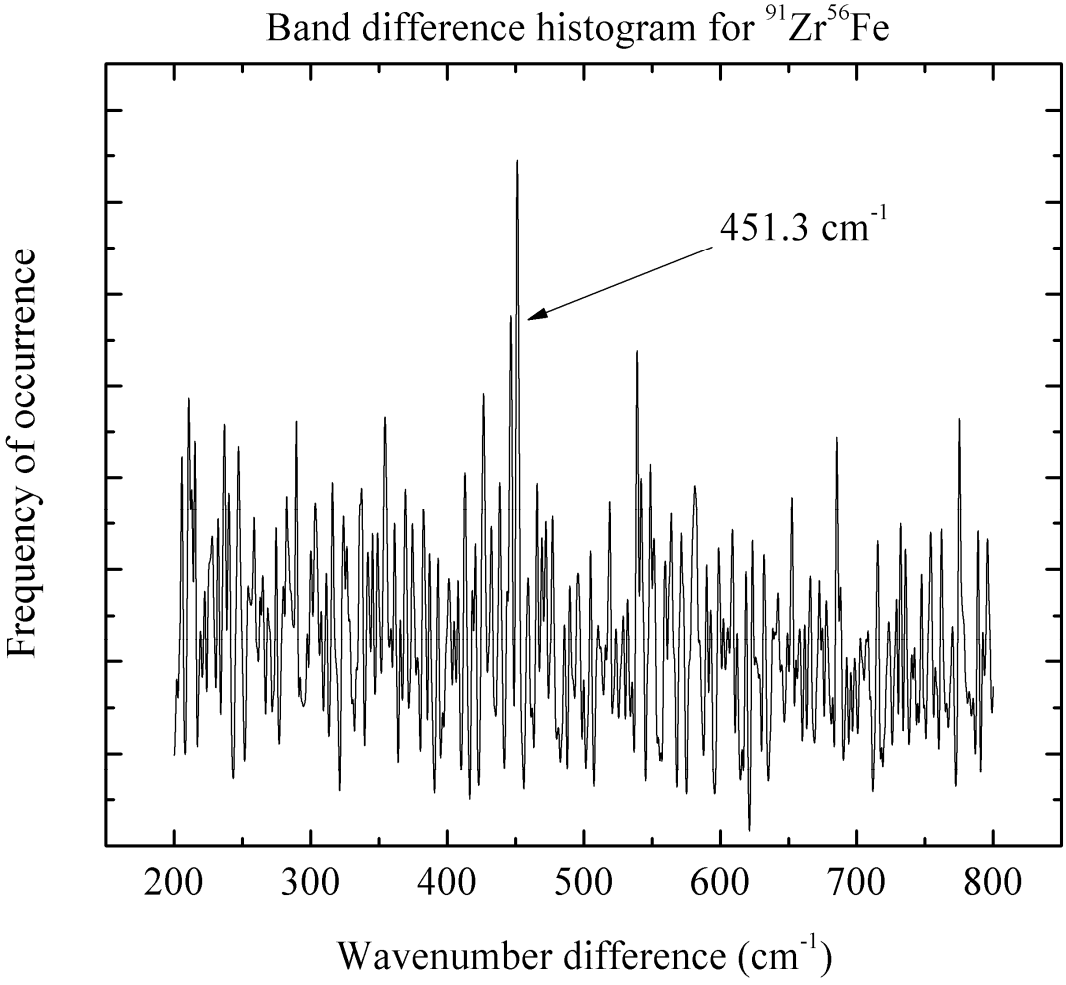

Figure C.7. Band difference histogram plot for $^{91}Zr^{56}Fe$, showing the peak at 451.3 cm^{-1} that corresponds to the ground state value of $\Delta G''_{1/2}$.

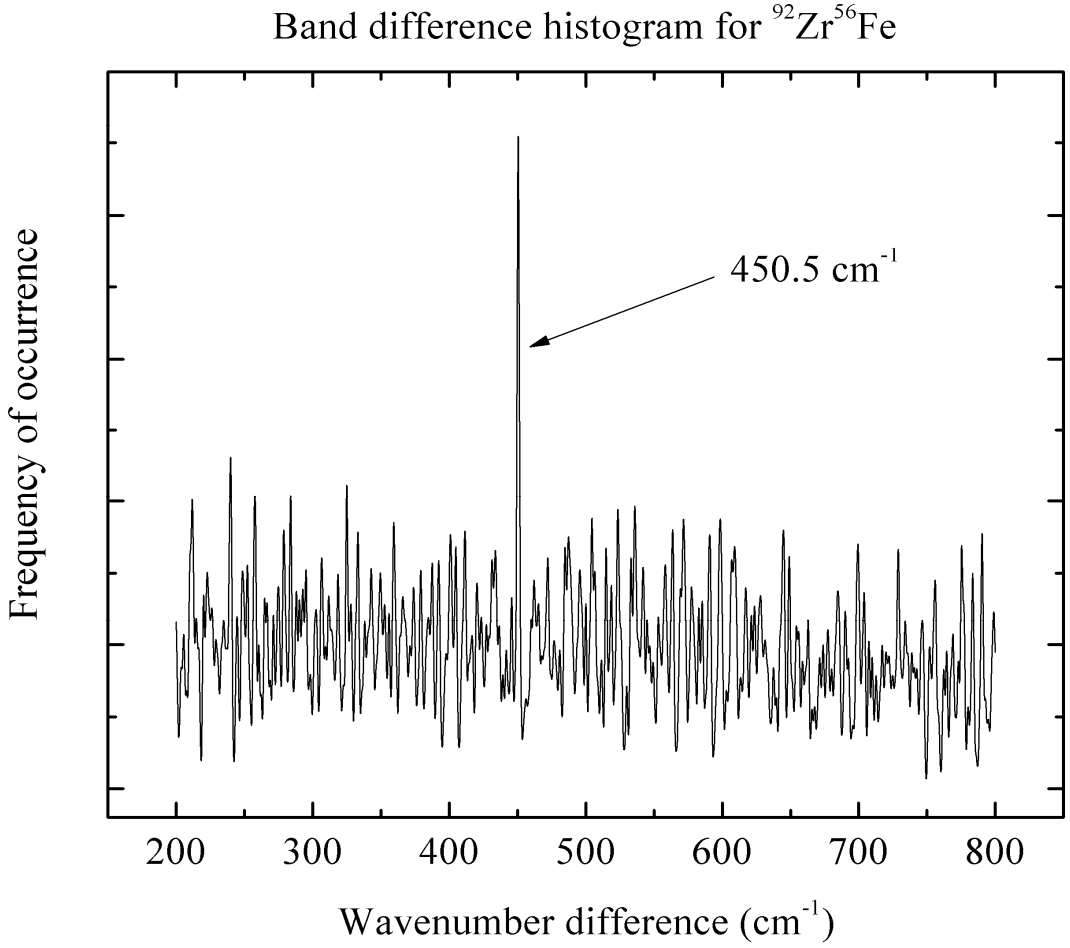

Figure C.8. Band difference histogram plot for $^{92}Zr^{56}Fe$, showing the peak at 450.5 cm^{-1} that corresponds to the ground state value of $\Delta G''_{1/2}$.

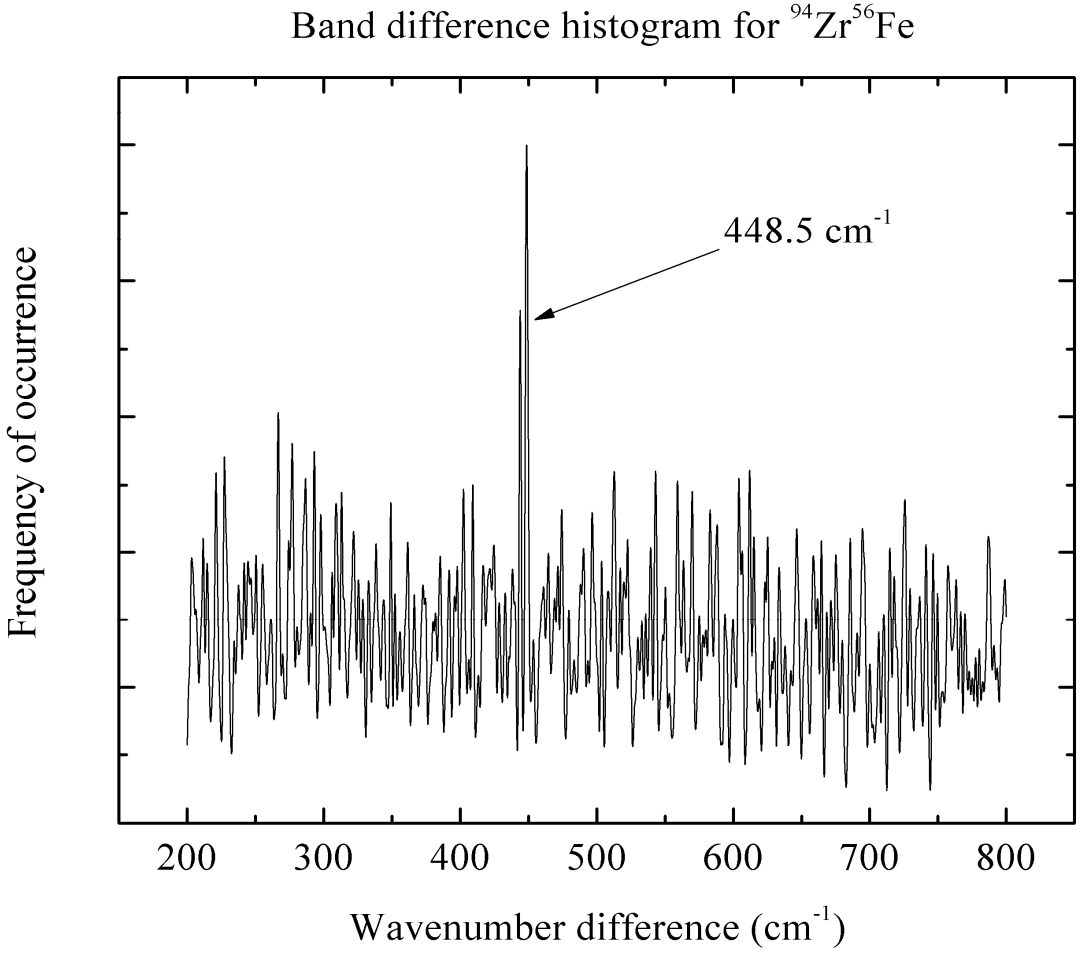

Figure C.9. Band difference histogram plot for $^{94}Zr^{56}Fe$, showing the peak at 448.5 cm^{-1} that corresponds to the ground state value of $\Delta G''_{1/2}$.

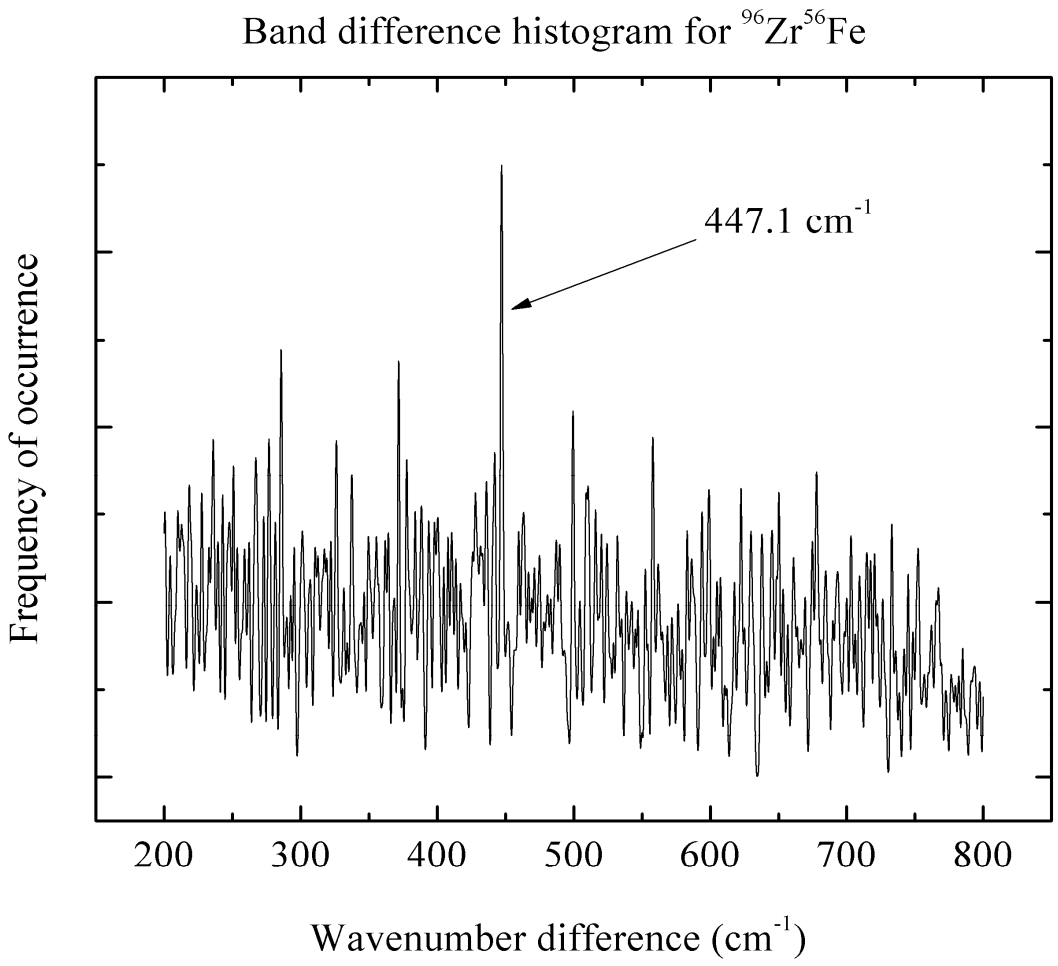

Figure C.10. Band difference histogram plot for $^{96}Zr^{56}Fe$, showing the peak at 447.1 cm^{-1} that corresponds to the ground state value of $\Delta G''_{1/2}$.

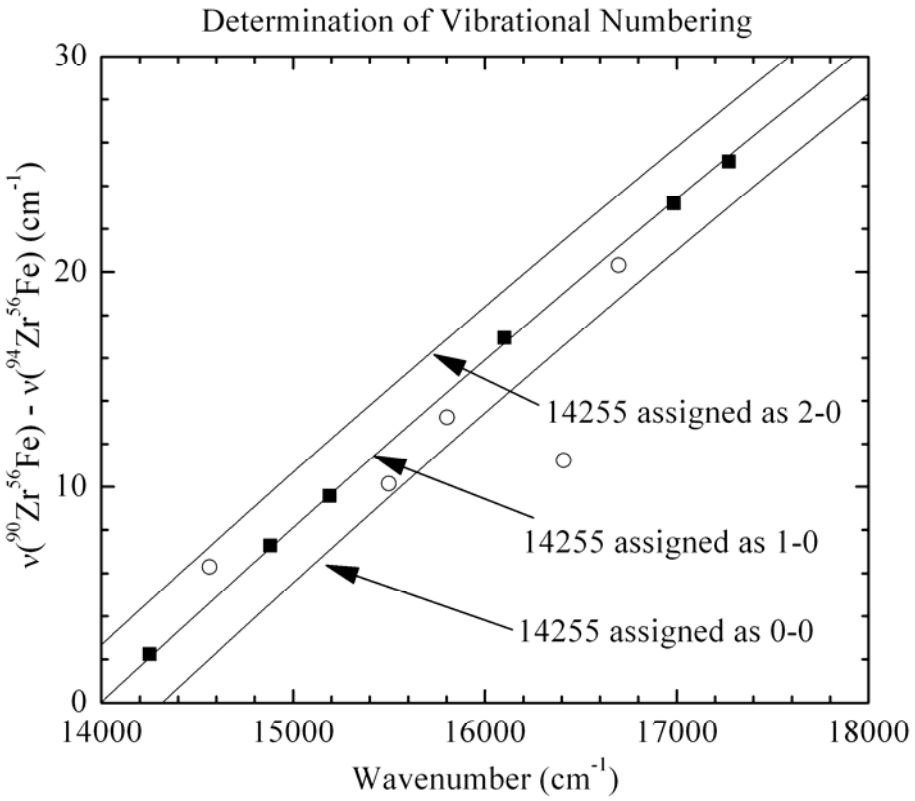

Figure C.11.Measured (symbols) vs. calculated (lines) isotope shifts, $\nu(^{90}Zr^{56}Fe)$-$\nu(^{94}Zr^{56}Fe)$, for bands belonging to the $[13.9]0^{+}\leftarrow{}^{1}\Sigma$ system. Filled squares correspond to unperturbed bands; open circles correspond to band that are perturbed. From this plot, the assignment of the 14255 cm^{-1} band as the 1-0 band seems definite.

Table C.2

Vibrational fit of the [13.9] $0^+ \leftarrow X\ ^1\Sigma^+$ system for ZrFe isotopomers; the band origin, ν_0, was determined for each band from the rotational fit. Only unperturbed bands were included in the fit to determine T_0, ω_e', and $\omega_e' x_e'$.

Band	$^{90}Zr^{56}Fe$	$^{91}Zr^{56}Fe$	$^{92}Zr^{56}Fe$	$^{94}Zr^{56}Fe$
1-0	14254.1492(0.3883)	14253.5418(0.3679)	14252.9977(0.2610)	14251.9054(0.3127)
3-0	14887.9450(-0.0287)	14886.0751(-0.0159)	14884.2327(0.0466)	14880.6580(-0.0116)
4-0	15199.3570(-0.9547)	15196.8856(-0.9173)	15194.4780(-0.7614)	15189.7750(-0.7646)
7-0	16118.8157(0.5634)	16114.4780(0.5254)	16110.2045(0.4902)	16101.8612(0.3849)
10-0	17008.3588(0.7761)	17002.3908(0.7677)	16996.5477(0.3865)	16985.1813(0.7783)
11-0	17296.9238(-0.7444)	17290.4567(-0.7278)	17284.9923(-0.4229)	17271.7876(-0.6997)
		Fitted constants		
T_0	13931.8862(1.2377)	13931.9688(1.1920)	13932.3408(0.8543)	13932.3860(1.0741)
ω_e'	325.0537(0.5460)	324.3694(0.5280)	323.5102(0.3784)	322.3190(0.4758)
$\omega_e' x_e'$	1.5895(0.0401)	1.5822(0.0388)	1.5571(0.0278)	1.5561(0.0349)

[a] Following each band origin listed, the residual in the fit (observed – calculated) is provided in the parentheses. Following each calculated constant, the 1σ error limit is presented. All quantities are presented in wavenumbers (cm^{-1}).

Table C.3. Calculated Franck-Condon factors for the [13.9] $0^+ \leftarrow X\ ^1\Sigma^+$ system of ZrFe[a]

Band	Franck-Condon factor	Band	Franck-Condon factor
0-0	0.0034	0-1	0.0137
1-0	0.0202	1-1	0.0579
2-0	0.0596	2-1	0.1102
3-0	0.1156	3-1	0.1177
4-0	0.1653	4-1	0.0668
5-0	0.1854	5-1	0.0102
6-0	0.1688	6-1	0.0068
7-0	0.1276	7-1	0.0587
8-0	0.0811	8-1	0.1194
9-0	0.0435	9-1	0.1452
10-0	0.0196	10-1	0.1280
11-0	0.0073	11-1	0.0877
12-0	0.0021	12-1	0.0480
13-0	0.0005	13-1	0.0209
14-0	0.0001	14-1	0.0071
15-0	0.0000	15-1	0.0017

[a] Calculations are based on an RKR model of the potential function of the [13.9]0^+ state and a harmonic model of the ground state, obtained using the RKR1 and LEVEL 8.0 programs of Professor Robert J. LeRoy. [R. J. Le Roy, RKR1: A Computer Program Implementing the First-Order RKR Method for Determining Diatom Potential Energy Curves from Spectroscopic Constants, University of Waterloo Chemical Physics
Research Report CP-425 (1992).; R. J. Le Roy, LEVEL 8.0: A Computer Program for Solving the Radial Schrödinger Equation for Bound and Quasibound Levels, University of Waterloo Chemical Physics Research Report CP-663 (2007)

C.2 Rotationally resolved spectra of ZrFe

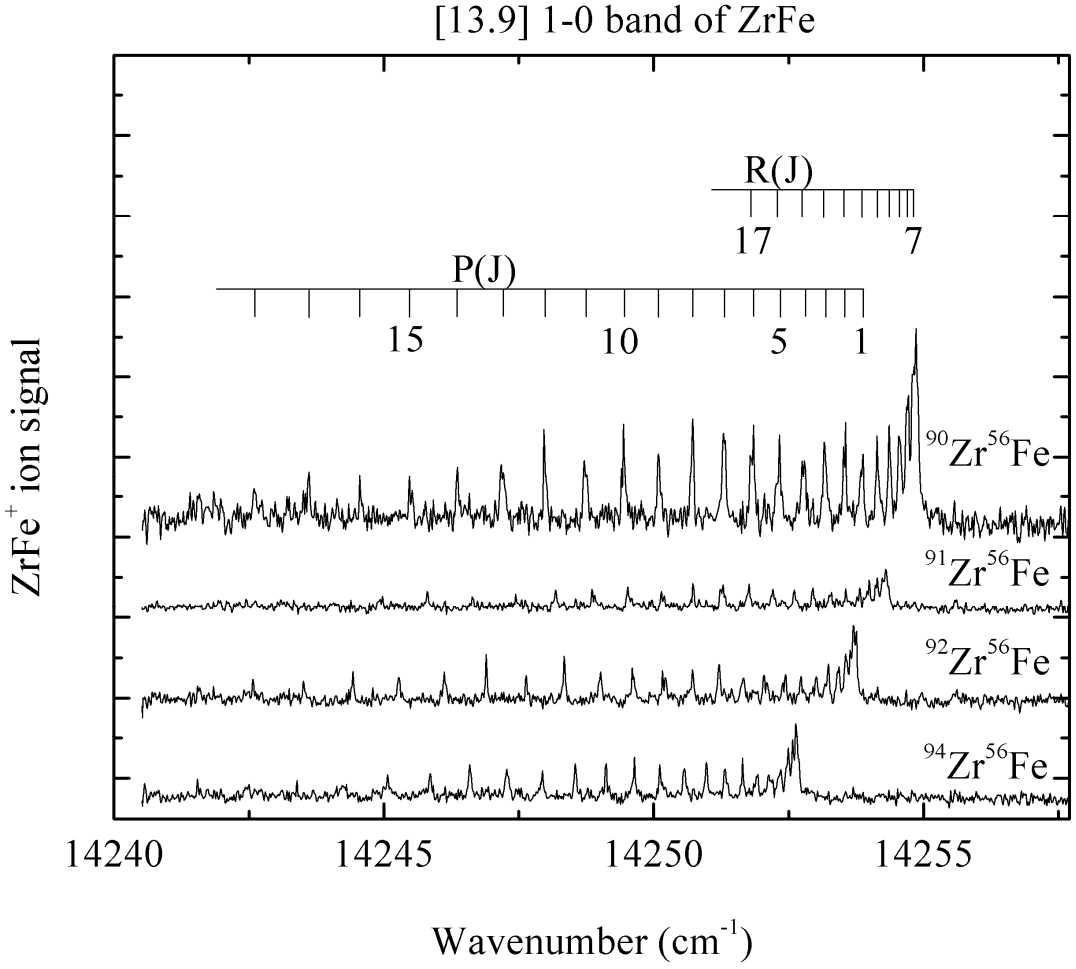

Figure C.12. Rotationally resolved spectra of the various ZrFe isotopic combinations for the 1-0 band of the [13.9] $0^{+}\leftarrow X\,^{1}\Sigma^{+}$ system. Line assignments are provided for the most abundant isotopomer, $^{90}Zr^{56}Fe$.

Table C.4

Fitted Rotational Lines of the 1-0 band of the $[13.9]0^+ \leftarrow X\ ^1\Sigma^+$ system of ZrFe.[a]

Line	$^{90}Zr^{54}Fe$	$^{90}Zr^{56}Fe$	$^{91}Zr^{56}Fe$	$^{92}Zr^{56}Fe$	$^{94}Zr^{56}Fe$	$^{96}Zr^{56}Fe$
P(1)		14253.875(-3)	14253.254(12)			
P(2)		14253.554(-3)	14252.947(-1)	14252.389(15)		
P(3)			14252.603(-18)	14252.041(3)	14250.978(-18)	
P(4)		14252.794(-13)	14252.178(4)	14251.660(-18)	14250.568(-7)	
P(5)		14252.331(1)	14251.729(7)	14251.211(-13)	14250.113(7)	
P(6)	14254.790(13)	14251.848(-8)	14251.258(-9)	14250.722(-11)	14249.642(-5)	14248.606(5)
P(7)		14251.302(3)	14250.731(-13)	14250.165(18)	14249.115(-3)	14248.085(5)
P(8)	14253.679(-8)	14250.725(2)	14250.142(5)	14249.603(9)	14248.547(-2)	14247.507(21)
P(9)	14253.043(-2)	14250.090(15)	14249.519(13)	14249.018(-20)	14247.940(-4)	14246.942(-20)
P(10)	14252.371(-4)	14249.441(0)	14248.858(17)	14248.343(0)	14247.279(6)	14246.302(-25)
P(11)	14251.666(-17)		14248.184(-8)	14247.636(10)	14246.591(1)	14245.563(26)
P(12)	14250.902(-13)	14247.970(15)	14247.444(-9)	14246.899(6)	14245.861(-4)	14244.873(-13)
P(13)	14250.092(-7)	14247.215(-22)	14246.647(4)	14246.118(5)	14245.073(7)	14244.082(6)
P(14)	14249.260(-22)	14246.361(-4)	14245.809(17)	14245.277(22)		14243.294(-19)
P(15)	14248.365(-18)	14245.474(4)	14244.974(-16)	14244.427(5)	14243.388(11)	14242.416(4)
P(16)	14247.409(3)	14244.555(2)		14243.512(12)	14242.498(-2)	
P(17)		14243.607(-15)		14242.577(-3)	14241.547(4)	
P(18)		14242.603(-18)		14241.573(7)		
R(0)			14253.766(10)			
R(1)			14253.957(11)			
R(2)			14254.105(13)	14253.557(14)		
R(3)			14254.236(-10)		14252.572(5)	

Table C.4 continued

R(4)	14257.934(-4)		14254.303(-12)	14253.754(-12)	14252.653(-13)	14251.599(-7)
R(5)	14257.934(21)		14254.303(11)	14253.754(11)	14252.653(8)	14251.599(14)
R(6)	14257.934(2)		14254.303(-8)	14253.754(-9)	14252.635(6)	14251.599(-6)
R(7)		14254.819(5)	14254.236(-2)	14253.703(-21)	14252.572(5)	14251.529(1)
R(8)	14257.749(19)	14254.714(2)	14254.141(-11)	14253.580(-1)	14252.456(17)	14251.449(-23)
R(9)	14257.610(9)	14254.563(0)	14253.995(-10)	14253.430(2)	14252.312(14)	14251.267(13)
R(10)	14257.427(0)	14254.363(7)	14253.817(-21)	14253.235(8)	14252.128(9)	14251.103(-10)
R(11)	14257.185(7)	14254.138(-6)	14253.557(9)	14253.009(3)	14251.916(-11)	14250.863(0)
R(12)	14256.938(-26)	14253.839(12)	14253.294(0)	14252.727(12)	14251.646(-14)	14250.566(27)
R(13)	14256.581(10)	14253.521(7)		14252.443(-20)	14251.316(1)	14250.266(14)
R(14)		14253.166(-5)		14252.100(-34)	14250.978(-18)	14249.939(-13)
R(15)	14255.778(38)	14252.752(0)	14252.211(12)	14251.660(6)		14249.530(0)
R(16)		14252.275(24)				
R(17)		14251.803(1)				
R(18)				14250.219(-6)		
R(19)		14250.689(-3)				
Fitted Spectroscopic Constants [b]						
ν_0 (cm^{-1})	14257.1582(76)	14254.1492(34)	14253.5418(32)	14252.9977(39)	14251.9054(32)	14250.8627(68)
B_1' (cm^{-1})	0.120489(121)	0.117322(28)	0.117179(45)	0.116666(46)	0.115509(48)	0.114667(124)
r_1' (Å)	2.03716(102)	2.04133(24)	2.03826(39)	2.03850(40)	2.04041(42)	2.03989(110)
B_0'' (cm^{-1})	0.142144(99)	0.138786(30)	0.138297(38)	0.137770(34)	0.136513(50)	0.135508(126)
r_0'' (Å)	1.87558(65)	1.87685(20)	1.87619(26)	1.87588(23)	1.87689(34)	1.87648(87)

[a] Residuals (ν(calculated) – ν(measured)) are given in parentheses following each line position, in units of 0.001 cm^{-1}.

[b] Error limits (1σ) are provided for each fitted spectroscopic constant, in units of the last digit quoted. B_0'' was constrained to take the same value in all of the unperturbed bands (the 1-0, 3-0, 4-0, 7-0, 10-0, and 11-0 bands), which all originated from the $v'' = 0$ level of the ground X $^1\Sigma^+$ state. For the $^{90}Zr^{54}Fe$ isotopic modification, only this band and the 18053 cm^{-1} band were resolved, so both were included in a combined fit. This band was included in the combined fit for all isotopic forms of ZrFe.

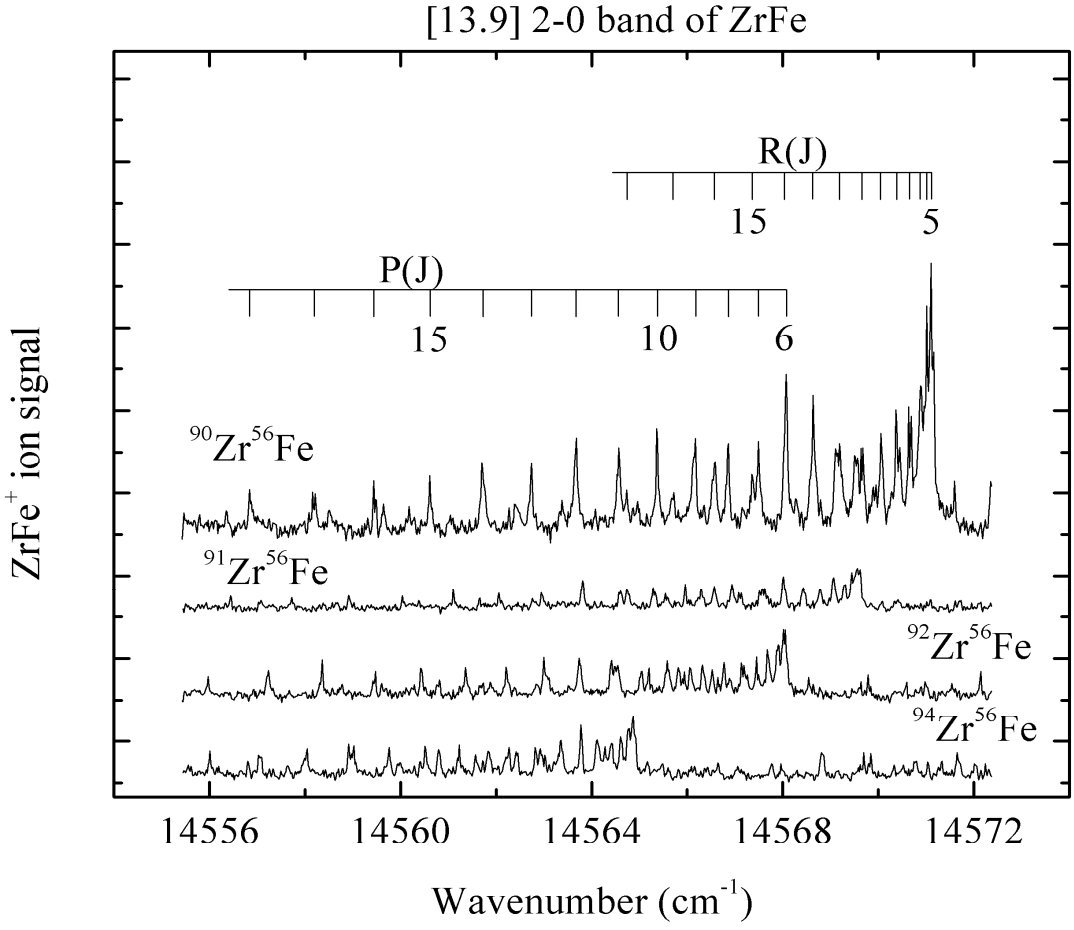

Figure C.13. Rotationally resolved spectra of the various ZrFe isotopic combinations for the 2-0 band of the [13.9] $0^{+}\leftarrow X\,^{1}\Sigma^{+}$ system. Line assignments are provided for the most abundant isotopomer, $^{90}Zr^{56}Fe$.

Table C.5

Assigned Rotational Lines of the 2-0 band of the $[13.9]0^+ \leftarrow X\ ^1\Sigma^+$ system of ZrFe.[a]

Line	$^{90}Zr^{56}Fe$	$^{91}Zr^{56}Fe$	$^{92}Zr^{56}Fe$	$^{94}Zr^{56}Fe$
P(2)			14566.898	
P(3)			14566.525	
P(4)			14566.067	14562.922
P(5)			14565.585	14562.428
P(6)	14568.071	14566.563	14565.047	14561.840
P(7)	14567.490	14565.963	14564.410	14561.229
P(8)	14566.859	14565.286	14563.745	14560.519
P(9)	14566.163	14564.603	14563.001	14559.756
P(10)	14565.369	14563.816	14562.216	14558.911
P(11)	14564.571	14562.957	14561.365	14558.036
P(12)	14563.667	14562.055	14560.437	14557.043
P(13)	14562.734	14561.102	14559.475	14556.007
P(14)	14561.711	14560.039	14558.364	
P(15)	14560.608	14558.914	14557.232	
P(16)	14559.480	14557.721	14555.969	
P(17)	14558.215	14556.445		
P(18)	14556.833			
R(1)			14567.899	
R(2)			14568.017	
R(3)			14568.053	14564.862
R(4)		14569.616	14568.053	14564.862
R(5)	14571.105	14569.557	14568.017	14564.776
R(6)	14571.015	14569.447	14567.873	14564.616
R(7)	14570.886	14569.298	14567.688	14564.415
R(8)	14570.638	14569.063	14567.449	14564.112
R(9)	14570.380	14568.782	14567.139	14563.782
R(10)	14570.057	14568.429	14566.771	14563.353
R(11)	14569.676	14568.012	14566.320	14562.829
R(12)	14569.192		14565.818	14562.269
R(13)	14568.641	14566.944	14565.198	14561.566
R(14)	14568.071	14566.293		14560.799
R(15)	14567.372	14565.547		
R(16)	14566.574	14564.745		
R(17)	14565.694	14563.816		
R(18)	14564.736			

[a] The upper state of this band is perturbed by a nearby state. Lines have been identified using combination differences calculated from the known ground state rotational constant, but no attempt has been made to deperturb the state. Perturbations in this upper state are so severe that it makes no sense to even attempt a fit to the standard form, $\nu = \nu_0 + B'J'(J'+1) - B''J''(J''+1)$.

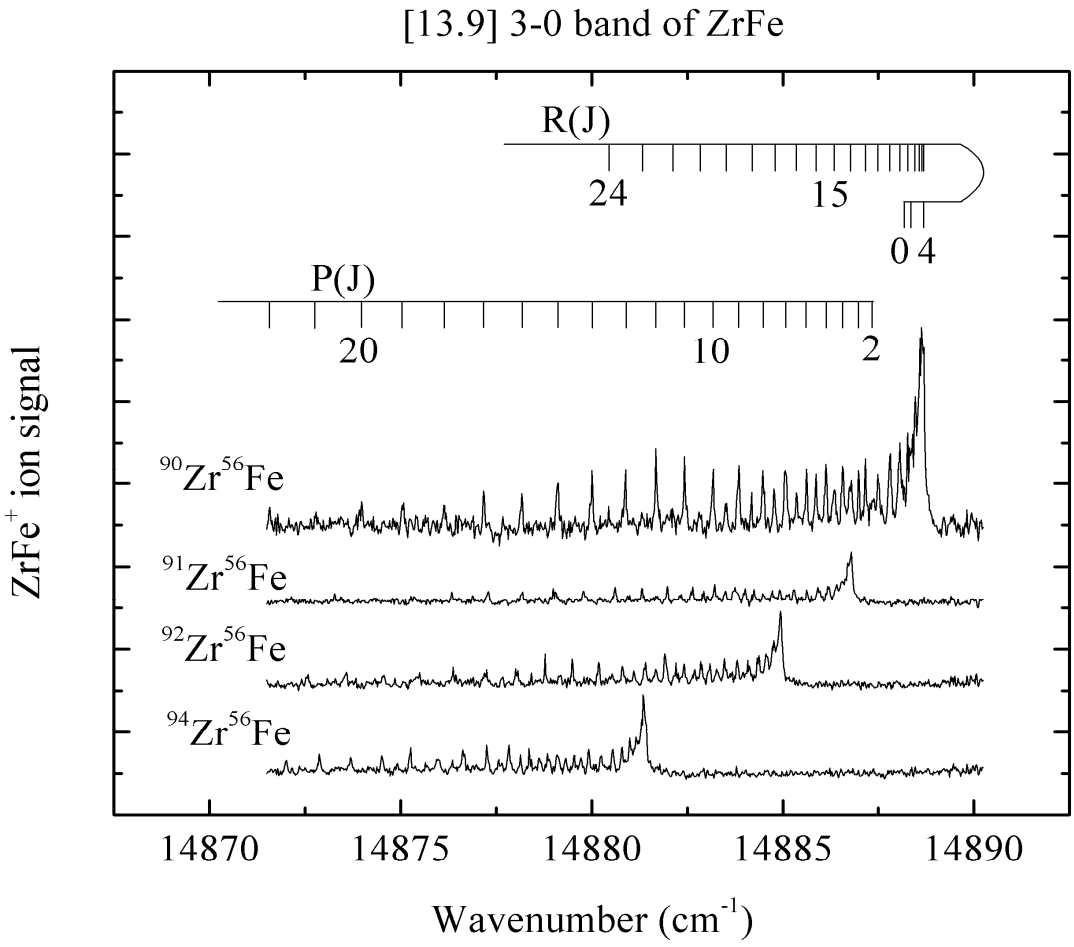

Figure C.14. Rotationally resolved spectra of the various ZrFe isotopic combinations for the 3-0 band of the [13.9] $0^{+}\leftarrow X\,^{1}\Sigma^{+}$ system. Line assignments are provided for the most abundant isotopomer, $^{90}Zr^{56}Fe$.

Table C.6

Fitted Rotational Lines of the 3-0 band of the $[13.9]0^+ \leftarrow X\ ^1\Sigma^+$ system of ZrFe.

Line	$^{90}Zr^{56}Fe$	$^{91}Zr^{56}Fe$	$^{92}Zr^{56}Fe$	$^{94}Zr^{56}Fe$	$^{96}Zr^{56}Fe$
P(2)	14887.366(-20)	14885.487(-10)		14880.092(-24)	
P(3)	14886.986(-7)		14883.277(-3)	14879.719(-11)	
P(4)	14886.568(0)	14884.718(-15)	14882.867(0)	14879.315(-11)	14875.903(-12)
P(5)	14886.129(-16)	14884.245(4)	14882.418(-3)	14878.843(15)	14875.459(-11)
P(6)	14885.624(-11)	14883.742(9)	14881.917(4)	14878.360(7)	14874.930(32)
P(7)	14885.066(3)	14883.218(-9)	14881.388(-7)	14877.834(-2)	14874.466(-33)
P(8)	14884.474(7)	14882.639(-16)	14880.802(-5)	14877.254(1)	14873.841(20)
P(9)	14883.849(-1)	14881.979(13)	14880.183(-13)	14876.640(-7)	14873.236(10)
P(10)	14883.173(-3)	14881.313(4)	14879.495(4)	14875.974(-5)	14872.581(7)
P(11)	14882.429(19)	14880.607(-9)	14878.777(8)	14875.263(-3)	14871.891(-4)
P(12)	14881.678(4)		14878.007(19)	14874.508(0)	
P(13)	14880.878(-7)		14877.251(-28)	14873.694(19)	
P(14)	14880.011(5)	14878.184(-10)	14876.377(-1)	14872.877(-3)	
P(15)	14879.104(12)	14877.294(-16)	14875.497(-12)	14872.005(-14)	
P(16)	14878.168(5)	14876.335(2)	14874.546(4)		
P(17)	14877.177(7)	14875.355(-2)	14873.579(-7)		
P(18)	14876.136(15)	14874.313(11)	14872.551(-2)		
P(19)	14875.056(18)	14873.275(-26)			
P(20)	14873.949(3)	14872.141(-9)			
P(21)	14872.772(14)				
P(22)	14871.574(2)				
R(0)	14888.177(2)			14880.867(21)	

Table C.6 continued

R(1)	14888.362(5)			14881.045(28)	14877.635(11)
R(2)		14886.640(-1)	14884.772(24)	14881.221(-5)	14877.773(15)
R(3)				14881.306(9)	14877.880(8)
R(4)	14888.682(-15)	14886.788(6)	14884.955(-4)		14877.941(2)
R(5)	14888.682(-4)	14886.788(17)	14884.955(8)		14877.941(15)
R(6)	14888.637(7)	14886.754(17)	14884.934(-3)	14881.354(-4)	14877.941(-15)
R(7)	14888.585(-19)	14886.702(-8)	14884.847(8)		14877.880(-26)
R(8)	14888.458(-14)	14886.549(23)	14884.729(6)	14881.164(-8)	14877.773(-36)
R(9)	14888.265(12)	14886.406(1)	14884.562(9)	14880.995(-2)	14877.576(2)
R(10)	14888.061(5)	14886.187(9)	14884.370(-7)	14880.794(-6)	14877.381(-4)
R(11)	14887.801(10)			14880.543(-4)	14877.133(-2)
R(12)	14887.494(17)	14885.629(13)	14883.801(15)	14880.242(3)	14876.827(16)
R(13)	14887.157(9)	14885.288(12)	14883.469(7)	14879.922(-13)	14876.505(7)
R(14)	14886.767(10)	14884.920(-8)	14883.095(-3)	14879.540(-12)	14876.138(0)
R(15)	14886.349(-5)	14884.477(3)	14882.691(-27)	14879.092(13)	
R(16)	14885.869(-2)	14884.015(-11)	14882.201(-8)	14878.622(16)	
R(17)	14885.359(-15)	14883.500(-16)	14881.683(-5)	14878.130(-3)	
R(18)	14884.774(3)	14882.927(-7)	14881.101(17)	14877.558(15)	
R(19)	14884.180(-14)	14882.307(3)	14880.529(-14)	14876.977(-2)	
R(20)	14883.513(-2)	14881.678(-21)		14876.355(-21)	
R(21)	14882.827(-15)	14880.942(18)	14879.187(-11)	14875.649(0)	
R(22)		14880.207(12)	14878.421(19)	14874.910(11)	
R(23)	14881.304(-26)	14879.414(18)	14877.647(14)		
R(24)	14880.443(2)				

Table C.6 continued

Fitted Spectroscopic Constants [b]					
ν_0 (cm^{-1})	14887.9450(27)	14886.0751(34)	14884.2327(32)	14880.6580(31)	14877.2332(60)
B_3' (cm^{-1})	0.116572(25)	0.116163(34)	0.115796(39)	0.114743(38)	0.114007(118)
r_3' (Å)	2.04789(22)	2.04715(30)	2.04614(35)	2.04721(34)	2.04579(106)
B_0'' (cm^{-1})	0.138786(30)	0.138297(38)	0.137770(34)	0.136513(50)	0.135508(126)
r_0'' (Å)	1.87685(20)	1.87619(26)	1.87588(23)	1.87689(34)	1.87648(87)

[a] Residuals (ν(calculated) – ν(measured)) are given in parentheses following each line position, in units of 0.001 cm^{-1}.

[b] Error limits (1σ) are provided for each fitted spectroscopic constant, in units of the last digit quoted. B_0'' was constrained to take the same value in all of the unperturbed bands (the 1-0, 3-0, 4-0, 7-0, 10-0, and 11-0 bands), which all originated from the $v'' = 0$ level of the ground $X\ ^1\Sigma^+$ state. This band was included in the combined fit, in which bands were fitted to the form $\nu = \nu_0 + B'J'(J'+1) - B''J''(J''+1)$.

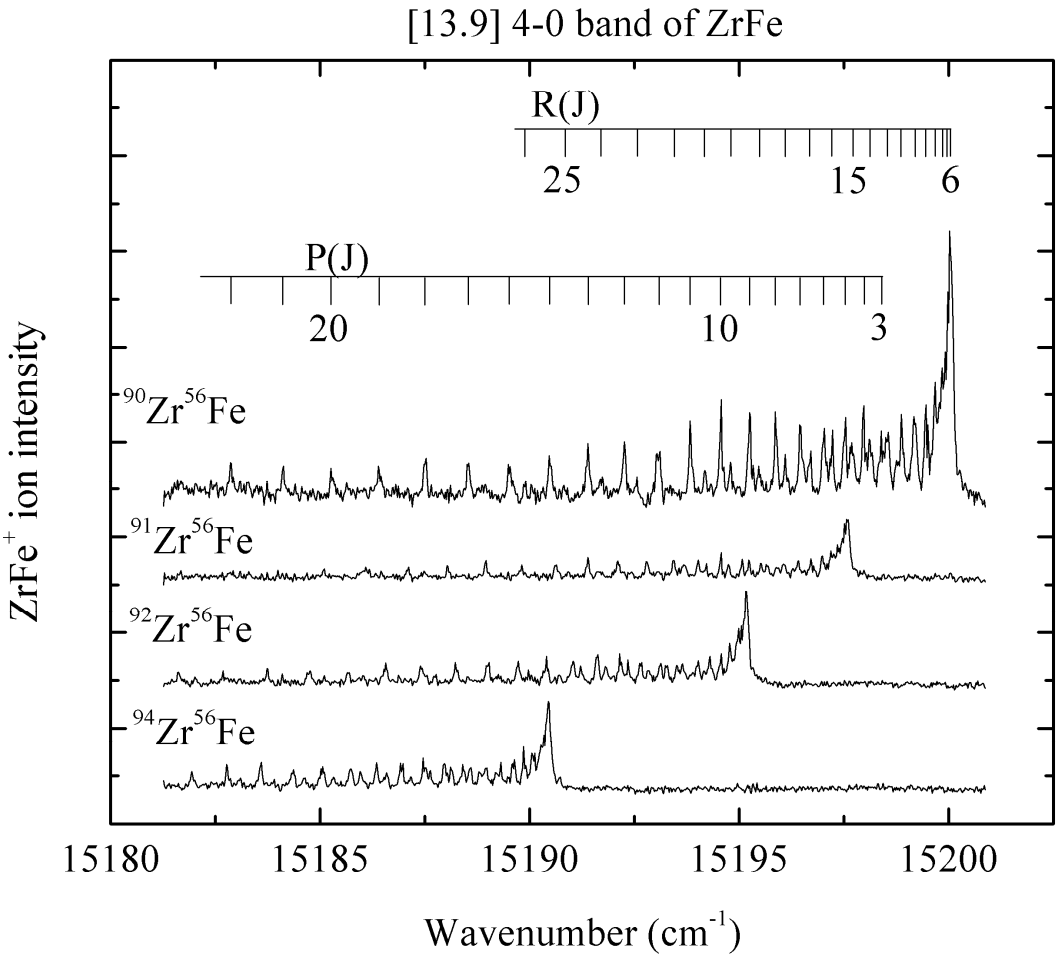

Figure C15. Rotationally resolved spectra of the various ZrFe isotopic combinations for the 4-0 band of the [13.9] $0^{+}\leftarrow X\ ^{1}\Sigma^{+}$ system. Line assignments are provided for the most abundant isotopomer, $^{90}Zr^{56}Fe$.

Table C.7

Fitted Rotational Lines of the 4-0 band of the $[13.9]0^{+} \leftarrow X\ ^{1}\Sigma^{+}$ system of ZrFe.

Line	$^{90}Zr^{56}Fe$	$^{91}Zr^{56}Fe$	$^{92}Zr^{56}Fe$	$^{94}Zr^{56}Fe$	$^{96}Zr^{56}Fe$
P(2)		15196.281(6)	15193.893(-10)	15189.202(-17)	
P(3)	15198.388(1)	15195.911(11)	15193.515(3)	15188.817(7)	
P(4)	15197.964(13)	15195.520(-9)	15193.114(-5)	15188.413(5)	15183.862(23)
P(5)	15197.536(-16)	15195.075(-19)	15192.653(2)	15187.964(5)	15183.462(-21)
P(6)	15197.021(-3)	15194.569(-13)	15192.167(-10)	15187.484(-9)	15182.936(16)
P(7)	15196.458(13)	15194.022(-10)	15191.608(5)	15186.942(-4)	15182.430(-10)
P(8)	15195.863(16)	15193.438(-16)	15191.039(-12)	15186.352(5)	15181.841(3)
P(9)	15195.254(-12)	15192.797(-9)	15190.402(-7)	15185.736(-6)	
P(10)	15194.569(-8)	15192.112(-2)	15189.713(5)	15185.060(1)	
P(11)	15193.834(1)	15191.391(-5)	15189.001(-4)	15184.362(-15)	
P(12)	15193.067(-5)	15190.622(-5)	15188.226(6)	15183.591(-2)	
P(13)	15192.261(-14)	15189.819(-14)	15187.409(12)	15182.777(10)	
P(14)	15191.390(-4)	15188.953(-5)	15186.572(-5)	15181.940(1)	
P(15)	15190.485(-6)	15188.038(8)	15185.690(-22)		
P(16)	15189.519(9)	15187.097(2)	15184.725(-1)		
P(17)	15188.537(-5)	15186.087(21)	15183.738(-3)		
P(18)	15187.507(-15)	15185.088(-16)	15182.682(21)		
P(19)	15186.399(6)				
P(20)	15185.256(19)				
P(21)	15184.114(-15)				
P(22)	15182.866(13)				
R(0)		15197.102(15)			

Table C.7 continued

R(1)	15199.785(-7)				
R(2)	15199.918(3)	15197.448(-1)		15190.340(-10)	15185.791(-8)
R(3)			15195.115(20)		15185.891(-12)
R(4)	15200.066(6)	15197.596(3)	15195.171(17)	15190.473(6)	15185.942(-9)
R(5)	15200.066(14)	15197.596(11)	15195.171(25)	15190.473(14)	15185.942(1)
R(6)	15200.034(9)	15197.568(3)	15195.171(-11)	15190.449(2)	15185.891(18)
R(7)	15199.985(-24)	15197.471(19)		15190.389(-17)	
R(8)	15199.844(-9)		15194.985(-32)		15185.701(11)
R(9)	15199.674(-10)	15197.190(5)	15194.774(10)	15190.065(16)	15185.562(-14)
R(10)	15199.452(-5)	15196.981(-1)	15194.572(-3)	15189.860(9)	15185.340(0)
R(11)	15199.185(0)	15196.712(8)	15194.300(10)	15189.618(-5)	15185.077(11)
R(12)	15198.873(7)	15196.413(3)	15194.016(-10)	15189.309(4)	15184.790(4)
R(13)	15198.512(17)	15196.065(2)	15193.650(9)	15188.967(2)	
R(14)	15198.117(16)	15195.666(8)	15193.270(-5)	15188.582(-2)	15184.093(-19)
R(15)	15197.690(2)	15195.235(0)	15192.831(-2)	15188.134(13)	
R(16)	15197.221(-15)	15194.749(4)	15192.349(-2)		15183.183(-3)
R(17)	15196.683(-8)	15194.219(6)	15191.818(2)	15187.168(-17)	15182.658(9)
R(18)	15196.096(5)			15186.589(-3)	
R(19)	15195.467(13)			15185.967(11)	
R(20)	15194.795(19)			15185.324(0)	
R(21)				15184.621(6)	
R(22)		15190.927(-10)		15183.903(-16)	
R(23)	15192.563(-13)			15183.097(5)	
R(25)	15190.812(3)				
R(26)	15189.893(-13)				

Table C.7 continued

Fitted Spectroscopic Constants [b]					
ν_0 (cm^{-1})	15199.3570(27)	15196.8856(27)	15194.4780(37)	15189.7750(25)	15185.2308(46)
B_4' (cm^{-1})	0.116337(27)	0.115960(40)	0.115497(41)	0.114469(48)	0.113749(128)
r_4' (Å)	2.04996(24)	2.04894(35)	2.04879(36)	2.04966(43)	2.04811(115)
B_0'' (cm^{-1})	0.138786(30)	0.138297(38)	0.137770(34)	0.136513(50)	0.135508(126)
r_0'' (Å)	1.87685(20)	1.87619(26)	1.87588(23)	1.87689(34)	1.87648(87)

[a] Residuals (ν(calculated) – ν(measured)) are given in parentheses following each line position, in units of 0.001 cm^{-1}.

[b] Error limits (1σ) are provided for each fitted spectroscopic constant, in units of the last digit quoted. B_0'' was constrained to take the same value in all of the unperturbed bands (the 1-0, 3-0, 4-0, 7-0, 10-0, and 11-0 bands), which all originated from the $v'' = 0$ level of the ground $X\ ^1\Sigma^+$ state. This band was included in the combined fit, in which bands were fitted to the form $\nu = \nu_0 + B'J'(J'+1) - B''J''(J''+1)$.

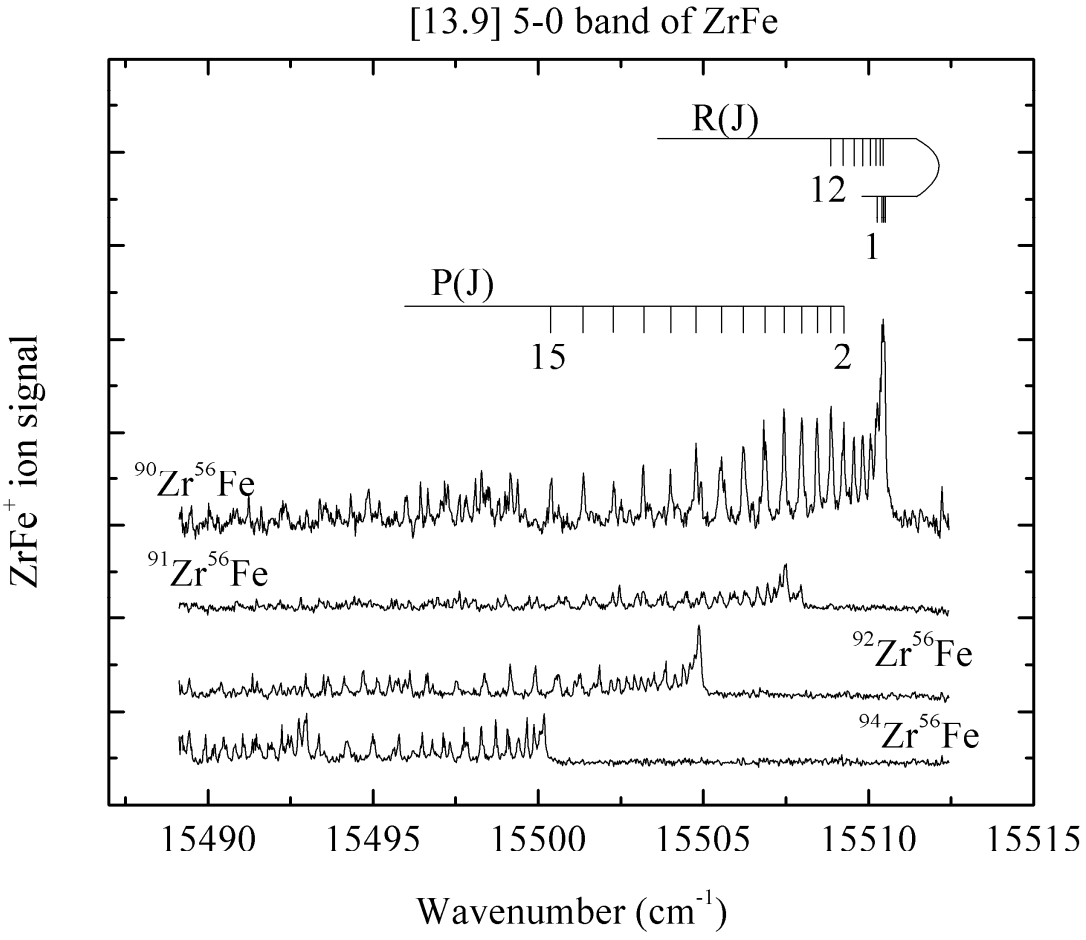

Figure C16. Rotationally resolved spectra of the various ZrFe isotopic combinations for the 5-0 band of the [13.9] $0^+ \leftarrow X\ ^1\Sigma^+$ system. Line assignments are provided for the most abundant isotopomer, $^{90}Zr^{56}Fe$.

Table C.8

Assigned Rotational Lines of the 5-0 band of the $[13.9]0^{+} \leftarrow X\ ^{1}\Sigma^{+}$ system of ZrFe.[a]

Line	$^{90}Zr^{56}Fe$	$^{91}Zr^{56}Fe$	$^{92}Zr^{56}Fe$	$^{94}Zr^{56}Fe$	$^{96}Zr^{56}Fe$
P(2)	15509.255			15499.131	
P(3)	15508.858		15503.331	15498.713	
P(4)	15508.439		15502.909	15498.274	
P(5)	15507.978		15502.401	15497.749	15494.433
P(6)	15507.445		15501.849	15497.118	15493.756
P(7)	15506.858		15501.256	15496.489	15493.036
P(8)	15506.216		15500.594	15495.780	15492.250
P(9)	15505.525		15499.909	15494.993	15491.424
P(10)	15504.780		15499.153	15494.214	
P(11)	15504.003		15498.368	15493.355	
P(12)	15503.179		15497.526	15492.429	
P(13)	15502.291		15496.630	15491.469	
P(14)	15501.368		15495.676		
P(15)	15500.386		15494.693		
P(16)	15499.380		15493.647		
P(17)	15498.290				
R(0)	15510.096				
R(1)	15510.270			15500.087	
R(2)	15510.364			15500.172	15496.873
R(3)	15510.453		15504.871	15500.172	15496.873
R(4)	15510.489		15504.871		15496.746
R(5)	15510.453			15500.044	15496.582

Table C.8 continued

R(6)	15510.364		15504.741	15499.876	15496.308
R(7)	15510.226		15504.595	15499.661	15496.000
R(8)	15510.056		15504.400	15499.405	15495.642
R(9)	15509.822		15504.138	15499.069	15495.179
R(10)	15509.554		15503.863	15498.713	15494.675
R(11)	15509.241		15503.513	15498.274	15494.145
R(12)	15508.858		15503.114		
R(13)	15508.439		15502.680		
R(14)	15507.978		15502.211		
R(15)	15507.445		15501.685		
R(16)	15506.858				
R(17)	15506.216				
Fitted Spectroscopic Constants [b]					
ν_0 (cm^{-1})	15509.8462(41)		15504.2799(78)	15499.6941(110)	15496.4720(144)
B_5' (cm^{-1})	0.113581(27)		0.111691(64)	0.106198(135)	0.099339(191)
r_5' (Å)	2.07468(25)		2.08341(60)	2.12798(135)	2.19163(211)
B_0'' (cm^{-1})	0.138786(30)	0.138297(38)	0.137770(34)	0.136513(50)	0.135508(126)
r_0'' (Å)	1.87685(20)	1.87619(26)	1.87588(23)	1.87689(34)	1.87648(87)

[a] The upper state of this band is perturbed by a nearby state. Lines have been identified using combination differences calculated from the known ground state rotational constant, but no attempt has been made to deperturb the state. For the $^{91}Zr^{56}Fe$ isotopic modification, the two states lie too close to reliably identify lines.

[b] For the rotational fit for this band, B_0'' was held fixed at the value found from the combined fit. Errors in the fit were somewhat larger than for unperturbed bands, as expected. The perturbation is evident from the variation in r′ values as a function of reduced mass.

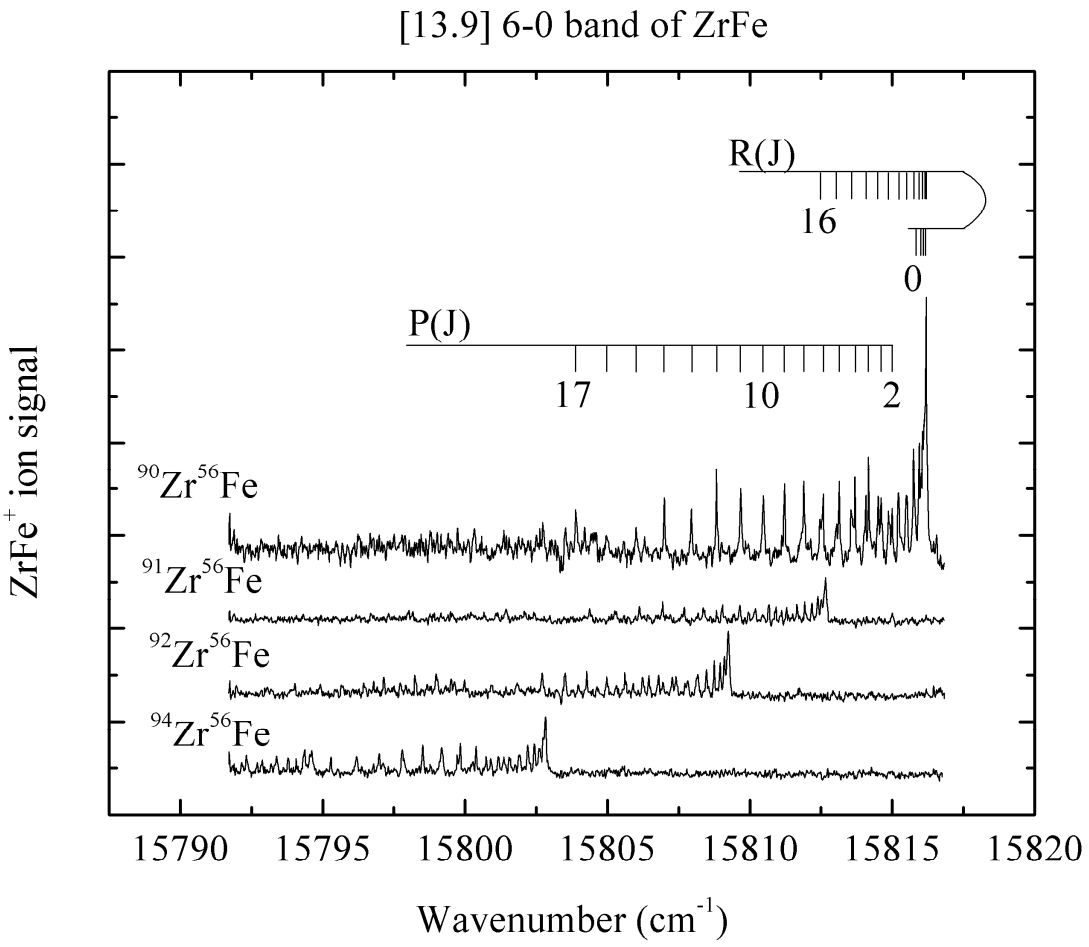

Figure C.17. Rotationally resolved spectra of the various ZrFe isotopic combinations for the 6-0 band of the [13.9] $0^{+}\leftarrow X\,^{1}\Sigma^{+}$ system. Line assignments are provided for the most abundant isotopomer, $^{90}Zr^{56}Fe$.

Table C.9

Assigned Rotational Lines of the 6-0 band of the $[13.9]0^{+} \leftarrow X\ ^{1}\Sigma^{+}$ system of ZrFe.[a]

Line	$^{90}Zr^{56}Fe$	$^{91}Zr^{56}Fe$	$^{92}Zr^{56}Fe$	$^{94}Zr^{56}Fe$	$^{96}Zr^{56}Fe$
P(2)	15814.994			15801.760	
P(3)	15814.608	15811.1184		15801.363	
P(4)	15814.169	15810.665	15807.273	15800.904	15795.050
P(5)	15813.694	15810.196	15806.778	15800.384	15794.563
P(6)	15813.139	15809.649	15806.233	15799.832	15793.986
P(7)	15812.573	15809.032	15805.611	15799.178	15793.325
P(8)	15811.896	15808.392	15804.979	15798.511	
P(9)	15811.217	15807.695	15804.273	15797.792	15791.858
P(10)	15810.476	15806.941	15803.506	15796.982	
P(11)	15809.682	15806.121	15802.709		
P(12)	15808.827	15805.281	15801.836		
P(13)	15807.945	15804.374	15800.937		
P(14)	15806.995		15799.976		
P(15)	15806.008				
P(17)	15803.893				
R(0)	15815.809				
R(2)	15816.116			15802.823	
R(3)	15816.188		15809.244	15802.846	15796.978
R(4)	15816.188	15812.673	15809.244	15802.823	15796.978
R(5)	15816.153		15809.206	15802.747	15796.848

Table C.9 continued

R(6)	15816.068	15812.524	15809.106	15802.612	15796.718
R(7)	15815.947	15812.387	15808.952	15802.438	15796.463
R(8)	15815.750	15812.178	15808.753	15802.191	15796.171
R(9)	15815.504	15811.923	15808.478		15795.835
R(10)	15815.218	15811.657			15795.453
R(11)	15814.867	15811.289	15807.820		
R(12)	15814.510		15807.410		
R(13)	15814.071		15806.949		
R(14)	15813.555		15806.451		
R(15)	15813.047				
R(16)	15812.460				
Fitted Spectroscopic Constants [b]					
ν_0 (cm^{-1})	15815.5760(49)	15812.0899(61)	15808.6691(50)	15802.3446(60)	15796.5229(83)
B_6' (cm^{-1})	0.113078(35)	0.111817(68)	0.111183(43)	0.107290(122)	0.104696(126)
r_6' (Å)	2.07929(32)	2.08656(63)	2.08816(40)	2.11712(120)	2.13482(129)
B_0'' (cm^{-1})	0.138786(30)	0.138297(38)	0.137770(34)	0.136513(50)	0.135508(126)
r_0'' (Å)	1.87685(20)	1.87619(26)	1.87588(23)	1.87689(34)	1.87648(87)

[a] The upper state of this band is perturbed by a nearby state. Lines have been identified using combination differences calculated from the known ground state rotational constant, but no attempt has been made to deperturb the state.

[b] For the rotational fit for this band, B_0'' was held fixed at the value found from the combined fit. Errors in the fit were somewhat larger than for unperturbed bands, as expected. The perturbation is evident from the variation in r′ values as a function of reduced mass.

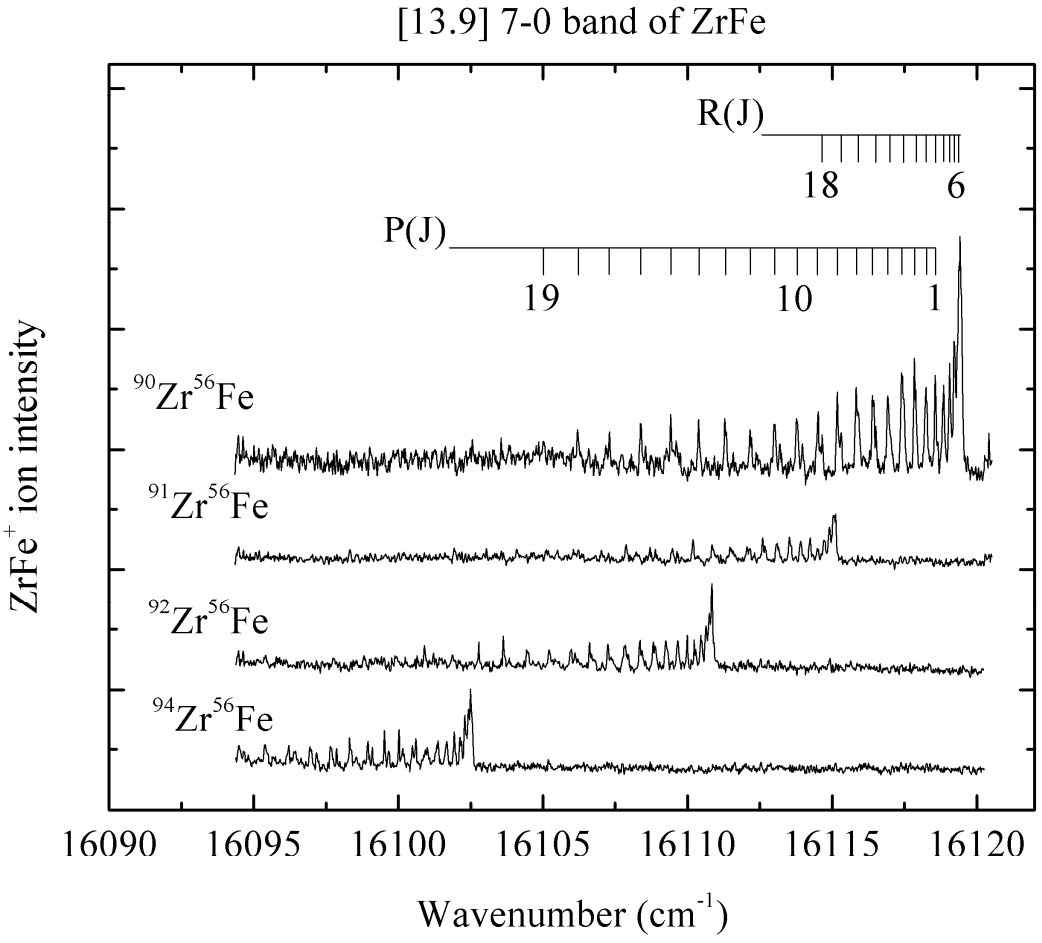

Figure C.18. Rotationally resolved spectra of the various ZrFe isotopic combinations for the 7-0 band of the [13.9] $0^{+}\leftarrow X\ ^{1}\Sigma^{+}$ system. Line assignments are provided for the most abundant isotopomer, $^{90}Zr^{56}Fe$.

Table C.10

Fitted Rotational Lines of the 7-0 band of the $[13.9]0^+ \leftarrow X\ ^1\Sigma^+$ system of ZrFe.

Line	$^{90}Zr^{56}Fe$	$^{91}Zr^{56}Fe$	$^{92}Zr^{56}Fe$	$^{94}Zr^{56}Fe$
P(1)	16118.560(-22)			
P(2)	16118.237(-27)			
P(3)	16117.841(-8)	16113.523(-24)	16109.247(-17)	
P(4)	16117.415(-9)	16113.081(-7)	16108.812(-5)	16100.484(-5)
P(5)	16116.923(7)	16112.599(0)	16108.349(-14)	16100.021(-8)
P(6)	16116.413(-10)	16112.059(15)	16107.834(-21)	16099.521(-22)
P(7)	16115.829(-3)		16107.249(-7)	16098.945(-9)
P(8)	16115.176(25)	16110.852(24)	16106.610(12)	16098.315(10)
P(9)	16114.508(16)	16110.186(17)	16105.962(-10)	16097.666(0)
P(10)	16113.778(20)	16109.475(4)	16105.224(11)	16096.958(1)
P(11)	16113.007(15)	16108.696(10)	16104.460(6)	16096.212(-9)
P(12)	16112.214(-17)	16107.869(15)	16103.631(18)	16095.395(4)
P(13)	16111.334(-13)	16107.024(-12)	16102.781(2)	
P(14)	16110.383(13)	16106.056(34)	16101.872(-5)	
P(15)	16109.418(4)	16105.108(11)	16100.905(-2)	
P(16)	16108.384(12)	16104.100(-2)	16099.916(-27)	
P(17)	16107.296(26)	16103.049(-22)		
P(18)	16106.201(-4)			
P(19)	16105.023(0)			
R(0)	16119.060(-17)			
R(1)	16119.225(-3)	16114.878(4)		
R(2)	16119.332(18)			
R(3)	16119.423(4)			
R(4)	16119.459(-3)	16115.120(-3)	16110.838(6)	16102.495(7)
R(5)	16119.423(12)	16115.120(-24)	16110.838(-14)	16102.495(-9)
R(6)	16119.382(-18)	16115.040(-16)	16110.751(4)	16102.426(-5)
R(7)	16119.225(18)	16114.907(-3)	16110.637(0)	16102.299(8)
R(8)	16119.060(12)	16114.742(-7)	16110.458(12)	16102.125(20)
R(9)	16118.858(-7)	16114.519(-4)	16110.230(23)	16101.937(-1)
R(10)		16114.238(8)	16109.988(-1)	16101.676(2)
R(11)	16118.277(-16)	16113.907(20)	16109.667(4)	16101.377(-5)
R(12)	16117.888(2)	16113.580(-22)	16109.299(8)	16101.002(15)
R(13)	16117.474(-4)	16113.147(-7)	16108.885(10)	16100.604(10)
R(14)	16116.970(31)	16112.684(-12)	16108.423(8)	16100.151(12)
R(15)	16116.513(-31)	16112.150(5)	16107.904(15)	16099.669(-6)
R(16)	16115.890(23)		16107.357(1)	16099.100(16)
R(17)	16115.306(-13)			16098.544(-25)
R(18)	16114.657(-32)			16097.869(6)

Table C.10 continued

R(19)				16097.178(4)
R(20)				16096.422(20)
R(21)			16103.832(-18)	16095.682(-30)
R(22)				16094.817(-2)
R(25)	16108.548(-1)			
Fitted Spectroscopic Constants [b]				
ν_0 (cm^{-1})	16118.8157(38)	16114.4780(52)	16110.2045(38)	16101.8612(37)
B_7' (cm^{-1})	0.113877(28)	0.113486(48)	0.113160(39)	0.112372(48)
r_7' (Å)	2.07198(26)	2.07116(44)	2.06984(36)	2.06869(44)
B_0'' (cm^{-1})	0.138786(30)	0.138297(38)	0.137770(34)	0.136513(50)
r_0'' (Å)	1.87685(20)	1.87619(26)	1.87588(23)	1.87689(34)

[a] Residuals (ν(calculated) – ν(measured)) are given in parentheses following each line position, in units of 0.001 cm^{-1}.

[b] Error limits (1σ) are provided for each fitted spectroscopic constant, in units of the last digit quoted. B_0'' was constrained to take the same value in all of the unperturbed bands (the 1-0, 3-0, 4-0, 7-0, 10-0, and 11-0 bands), which all originated from the v″ = 0 level of the ground X $^1\Sigma^+$ state. This band was included in the combined fit, in which bands were fitted to the form

$\nu = \nu_0 + B'J'(J'+1) - B''J''(J''+1)$.

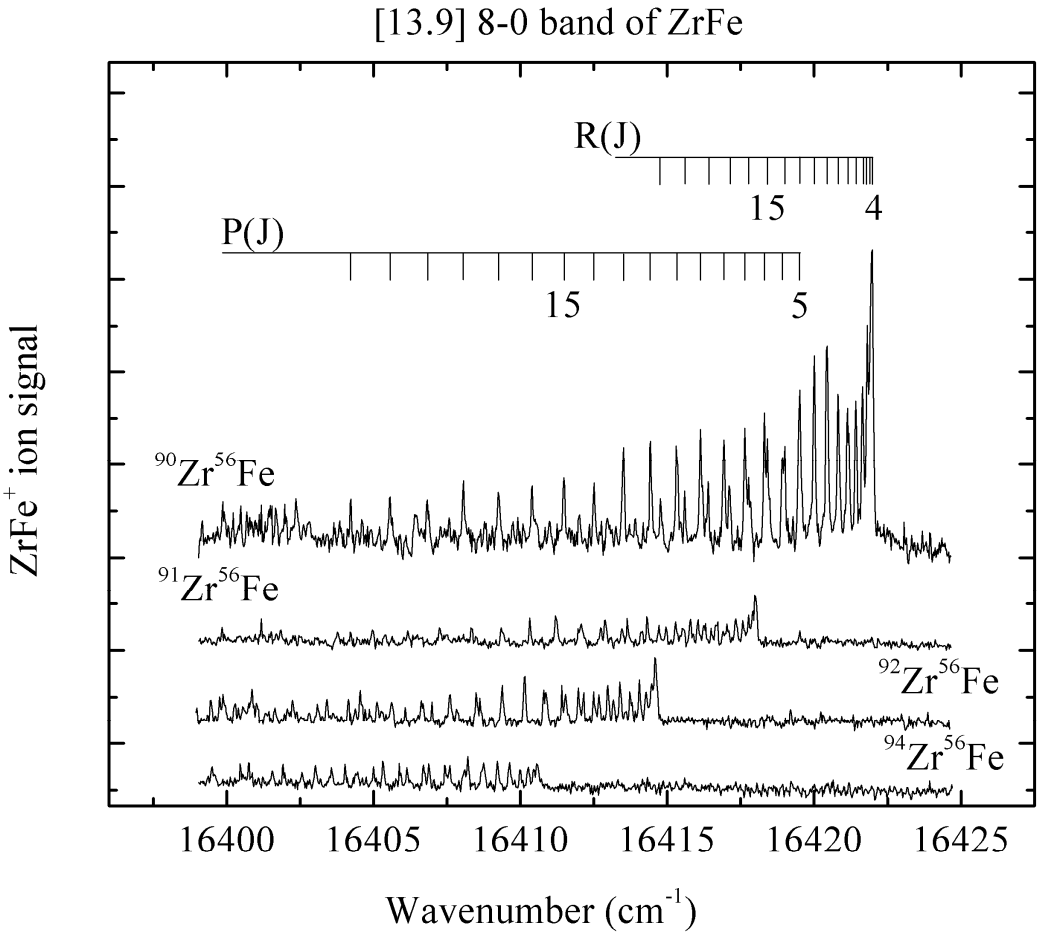

Figure C.19. Rotationally resolved spectra of the various ZrFe isotopic combinations for the 8-0 band of the [13.9] $0^{+}\leftarrow X\,^{1}\Sigma^{+}$ system. Line assignments are provided for the most abundant isotopomer, $^{90}Zr^{56}Fe$.

Table C.11

Assigned Rotational Lines of the 8-0 band of the $[13.9]0^+ \leftarrow X\ ^1\Sigma^+$ system of ZrFe.[a]

Line	$^{90}Zr^{56}Fe$	$^{91}Zr^{56}Fe$	$^{92}Zr^{56}Fe$	$^{94}Zr^{56}Fe$
P(2)		16416.895		
P(3)		16416.491	16413.167	
P(4)		16416.042	16412.677	16408.673
P(5)	16419.482	16415.537		16408.100
P(6)	16418.921	16414.963	16411.541	16407.436
P(7)	16418.309	16414.315	16410.865	16406.696
P(8)	16417.645	16413.643	16410.150	16405.881
P(9)	16416.929	16412.884	16409.379	16404.999
P(10)	16416.133	16412.067	16408.498	16404.034
P(11)	16415.324	16411.215	16407.604	16403.022
P(12)	16414.425	16410.317	16406.638	16401.916
P(13)	16413.510	16409.363	16405.622	16400.755
P(14)	16412.505	16408.345	16404.551	16399.501
P(15)	16411.485	16407.258	16403.412	
P(16)			16402.246	
P(17)	16410.391	16406.165		
P(18)	16409.255	16404.969		
P(19)		16403.780		
R(2)				16410.570
R(3)	16421.971		16414.586	16410.570
R(4)	16421.971	16417.991		16410.458
R(5)	16421.917	16417.912	16414.465	16410.261
R(6)	16421.808	16417.768	16414.279	16409.990
R(7)	16421.640	16417.574	16414.048	16409.632
R(8)	16421.421	16417.329	16413.737	16409.224
R(9)	16421.181	16417.031	16413.391	16408.751
R(10)	16420.818	16416.677	16412.975	16408.208
R(11)	16420.436	16416.274	16412.491	16407.596
R(12)	16420.004	16415.785	16411.980	16406.887
R(13)	16419.515	16415.283	16411.413	16406.141
R(14)	16418.998	16414.715	16410.794	16405.325
R(15)	16418.412	16414.105		16404.394
R(16)		16413.460		16403.574
R(17)		16412.741		

Table C.11 continued

Fitted spectroscopic constants[b]				
ν_0 (cm^{-1})	16421.3937(58)	16417.4386(124)	16414.0982(122)	16410.1628(170)
B_9' (cm^{-1})	0.111431(37)	0.109781(70)	0.106540(91)	0.099238(125)
r_9' (Å)	2.09460(35)	2.10582(67)	2.13318(91)	2.20133(139)
B_0'' (cm^{-1})	0.138786(30)	0.138297(38)	0.137770(34)	0.136513(50)
r_0'' (Å)	1.87685(20)	1.87619(26)	1.87588(23)	1.87689(34)

[a] The upper state of this band is perturbed by a nearby state. Lines have been identified using combination differences calculated from the known ground state rotational constant, but no attempt has been made to deperturb the upper state.
[b] For the rotational fit for this band, B_0'' was held fixed at the value found from the combined fit. Errors in the fit were somewhat larger than for unperturbed bands, as expected. The perturbation is evident from the variation in r′ values as a function of reduced mass.

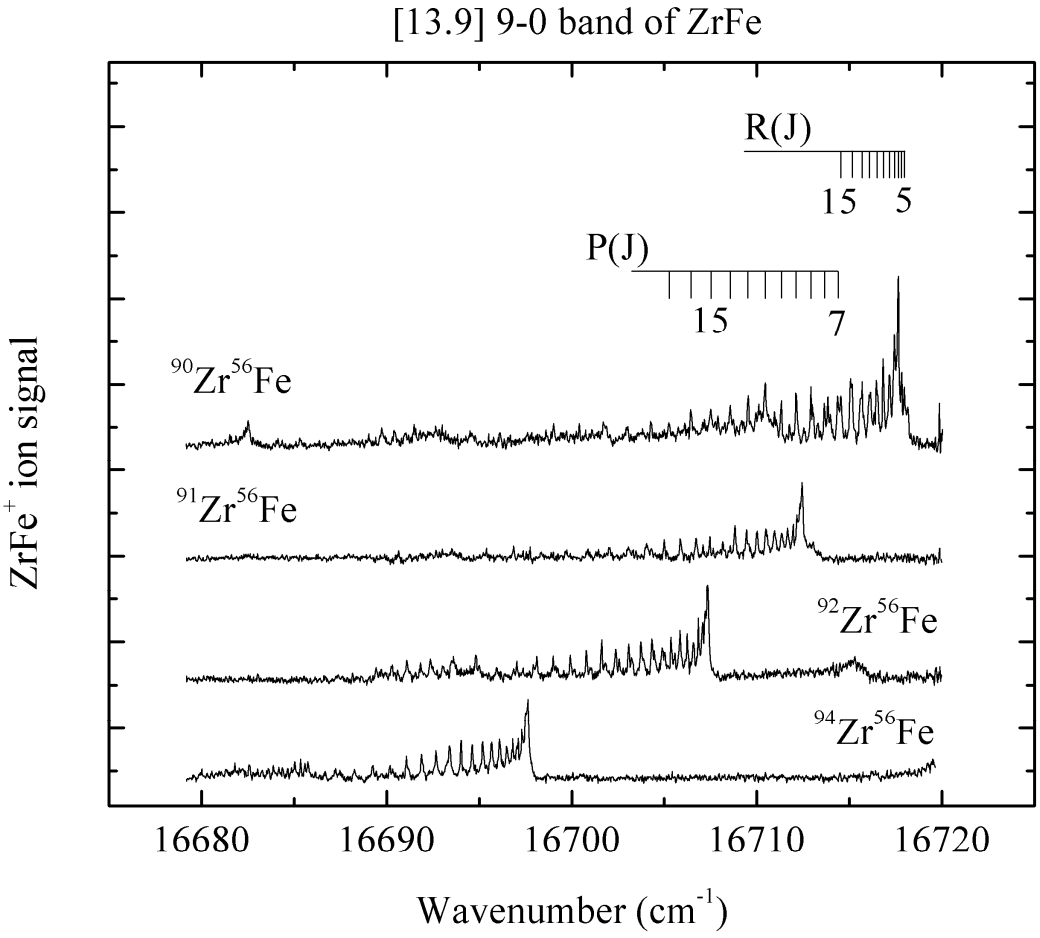

Figure C.20. Rotationally resolved spectra of the various ZrFe isotopic combinations for the 9-0 band of the [13.9] $0^{+}\leftarrow X\,^{1}\Sigma^{+}$ system. Line assignments are provided for the most abundant isotopomer, $^{90}Zr^{56}Fe$.

Table C.12

Assigned Rotational Lines of the 9-0 band of the $[13.9]0^{+} \leftarrow X\ ^{1}\Sigma^{+}$ system of ZrFe.[a]

Line	$^{90}Zr^{56}Fe$	$^{91}Zr^{56}Fe$	$^{92}Zr^{56}Fe$	$^{94}Zr^{56}Fe$	$^{96}Zr^{56}Fe$
P(4)		16710.496	16705.363	16695.6605	16686.894
P(5)		16710.005	16704.888	16695.1796	16686.375
P(6)		16709.437	16704.332	16694.6183	16685.824
P(7)	16714.363	16708.818	16703.741	16694.0296	16685.186
P(8)	16713.649	16708.154	16703.077	16693.3937	16684.502
P(9)	16712.924	16707.462	16702.369	16692.6600	16683.729
P(10)	16712.142	16706.719	16701.612	16691.8864	16682.930
P(11)	16711.335	16705.865	16700.780	16691.0674	16682.078
P(12)	16710.471	16704.997	16699.919	16690.1659	16681.168
P(13)	16709.531	16704.030	16698.988	16689.2360	16680.156
P(14)	16708.574	16703.060		16688.2574	
P(15)	16707.509	16702.032	16697.027	16687.2411	
P(16)	16706.445	16700.873	16695.924		
P(17)	16705.238	16699.654	16694.807		
P(18)	16704.287	16698.336	16693.627		
P(19)	16703.003		16692.359		
P(20)	16701.749		16691.091		
P(21)	16700.419		16689.712		
P(22)	16699.032				
P(23)	16697.612				

Table C.12 continued

P(24)	16696.126				
R(2)		16712.441		16697.5874	16688.800
R(3)		16712.495	16707.357	16697.6298	16688.800
R(4)		16712.495	16707.357	16697.6298	16688.800
R(5)	16717.971	16712.402	16707.321	16697.5874	16688.698
R(6)	16717.828	16712.327	16707.211	16697.5021	16688.591
R(7)	16717.651	16712.161	16707.066	16697.3034	16688.360
R(8)	16717.434	16711.962	16706.837	16697.0996	16688.117
R(9)	16717.151	16711.667	16706.571	16696.8181	16687.759
R(10)	16716.837	16711.343	16706.241	16696.4735	16687.392
R(11)	16716.471	16710.957	16705.857	16696.0898	16686.894
R(12)	16716.070	16710.496		16695.6340	
R(13)	16715.601	16710.005	16705.021	16695.1796	
R(14)	16715.062	16709.437	16704.458		
R(15)	16714.363	16708.818	16703.882		
R(16)	16713.981		16703.244		
R(17)	16713.294		16702.557		
R(18)			16701.816		
R(19)	16711.761		16701.009		
R(20)	16710.954		16700.138		
R(21)	16710.100		16699.240		

Table C.12 continued

Fitted spectroscopic constants[b]					
ν_0 (cm^{-1})	16717.4098(140)	16711.9520(113)	16706.7850(43)	16697.0953(58)	16688.3375(71)
B_9' (cm^{-1})	0.111467(89)	0.110493(75)	0.110897(18)	0.109049(51)	0.105656(82)
r_9' (Å)	2.09426(84)	2.09902(71)	2.09085(17)	2.09998(49)	2.12510(83)
B_0'' (cm^{-1})	0.138786(30)	0.138297(38)	0.137770(34)	0.136513(50)	0.135508(126)
r_0'' (Å)	1.87685(20)	1.87619(26)	1.87588(23)	1.87689(34)	1.87648(87)

[a] The upper state of this band is perturbed by a nearby state. Lines have been identified using combination differences calculated from the known ground state rotational constant, but no attempt has been made to deperturb the state.
[b] For the rotational fit for this band, B_0'' was held fixed at the value found from the combined fit. Errors in the fit were somewhat larger than for unperturbed bands, as expected. The perturbation is evident from the variation in r′ values as a function of reduced mass.

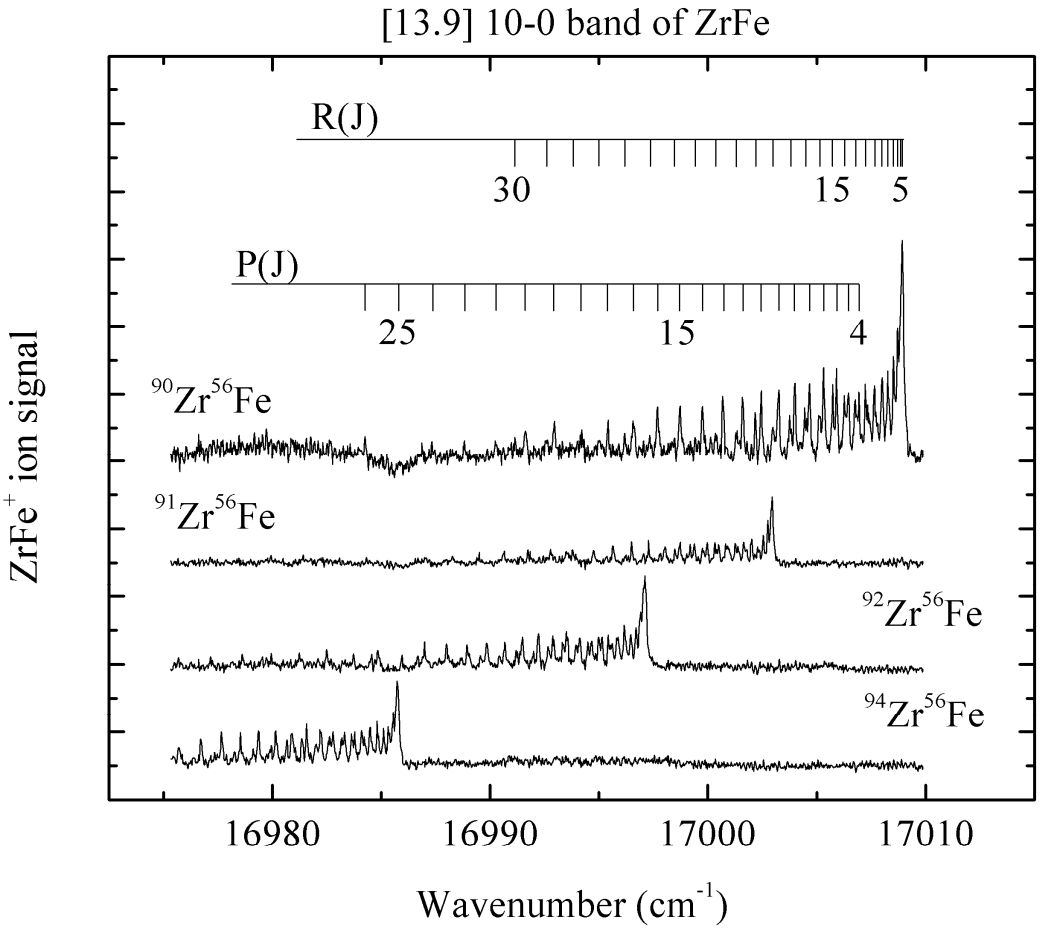

Figure C.21. Rotationally resolved spectra of the various ZrFe isotopic combinations for the 10-0 band of the [13.9] $0^{+}\leftarrow X\ ^{1}\Sigma^{+}$ system. Line assignments are provided for the most abundant isotopomer, $^{90}Zr^{56}Fe$.

Table C.13

Fitted Rotational Lines of the 10-0 band of the $[13.9]0^+ \leftarrow X\ ^1\Sigma^+$ system of ZrFe.

Line	$^{90}Zr^{56}Fe$	$^{91}Zr^{56}Fe$	$^{92}Zr^{56}Fe$	$^{94}Zr^{56}Fe$
P(2)		17001.782(4)		16984.568(17)
P(3)		17001.387(19)	16995.562(4)	16984.226(-17)
P(4)	17006.947(-10)	17000.975(-2)	16995.137(-1)	16983.778(5)
P(5)	17006.452(-1)	17000.500(-10)	16994.646(8)	16983.313(-7)
P(6)	17005.902(11)	16999.974(-21)	16994.110(11)	16982.778(0)
P(7)	17005.307(16)	16999.380(-14)	16993.534(2)	16982.217(-18)
P(8)	17004.668(14)	16998.715(12)	16992.895(4)	16981.562(6)
P(9)	17003.997(-8)	16998.046(-10)	16992.220(-9)	16980.890(-3)
P(10)	17003.256(-13)	16997.280(12)	16991.487(-16)	16980.149(5)
P(11)	17002.454(-9)	16996.492(6)	16990.684(-5)	16979.366(5)
P(12)	17001.596(0)	16995.640(10)	16989.847(-10)	16978.538(-2)
P(13)	17000.690(3)	16994.755(-4)	16988.941(1)	16977.665(-15)
P(14)	16999.745(-5)	16993.786(15)	16987.992(4)	16976.723(-9)
P(15)	16998.721(13)	16992.776(24)	16986.983(15)	16975.715(12)
P(16)	16997.683(-6)	16991.737(8)	16985.946(3)	
P(17)	16996.575(-8)	16990.650(-11)	16984.841(7)	
P(18)	16995.420(-15)	16989.499(-18)	16983.721(-25)	
P(19)	16994.214(-22)	16988.267(4)	16982.496(-5)	
P(20)	16992.949(-23)		16981.230(5)	
P(21)	16991.620(-12)		16979.944(-15)	
P(22)	16990.240(-1)	16984.318(13)		
P(23)	16988.820(-3)		16977.154(5)	
P(24)	16987.332(11)	16981.414(32)	16975.683(14)	
P(25)		16979.929(-4)		
P(26)	16984.258(-19)			
R(0)	17008.586(-1)			16985.388(15)
R(1)				16985.564(10)
R(2)	17008.871(9)			
R(3)	17008.924(25)			16985.771(-9)
R(4)			16997.155(-3)	16985.771(9)
R(5)	17008.924(8)		16997.111(7)	16985.733(15)
R(6)	17008.833(12)		16997.044(-12)	16985.664(-1)
R(7)	17008.722(-15)	17002.758(-20)	16996.894(1)	16985.519(9)
R(8)	17008.519(-2)	17002.550(-2)	16996.708(-1)	16985.331(10)
R(9)	17008.259(15)	17002.290(15)	16996.457(9)	16985.108(-4)
R(10)	17008.004(-25)	17002.019(-7)	16996.164(11)	16984.814(2)
R(11)	17007.647(-14)	17001.654(13)	16995.836(-5)	16984.484(-7)
R(12)	17007.232(2)	17001.269(0)	16995.424(12)	16984.105(-20)

Table C.13 continued

R(13)	17006.757(27)	17000.820(0)	16994.986(3)	16983.652(-7)
R(14)	17006.269(13)	17000.317(2)	16994.494(-3)	16983.172(-20)
R(15)	17005.730(-3)	16999.784(-18)	16993.950(-9)	16982.631(-23)
R(16)	17005.128(-8)	16999.194(-32)	16993.339(0)	16982.007(7)
R(17)	17004.450(12)	16998.487(18)	16992.678(9)	16981.357(11)
R(18)	17003.759(-8)	16997.804(-6)	16991.996(-14)	16980.667(4)
R(19)	17002.980(9)	16997.045(-8)	16991.226(0)	
R(20)	17002.178(-4)		16990.430(-12)	16979.116(8)
R(21)			16989.558(1)	16978.264(11)
R(22)			16988.656(-8)	
R(23)	16999.413(5)	16993.499(-21)	16987.669(16)	
R(24)			16986.670(1)	
R(25)	16997.331(-10)			
R(26)	16996.176(19)			
R(27)	16995.012(4)			
R(30)	16991.151(17)			
Fitted Spectroscopic Constants [b]				
ν_0 (cm^{-1})	17008.3588(29)	17002.3908(40)	16996.5477(24)	16985.1813(29)
B_{10}' (cm^{-1})	0.112782(27)	0.112379(33)	0.111978(37)	0.110992(39)
r_{10}' (Å)	2.08201(25)	2.08133(31)	2.08073(34)	2.08151(37)
B_0'' (cm^{-1})	0.138786(30)	0.138297(38)	0.137770(34)	0.136513(50)
r_0'' (Å)	1.87685(20)	1.87619(26)	1.87588(23)	1.87689(34)

[a] Residuals (ν(calculated) – ν(measured)) are given in parentheses following each line position, in units of 0.001 cm^{-1}.
[b] Error limits (1σ) are provided for each fitted spectroscopic constant, in units of the last digit quoted. B_0'' was constrained to take the same value in all of the unperturbed bands (the 1-0, 3-0, 4-0, 7-0, 10-0, and 11-0 bands), which all originated from the $v'' = 0$ level of the ground $X\ ^1\Sigma^+$ state. This band was included in the combined fit, in which bands were fitted to the form $\nu = \nu_0 + B'J'(J'+1) - B''J''(J''+1)$.

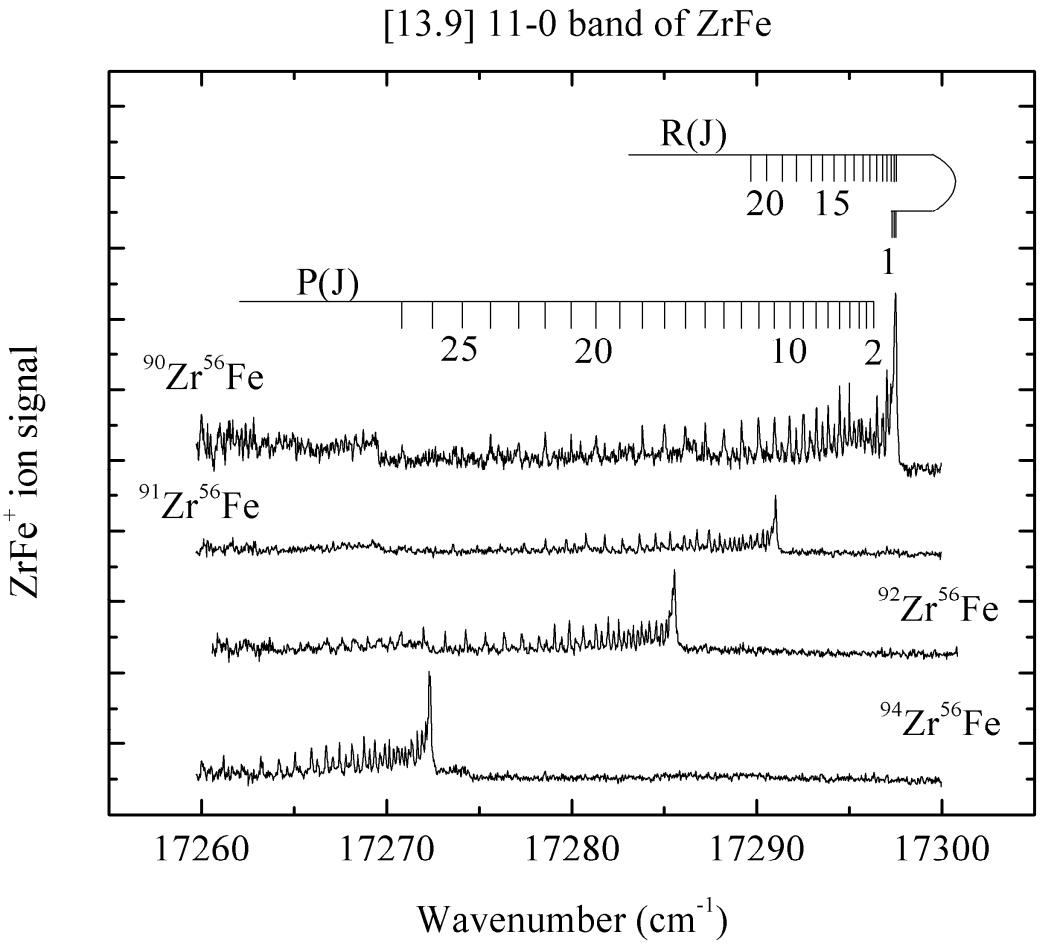

Figure C.22. Rotationally resolved spectra of the various ZrFe isotopic combinations for the 11-0 band of the [13.9] $0^{+}\leftarrow X\ ^{1}\Sigma^{+}$ system. Line assignments are provided for the most abundant isotopomer, $^{90}Zr^{56}Fe$.

Table C.14

Fitted Rotational Lines of the 11-0 band of the $[13.9]0^+ \leftarrow X\ ^1\Sigma^+$ system of ZrFe.

Line	$^{90}Zr^{56}Fe$	$^{91}Zr^{56}Fe$	$^{92}Zr^{56}Fe$	$^{94}Zr^{56}Fe$
P(2)	17296.329(-13)	17289.864(-13)		17271.198(-9)
P(3)	17295.901(31)	17289.452(16)	17284.010(-2)	17270.817(-5)
P(4)	17295.505(-9)	17289.032(1)	17283.570(5)	17270.376(7)
P(5)	17294.993(13)	17288.549(-3)	17283.078(11)	17269.908(-7)
P(6)	17294.471(-8)	17287.996(10)	17282.537(13)	17269.359(8)
P(7)	17293.857(10)	17287.410(3)	17281.971(-12)	17268.777(5)
P(8)	17293.217(2)	17286.765(2)	17281.310(5)	17268.118(26)
P(9)	17292.514(4)	17286.070(-2)	17280.619(0)	17267.444(10)
P(10)	17291.772(-9)	17285.313(4)	17279.867(3)	17266.733(-21)
P(11)	17290.947(8)	17284.521(-8)	17279.075(-6)	17265.936(-18)
P(12)	17290.089(5)	17283.661(-5)	17278.225(-10)	17265.051(20)
P(13)	17289.173(9)	17282.741(5)	17277.296(12)	17264.173(-1)
P(14)	17288.224(-9)	17281.784(0)	17276.342(7)	17263.202(19)
P(15)	17287.212(-16)	17280.767(2)	17275.334(3)	
P(16)	17286.131(-9)	17279.704(-3)	17274.265(7)	
P(17)	17285.004(-7)	17278.585(-4)	17273.158(-3)	
P(18)	17283.820(-2)		17271.989(-3)	
P(19)	17282.597(-10)			
P(20)	17281.317(-15)	17274.899(3)		
P(21)	17279.964(0)	17273.593(-23)		
P(22)	17278.567(7)			
P(23)	17277.134(-3)			
P(24)	17275.610(24)			
P(25)	17274.074(10)			
P(27)	17270.823(3)			
R(1)	17297.313(7)			
R(2)	17297.445(-6)	17290.961(9)		17272.297(-3)
R(3)	17297.497(7)		17285.575(-6)	17272.355(4)
R(4)	17297.497(19)		17285.575(6)	17272.355(16)
R(5)	17297.497(-21)		17285.538(3)	
R(6)	17297.374(9)	17290.924(-8)	17285.454(-6)	17272.222(17)
R(7)	17297.235(2)	17290.791(-20)		17272.115(-20)
R(8)	17297.024(13)	17290.578(-6)	17285.125(-20)	17271.904(-4)
R(9)	17296.800(-15)	17290.319(2)	17284.857(-2)	17271.660(-9)
R(10)	17296.492(-13)	17290.017(0)	17284.554(-2)	17271.364(-13)
R(11)	17296.121(0)	17289.661(0)	17284.198(-2)	17271.002(-4)
R(12)	17295.679(30)	17289.234(18)	17283.772(16)	17270.604(-10)
R(13)	17295.248(-3)	17288.799(-8)	17283.327(1)	17270.139(-2)

Table C.14 continued

R(14)	17294.738(-11)	17288.275(0)	17282.816(-2)	17269.639(-11)
R(15)	17294.183(-26)	17287.714(-6)	17282.269(-21)	17269.078(-11)
R(16)	17293.538(-5)	17287.069(19)	17281.619(11)	17268.443(11)
R(17)	17292.864(-7)	17286.402(12)	17280.977(-18)	17267.791(-3)
R(18)	17292.128(0)	17285.698(-9)		17267.088(-16)
R(19)	17291.352(-6)		17279.455(4)	17266.276(26)
R(20)	17290.526(-17)	17284.067(12)	17278.632(-3)	
R(21)	17289.594(27)		17277.735(12)	
Fitted Spectroscopic Constants [b]				
ν_0 (cm^{-1})	17296.9238(30)	17290.4567(28)	17284.9923(27)	17271.7876(38)
B_{11}'	0.112286(30)	0.111921(33)	0.111473(37)	0.110449(39)
r_{11}' (Å)	2.08661(28)	2.08559(31)	2.08544(35)	2.08662(39)
B_0'' (cm^{-1})	0.138786(30)	0.138297(38)	0.137770(34)	0.136513(50)
r_0'' (Å)	1.87685(20)	1.87619(26)	1.87588(23)	1.87689(34)

[a] Residuals (ν(calculated) – ν(measured)) are given in parentheses following each line position, in units of 0.001 cm^{-1}.

[b] Error limits (1σ) are provided for each fitted spectroscopic constant, in units of the last digit quoted. B_0'' was constrained to take the same value in all of the unperturbed bands (the 1-0, 3-0, 4-0, 7-0, 10-0, and 11-0 bands), which all originated from the $v'' = 0$ level of the ground $X\ ^1\Sigma^+$ state. This band was included in the combined fit, in which bands were fitted to the form $\nu = \nu_0 + B'J'(J'+1) - B''J''(J''+1)$.

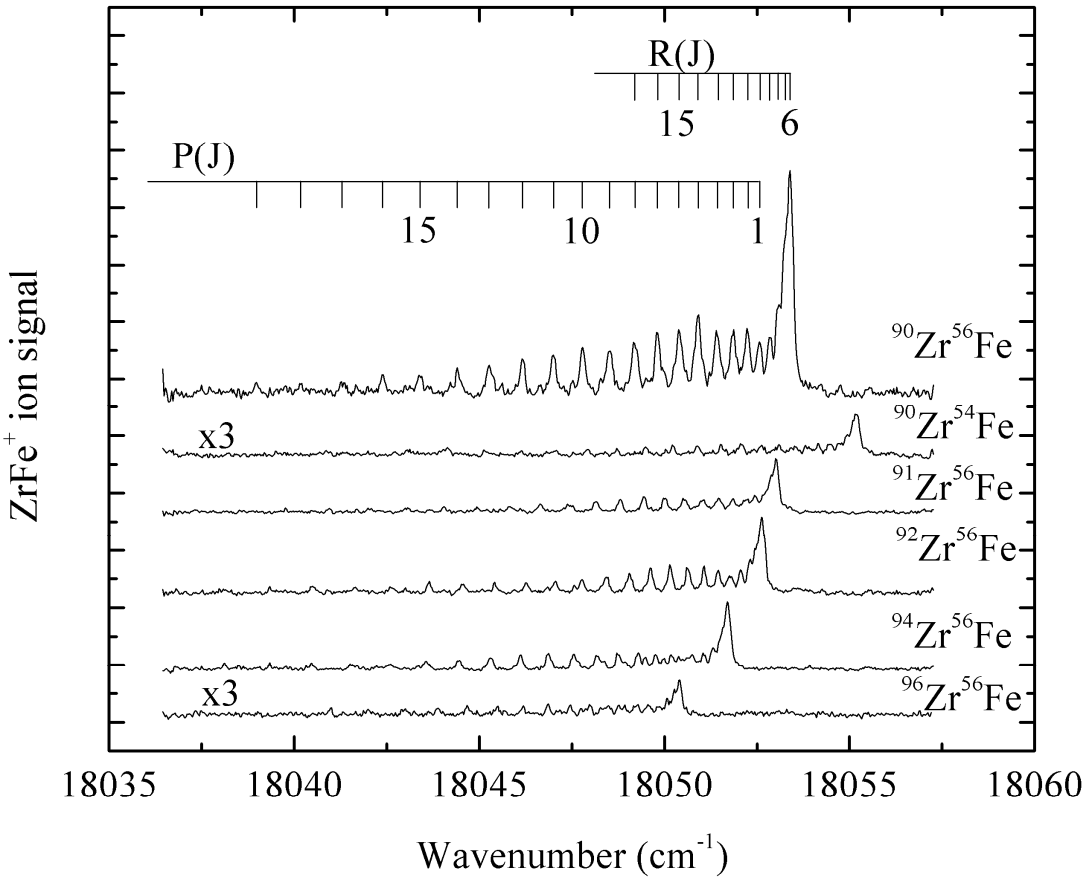

Figure C.23. Rotationally resolved spectra of the various ZrFe isotopic combinations of the 18053 cm^{-1} band. Line assignments are provided for the most abundant isotopomer, $^{90}Zr^{56}Fe$

Table C.15

Assigned Rotational Lines of the 18053 cm^{-1} band of ZrFe.[a]

Line	$^{90}Zr^{54}Fe$	$^{90}Zr^{56}Fe$	$^{91}Zr^{56}Fe$	$^{92}Zr^{56}Fe$	$^{94}Zr^{56}Fe$	$^{96}Zr^{56}Fe$
P(1)		18052.571				
P(2)		18052.240				
P(3)		18051.853			18050.191	18048.927
P(4)	18053.093(14)	18051.414			18049.764	18048.501
P(5)	18052.624(5)	18050.912	18050.566		18049.295	18047.994
P(6)	18052.082(21)	18050.391	18049.997		18048.756	18047.457
P(7)	18051.523(4)	18049.808	18049.450	18049.061	18048.186	18046.856
P(8)	18050.889(13)	18049.189	18048.810	18048.436	18047.553	18046.187
P(9)	18050.227(2)	18048.519	18048.153	18047.777	18046.865	18045.488
P(10)	18049.498(10)	18047.787	18047.389	18047.060	18046.112	18044.675
P(11)	18048.727(11)	18047.004	18046.648	18046.263	18045.309	18043.874
P(12)	18047.927(-7)	18046.170	18045.808	18045.408	18044.449	18042.956
P(13)	18047.055(-2)	18045.265	18044.939	18044.554	18043.554	18041.998
P(14)	18046.140(-3)	18044.403	18044.041	18043.639	18042.579	18040.992
P(15)	18045.160(14)	18043.389	18043.048	18042.629	18041.521	
P(16)	18044.139(22)	18042.394	18042.017	18041.636	18040.467	
P(17)		18041.310	18040.947	18040.492	18039.338	
P(18)		18040.174		18039.338	18038.115	
P(19)		18038.982		18038.104		
P(20)				18036.834		
R(1)	18054.964(-5)					
R(2)	18055.094(4)					18050.404

Table C.15 continued

R(3)	18055.184(4)				18051.770	18050.454
R(4)	18055.244(-15)				18051.770	18050.454
R(5)	18055.244(-22)			18052.632	18051.770	
R(6)	18055.184(-17)	18053.385		18052.559	18051.639	18050.267
R(7)	18055.094(-31)	18053.253	18052.874	18052.456	18051.498	18050.072
R(8)	18054.916(-6)	18053.080	18052.676	18052.314	18051.313	18049.838
R(9)	18054.708(1)	18052.853	18052.445	18052.060	18051.062	18049.553
R(10)	18054.470(-12)	18052.571	18052.209	18051.774	18050.748	18049.171
R(11)	18054.153(7)	18052.240	18051.857	18051.452	18050.382	18048.766
R(12)	18053.806(7)	18051.853	18051.471	18051.065	18049.974	18048.278
R(13)	18053.424(-6)	18051.414	18051.054	18050.632	18049.479	18047.746
R(14)		18050.912	18050.566	18050.151	18048.942	
R(15)		18050.391		18049.624	18048.358	
R(16)		18049.808			18047.673	
R(17)		18049.189				
R(18)				18047.569		
			Fitted Spectroscopic Constants[b]			
ν_0 (cm^{-1})	18054.5361(39)	18052.8305(77)	18052.4322(77)	18052.101(14)	18051.2214(90)	18049.9399(65)
B' (cm^{-1})	0.11787(11)	0.113625(43)	0.113331(51)	0.112263(71)	0.109924(57)	0.107155(62)
r' (Å)	2.05970(98)	2.07428(39)	2.07257(47)	2.07809(66)	2.09160(54)	2.11018(61)
B_0'' (cm^{-1})	0.142144(99)	0.138786(30)	0.138297(38)	0.137770(34)	0.136513(50)	0.135508(126)
r_0'' (Å)	1.87558(65)	1.87685(20)	1.87619(26)	1.87588(23)	1.87689(34)	1.87648(87)

[a] The upper state of this band is perturbed by a nearby state. Lines have been identified using combination differences calculated from the known ground state rotational constant, but no attempt has been made to deperturb the state.

Table C.15 continued

[b] For the rotational fit for this band, B_0'' was held fixed at the value found from the combined fit in all isotopes except $^{90}Zr^{54}Fe$, where only two bands were recorded due to the weak signal for this isotopic modification. For $^{90}Zr^{54}Fe$, this band and the 1-0 band of the
$[13.9]0^+ \leftarrow X^1\Sigma^+$ system were combined in a single fit, in which bands were fitted to the form $\nu = \nu_0 + B'J'(J'+1) - B''J''(J''+1)$. Errors in the fit were somewhat larger than for unperturbed bands. The perturbation is evident from the variation in r' values as a function of reduced mass.

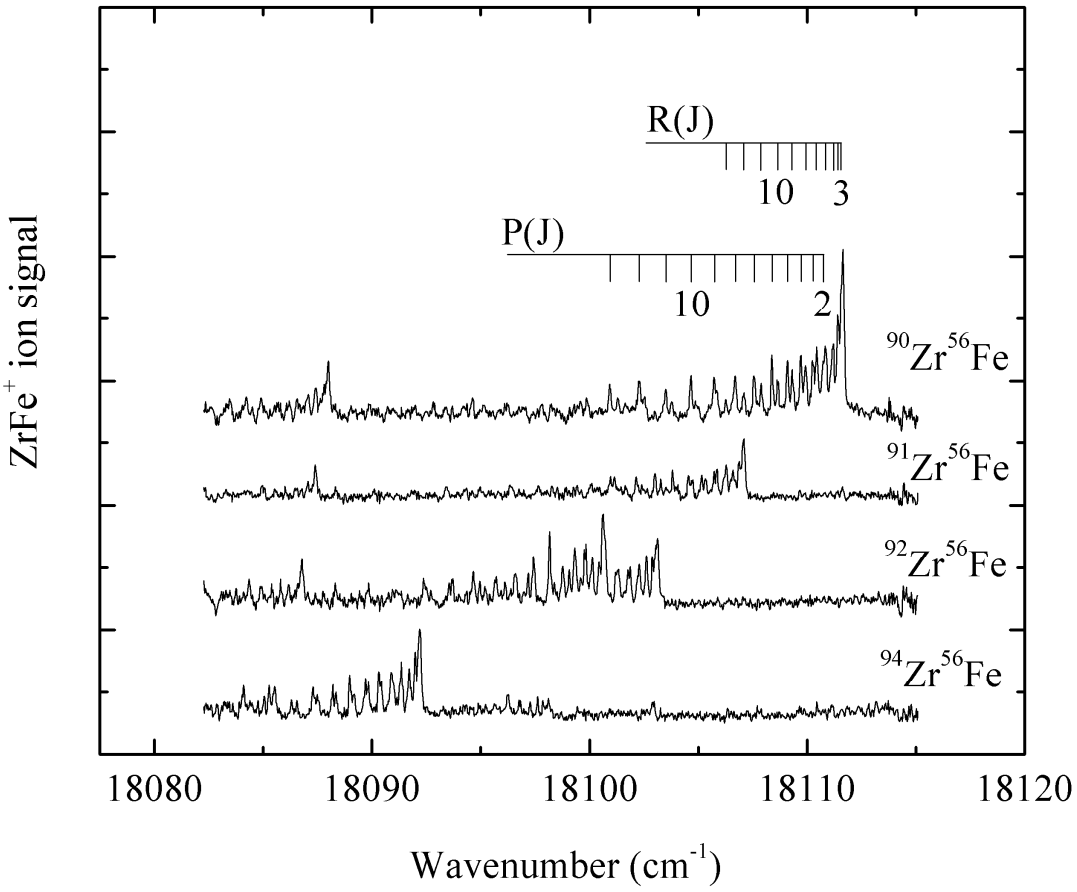

Figure C.24. Rotationally resolved spectra of the various ZrFe isotopic combinations of the 18111 cm^{-1} band. Line assignments are provided for the most abundant isotopomer, $^{90}Zr^{56}Fe$.

Table C.16

Assigned Rotational Lines of the 18111 cm^{-1} band of ZrFe.[a]

Line	$^{90}Zr^{56}Fe$	$^{91}Zr^{56}Fe$	$^{92}Zr^{56}Fe$	$^{94}Zr^{56}Fe$
P(2)	18110.732			
P(3)	18110.262			
P(4)	18109.708			18090.315
P(5)	18109.096			18089.704
P(6)	18108.375	18105.726		18088.976
P(7)	18107.566	18105.151		18088.202
P(8)	18106.690	18104.545		18087.289
P(9)	18105.724	18103.816		18086.305
P(10)	18104.665	18103.007		18085.274
P(11)	18103.500	18102.139		18084.110
P(12)	18102.282	18101.140		
P(13)	18100.935	18100.066		
P(14)		18098.911		
P(15)		18097.656		
P(16)		18096.378		
P(17)		18094.970		
P(18)		18093.421		
R(1)	18111.640			18092.232
R(2)	18111.673			18092.232
R(3)	18111.563			18092.148
R(4)	18111.422			18091.991
R(5)	18111.197	18107.077		18091.709
R(6)	18110.839			
R(7)	18110.438	18106.872		18090.981
R(8)	18109.926	18106.586		18090.424
R(9)	18109.306	18106.277		18089.841
R(10)	18108.650	18105.853		18089.161
R(11)	18107.880	18105.326		
R(12)		18104.711		
R(14)		18103.273		
R(15)		18102.405		
R(16)		18101.450		

Table C.16 continued

Fitted Spectroscopic Constants[b]				
ν_0 (cm^{-1})	18111.3512(43)	18106.7937(64)		18091.9441(59)
B' (cm^{-1})	0.095181(54)	0.094423(56)		0.092549(63)
r' (Å)	2.26636(64)	2.27062(67)		2.27950(78)
B_0'' (cm^{-1})	0.138786(30)	0.138297(38)	0.137770(34)	0.136513(50)
r_0'' (Å)	1.87685(20)	1.87619(26)	1.87588(23)	1.87689(34)

[a] The upper state of this band is perturbed by a nearby state. Lines have been identified using combination differences calculated from the known ground state rotational constant, but no attempt has been made to deperturb the state. The $^{92}Zr^{56}Fe$ isotopic modification overlaps badly with another band; as a result, lines have not been assigned.

[b] For the rotational fit for this band, B_0'' was held fixed at the value found from the combined fit. Errors in the fit were somewhat larger than for unperturbed bands.

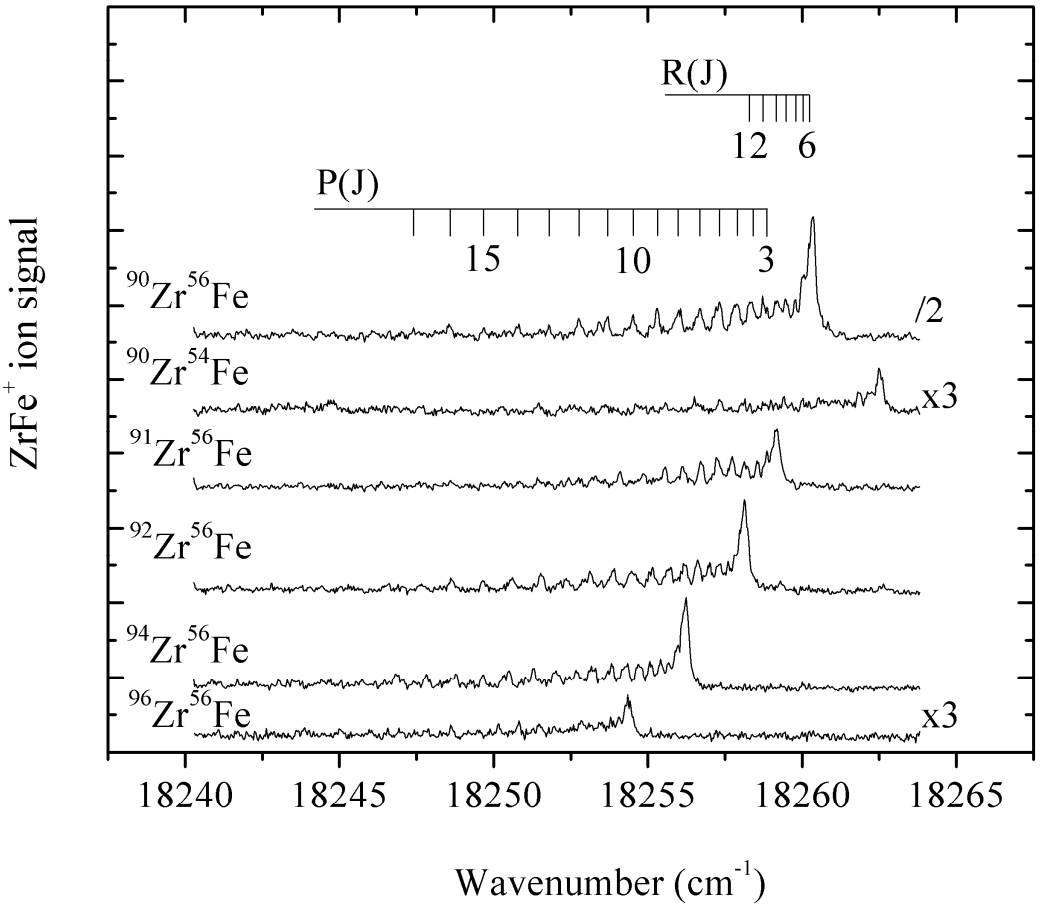

Figure C.25. Rotationally resolved spectra of the various ZrFe isotopic combinations of the 18260 cm^{-1} band. Line assignments are provided for the most abundant isotopomer, $^{90}Zr^{56}Fe$.

Table C.17

Assigned Rotational Lines of the 18260 cm^{-1} band of ZrFe.[a]

Line	$^{90}Zr^{56}Fe$	$^{91}Zr^{56}Fe$	$^{92}Zr^{56}Fe$	$^{94}Zr^{56}Fe$
P(3)	18258.873			
P(4)		18257.250		
P(5)	18257.874	18256.741	18255.695	18253.832
P(6)	18257.322	18256.139	18255.144	18253.295
P(7)	18256.688	18255.556	18254.487	18252.697
P(8)	18255.999	18254.879	18253.879	18252.017
P(9)	18255.303	18254.095	18253.139	18251.295
P(10)	18254.516	18253.300	18252.363	18250.500
P(11)	18253.672	18252.442	18251.553	18249.643
P(12)	18252.764		18250.595	18248.781
P(13)	18251.802		18249.645	18247.812
P(14)	18250.774		18248.647	18246.842
P(15)	18249.680		18247.682	
P(16)	18248.570		18246.593	
P(17)	18247.410			
R(2)	18260.340	18259.180		
R(3)	18260.401	18259.253		18256.293
R(4)	18260.401	18259.180		18256.293
R(5)			18258.070	18256.228
R(6)	18260.222	18259.017	18257.981	18256.106
R(7)	18260.024		18257.821	18255.947
R(8)	18259.778	18258.545	18257.602	18255.669
R(9)	18259.461	18258.224	18257.345	18255.415
R(10)	18259.176			18255.091
R(11)	18258.730			
R(12)	18258.325			
Fitted Spectroscopic Constants[b]				
ν_0 (cm^{-1})	18259.8482	18258.7100	18257.6089	18255.7710
B' (cm^{-1})	0.11034	0.10889	0.11004	0.10838
r' (Å)	2.1049	2.1144	2.0990	2.1064
B_0'' (cm^{-1})	0.138786(30)	0.138297(38)	0.137770(34)	0.136513(50)
r_0'' (Å)	1.87685(20)	1.87619(26)	1.87588(23)	1.87689(34)

[a] The lines of this band are broadened, and the P lines overlap with the returning R lines. As a result the line positions are imprecise compared to the other bands, so this feature has not been included in the combined fit. The band is a strong one, however, so it might be a good candidate for further study, for example to measure the dipole moment of ZrFe by Stark spectroscopy.

Table C.17 continued

[b] For the rotational fit for this band, B_0'' was held fixed at the value found from the combined fit. Errors are not provided for the fitted parameters, owing to the difficulty in measuring precise line positions of the blended lines.

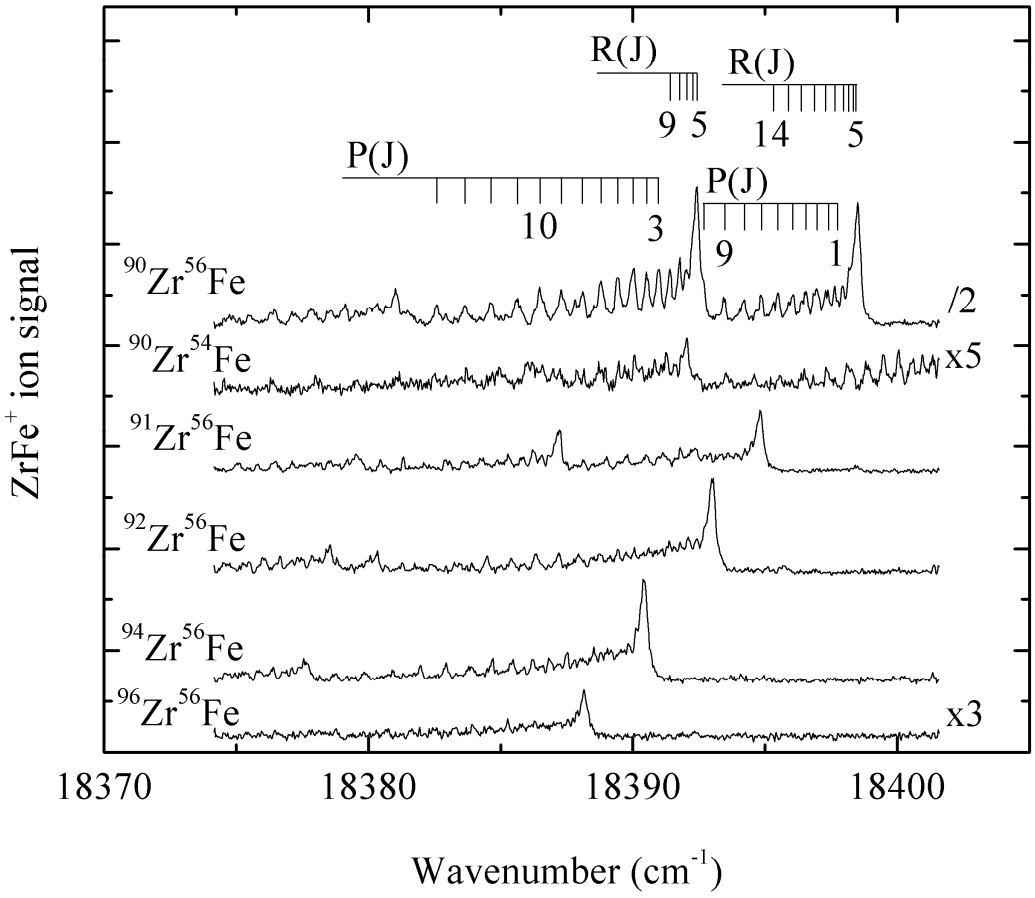

Figure C.26. Rotationally resolved spectra of the various ZrFe isotopic combinations of the 18392 and 18398 cm^{-1} bands. Line assignments are provided for the most abundant isotopomer, $^{90}Zr^{56}Fe$.

Table C.18

Assigned Rotational Lines of the 18392 cm^{-1} band of ZrFe.[a]

Line	$^{90}Zr^{56}Fe$	$^{91}Zr^{56}Fe$	$^{92}Zr^{56}Fe$	$^{94}Zr^{56}Fe$
P(3)	18390.970			
P(4)	18390.533			
P(5)	18390.016	18384.877		
P(6)	18389.429	18384.281		
P(7)	18388.789	18383.656		
P(8)	18388.109	18382.894		
P(9)	18387.305	18382.113		
P(10)	18386.483	18381.313		
P(11)	18385.611	18380.457		
P(12)	18384.648			
P(13)	18383.651			
P(14)	18382.579			
R(2)	18392.482			
R(3)	18392.482			
R(4)	18392.482			
R(5)	18392.409			
R(6)	18392.278	18387.033		
R(7)	18392.030	18386.825		
R(8)	18391.767	18386.550		
R(9)	18391.396	18386.243		
R(10)		18385.803		
R(12)		18384.877		
Fitted Spectroscopic Constants[b]				
ν_0 (cm^{-1})	18392.0083(63)	18386.8461(164)		
B' (cm^{-1})	0.108310(76)	0.107570(178)		
r' (Å)	2.12456(75)	2.12735(176)		
B_0'' (cm^{-1})	0.138786(30)	0.138297(38)	0.137770(34)	0.136513(50)
r_0'' (Å)	1.87685(20)	1.87619(26)	1.87588(23)	1.87689(34)

[a] The lines of this band are broadened, and the P lines overlap with the returning R lines. As a result the line positions are imprecise compared to the other bands, so this feature has not been included in the combined fit.

[b] For the rotational fit for this band, B_0'' was held fixed at the value found from the combined fit. Corresponding bands for the $^{92}Zr^{56}Fe$ and $^{94}Zr^{56}Fe$ were either out of the range scanned, or were severely overlapped. In any case, reliable data for these isotopic modifications were not collected.

Table C.19

Assigned Rotational Lines of the 18398 cm^{-1} band of ZrFe.[a]

Line	$^{90}Zr^{56}Fe$	$^{91}Zr^{56}Fe$	$^{92}Zr^{56}Fe$	$^{94}Zr^{56}Fe$
P(1)	18397.740			
P(2)	18397.381			
P(3)	18396.977		18391.566	18389.044
P(4)	18396.538		18391.083	
P(5)	18396.054	18392.366	18390.587	
P(6)	18395.490	18391.804	18390.057	18387.518
P(7)	18394.859	18391.131	18389.435	18386.878
P(8)	18394.210	18390.521	18388.747	18386.208
P(9)	18393.447	18389.758	18387.972	18385.472
P(10)	18392.672	18388.988	18387.198	18384.687
P(11)		18388.142	18386.324	18383.798
P(12)		18387.229	18385.404	18382.941
P(13)			18384.484	18381.953
P(14)			18383.458	18380.916
P(15)			18382.364	18379.846
R(2)				18390.500
R(3)				18390.500
R(4)			18393.093	18390.500
R(5)	18398.442	18394.722		18390.448
R(6)	18398.364	18394.629		18390.300
R(7)	18398.175	18394.477	18392.695	18390.126
R(8)	18397.933	18394.239	18392.420	18389.851
R(9)	18397.637		18392.096	18389.546
R(10)	18397.290	18393.591	18391.792	18389.183
R(11)	18396.857		18391.375	18388.789
R(12)	18396.379	18392.726	18390.858	
R(13)	18395.895	18392.187	18390.349	18387.788
R(14)	18395.303		18389.733	
R(15)		18390.981	18389.137	
R(16)			18388.449	
Fitted Spectroscopic Constants[b]				
ν_0 (cm^{-1})	18398.0057	18394.3011	18392.5505	18390.0117
B' (cm^{-1})	0.11017	0.10984	0.10894	0.107606
r' (Å)	2.1066	2.1053	2.1095	2.1140
B_0'' (cm^{-1})	0.138786(30)	0.138297(38)	0.137770(34)	0.136513(50)
r_0'' (Å)	1.87685(20)	1.87619(26)	1.87588(23)	1.87689(34)

Table C.19 continued

[a] The lines of this band are broadened, and the higher P lines overlap with another band. As a result the line positions are imprecise compared to the other bands, so this feature has not been included in the combined fit.
[b] For the rotational fit for this band, B_0'' was held fixed at the value found from the combined fit. Errors in the fitted parameters are omitted in this instance, because of the imprecise measurement of the line positions.

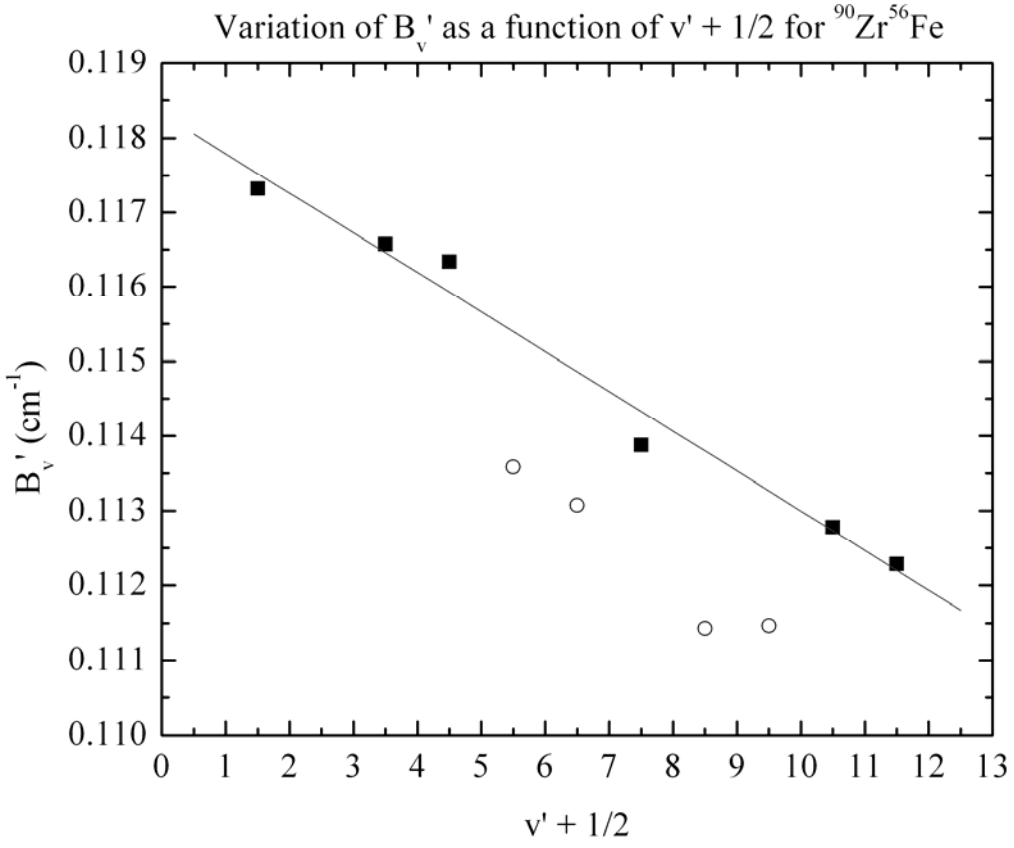

Figure C.27. Variation of $B_{v'}$ values for the $[13.9]0^+$ state of $^{90}Zr^{56}Fe$ as a function of $v'+1/2$. Unperturbed bands are indicated by filled squares, perturbed bands by open circles. The fitted line through the $B_{v'}$ values of the unperturbed states provides the values of B_e' and α_e' that are given in Table 5.3.

APPENDIX D

VIBRONICALLY AND ROTATIONALLY RESOLVED SPECTRA, TABULATED LINE POSITIONS AND FITTED PARAMETERS OF TiFe

D.1 Vibronically resolved spectra of TiFe

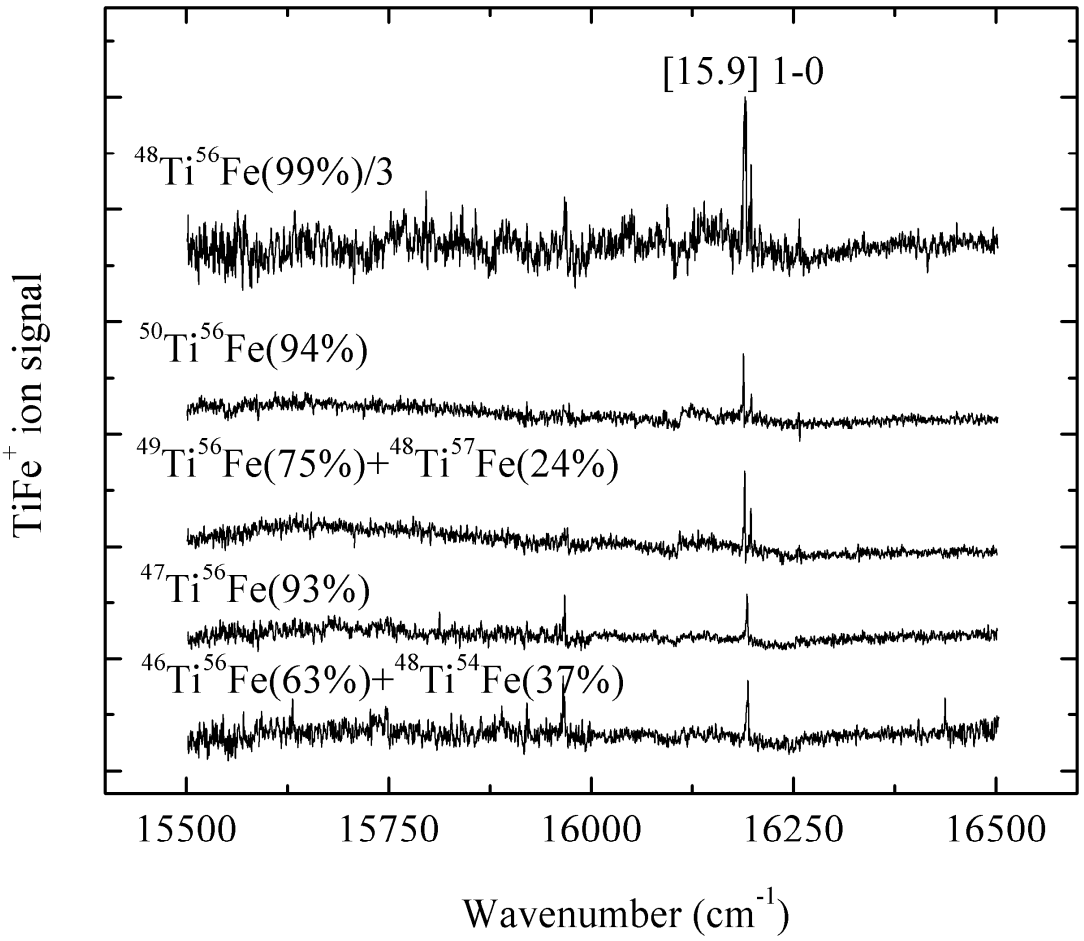

Figure D.1. Spectra of the various isotopomers of TiFe in the 15500 - 16500 cm^{-1} range

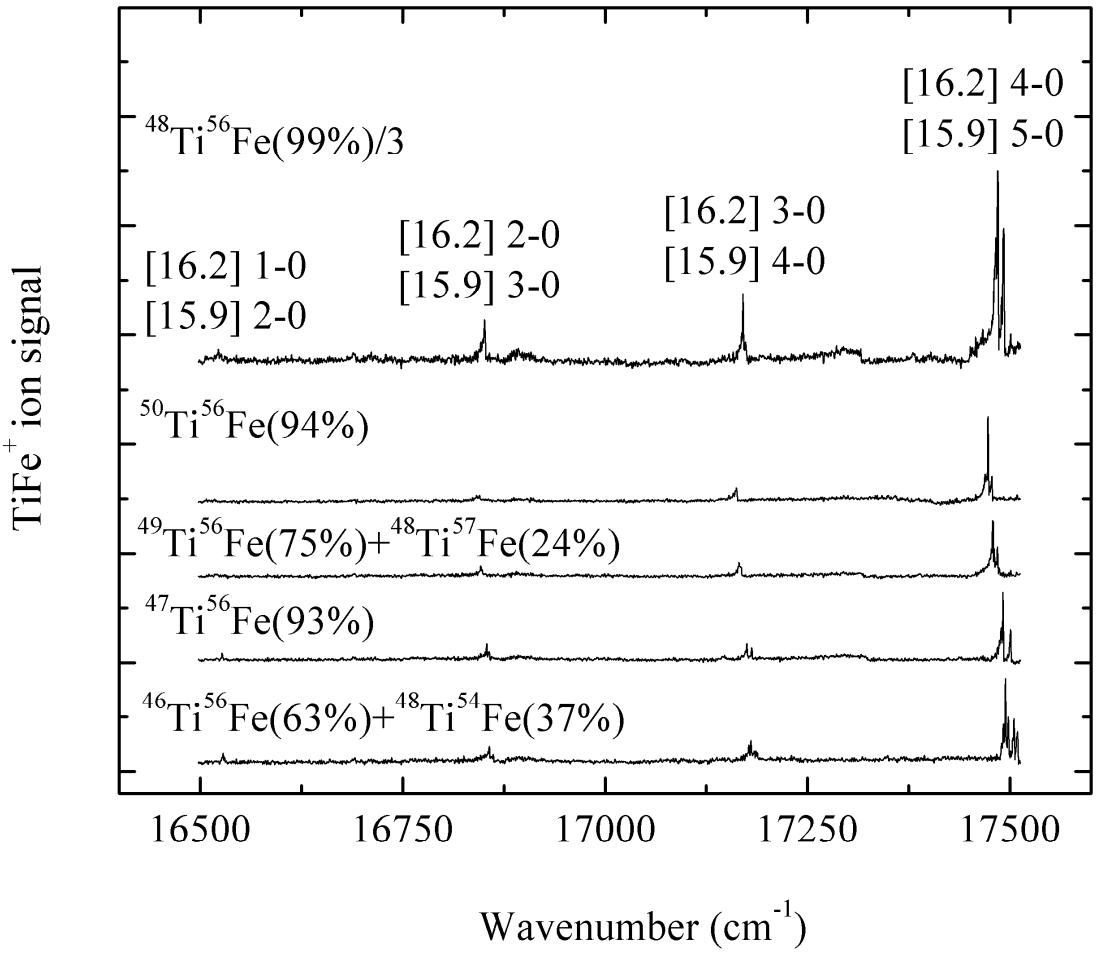

Figure D.2. Spectra of the various isotopomers of TiFe in the 16500 - 17500 cm^{-1} range

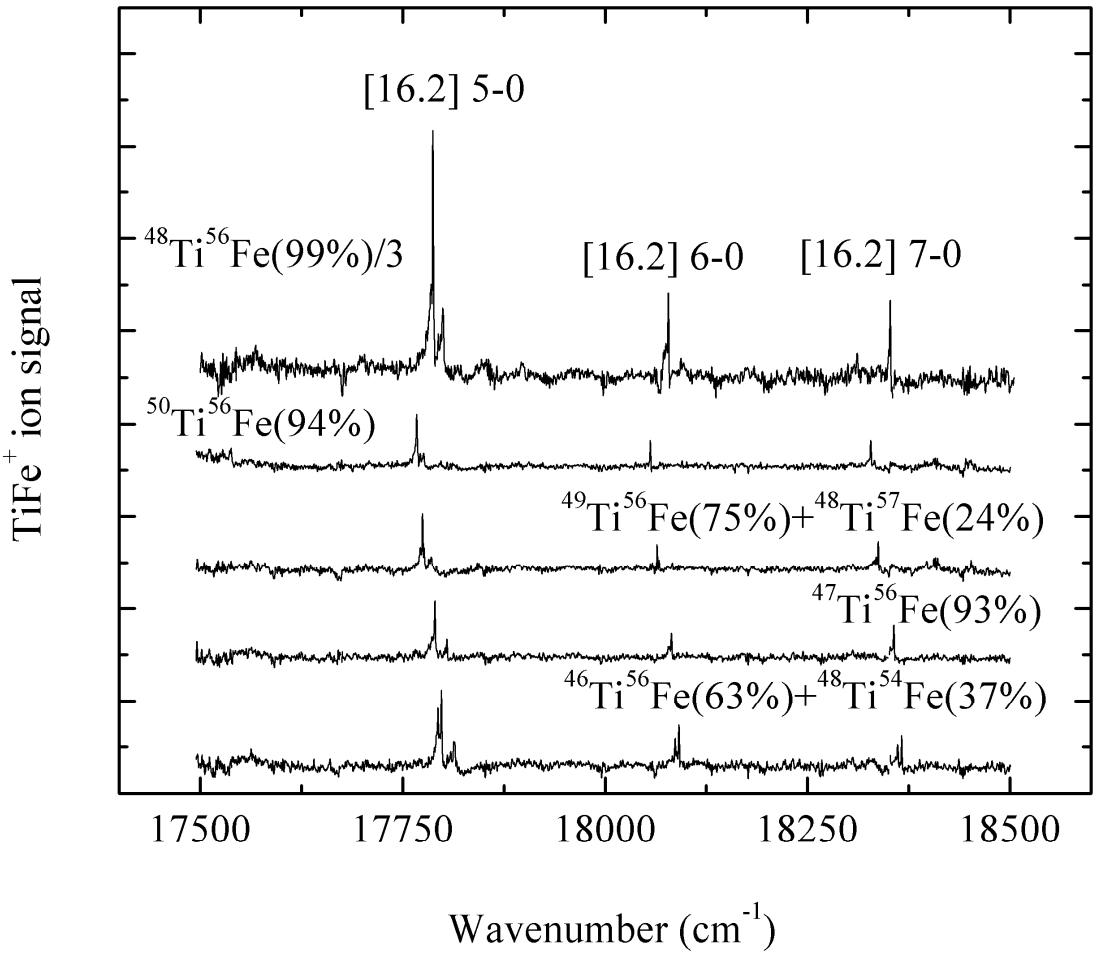

Figure D.3. Spectra of the various isotopomers of TiFe in the 17500 - 18500 cm^{-1} range

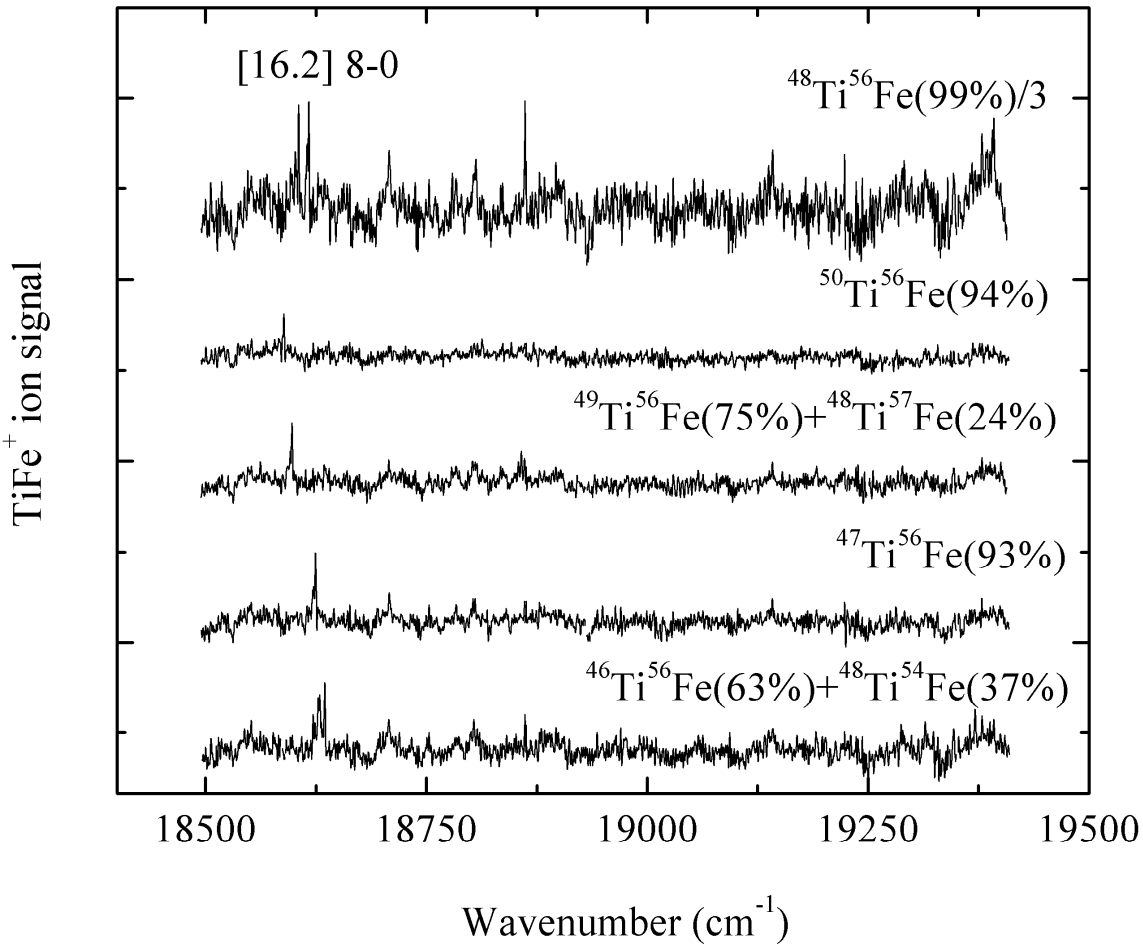

Figure D.4. Spectra of the various isotopomers of TiFe in the 18500 - 19400 cm^{-1} range

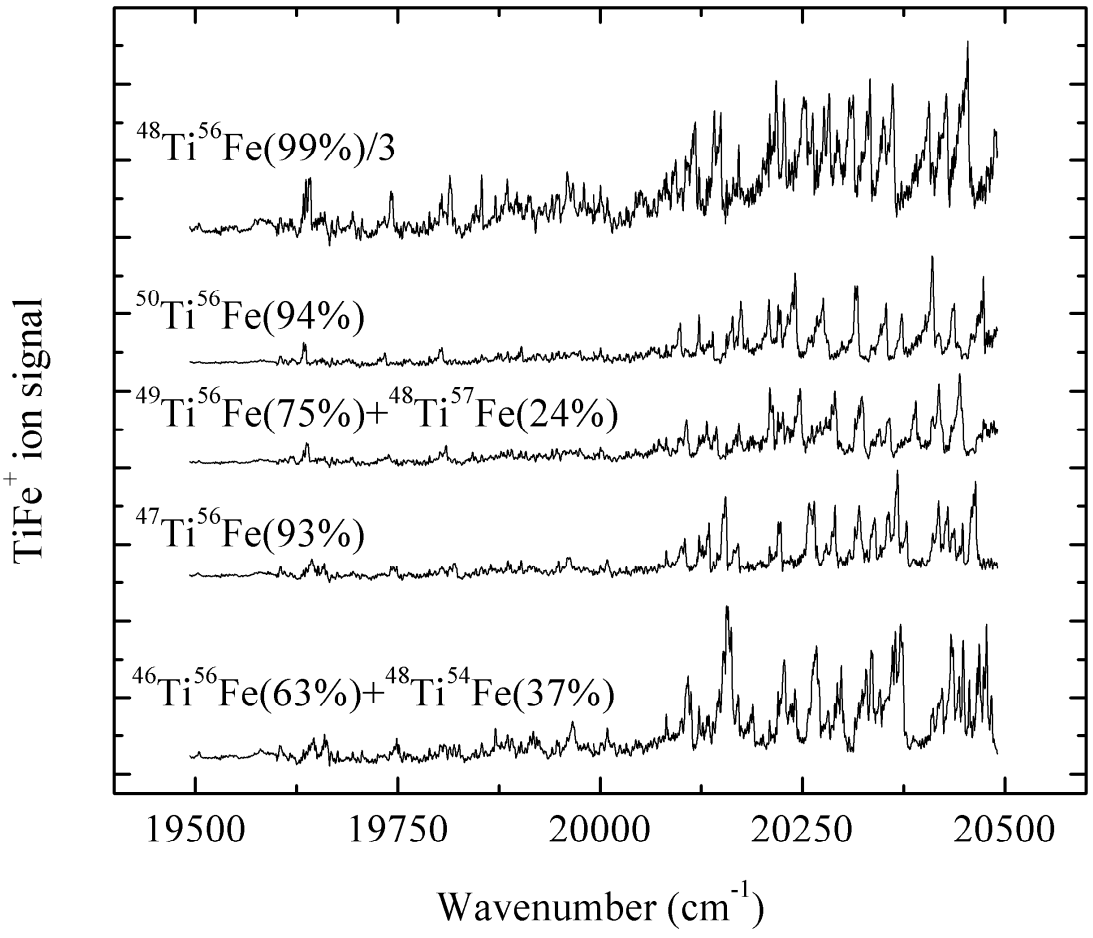

Figure D.5. Spectra of the various isotopomers of TiFe in the 19500 - 20500 cm^{-1} range

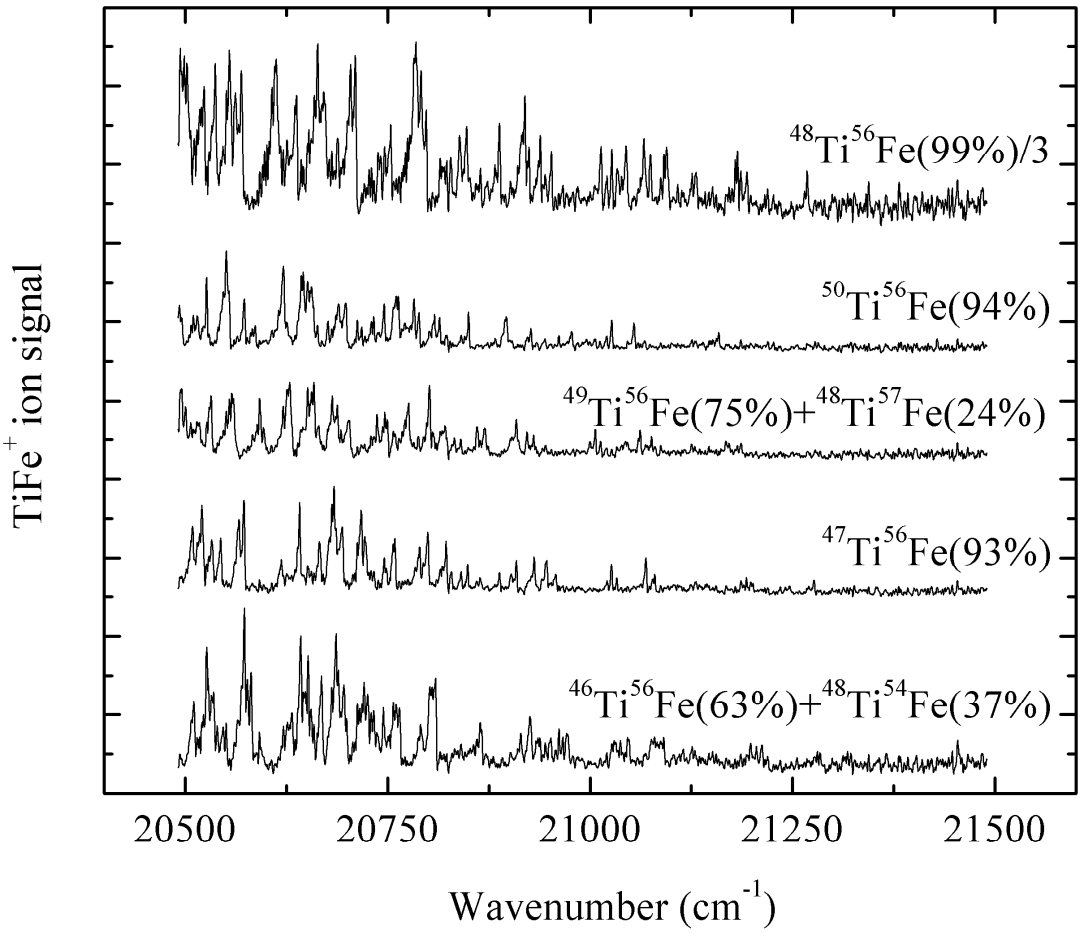

Figure D.6. Spectra of the various isotopomers of TiFe in the 20500 - 21500 cm^{-1} range

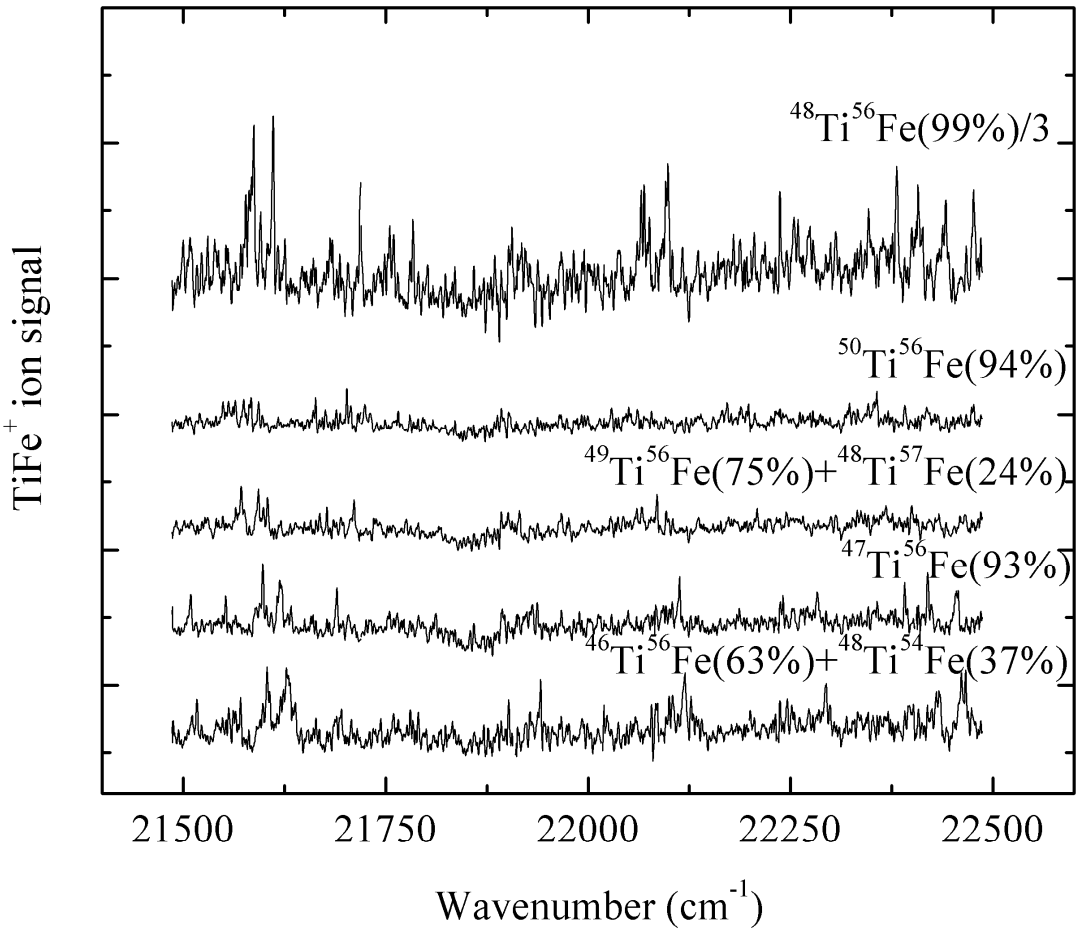

Figure D.7. Spectra of the various isotopomers of TiFe in the 21500 - 22500 cm^{-1} range

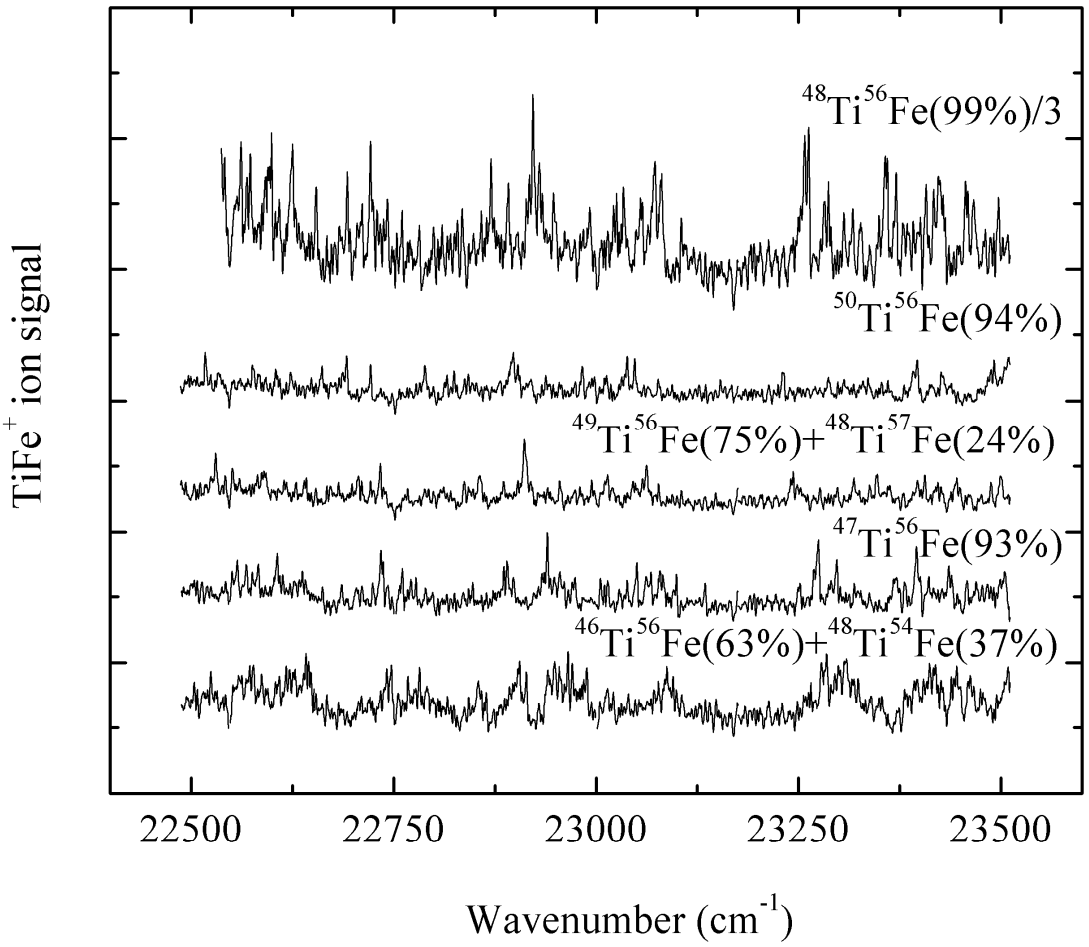

Figure D.8. Spectra of the various isotopomers of TiFe in the 22500 - 23500 cm^{-1} range

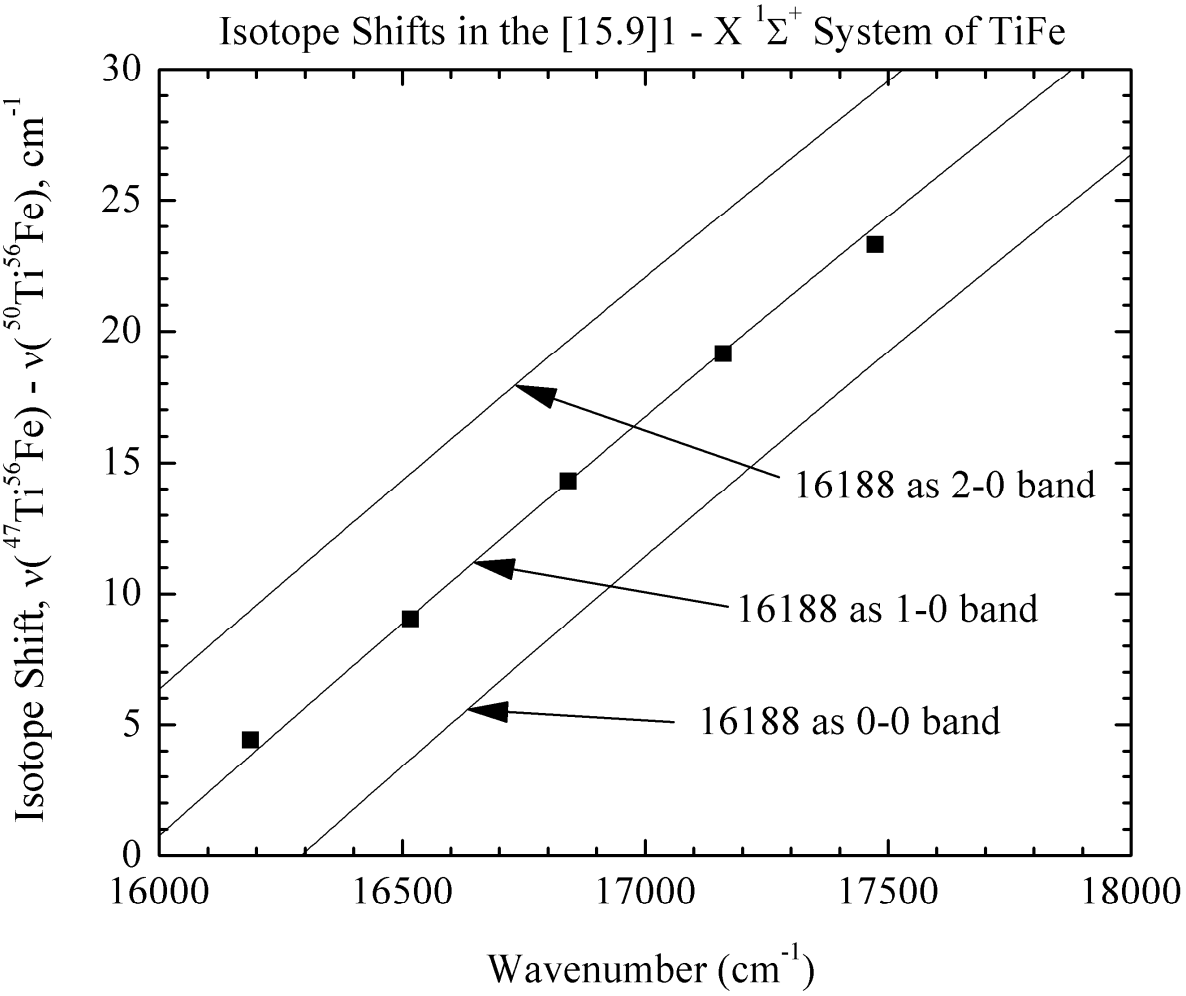

Figure D.9. Measured (symbols) *vs*. calculated (lines) isotope shifts, $\nu(^{47}Ti^{56}Fe)$-$\nu(^{50}Ti^{56}Fe)$, for bands belonging to the [15.9] 1 - X $^1\Sigma^+$ system of TiFe. From these plots, the assignment of the 16188 cm^{-1} band as the 1-0 band is definite.

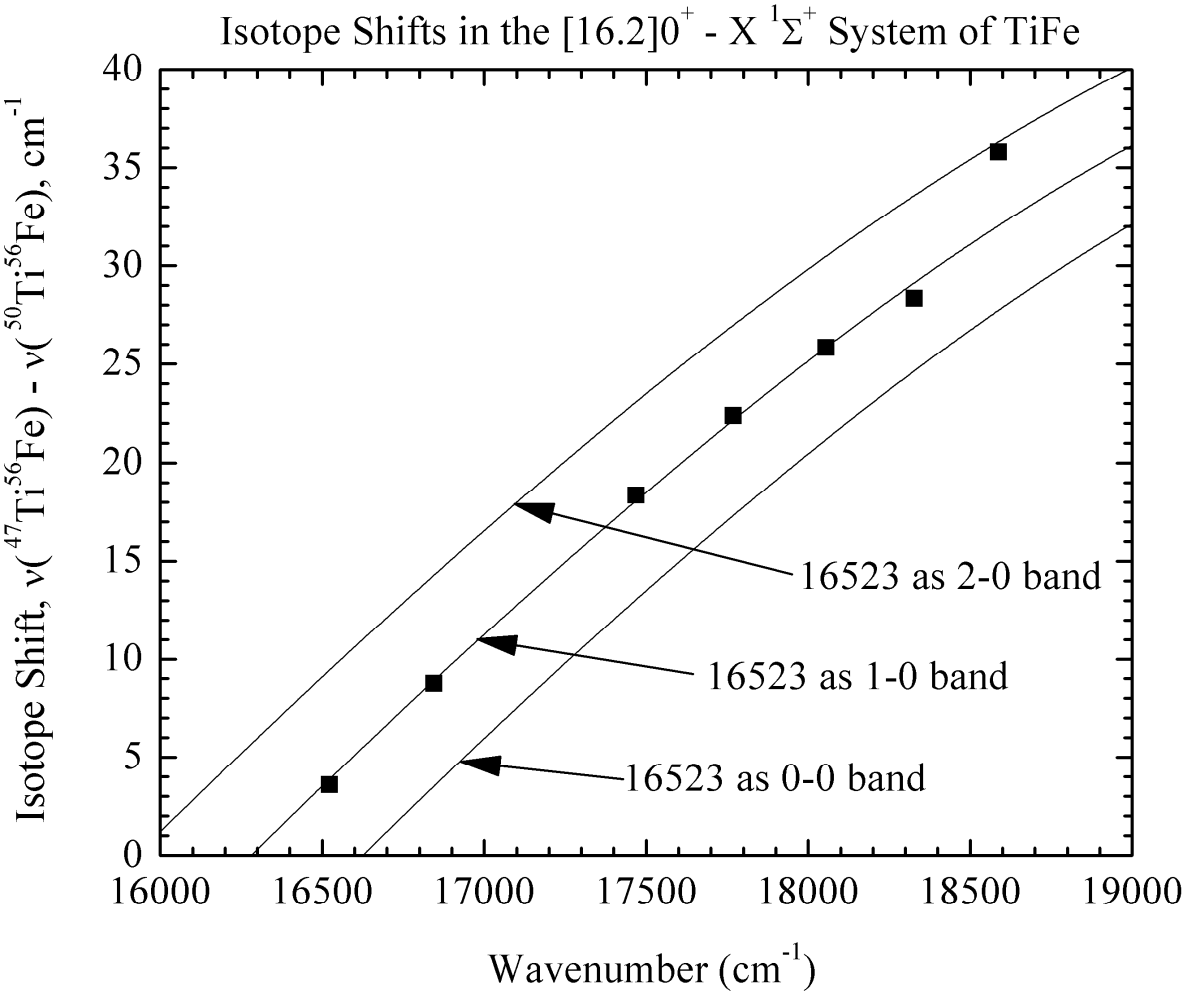

Figure D.10. Measured (symbols) *vs*. calculated (lines) isotope shifts, $\nu(^{47}Ti^{56}Fe)$-$\nu(^{50}Ti^{56}Fe)$, for bands belonging to the [16.2] 0^+ - X $^1\Sigma^+$ system of TiFe. From these plots, the assignment of the 16523 cm^{-1} band as the 1-0 band is definite.

Table D.1

Vibronic fit of bands belonging to the [15.9]1 ← X $^1\Sigma^+$ system of TiFe

Band	ν_0 (^{46}Ti^{56}Fe)	ν_0 (^{47}Ti^{56}Fe)	ν_0 (^{48}Ti^{56}Fe)	ν_0 (^{49}Ti^{56}Fe)	ν_0 (^{50}Ti^{56}Fe)
1-0	16192.87(3)	16192.19(18)	16190.78(16)	16189.31(6)	16187.77(4)
2-0		16526.46(-35)	16523.33(-31)	16520.31(-17)	16517.41(-4)
3-0	16861.02(-17)	16855.89(-3)	16850.95(-6)	16846.24(13)	16841.58(-10)
4-0	17186.60(23)	17179.73(39)	17173.13(38)		17160.59(17)
5-0	17505.46(-9)	17496.90(-19)	17488.65(-18)	17480.49(-2)	17473.61(-7)
Fitted spectroscopic constants					
T_0 (cm^{-1})	15849.67(64)	15851.54(89)	15851.95(84)	15852.39(51)	15852.54(32)
ω_e' (cm^{-1})	349.175(589)	346.156(784)	344.309(741)	342.471(459)	340.683(287)
$\omega_e'x_e'$ (cm^{-1})	3.000(85)	2.841(110)	2.822(104)	2.808(63)	2.743(40)
k_e' (mdyn/Å)	1.812	1.802	1.803	1.804	1.804

[a] Residuals in the fit of the vibronic band origins are provided in parentheses following each band origin, in units of 0.01 cm^{-1}. Error limits (1σ) for the resulting fitted spectroscopic constants are provided in units of the last digit quoted.

Table D.2

Vibronic fit of bands belonging to the $[16.2]0^+ \leftarrow X\,^1\Sigma^+$ system of TiFe

Band	ν_0 ($^{46}Ti^{56}Fe$)	ν_0 ($^{48}Ti^{54}Fe$)	ν_0 ($^{47}Ti^{56}Fe$)	ν_0 ($^{48}Ti^{56}Fe$)	ν_0 ($^{49}Ti^{56}Fe$)	ν_0 ($^{50}Ti^{56}Fe$)
1-0	16527.94(332)	16527.27(263)	16526.65(318)	16525.41(252)	16524.20(313)	16523.05(300)
2-0	16856.09(-274)	16854.46(-248)	16852.97(-263)	16849.96(-235)	16847.04(-376)	16844.22(-364)
3-0	17178.65(-352)	17176.07(-282)	17173.73(-337)	17168.96(-274)		17468.89(-252)
4-0	17493.86(-76)	17490.38(-13)	17487.25(-72)	17480.90(-14)	17474.79(-266)	17768.26(111)
5-0	17798.64(246)	17794.45(267)	17790.64(242)	17782.92(258)	17775.46(108)	18055.51(333)
6-0	18090.59(373)	18085.69(296)	18081.35(352)	18072.45(285)	18063.84(346)	18327.43(91)
7-0	18365.66(-100)	18360.49(-283)	18355.78(-103)	18346.10(-272)	18336.60(116)	18587.98(-219)
8-0	18634.08(-149)		18623.79(-137)		18597.16(-241)	
			Fitted spectroscopic constants			
T_0 (cm^{-1})	16179.51(461)	16182.00(522)	16180.71(442)	16183.42(502)	16180.41(500)	16181.54(476)
ω_e' (cm^{-1})	355.99(260)	352.98(3351)	353.39(249)	349.51(322)	351.59(288)	349.20(274)
$\omega_e'x_e'$(cm^{-1})	5.443(255)	5.170(366)	5.315(244)	5.021(352)	5.466(286)	5.347(272)
k_e' (mdyn/Å)	1.884	1.895	1.874	1.900	1.879	1.922

[a] Residuals in the fit of the vibronic band origins are provided in parentheses following each band origin, in units of 0.01 cm^{-1}. Error limits (1σ) for the resulting fitted spectroscopic constants are provided in units of the last digit quoted.

D.2 Rotationally resolved spectra of TiFe

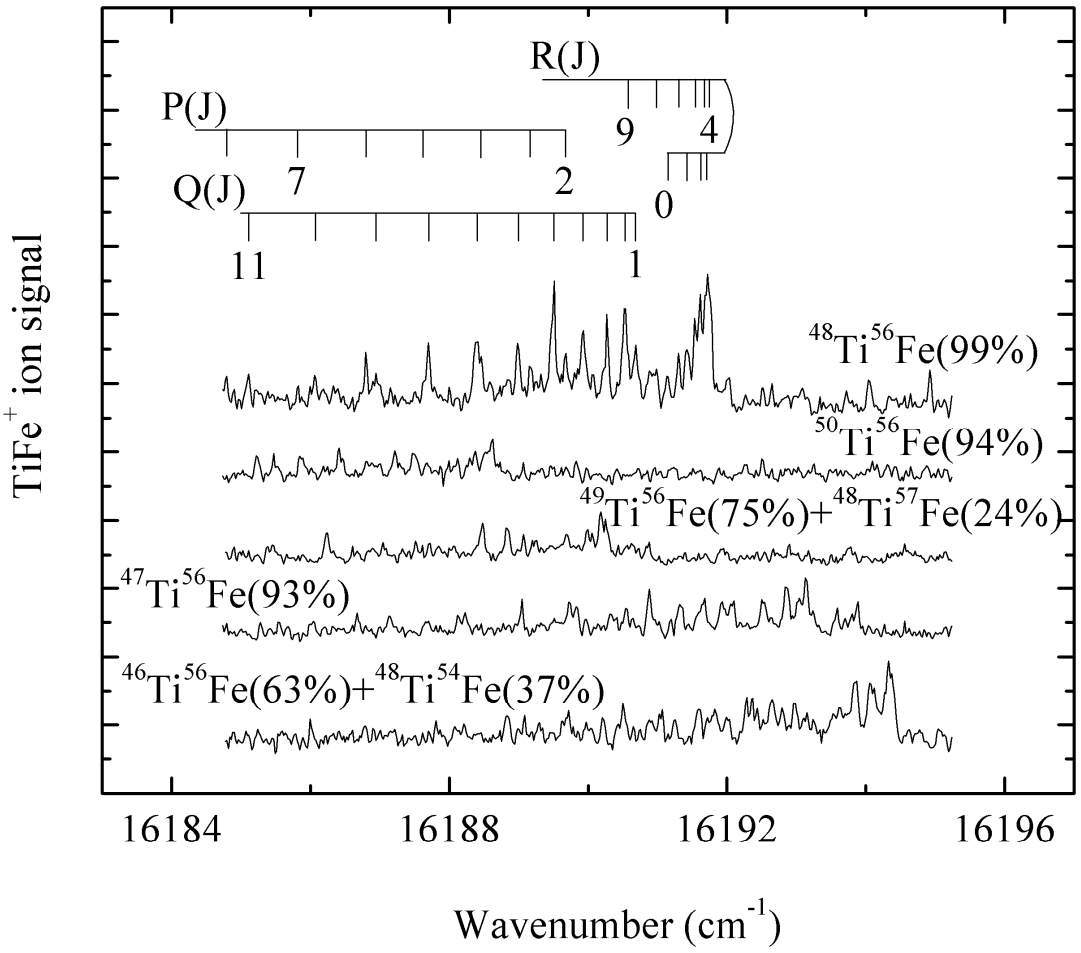

Figure D.11. Rotationally resolved spectra of the various TiFe isotopic combinations for the 1-0 band of the [15.9]1 ← $X\,^1\Sigma^+$ system. Line assignments are provided for the most abundant isotopomer, $^{48}Ti^{56}Fe$.

Table D.3

Fitted Rotational Lines of the 1-0 band of the [15.9]1 ← X $^1\Sigma^+$ system of TiFe[a]

Line	$^{46}Ti^{56}Fe$	$^{47}Ti^{56}Fe$	$^{48}Ti^{56}Fe$	$^{49}Ti^{56}Fe$	$^{50}Ti^{56}Fe$
P(2)		16191.191(1)			16186.815(-14)
P(3)	16191.245(-12)	16190.552(9)	16189.165(5)	16187.710(17)	
P(4)	16190.501(13)	16189.835(7)	16188.459(4)	16187.045(-5)	16185.470(-7)
P(5)	16189.706(4)	16189.048(-14)		16186.237(34)	
P(6)	16188.833(-13)	16188.129(10)	16186.798(-6)	16185.379(43)	
P(7)		16187.142(15)	16185.816(14)		
P(8)	16186.790(-8)		16184.765(15)		
Q(1)	16192.794(-6)	16192.095(9)	16190.686(6)	16189.251(-25)	16187.679(4)
Q(2)	16192.639(-23)	16191.926(2)	16190.530(-9)	16189.071(-7)	16187.496(4)
Q(3)	16192.343(16)	16191.669(-5)	16190.274(-9)	16188.822(0)	16187.220(7)
Q(4)	16192.010(6)	16191.329(-16)	16189.926(-3)	16188.479(21)	
Q(5)	16191.598(-11)	16190.878(-4)	16189.507(-11)	16188.067(28)	16186.412(-5)
Q(6)	16191.051(21)	16190.330(17)	16188.986(-3)		16185.862(-2)
Q(7)		16189.731(1)	16188.395(-10)	16187.045(2)	16185.223(-1)
Q(8)		16189.048(-18)	16187.701(0)		
Q(9)		16188.226(13)	16186.944(-13)		
Q(10)			16186.067(9)		
R(0)	16193.248(2)		16191.143(0)	16189.689(-17)	16188.121(3)
R(1)	16193.536(3)		16191.423(-1)	16189.982(-26)	16188.376(7)
R(2)	16193.742(1)	16193.048(-16)	16191.614(2)	16190.180(-20)	
R(3)	16193.847(14)	16193.141(-5)	16191.722(3)	16190.287(-5)	16188.619(8)
R(4)		16193.141(12)	16191.749(-1)		16188.619(-6)

Table D.3 continued

R(5)	16193.847(-7)		16191.682(4)	16190.287(-1)	16188.520(-13)
R(6)	16193.701(-1)	16192.941(-18)	16191.533(4)	16190.180(-14)	16188.296(14)
R(7)			16191.300(3)	16189.982(-16)	
R(8)			16190.987(-2)	16189.689(-4)	
R(9)			16190.578(3)	16189.326(-3)	
R(12)			16188.858(-3)		
			Fitted Spectroscopic Constants[b]		
ν_0 (cm^{-1})	16192.8742(48)	16192.1915(44)	16190.7778(21)	16189.3066(68)	16187.7740(36)
B_1' (cm^{-1})	0.187717(171)	0.183991(125)	0.182483(40)	0.182464(154)	0.174963(127)
r_1' (Å)	1.88673(86)	1.89458(64)	1.89161(21)	1.88128(79)	1.91093(69)
B_0'' (cm^{-1})	0.230619(56)	0.227903(41)	0.225228(31)	0.222829(51)	0.220525(56)
r_0'' (Å)	1.70222(21)	1.70230(15)	1.70268(12)	1.70238(19)	1.70212(22)

[a] Residuals in the fit of the rotational lines are provided in parentheses following each line, in units of 0.001 cm^{-1}. In the case of $^{46}Ti^{56}Fe$, because of the poor quality of the data for this band it was decided to exclude the band from the combined fit. Likewise, because of the overlap between different isotopic modifications, the lines identified for $^{49}Ti^{56}Fe$ were excluded from the combined fit. Instead, B_0'' was held fixed at the value obtained for the other bands, and the band for these isotopomers was fitted separately. All of the observed bands originated from the $v''=0$ level of the $X\ ^1\Sigma^+$ ground state. Unless stated otherwise, all bands were used in a combined fit to extract the most accurate values of the spectroscopic constants.

[b] Errors (1σ) are provided for all fitted spectroscopic constants in parentheses following the reported value, in units of the last digit quoted.

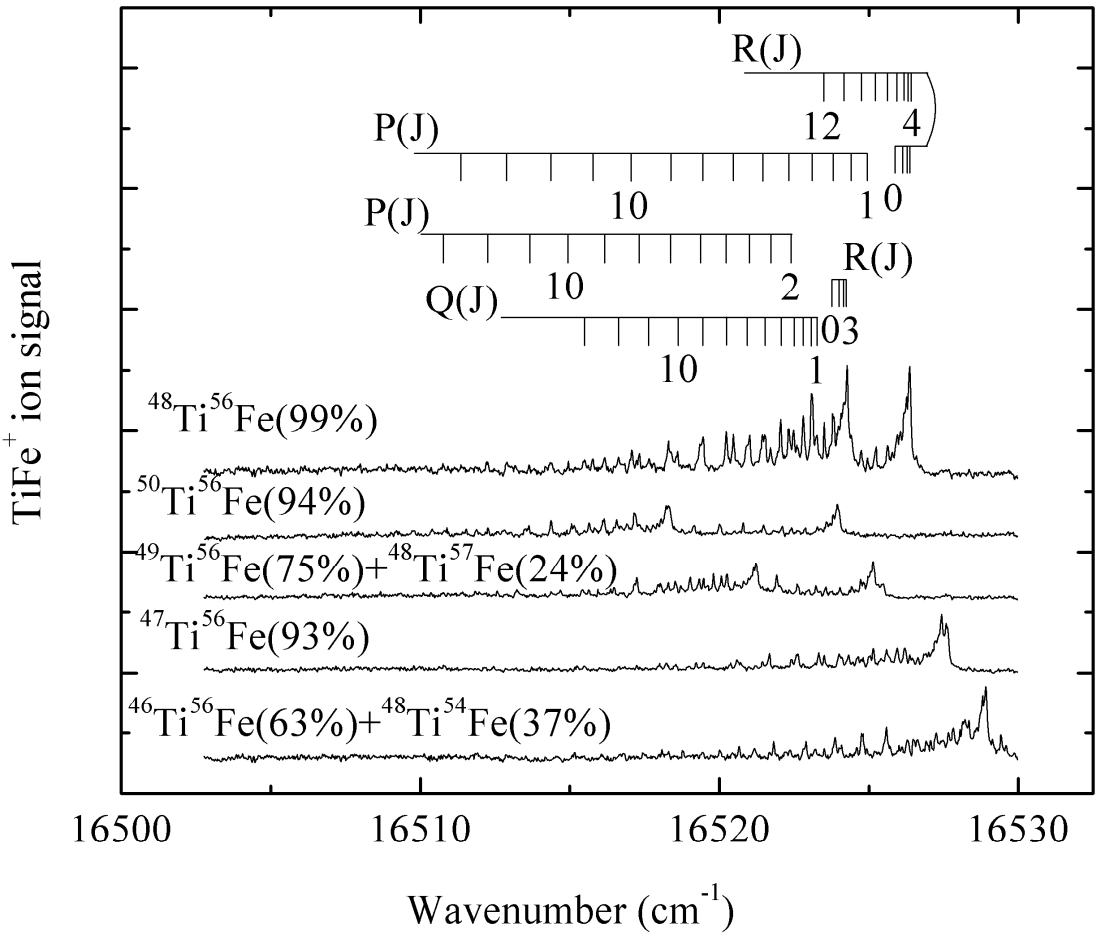

Figure D.12. Rotationally resolved spectra of the various TiFe isotopic combinations for the 2-0 band of the [15.9]1 ← X $^1\Sigma^+$ system and the 1-0 band of the [16.2]0^+ ← X $^1\Sigma^+$ system. Line assignments are provided for the most abundant isotopomer, $^{48}Ti^{56}Fe$.

Table D.4

Fitted Rotational Lines of the 2-0 band of the [15.9]1 ← X $^1\Sigma^+$ system of TiFe[a]

Line	$^{47}Ti^{56}Fe$	$^{48}Ti^{56}Fe$	$^{49}Ti^{56}Fe$	$^{50}Ti^{56}Fe$
P(2)			16519.321(14)	
P(3)	16524.801(26)	16521.705(15)	16518.703(16)	16515.849(-15)
P(4)	16524.090(20)	16521.012(-1)	16518.029(-11)	16515.136(4)
P(5)	16523.314(-8)	16520.226(-10)	16517.231(0)	16514.372(-10)
P(6)	16522.402(12)	16519.342(-7)	16516.357(3)	16513.489(10)
P(7)	16521.433(2)	16518.375(-8)	16515.412(-8)	
P(8)	16520.375(-5)	16517.319(-5)	16514.370(-8)	16511.536(-17)
P(9)	16519.211(7)	16516.157(17)	16513.220(15)	16510.389(14)
P(10)	16517.991(-13)	16514.955(-7)		16509.196(6)
P(11)	16516.635(16)	16513.630(5)		16507.916(1)
P(12)	16515.247(-9)	16512.225(12)		
P(13)	16513.726(11)	16510.750(3)		
P(14)	16512.150(-1)			
Q(1)	16526.360(8)	16523.250(-6)	16520.210(16)	
Q(2)	16526.201(-7)	16523.090(-19)	16520.064(-8)	16517.161(-4)
Q(3)	16525.941(-8)	16522.801(12)	16519.798(2)	16516.905(-1)
Q(4)	16525.586(-1)	16522.477(-8)	16519.464(-4)	16516.565(2)
Q(5)	16525.144(5)	16522.047(-9)	16519.019(15)	16516.146(-2)
Q(6)	16524.635(-8)	16521.516(4)	16518.523(0)	16515.634(4)
Q(7)	16523.998(19)	16520.907(10)	16517.944(-17)	16515.053(-6)
Q(8)	16523.314(6)	16520.226(2)	16517.231(15)	16514.372(1)
Q(9)	16522.559(-23)		16516.476(4)	16513.604(8)

Table D.4 continued

Q(10)	16521.665(0)	16518.592(-1)	16515.634(-6)	
Q(11)	16520.702(5)	16517.641(2)	16514.677(14)	
Q(12)	16519.658(5)	16516.624(-15)		
Q(13)	16518.537(-7)	16515.495(-7)	16512.571(-8)	16509.725(5)
Q(14)			16511.355(16)	16508.547(1)
Q(15)	16516.003(2)		16510.098(-5)	
R(0)	16526.829(-5)	16523.693(1)	16520.681(-10)	16517.774(-6)
R(1)	16527.125(-19)	16523.977(-5)	16520.962(-15)	16518.048(-8)
R(2)		16524.152(12)	16521.144(-7)	16518.219(8)
R(3)	16527.420(-13)	16524.269(1)	16521.221(22)	16518.318(13)
R(4)	16527.420(8)		16521.274(-12)	
R(5)	16527.379(-18)			16518.282(3)
R(6)	16527.217(-10)	16524.056(15)	16521.064(-17)	16518.132(3)
R(7)			16520.799(12)	
R(8)	16526.636(2)		16520.504(-13)	16517.568(14)
R(10)		16522.602(-4)	16519.607(-13)	16516.702(-10)
R(12)	16524.456(0)			16515.479(-15)
R(13)	16523.696(-3)			
R(16)		16517.804(0)		
Fitted Spectroscopic Constants[b]				
ν_0 (cm^{-1})	16526.4553(30)	16523.3300(24)	16520.3112(31)	16517.4107(25)
B_2' (cm^{-1})	0.184359(55)	0.182143(30)	0.180255(64)	0.178323(51)
r_2' (Å)	1.89268(28)	1.89338(16)	1.89277(34)	1.89284(27)
B_0'' (cm^{-1})	0.227903(41)	0.225228(31)	0.222829(51)	0.220525(56)
r_0'' (Å)	1.70230(15)	1.70268(12)	1.70238(19)	1.70212(22)

Table D.4 continued

[a] Residuals in the fit of the rotational lines are provided in parentheses following each line, in units of 0.001 cm^{-1}. All of the observed bands originated from the v″=0 level of the $X\ ^1\Sigma^+$ ground state. Unless stated otherwise, all bands were used in a combined fit to extract the most accurate values of the spectroscopic constants.
[b] Errors (1σ) are provided for all fitted spectroscopic constants in parentheses following the reported value, in units of the last digit quoted.

Table D.5

Fitted Rotational Lines of the 1-0 band of the $[16.2]0^{+} \leftarrow X\ ^{1}\Sigma^{+}$ system of TiFe[a]

Line	$^{46}Ti^{56}Fe$	$^{48}Ti^{54}Fe$	$^{47}Ti^{56}Fe$	$^{48}Ti^{56}Fe$	$^{49}Ti^{56}Fe$	$^{50}Ti^{56}Fe$
P(1)	16527.479(-3)	16526.821(-13)		16524.952(3)	16523.772(-17)	16522.622(-12)
P(2)	16526.916(13)	16526.274(-12)		16524.403(16)	16523.222(2)	16522.096(-11)
P(3)	16526.290(3)		16525.042(-18)	16523.787(11)	16522.599(12)	16521.477(2)
P(4)	16525.571(0)	16524.921(-11)	16524.309(2)	16523.090(2)	16521.912(1)	16520.787(0)
P(5)	16524.752(11)	16524.083(20)	16523.502(10)	16522.307(-6)	16521.144(-13)	16520.008(5)
P(6)	16523.861(5)	16523.194(16)	16522.625(2)	16521.435(-11)	16520.251(13)	16519.149(6)
P(7)	16522.897(-13)	16522.210(21)	16521.665(-9)	16520.462(1)	16519.321(-7)	16518.219(-6)
P(8)	16521.806(8)	16521.172(-9)	16520.588(11)	16519.435(-19)	16518.289(-10)	16517.169(20)
P(9)	16520.650(7)	16520.017(-7)	16519.457(-1)	16518.288(-5)	16517.166(-5)	
P(10)	16519.423(-9)	16518.778(-9)	16518.232(-4)	16517.062(4)	16515.969(-11)	16514.889(2)
P(11)	16518.075(8)	16517.443(-1)		16515.755(8)	16514.677(-5)	16513.626(-10)
P(12)	16516.665(1)			16514.364(11)		16512.260(-2)
P(13)	16515.154(8)			16512.885(17)	16511.837(10)	16510.805(12)
P(14)			16512.449(8)	16511.355(-11)		16509.288(5)
R(0)		16527.654(-15)		16525.776(-5)	16524.550(11)	16523.395(14)
R(1)	16528.610(-10)			16526.053(-3)	16524.838(1)	16523.692(-9)
R(2)	16528.794(6)	16528.131(-8)		16526.251(-5)	16525.042(-10)	16523.887(-12)
R(3)			16527.619(-5)	16526.352(3)	16525.137(4)	16523.990(-8)
R(5)	16528.897(-17)		16527.575(6)			16523.941(6)
R(6)	16528.732(1)	16528.037(13)		16526.175(-3)	16524.965(0)	16523.798(7)
R(7)		16527.813(2)		16525.944(-3)	16524.718(20)	16523.573(6)
R(8)	16528.195(-17)	16527.479(14)	16526.901(-12)	16525.625(0)	16524.421(5)	16523.269(1)

Table D.5 continued

R(9)		16527.068(16)	16526.462(24)	16525.230(-7)	16524.026(5)	16522.868(10)
R(10)		16526.596(-8)		16524.738(-2)	16523.552(0)	16522.408(-6)
R(11)		16526.006(-1)		16524.152(11)	16522.987(1)	
R(12)				16523.503(3)	16522.338(2)	16521.204(-3)
R(13)		16524.583(-3)			16521.619(-10)	16520.490(-15)
R(14)		16523.732(5)	16523.199(-13)	16521.944(-9)		
R(15)		16522.799(8)				
R(16)		16521.806(-16)				
Fitted Spectroscopic Constants[b]						
ν_0 (cm^{-1})	16527.9376(35)	16527.2668(39)	16526.6488(47)	16525.4055(27)	16524.2000(29)	16523.0512(28)
B_1' (cm^{-1})	0.187158(72)	0.186153(79)	0.184987(62)	0.182614(40)	0.180778(64)	0.178853(52)
r_1' (Å)	1.88955(36)	1.88879(40)	1.88947(32)	1.89094(21)	1.89003(34)	1.89004(28)
B_0'' (cm^{-1})	0.230619(56)	0.229557(86)	0.227903(41)	0.225228(31)	0.222829(51)	0.220525(56)
r_0''(Å)	1.70222(21)	1.70088(32)	1.70230(15)	1.70268(12)	1.70238(19)	1.70212(22)

[a] Residuals in the fit of the rotational lines are provided in parentheses following each line, in units of 0.001 cm^{-1}. All of the observed bands originated from the v″=0 level of the X $^1\Sigma^+$ ground state. Unless stated otherwise, all bands were used in a combined it to extract the most accurate values of the spectroscopic constants.

[b] Errors (1σ) are provided for all fitted spectroscopic constants in parentheses following the reported value, in units of the last digit quoted.

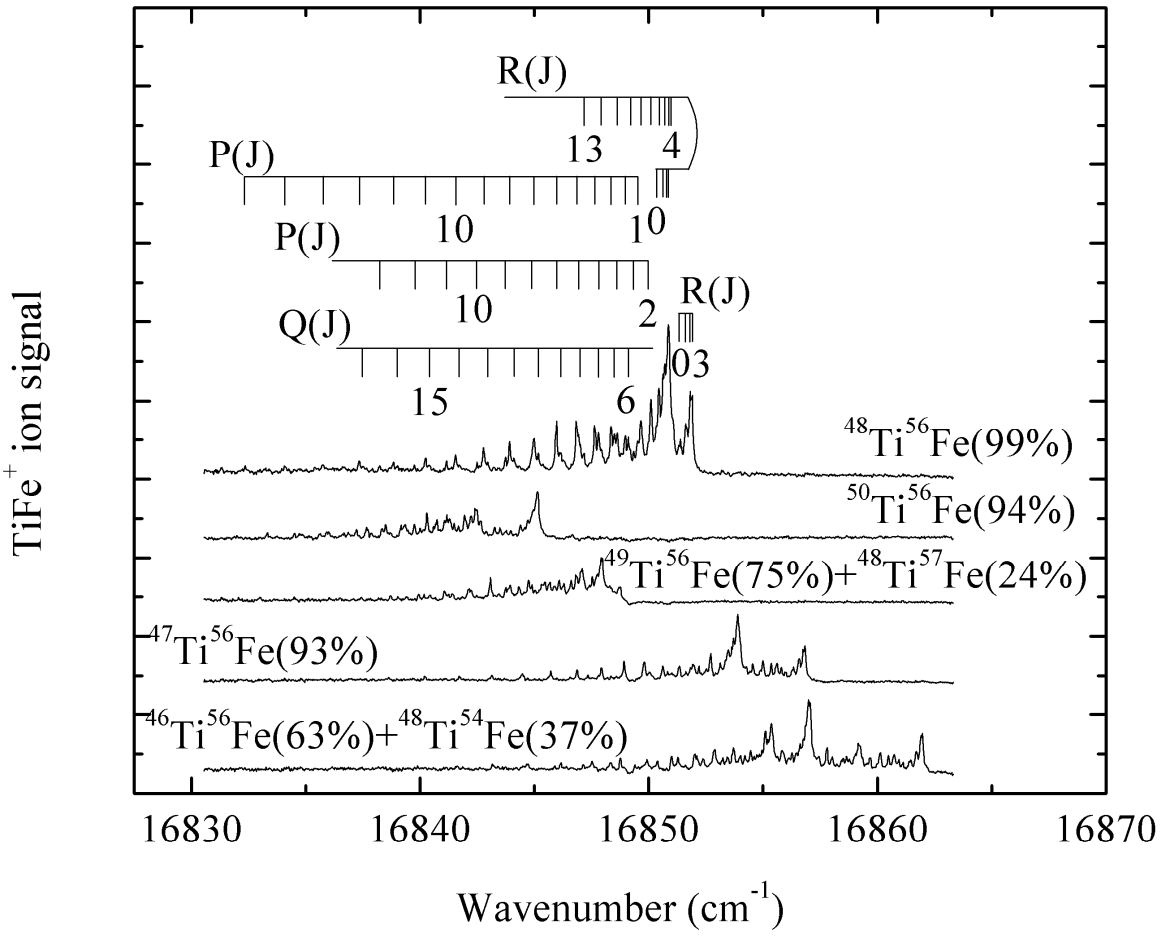

Figure D.13. Rotationally resolved spectra of the various TiFe isotopic combinations for the 3-0 band of the [15.9]1 ← X $^1\Sigma^+$ system and the 2-0 band of the [16.2]0^+ ← X $^1\Sigma^+$ system. Line assignments are provided for the most abundant isotopomer, $^{48}Ti^{56}Fe$

Table D.6

Fitted Rotational Lines of the 2-0 band of the $[16.2]0^{+} \leftarrow X\ ^{1}\Sigma^{+}$ system of TiFe[a]

Line	$^{46}Ti^{56}Fe$	$^{48}Ti^{54}Fe$	$^{47}Ti^{56}Fe$	$^{48}Ti^{56}Fe$	$^{49}Ti^{56}Fe$	$^{50}Ti^{56}Fe$
P(1)	16855.629(3)	16854.008(-7)	16852.517(-2)	16849.513(-1)	16846.600(-7)	16843.766(13)
P(2)	16855.096(-14)	16853.445(9)	16851.979(-6)	16848.969(6)	16846.074(-12)	16843.262(-9)
P(3)	16854.451(-7)	16852.830(-12)	16851.347(-5)	16848.350(1)	16845.454(-10)	16842.645(-2)
P(4)	16853.709(8)	16852.096(-3)	16850.616(7)	16847.635(5)	16844.738(4)	16841.937(11)
P(5)	16852.886(15)	16851.271(10)	16849.804(12)	16846.831(12)	16843.934(19)	16841.166(2)
P(6)	16852.011(-14)	16850.379(0)	16848.920(3)	16845.960(-2)	16843.077(2)	16840.291(13)
P(7)	16850.995(8)	16849.393(-4)	16847.935(7)	16844.967(19)	16842.126(-7)	16839.339(16)
P(8)	16849.927(-5)	16848.327(-16)	16846.868(5)	16843.913(16)	16841.063(10)	16838.339(-18)
P(9)	16848.754(-3)	16847.126(18)	16845.711(6)	16842.777(7)	16839.937(5)	16837.217(-14)
P(10)		16845.883(5)	16844.466(6)	16841.544(9)	16838.709(16)	16836.014(-14)
P(11)	16846.156(-11)		16843.133(8)	16840.235(-1)	16837.430(-8)	16834.712(1)
P(12)	16844.684(24)		16841.714(8)	16838.832(-4)	16836.041(-7)	
P(13)	16843.175(9)		16840.210(6)	16837.332(4)		
P(14)			16838.623(-2)	16835.744(13)	16832.996(4)	
P(15)				16834.090(2)		
P(16)				16832.342(-2)		
R(0)	16856.444(22)	16854.835(-4)	16853.352(-12)	16850.329(-2)	16847.398(1)	16844.571(6)
R(1)	16856.757(-7)	16855.096(17)	16853.632(-12)	16850.619(-16)	16847.676(-3)	16844.847(1)
R(2)		16855.304(3)		16850.797(-4)		
R(3)	16857.054(-2)				16847.968(-5)	16845.138(0)
R(4)	16857.054(16)	16855.429(0)			16847.968(13)	
R(5)	16856.983(16)	16855.361(-4)	16853.889(-22)	16850.858(-15)	16847.918(-5)	

Table D.6 continued

R(6)	16856.857(-17)	16855.198(-1)	16853.699(11)	16850.702(-16)	16847.748(10)	16844.956(-19)
R(7)	16856.608(-15)	16854.956(-7)	16853.479(-14)	16850.446(-4)	16847.531(-13)	16844.709(-8)
R(8)	16856.263(-6)	16854.608(4)	16853.129(4)	16850.094(17)		16844.388(-8)
R(9)	16855.845(-14)	16854.197(-11)	16852.713(0)	16849.703(-10)		16843.963(11)
R(10)			16852.190(15)	16849.200(-11)	16846.290(-6)	16843.489(-5)
R(11)	16854.737(-23)		16851.621(-11)	16848.615(-17)		16842.892(17)
R(12)	16854.008(16)	16852.371(8)		16847.931(-11)	16845.025(8)	
R(13)	16853.242(2)	16851.603(-3)	16850.165(-8)	16847.169(-14)		
R(14)				16846.285(19)	16843.445(-7)	16840.672(5)
R(15)			16848.342(12)	16845.370(-5)		
R(16)			16847.338(-17)	16844.347(-7)		
R(17)				16843.217(11)		
Fitted Spectroscopic Constants[b]						
ν_0 (cm^{-1})	16856.0934(42)	16854.4604(28)	16852.9715(30)	16849.9628(30)	16847.0384(28)	16844.2203(37)
B_2' (cm^{-1})	0.186303(54)	0.185327(88)	0.184115(48)	0.181828(33)	0.179975(51)	0.178194(52)
r_2' (Å)	1.89388(27)	1.89300(45)	1.89394(25)	1.89502(17)	1.89424(27)	1.89353(28)
B_0'' (cm^{-1})	0.230619(56)	0.229557(86)	0.227903(41)	0.225228(31)	0.222829(51)	0.220525(56)
r_0'' (Å)	1.70222(21)	1.70088(32)	1.70230(15)	1.70268(12)	1.70238(19)	1.70212(22)

[a] Residuals in the fit of the rotational lines are provided in parentheses following each line, in units of 0.001 cm^{-1}. All of the observed bands originated from the v″=0 level of the $X\ ^1\Sigma^+$ ground state. Unless stated otherwise, all bands were used in a combined it to extract the most accurate values of the spectroscopic constants.

[b] Errors (1σ) are provided for all fitted spectroscopic constants in parentheses following the reported value, in units of the last digit quoted.

Table D.7

Fitted Rotational Lines of the 3-0 band of the [15.9]1 ← X $^1\Sigma^+$ system of TiFe[a]

Line	$^{46}Ti^{56}Fe$	$^{47}Ti^{56}Fe$	$^{48}Ti^{56}Fe$	$^{49}Ti^{56}Fe$	$^{50}Ti^{56}Fe$
P(1)				16845.832(-41)	
P(2)	16859.998(13)	16854.888(-3)	16849.973(-8)		16840.592(20)
P(3)	16859.358(12)	16854.270(-18)	16849.340(-1)		16840.001(-2)
P(4)	16858.653(-15)		16848.615(10)	16843.934(-18)	16839.281(18)
P(5)			16847.803(20)	16843.150(-38)	16838.493(20)
P(6)		16851.821(-1)	16846.928(4)	16842.232(-14)	
P(7)		16850.828(3)	16845.960(-6)	16841.241(-7)	16836.680(2)
P(8)			16844.876(12)	16840.178(-16)	16835.628(9)
P(9)		16848.575(13)	16843.735(-1)	16839.022(-24)	16834.507(0)
P(10)		16847.338(-4)	16842.482(10)		
P(11)		16845.992(-1)	16841.150(12)		
P(12)			16839.748(-4)		
P(13)			16838.222(16)		
Q(1)	16860.940(-6)	16855.790(7)			
Q(2)	16860.735(19)	16855.607(13)			16841.342(-20)
Q(3)	16860.483(0)	16855.355(-2)		16845.677(22)	16841.061(2)
Q(4)	16860.126(-5)	16854.983(15)		16845.315(25)	16840.731(-12)
Q(5)	16859.659(12)	16854.542(13)		16844.889(3)	16840.291(-4)
Q(6)		16854.016(6)	16849.100(8)	16844.317(37)	16839.750(20)
Q(7)	16858.501(-4)		16848.494(-3)		16839.161(5)
Q(8)	16857.783(-8)				
Q(9)			16847.008(-12)		

Table D.7 continued

Q(10)		16851.013(-9)	16846.128(-11)		16836.852(-15)
Q(11)		16850.035(-7)	16845.159(-10)		
Q(12)			16844.107(-12)		
Q(13)		16847.808(1)	16842.951(0)		
Q(14)		16846.573(-7)	16841.723(-4)		
Q(15)			16840.397(4)		
Q(16)			16838.998(-5)		
Q(17)			16837.494(4)		
R(0)	16861.389(7)	16856.269(-16)	16851.315(2)	16846.600(-7)	16841.937(-2)
R(1)	16861.699(-23)		16851.604(-13)	16846.870(-11)	16842.223(-19)
R(2)		16856.740(-19)	16851.785(-7)	16847.016(19)	16842.406(-20)
R(3)	16861.969(-3)	16856.830(-8)	16851.886(-9)	16847.087(36)	16842.481(1)
R(4)	16861.969(7)	16856.830(4)	16851.886(1)	16847.087(33)	16842.481(11)
R(5)	16861.910(-14)		16851.807(2)		
R(6)			16851.650(-5)		
R(7)	16861.466(-2)				
R(8)	16861.119(-5)	16855.979(15)	16851.045(6)		16841.681(-12)
R(9)	16860.657(15)				
R(11)		16854.428(4)			
R(12)					16839.465(1)
R(13)					16838.707(-7)
R(14)					16837.860(-13)
R(15)					16836.907(1)
R(16)					16835.868(15)

Table D.7 continued

Fitted Spectroscopic Constants[b]					
ν_0 (cm^{-1})	16861.0243(40)	16855.8859(31)	16850.9541(24)	16846.2364(110)	16841.5805(34)
B_3' (cm^{-1})	0.185487(113)	0.183525(59)	0.181254(35)	0.178013(346)	0.177405(43)
r_3' (Å)	1.89804(58)	1.89698(30)	1.89802(18)	1.90465(185)	1.89773(23)
B_0'' (cm^{-1})	0.230619(56)	0.227903(41)	0.225228(31)	0.222829(51)	0.220525(56)
r_0'' (Å)	1.70222(21)	1.70230(15)	1.70268(12)	1.70238(19)	1.70212(22)

[a] Residuals in the fit of the rotational lines are provided in parentheses following each line, in units of 0.001 cm^{-1}. In the case of $^{49}Ti^{56}Fe$, because of the poor quality of the data for this band it was decided to exclude the band from the combined fit. Instead, B_0'' was held fixed at the value obtained for the other bands, and the band for this isotopomer was fitted separately. All of the observed bands originated from the v″=0 level of the $X\ ^1\Sigma^+$ ground state. Unless stated otherwise, all bands were used in a combined fit to extract the most accurate values of the spectroscopic constants.

[b] Errors (1σ) are provided for all fitted spectroscopic constants in parentheses following the reported value, in units of the last digit quoted.

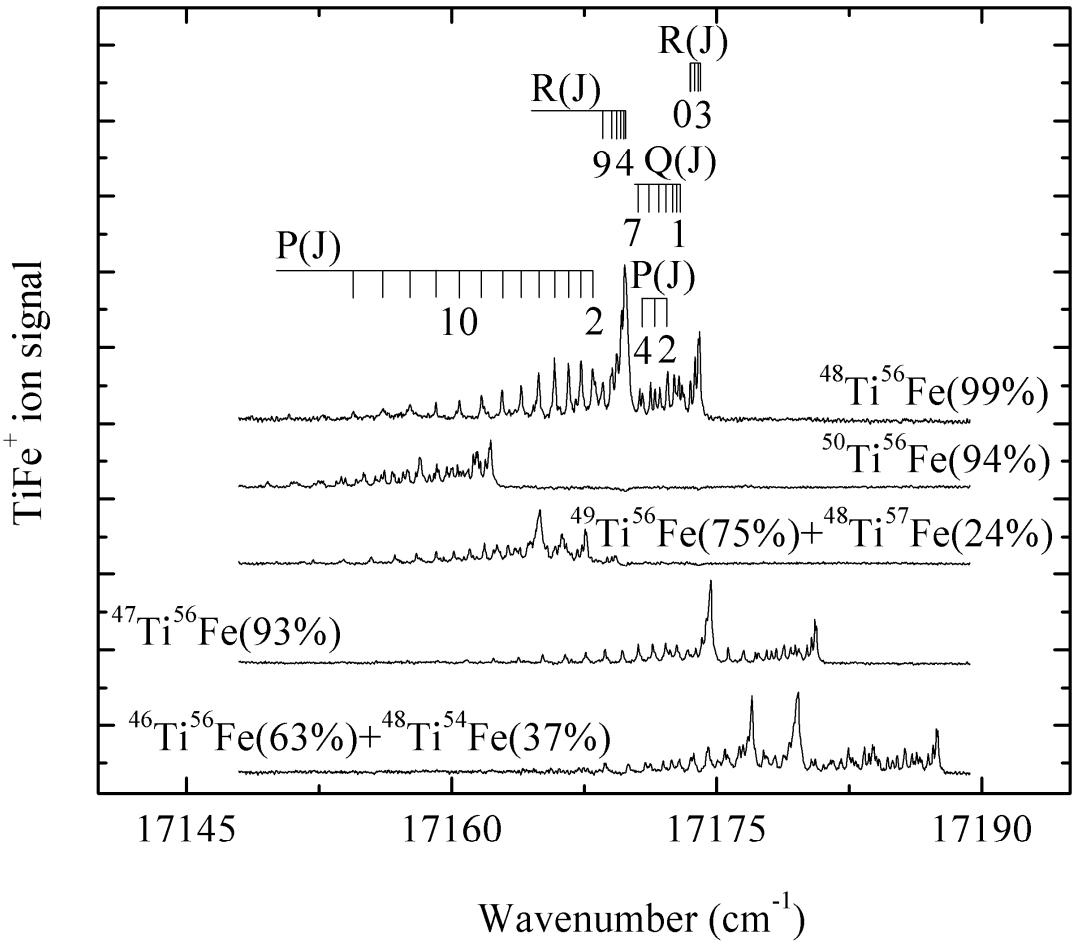

Figure D.14. Rotationally resolved spectra of the various TiFe isotopic combinations for the 4-0 band of the [15.9]1 ← X $^1\Sigma^+$ system and the 3-0 band of the [16.2]0^+ ← X $^1\Sigma^+$ system. Line assignments are provided for the most abundant isotopomer, $^{48}Ti^{56}Fe$

Table D.8

Fitted Rotational Lines of the 3-0 band of the $[16.2]0^+ \leftarrow X\ ^1\Sigma^+$ system of TiFe[a]

Line	$^{46}Ti^{56}Fe$	$^{48}Ti^{54}Fe$	$^{47}Ti^{56}Fe$	$^{48}Ti^{56}Fe$	$^{49}Ti^{56}Fe$
P(1)		17175.600(11)			17163.728(26)
P(2)	17177.653(-13)	17175.048(14)	17172.739(-8)	17167.968(5)	17163.188(25)
P(3)	17176.993(6)	17174.437(-15)	17172.098(-2)	17167.334(10)	17162.566(10)
P(4)		17173.702(-9)	17171.369(4)	17166.614(10)	17161.854(-11)
P(5)	17175.455(-8)	17172.886(-12)	17170.557(4)	17165.821(-4)	17161.023(-8)
P(6)	17174.536(0)	17171.972(-7)	17169.659(-1)	17164.921(-2)	17160.125(-33)
P(7)	17173.545(-8)	17170.978(-14)	17168.674(-7)	17163.930(2)	
P(8)	17172.449(-4)		17167.583(4)	17162.852(3)	17158.005(-48)
P(9)	17171.251(14)	17168.687(7)	17166.425(-7)	17161.685(4)	17156.785(-40)
P(10)	17169.999(-3)	17167.425(-1)	17165.148(11)	17160.438(-4)	17155.462(-22)
P(11)			17163.795(15)	17159.111(-22)	
P(12)	17167.207(-21)		17162.370(3)	17157.650(4)	
P(13)			17160.856(-9)	17156.114(16)	
R(1)		17176.708(10)			
R(3)		17176.993(13)	17174.667(-4)	17169.876(-6)	17164.998(28)
R(4)	17179.617(-7)		17174.667(6)	17169.876(-3)	
R(5)	17179.505(27)	17176.937(-4)	17174.601(-8)	17169.802(-14)	
R(6)	17179.376(-12)	17176.770(-8)	17174.420(4)	17169.615(-3)	
R(7)	17179.085(22)	17176.495(5)	17174.172(-6)	17169.336(10)	17164.324(-2)
R(8)	17178.766(-6)	17176.147(1)	17173.811(8)	17168.996(-4)	17163.870(37)
R(9)	17178.316(5)	17175.690(16)	17173.373(10)	17168.551(-3)	17163.398(-2)

Table D.8 continued

R(10)	17177.782(12)	17175.181(-7)	17172.859(-2)		17162.750(39)
R(11)	17177.182(-5)		17172.257(-15)		
R(12)		17173.842(-2)			
Fitted Spectroscopic Constants[b]					
ν_0 (cm^{-1})	17178.6520(58)	17176.0702(37)	17173.7316(30)	17168.9634(36)	17164.1998(126)
B_3' (cm^{-1})	0.185686(94)	0.184508(69)	0.183293(69)	0.180502(56)	0.175006(191)
r_3' (Å)	1.89702(48)	1.89720(36)	1.89818(36)	1.90197(30)	1.92095(105)
B_0'' (cm^{-1})	0.230619(56)	0.229557(86)	0.227903(41)	0.225228(31)	0.222829(51)
r_0'' (Å)	1.70222(21)	1.70088(32)	1.70230(15)	1.70268(12)	1.70238(19)

[a] Residuals in the fit of the rotational lines are provided in parentheses following each line, in units of 0.001 cm^{-1}. In the case of $^{49}Ti^{56}Fe$, because of the poor quality of the data for this band it was decided to exclude the band from the combined fit. Instead, B_0'' was held fixed at the value obtained for the other bands, and the band for this isotopomer was fitted separately. All of the observed bands originated from the $v''=0$ level of the $X\ ^1\Sigma^+$ ground state. Unless stated otherwise, all bands were used in a combined fit to extract the most accurate values of the spectroscopic constants.
[b] Errors (1σ) are provided for all fitted spectroscopic constants in parentheses following the reported value, in units of the last digit quoted.

Table D.9

Fitted Rotational Lines of the 4-0 band of the [15.9]1 ← X $^1\Sigma^+$ system of TiFe[a]

Line	$^{46}Ti^{56}Fe$	$^{48}Ti^{54}Fe$	$^{47}Ti^{56}Fe$	$^{48}Ti^{56}Fe$	$^{50}Ti^{56}Fe$
P(2)	17185.606(-20)	17181.975(-11)	17178.750(-20)	17172.135(6)	17159.619(-1)
P(3)	17184.957(-16)	17181.332(-9)	17178.105(-13)	17171.502(10)	17159.007(-5)
P(4)	17184.196(9)	17180.580(11)	17177.361(4)	17170.797(-4)	
P(5)	17183.369(7)		17176.533(13)		17157.515(-9)
P(6)	17182.454(3)	17178.868(-15)	17175.644(-8)	17169.091(-2)	17156.632(-7)
P(7)	17181.444(1)	17177.868(-19)		17168.119(-17)	17155.672(-15)
P(8)			17173.555(-9)	17167.023(3)	17154.594(7)
P(9)			17172.367(-3)		17153.471(-14)
P(10)				17164.619(-12)	17152.225(1)
P(11)				17163.269(-6)	17150.920(-13)
P(12)				17161.834(-4)	17149.485(14)
Q(1)	17186.489(19)	17182.867(15)	17179.641(0)	17173.043(-1)	17160.483(18)
Q(2)	17186.315(10)	17182.694(6)	17179.451(9)	17172.861(2)	17160.325(0)
Q(3)	17186.055(-6)	17182.411(16)	17179.182(6)	17172.603(-7)	17160.049(13)
Q(4)	17185.689(-7)	17182.049(14)	17178.815(10)	17172.234(4)	17159.718(-8)
Q(5)	17185.216(7)	17181.615(-6)	17178.370(2)	17171.785(7)	17159.259(12)
Q(6)	17184.672(1)	17181.056(6)	17177.827(0)	17171.259(-3)	17158.743(1)
Q(7)	17184.023(8)	17180.411(15)	17177.192(0)	17170.632(-2)	
Q(8)	17183.316(-19)		17176.476(-10)		
Q(9)			17175.644(6)		
Q(10)	17181.553(1)				

Table D.9 continued

R(0)	17186.967(3)		17180.113(-16)		17160.953(-11)
R(1)	17187.250(-3)	17183.627(-9)	17180.367(5)	17173.773(-9)	17161.225(-18)
R(2)	17187.442(-9)	17183.818(-13)	17180.559(-4)	17173.958(-11)	17161.383(2)
R(3)	17187.523(4)	17183.903(-3)	17180.640(8)	17174.036(4)	17161.459(15)
R(4)	17187.523(7)	17183.903(1)	17180.640(10)	17174.036(8)	17161.459(17)
R(5)			17180.559(3)	17173.958(0)	
R(6)			17180.367(16)	17173.773(10)	
R(7)			17180.113(0)	17173.518(2)	
R(8)	17186.608(14)	17183.009(3)	17179.758(-5)	17173.150(16)	
R(9)	17186.182(-16)	17182.563(-3)	17179.310(-8)	17172.717(6)	
R(10)	17185.629(-11)		17178.756(3)		
R(11)	17184.963(15)				
Fitted Spectroscopic Constants[b]					
ν_0 (cm^{-1})	17186.5998(32)	17182.9730(39)	17179.7320(27)	17173.1313(24)	17160.5888(36)
B_4' (cm^{-1})	0.184744(73)	0.184072(91)	0.182549(65)	0.180565(70)	0.176610(80)
r_4' (Å)	1.90185(38)	1.89944(47)	1.90204(34)	1.90163(37)	1.90200(43)
B_0'' (cm^{-1})	0.230619(56)	0.229557(86)	0.227903(41)	0.225228(31)	0.220525(56)
r_0'' (Å)	1.70222(21)	1.70088(32)	1.70230(15)	1.70268(12)	1.70212(22)

[a] Residuals in the fit of the rotational lines are provided in parentheses following each line, in units of 0.001 cm^{-1}. All of the observed bands originated from the v″=0 level of the X $^1\Sigma^+$ ground state. Unless stated otherwise, all bands were used in a combined it to extract the most accurate values of the spectroscopic constants.

[b] Errors (1σ) are provided for all fitted spectroscopic constants in parentheses following the reported value, in units of the last digit quoted.

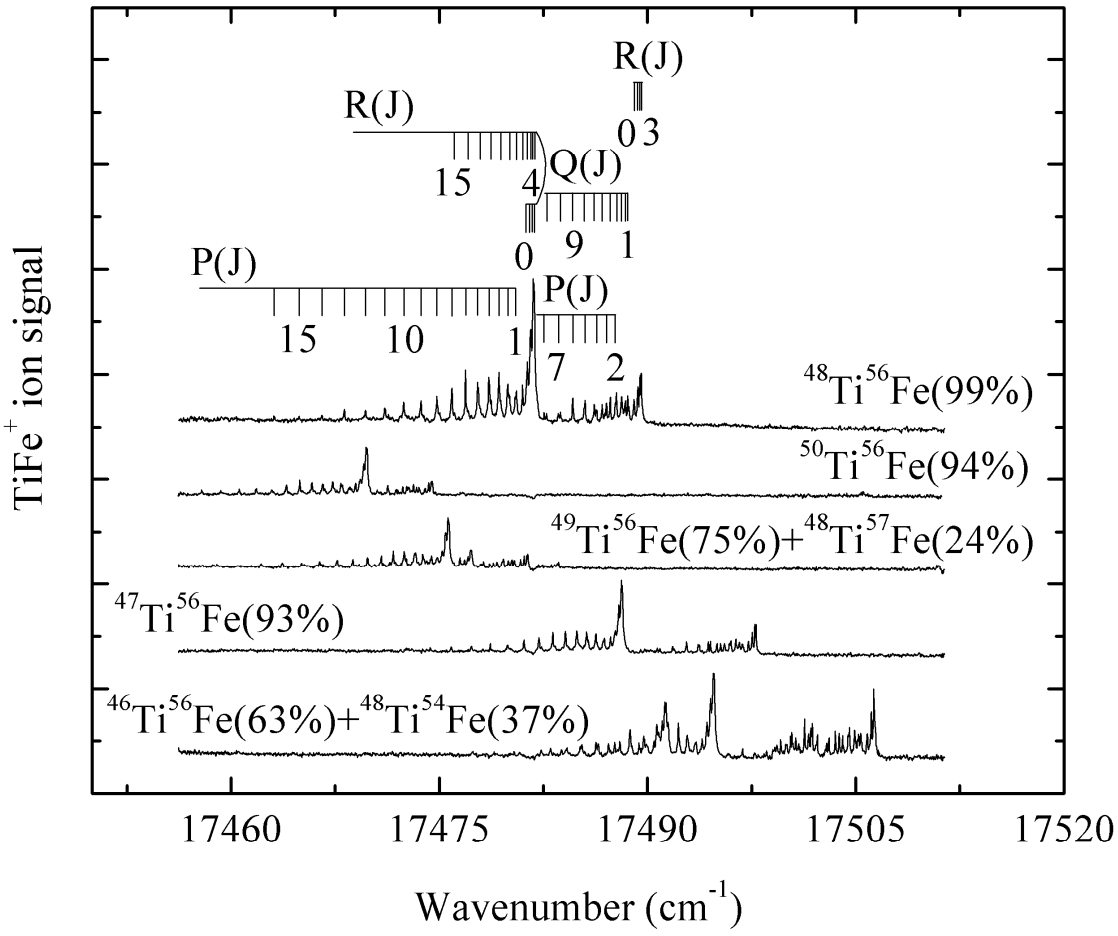

Figure D.15. Rotationally resolved spectra of the various TiFe isotopic combinations for the 5-0 band of the [15.9]1 ← X $^1\Sigma^+$ system and the 4-0 band of the [16.2]0^+ ← X $^1\Sigma^+$ system. Line assignments are provided for the most abundant isotopomer, $^{48}Ti^{56}Fe$.

Table D.10

Fitted Rotational Lines of the 4-0 band of the $[16.2]0^{+} \leftarrow X\ ^{1}\Sigma^{+}$ system of TiFe[a]

Line	$^{46}Ti^{56}Fe$	$^{48}Ti^{54}Fe$	$^{47}Ti^{56}Fe$
P(1)		17489.907(10)	17486.799(-1)
P(2)	17492.842(5)	17489.379(-11)	17486.261(-9)
P(3)	17492.214(-10)	17488.732(-3)	17485.603(14)
P(4)	17491.479(-9)	17487.999(1)	17484.906(-13)
P(5)	17490.661(-16)	17487.179(1)	17484.080(-2)
P(6)	17489.712(17)	17486.279(-8)	17483.181(-7)
P(7)	17488.732(-9)	17485.261(10)	17482.165(16)
P(8)	17487.630(-4)	17484.190(-8)	17481.106(-9)
P(9)	17486.434(3)	17483.009(-7)	17479.911(14)
P(10)	17485.144(13)		17478.665(-3)
P(11)	17483.792(-4)		17477.314(-4)
P(12)	17482.332(-6)		17475.861(8)
P(13)	17480.780(-6)		17474.344(-7)
P(14)			
P(15)			
P(16)			
R(0)			
R(1)			
R(2)			
R(3)	17494.790(7)	17491.323(-11)	17488.181(0)
R(4)	17494.790(13)	17491.323(-2)	17488.181(7)
R(5)	17494.725(-6)	17491.234(6)	17488.110(-4)
R(6)	17494.542(2)	17491.049(19)	17487.925(9)
R(7)	17494.274(4)	17490.794(14)	17487.679(-5)
R(8)	17493.928(-7)	17490.462(-5)	17487.324(-1)
R(9)	17493.463(10)		17486.888(-6)
R(10)	17492.933(2)	17489.486(-3)	17486.352(1)
R(11)		17488.864(-3)	17485.734(-2)
R(12)			17485.026(-2)
R(13)			17484.212(13)
R(14)			17483.340(-4)
R(15)			17482.360(-2)

Table D.10 continued

Fitted Spectroscopic Constants[b]			
ν_0 (cm^{-1})	17493.8609(36)	17490.3765(34)	17487.2536(25)
B_4' (cm^{-1})	0.185164(83)	0.184529(84)	0.183091(43)
r_4' (Å)	1.89970(43)	1.89709(43)	1.89923(22)
B_0'' (cm^{-1})	0.230619(56)	0.229557(86)	0.227903(41)
r_0'' (Å)	1.70222(21)	1.70088(32)	1.70230(15)

[a] Residuals in the fit of the rotational lines are provided in parentheses following each line, in units of 0.001 cm^{-1}. All of the observed bands originated from the $v''=0$ level of the $X\ ^1\Sigma^+$ ground state. Unless stated otherwise, all bands were used in a combined it to extract the most accurate values of the spectroscopic constants.

[b] Errors (1σ) are provided for all fitted spectroscopic constants in parentheses following the reported value, in units of the last digit quoted.

Table D.10 continued

Line	$^{48}Ti^{56}Fe$	$^{48}Ti^{57}Fe$	$^{49}Ti^{56}Fe$	$^{50}Ti^{56}Fe$
P(1)	17480.456(-2)	17475.919(19)	17474.363(-18)	17468.464(-18)
P(2)	17479.922(-7)	17475.422(-19)	17473.801(11)	17467.903(15)
P(3)	17479.286(1)	17474.773(7)	17473.209(-18)	17467.310(-6)
P(4)	17478.559(13)	17474.084(-13)	17472.465(17)	17466.603(1)
P(5)	17477.782(-13)		17471.681(5)	17465.819(-2)
P(6)	17476.880(-3)	17472.377(12)	17470.806(-4)	17464.943(1)
P(7)	17475.901(-5)	17471.434(-16)	17469.823(7)	17463.987(-2)
P(8)	17474.823(5)	17470.343(14)	17468.764(7)	17462.935(3)
P(9)	17473.678(-7)	17469.215(-4)	17467.633(-9)	17461.800(7)
P(10)	17472.426(0)		17466.378(12)	17460.586(2)
P(11)	17471.076(17)		17465.071(-3)	17459.259(24)
P(12)	17469.680(-9)		17463.679(-21)	17457.882(9)
P(13)	17468.157(4)		17462.157(4)	
P(14)	17466.552(11)			
P(15)	17464.886(-10)			
P(16)	17463.090(12)			
R(0)	17481.274(-8)			17469.240(1)
R(1)	17481.521(19)			
R(2)	17481.719(6)			
R(3)	17481.826(-3)	17477.304(-3)	17475.688(9)	17469.791(-4)
R(4)	17481.826(6)	17477.304(7)	17475.688(16)	17469.791(5)
R(5)	17481.759(-7)	17477.239(-5)	17475.621(3)	17469.729(-10)
R(6)	17481.583(2)	17477.063(6)	17475.474(-18)	17469.554(1)
R(7)	17481.333(-4)	17476.814(3)	17475.209(-8)	17469.309(-5)
R(8)	17480.990(-5)	17476.492(-14)	17474.859(-2)	17468.970(-2)
R(9)	17480.544(8)	17476.044(7)	17474.434(-7)	17468.559(-14)
R(10)	17480.041(-9)		17473.897(11)	17468.029(6)
R(11)	17479.424(-2)		17473.294(8)	17467.448(-8)
R(12)	17478.717(8)		17472.622(-14)	17466.744(13)
R(13)	17477.956(-16)		17471.830(-3)	
R(14)	17477.076(-10)		17470.944(14)	17465.151(-18)
R(15)	17476.096(7)			

Table D.10 continued

Fitted Spectroscopic Constants[b]				
ν_0 (cm^{-1})	17480.9037(25)	17476.3850(55)	17474.7905(39)	17468.8866(32)
B_4' (cm^{-1})	0.181083(41)	0.179995(244)	0.179006(48)	0.177323(71)
r_4' (Å)	1.89891(22)	1.89690(129)	1.89936(26)	1.89817(38)
B_0'' (cm^{-1})	0.225228(31)	0.223705(273)	0.222829(51)	0.220525(56)
r_0'' (Å)	1.70268(12)	1.70152(104)	1.70238(19)	1.70212(22)

[a] Residuals in the fit of the rotational lines are provided in parentheses following each line, in units of 0.001 cm^{-1}. All of the observed bands originated from the v″=0 level of the $X\ ^1\Sigma^+$ ground state. Unless stated otherwise, all bands were used in a combined it to extract the most accurate values of the spectroscopic constants.

[b] Errors (1σ) are provided for all fitted spectroscopic constants in parentheses following the reported value, in units of the last digit quoted.

Table D.11

Fitted Rotational Lines of the 5-0 band of the [15.9]1 ← X $^1\Sigma^+$ system of TiFe[a]

Line	$^{46}Ti^{56}Fe$	$^{48}Ti^{54}Fe$	$^{47}Ti^{56}Fe$
P(2)	17504.447(-1)	17499.958(-11)	17495.901(-2)
P(3)	17503.801(-2)	17499.311(-7)	17495.257(4)
P(4)	17503.060(1)	17498.567(2)	17494.527(5)
P(5)	17502.223(7)		17493.717(-6)
P(6)	17501.313(-6)	17496.845(-20)	17492.803(-3)
P(7)	17500.290(1)	17495.814(1)	17491.799(-1)
P(8)	17499.175(8)		17490.698(7)
P(9)	17497.974(9)		17489.506(14)
Q(1)	17505.350(18)	17500.882(-17)	17496.823(-12)
Q(2)	17505.195(-12)	17500.666(15)	17496.616(12)
Q(3)	17504.913(-7)	17500.388(18)	17496.349(6)
Q(4)	17504.544(-8)	17500.046(-8)	17495.997(-7)
Q(5)	17504.045(29)	17499.583(-3)	17495.533(2)
Q(6)	17503.518(2)	17499.022(7)	17495.007(-18)
Q(7)	17502.899(-26)	17498.401(-15)	17494.371(-20)
Q(8)	17502.142(-8)		17493.630(-8)
Q(9)	17501.313(-10)		17492.803(-1)
Q(10)			17491.900(-8)
Q(11)			17490.882(7)
Q(12)	17498.259(-6)		17489.800(-4)
R(0)	17505.827(2)		17497.262(4)
R(1)	17506.109(-3)	17501.600(-1)	17497.540(-1)
R(2)	17506.300(-10)	17501.768(15)	17497.723(-1)
R(3)		17501.858(16)	17497.807(7)
R(4)			17497.807(7)
R(5)			17497.723(0)
R(6)			17497.540(1)
R(7)	17505.826(-2)		17497.262(7)
R(8)	17505.436(17)	17500.950(7)	17496.907(-3)
R(9)	17504.983(8)		17496.440(10)
R(10)			

Table D.11 continued

Fitted Spectroscopic Constants			
ν_0 (cm^{-1})	17505.4601(35)	17500.9567(47)	17496.9014(23)
B_5' (cm^{-1})	0.184424(90)	0.183649(131)	0.182358(60)
r_5' (Å)	1.90350(46)	1.90163(68)	1.90304(31)
B_0'' (cm^{-1})	0.230619(56)	0.229557(86)	0.227903(41)
r_0'' (Å)	1.70222(21)	1.70088(32)	1.70230(15)

[a] Residuals in the fit of the rotational lines are provided in parentheses following each line, in units of 0.001 cm^{-1}. All of the observed bands originated from the $v''=0$ level of the X $^1\Sigma^+$ ground state. Unless stated otherwise, all bands were used in a combined it to extract the most accurate values of the spectroscopic constants.

[b] Errors (1σ) are provided for all fitted spectroscopic constants in parentheses following the reported value, in units of the last digit quoted.

Table D.11 continued

Line	$^{48}Ti^{56}Fe$	$^{48}Ti^{57}Fe$	$^{49}Ti^{56}Fe$	$^{50}Ti^{56}Fe$
P(2)	17487.679(-17)		17479.507(3)	17472.643(0)
P(3)	17487.033(0)		17478.888(-3)	17472.007(29)
P(4)	17486.312(1)		17478.184(-12)	17471.365(-17)
P(5)	17485.491(12)			
P(6)	17484.601(3)			
P(7)				
P(8)	17482.540(-5)			
P(9)				
Q(1)	17488.564(0)	17482.610(-3)	17480.401(0)	17473.527(-2)
Q(2)	17488.395(-11)	17482.432(-4)	17480.232(-10)	17473.360(0)
Q(3)	17488.124(-9)	17482.142(18)	17479.958(-4)	17473.130(-18)
Q(4)	17487.752(4)		17479.606(-9)	
Q(5)	17487.315(-8)		17479.153(-2)	17472.367(0)
Q(6)			17478.617(-3)	17471.883(-12)
Q(7)	17486.161(-22)		17477.988(1)	17471.280(12)
Q(8)	17485.421(0)			
Q(9)				
Q(10)	17483.714(1)			
Q(11)	17482.732(-5)			
Q(12)				
R(0)			17480.844(3)	17473.968(-2)
R(1)	17489.288(-3)	17483.339(-16)	17481.110(3)	17474.238(3)
R(2)	17489.458(9)	17483.506(-4)	17481.293(-2)	17474.427(8)
R(3)	17489.545(12)	17483.591(1)	17481.363(16)	
R(4)	17489.545(14)	17483.591(1)	17481.363(15)	
R(5)	17489.458(13)			
R(6)	17489.288(4)	17483.301(23)		
R(7)	17489.023(2)	17483.064(-7)		
R(8)	17488.661(6)	17482.709(-10)	17480.468(13)	
R(9)	17488.224(-5)		17480.036(-2)	
R(10)	17487.680(2)		17479.505(-9)	

Fitted Spectroscopic Constants[b]				
ν_0 (cm^{-1})	17488.6536(27)	17482.6964(58)	17480.4904(26)	17473.6078(54)
B_5' (cm^{-1})	0.180329(50)	0.178995(251)	0.178162(68)	0.179171(231)
r_5' (Å)	1.90288(26)	1.90219(133)	1.90386(36)	1.88836(122)
B_0'' (cm^{-1})	0.225228(31)	0.223705(273)	0.222829(51)	0.220525(56)
r_0'' (Å)	1.70268(12)	1.70152(104)	1.70238(19)	1.70212(22)

[a] Residuals in the fit of the rotational lines are provided in parentheses following each line, in units of 0.001 cm^{-1}. All of the observed bands originated from the v″=0 level of the X $^1\Sigma^+$ ground state. Unless stated otherwise, all bands were used in a combined it to extract the most accurate values of the spectroscopic constants.

[b] Errors (1σ) are provided for all fitted spectroscopic constants in parentheses following the reported value, in units of the last digit quoted.

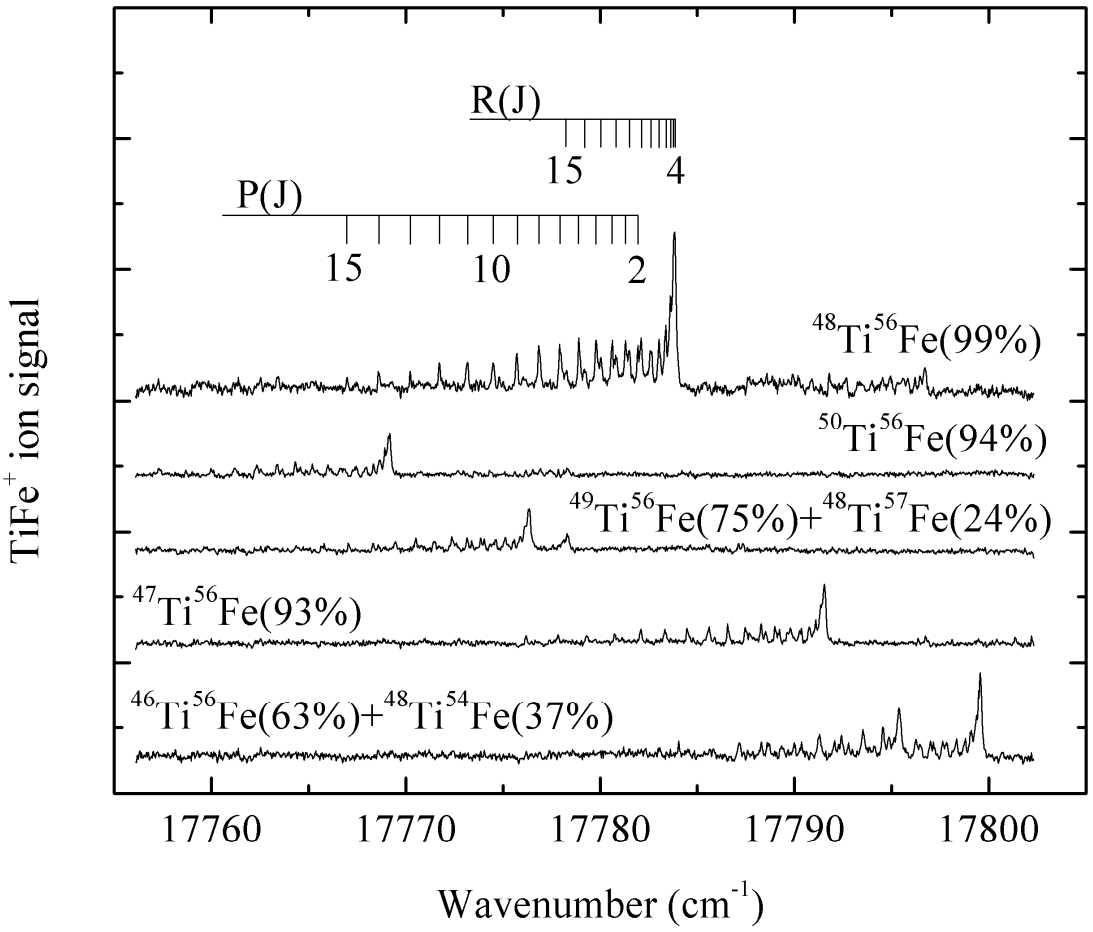

Figure D.16. Rotationally resolved spectra of the various TiFe isotopic combinations for the 5-0 band of the $[16.2]0^{+} \leftarrow X\ ^{1}\Sigma^{+}$ system. Line assignments are provided for the most abundant isotopomer, $^{48}Ti^{56}Fe$.

Table D.12

Fitted Rotational Lines of the 5-0 band of the $[16.2]0^{+} \leftarrow X\ ^{1}\Sigma^{+}$ system of TiFe[a]

Line	$^{46}Ti^{56}Fe$	$^{48}Ti^{54}Fe$	$^{47}Ti^{56}Fe$	$^{48}Ti^{56}Fe$	$^{49}Ti^{56}Fe$	$^{50}Ti^{56}Fe$
P(1)						17767.834(-19)
P(2)	17797.633(-1)	17793.460(-14)	17789.631(6)	17781.941(-6)	17774.502(-18)	17767.277(11)
P(3)	17797.002(-10)	17792.796(10)	17789.006(-2)	17781.311(-1)	17773.856(9)	17766.657(18)
P(4)	17796.247(15)	17792.077(-2)	17788.286(-2)	17780.606(-9)	17773.165(-5)	17765.984(-8)
P(5)			17787.478(-5)	17779.789(6)	17772.369(-2)	17765.191(1)
P(6)	17794.545(-11)	17790.366(-21)	17786.573(2)	17778.900(7)	17771.472(15)	17764.317(4)
P(7)	17793.541(-5)	17789.351(-8)	17785.596(-8)	17777.941(-9)	17770.517(5)	17763.379(-15)
P(8)	17792.430(19)		17784.510(3)	17776.864(4)	17769.459(10)	17762.326(-5)
P(9)	17791.275(-3)		17783.346(3)	17775.719(-2)	17768.325(5)	17761.192(1)
P(10)	17789.992(13)	17785.815(-17)	17782.099(-3)	17774.494(-15)		17759.995(-16)
P(11)	17788.659(-10)		17780.751(4)	17773.168(-16)	17765.799(-7)	17758.693(-15)
P(12)		17782.990(-6)	17779.318(8)	17771.726(12)	17764.375(17)	17757.301(-9)
P(13)			17777.827(-19)	17770.218(18)	17762.925(-19)	
P(14)	17784.048(-4)		17776.199(2)	17768.632(16)	17761.325(8)	
P(15)	17782.321(9)			17766.981(-10)	17759.687(-14)	
P(16)			17772.735(-13)			
P(20)				17757.272(3)		
R(0)			17790.989(16)			
R(1)					17776.100(-7)	
R(3)	17799.596(-2)			17783.846(4)		17769.172(-11)
R(4)	17799.596(12)	17795.379(16)		17783.846(17)	17776.382(8)	17769.172(0)
R(5)		17795.303(10)		17783.790(-2)	17776.323(-8)	17769.099(-1)

Table D.12 continued

R(6)	17799.379(-12)	17795.130(9)	17791.356(-6)	17783.625(0)	17776.173(-19)	17768.915(22)
R(7)	17799.110(2)	17794.861(14)	17791.097(0)	17783.371(4)	17775.895(11)	17768.672(19)
R(8)	17798.776(-7)		17790.773(-17)	17783.033(4)	17775.590(-19)	17768.345(14)
R(9)	17798.344(-9)	17794.070(8)		17782.610(2)	17775.128(22)	17767.949(-9)
R(10)	17797.821(-9)		17789.795(14)	17782.109(-10)	17774.642(0)	
R(11)	17797.181(18)		17789.209(-6)	17781.493(5)	17774.035(12)	17766.832(14)
R(12)	17796.494(3)		17788.512(-4)	17780.828(-18)	17773.389(-23)	17766.146(24)
R(13)			17787.700(24)	17780.035(0)	17772.583(14)	17765.419(-11)
R(14)				17779.174(-2)	17771.726(17)	17764.578(-18)
R(15)	17793.860(-6)		17785.887(5)		17770.815(-14)	17763.617(9)
Fitted Spectroscopic Constants[b]						
ν_0 (cm^{-1})	17798.6441(37)	17794.4544(64)	17790.6376(35)	17782.9238(30)	17775.4623(45)	17768.2562(43)
B_5' (cm^{-1})	0.185877(71)	0.184392(118)	0.183643(46)	0.181439(35)	0.179475(46)	0.177559(58)
r_5' (Å)	1.89605(36)	1.89779(61)	1.89637(24)	1.89705(18)	1.89688(24)	1.89691(31)
B_0'' (cm^{-1})	0.230619(56)	0.229557(86)	0.227903(41)	0.225228(31)	0.222829(51)	0.220525(56)
r_0'' (Å)	1.70222(21)	1.70088(32)	1.70230(15)	1.70268(12)	1.70238(19)	1.70212(22)

[a] Residuals in the fit of the rotational lines are provided in parentheses following each line, in units of 0.001 cm^{-1}. All of the observed bands originated from the v″=0 level of the X $^1\Sigma^+$ ground state. Unless stated otherwise, all bands were used in a combined it to extract the most accurate values of the spectroscopic constants.

[b] Errors (1σ) are provided for all fitted spectroscopic constants in parentheses following the reported value, in units of the last digit quoted.

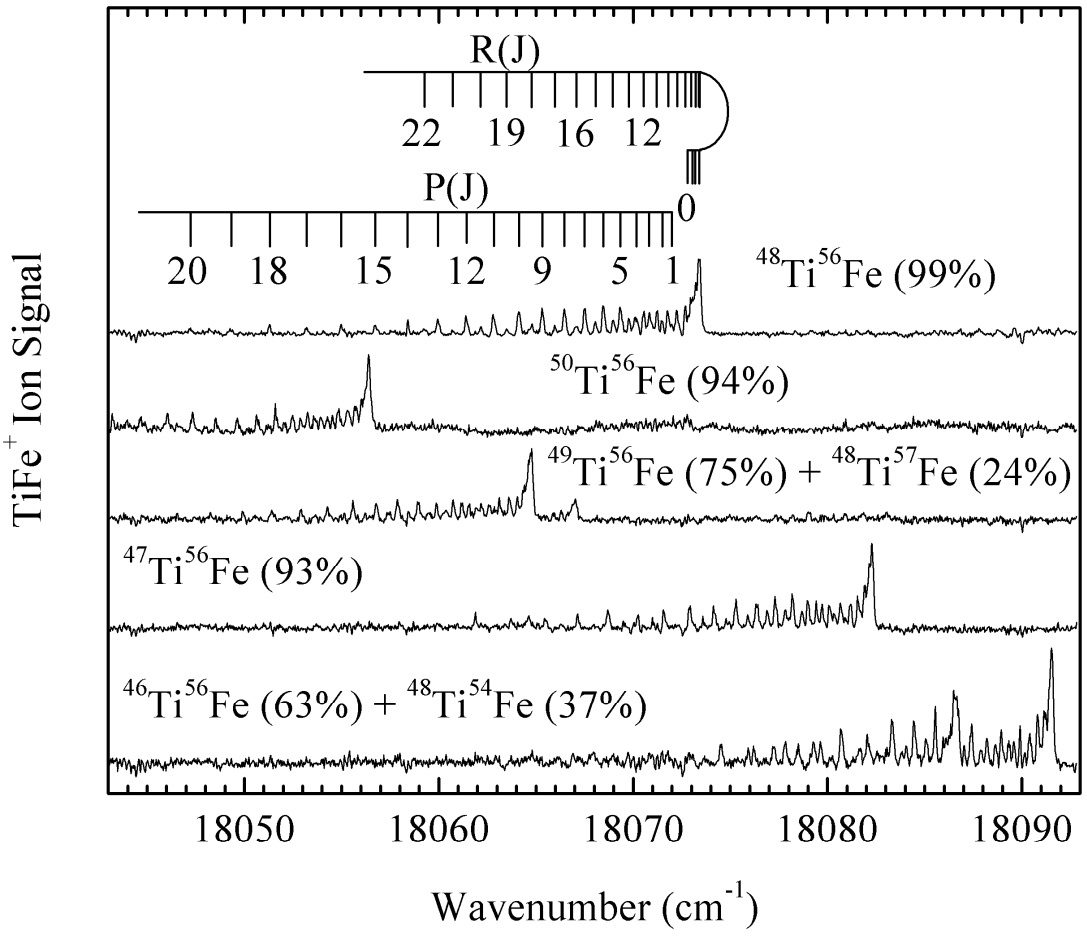

Figure D.17. Rotationally resolved spectra of the various TiFe isotopic combinations for the 6-0 band of the $[16.2]0^{+} \leftarrow X\ ^{1}\Sigma^{+}$ system. Line assignments are provided for the most abundant isotopomer, $^{48}Ti^{56}Fe$

Table D.13

Fitted Rotational Lines of the 6-0 band of the $[16.2]0^{+} \leftarrow X\ ^{1}\Sigma^{+}$ system of TiFe[a]

Line	$^{46}Ti^{56}Fe$	$^{48}Ti^{54}Fe$	$^{47}Ti^{56}Fe$	$^{48}Ti^{56}Fe$	$^{49}Ti^{56}Fe$	$^{50}Ti^{56}Fe$
P(1)	18090.143(-14)		18080.894(-4)	18071.983(19)	18063.383(7)	
P(2)	18089.572(8)		18080.347(1)	18071.483(-16)	18062.873(-13)	
P(3)	18088.936(9)	18084.042(11)	18079.717(3)	18070.833(12)		18053.947(-9)
P(4)	18088.213(9)	18083.324(15)	18078.997(9)	18070.135(4)	18061.538(7)	18053.260(-14)
P(5)	18087.420(-7)	18082.538(1)	18078.192(14)	18069.341(6)	18060.758(3)	18052.484(-15)
P(6)		18081.667(-12)	18077.323(-4)	18068.463(7)	18059.888(4)	18051.589(20)
P(7)	18085.543(-12)	18080.690(-6)	18076.359(-13)	18067.501(6)	18058.956(-18)	
P(8)	18084.457(2)	18079.628(2)	18075.285(1)	18066.452(7)		18049.636(1)
P(9)	18083.315(-15)	18078.493(-3)	18074.136(5)	18065.312(13)	18056.792(-15)	18048.521(5)
P(10)	18082.033(21)	18077.252(14)	18072.908(2)	18064.121(-14)		18047.342(-12)
P(11)		18075.938(17)	18071.594(-1)	18062.791(12)	18054.277(1)	18046.045(6)
P(12)	18079.290(11)	18074.555(5)		18061.413(-1)	18052.904(-3)	18044.675(13)
P(13)			18068.711(-12)	18059.954(-16)	18051.423(17)	18043.234(7)
P(14)	18076.207(-9)		18067.135(-12)	18058.403(-26)	18049.912(-18)	
P(15)			18065.451(10)	18056.737(-5)	18048.263(1)	
P(16)			18063.715(-3)	18054.986(15)	18046.546(2)	
P(17)			18061.891(-14)	18053.186(-3)		
P(18)	18068.959(-13)			18051.299(-16)	18042.850(13)	
P(19)	18066.916(0)			18049.306(-11)		
P(20)				18047.230(-8)		
R(0)	18090.960(5)		18081.725(-9)	18072.831(-13)	18064.195(2)	
R(1)						18056.130(13)

Table D.13 continued

R(2)	18091.458(-7)					
R(3)				18073.384(18)		
R(4)		18086.729(-24)	18082.335(-2)	18073.427(-3)	18064.780(14)	
R(5)	18091.534(-7)	18086.652(1)	18082.268(3)	18073.371(-8)	18064.717(15)	18056.396(2)
R(6)	18091.383(-5)			18073.219(-3)		
R(7)	18091.150(-9)					18056.017(7)
R(8)	18090.813(5)		18081.558(12)	18072.678(-13)	18064.047(-9)	
R(9)	18090.396(11)		18081.179(-15)	18072.244(18)	18063.635(2)	18055.322(-9)
R(10)	18089.899(10)	18085.140(-20)	18080.671(1)	18071.768(6)		18054.835(-2)
R(11)	18089.332(-8)		18080.099(-5)	18071.222(-23)		18054.267(1)
R(12)	18088.644(7)		18079.415(14)	18070.533(7)	18061.935(-8)	
R(13)	18087.898(-6)		18078.696(-17)	18069.785(10)	18061.198(-11)	18052.900(-13)
R(14)	18087.033(13)		18077.832(10)	18068.969(-5)	18060.360(3)	18052.069(2)
R(15)			18076.909(10)	18068.063(-14)		
R(16)			18075.890(20)	18067.057(-10)	18058.447(14)	
R(17)				18065.961(0)		
R(18)				18064.794(-4)	18056.231(-10)	
R(19)				18063.509(24)		
R(20)			18071.017(-6)	18062.176(14)		
R(22)				18059.237(13)		

Table D.13 continued

Fitted Spectroscopic Constants[b]						
ν_0 (cm^{-1})	18090.5906(30)	18085.6853(65)	18081.3463(29)	18072.4531(32)	18063.8357(35)	18055.5122(43)
B_6' (cm^{-1})	0.187019(59)	0.187012(114)	0.184814(31)	0.182538(29)	0.180506(57)	0.178620(64)
r_6' (Å)	1.89025(30)	1.88445(57)	1.89033(16)	1.89133(15)	1.89146(30)	1.89127(34)
B_0'' (cm^{-1})	0.230619(56)	0.229557(86)	0.227903(41)	0.225228(31)	0.222829(51)	0.220525(56)
r_0'' (Å)	1.70222(21)	1.70088(32)	1.70230(15)	1.70268(12)	1.70238(19)	1.70212(22)

[a] Residuals in the fit of the rotational lines are provided in parentheses following each line, in units of 0.001 cm^{-1}. All of the observed bands originated from the v″=0 level of the X $^1\Sigma^+$ ground state. Unless stated otherwise, all bands were used in a combined it to extract the most accurate values of the spectroscopic constants.

[b] Errors (1σ) are provided for all fitted spectroscopic constants in parentheses following the reported value, in units of the last digit quoted.

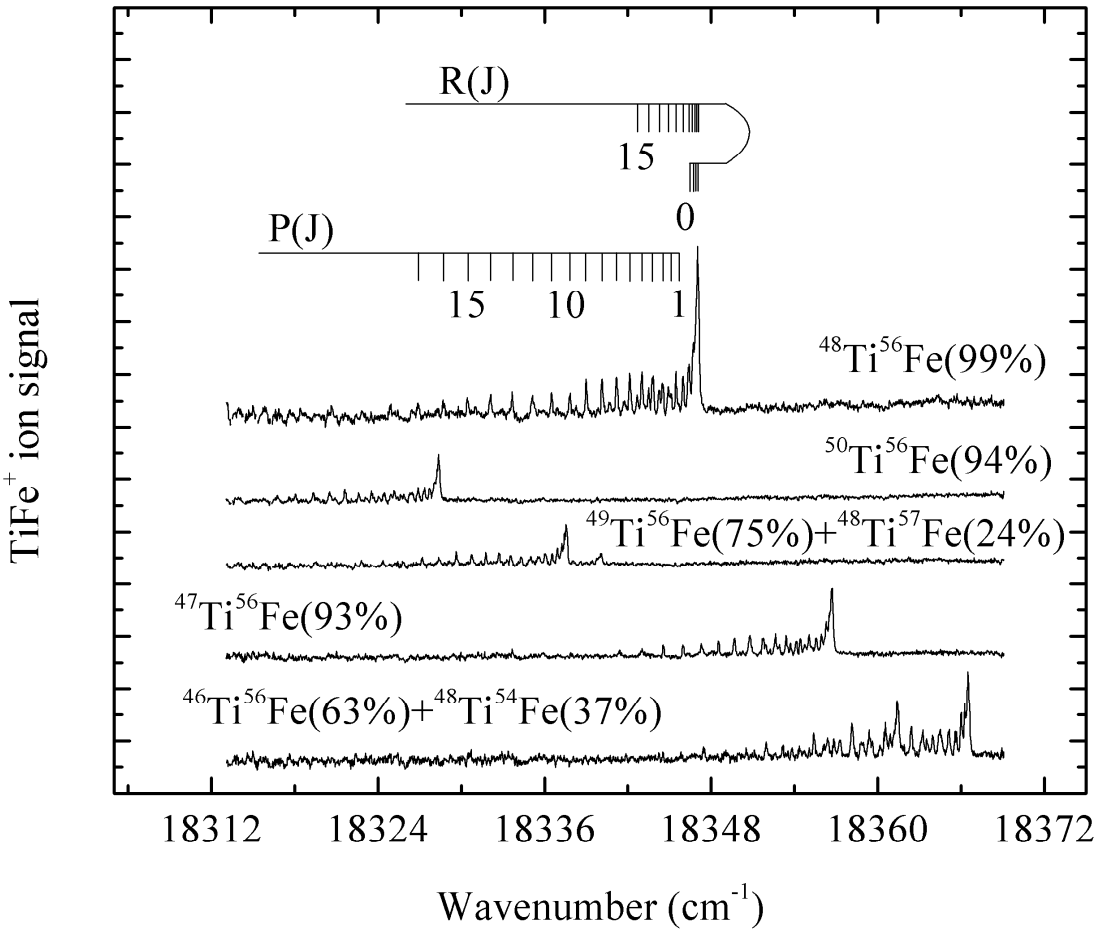

Figure D.18. Rotationally resolved spectra of the various TiFe isotopic combinations for the 7-0 band of the $[16.2]0^+ \leftarrow X\ ^1\Sigma^+$ system. Line assignments are provided for the most abundant isotopomer, $^{48}Ti^{56}Fe$

Table D.14

Fitted Rotational Lines of the 7-0 band of the $[16.2]0^{+} \leftarrow X\ ^{1}\Sigma^{+}$ system of TiFe[a]

Line	$^{46}Ti^{56}Fe$	$^{48}Ti^{54}Fe$	$^{47}Ti^{56}Fe$	$^{48}Ti^{56}Fe$	$^{49}Ti^{56}Fe$	$^{50}Ti^{56}Fe$
P(1)				18345.640(10)	18336.152(6)	
P(2)			18354.766(15)	18345.107(9)	18335.620(10)	18326.469(-1)
P(3)	18363.971(22)		18354.133(17)	18344.504(-9)	18335.013(7)	18325.868(-4)
P(4)	18363.252(-2)	18358.125(-8)	18353.406(26)	18343.788(2)	18334.313(13)	18325.168(9)
P(5)	18362.427(-14)	18357.275(25)	18352.641(-14)	18343.000(0)	18333.563(-12)	
P(6)	18361.500(-20)	18356.384(10)	18351.740(-7)	18342.123(3)		18323.545(15)
P(7)	18360.449(5)	18355.392(7)	18350.778(-26)	18341.163(5)	18331.762(-9)	18322.625(4)
P(8)	18359.359(-26)		18349.673(12)	18340.131(-8)		18321.634(-18)
P(9)	18358.133(-14)	18353.143(-3)	18348.532(-3)	18338.984(10)	18329.648(-23)	18320.530(-9)
P(10)	18356.830(-19)		18347.287(-1)	18337.801(-20)	18328.424(14)	18319.344(1)
P(11)	18355.392(16)	18350.523(1)	18345.975(-19)	18336.495(-13)	18327.173(-5)	18318.068(19)
P(12)			18344.560(-23)	18335.110(-11)	18325.816(-1)	
P(13)		18347.523(27)	18343.035(-3)	18333.646(-15)	18324.365(15)	
P(14)			18341.410(30)	18332.091(-13)		
P(15)				18330.443(-3)		
P(16)				18328.727(-9)		
P(17)				18326.892(18)		
R(0)	18366.011(16)		18356.152(-3)			
R(1)		18361.121(19)	18356.438(-9)		18337.243(5)	18328.084(-15)
R(2)			18356.645(-22)			18328.270(-6)
R(3)		18361.424(8)	18356.729(0)	18347.049(6)		18328.366(13)

Table D.14 continued

R(4)	18366.549(5)	18361.454(-10)	18356.729(18)	18347.077(4)		18328.403(8)
R(5)	18366.436(15)	18361.388(-21)	18356.668(11)	18347.006(17)	18337.547(0)	18328.366(-4)
R(6)	18366.259(-7)	18361.202(-2)	18356.500(22)		18337.431(-16)	
R(7)		18360.978(-33)	18356.286(-8)	18346.649(3)		
R(8)	18365.581(-7)	18360.620(-20)	18355.937(9)	18346.340(-1)	18336.909(-4)	18327.723(2)
R(9)	18365.078(16)		18355.556(-28)	18345.956(-15)	18336.539(-13)	18327.359(-10)
R(10)	18364.497(22)		18355.040(-19)	18345.449(10)	18336.058(8)	18326.894(-3)
R(11)			18354.430(-2)	18344.900(-8)	18335.518(4)	
R(12)	18363.095(-8)		18353.719(26)	18344.253(-13)		
R(13)				18343.490(14)		
R(14)				18342.672(10)		
R(15)				18341.761(15)		
Fitted Spectroscopic Constants[b]						
ν_0 (cm^{-1})	18365.6599(66)	18360.4890(81)	18355.7804(55)	18346.1011(34)	18336.6037(43)	18327.4319(42)
B_7' (cm^{-1})	0.183541(73)	0.184875(95)	0.184166(40)	0.182828(35)	0.181615(75)	0.179671(90)
r_7' (Å)	1.90808(38)	1.89531(49)	1.89368(21)	1.88983(18)	1.88567(39)	1.88573(47)
B_0'' (cm^{-1})	0.230619(56)	0.229557(86)	0.227903(41)	0.225228(31)	0.222829(51)	0.220525(56)
r_0'' (Å)	1.70222(21)	1.70088(32)	1.70230(15)	1.70268(12)	1.70238(19)	1.70212(22)

[a] Residuals in the fit of the rotational lines are provided in parentheses following each line, in units of 0.001 cm^{-1}. All of the observed bands originated from the v″=0 level of the X $^1\Sigma^+$ ground state. Unless stated otherwise, all bands were used in a combined it to extract the most accurate values of the spectroscopic constants.

[b] Errors (1σ) are provided for all fitted spectroscopic constants in parentheses following the reported value, in units of the last digit quoted.

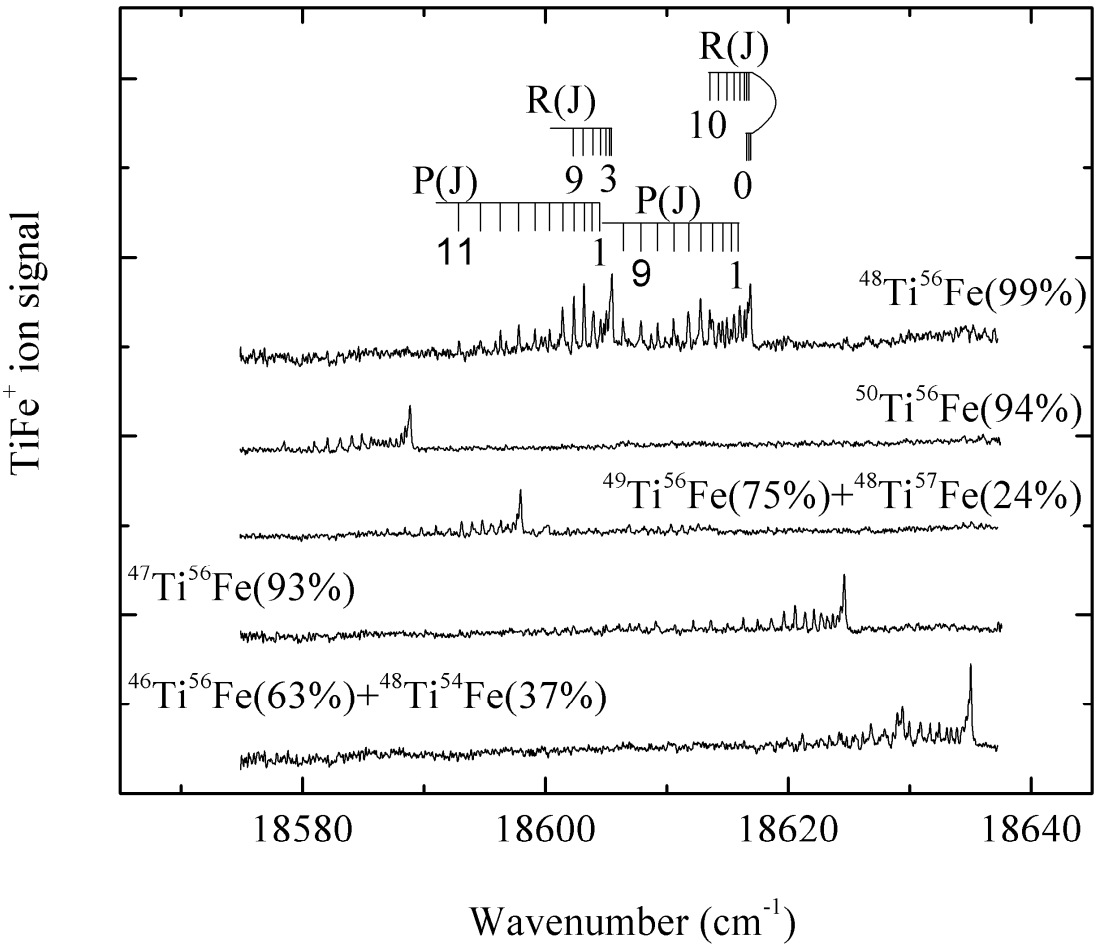

Figure D.19. Rotationally resolved spectra of the various TiFe isotopic combinations for the 8-0 band of the $[16.2]0^{+} \leftarrow X\ ^{1}\Sigma^{+}$ system and the interacting [18.6] band for $^{48}Ti^{56}Fe$ isotopomer. Line assignments are provided for the most abundant isotopomer, $^{48}Ti^{56}Fe$.

Table D.15

Fitted Rotational Lines of the 8-0 band of the $[16.2]0^+ \leftarrow X\ ^1\Sigma^+$ system of TiFe[a]

Line	$^{46}Ti^{56}Fe$	$^{47}Ti^{56}Fe$	$^{49}Ti^{56}Fe$	$^{50}Ti^{56}Fe$
P(1)			18596.723(-4)	
P(2)	18633.071(-3)	18622.770(12)	18596.166(14)	
P(3)	18632.440(-6)	18622.145(-6)	18595.536(12)	
P(4)	18631.706(6)	18621.414(-11)	18594.817(6)	18585.688(22)
P(5)	18630.913(-10)	18620.583(-10)		18584.930(2)
P(6)	18629.985(21)	18619.668(-17)	18593.099(-7)	18584.087(-17)
P(7)	18629.016(8)	18618.619(16)	18592.109(-21)	18583.138(-16)
P(8)	18627.949(4)	18617.509(16)	18590.993(-3)	18582.089(3)
P(9)	18626.802(-5)	18616.316(6)	18589.798(1)	18580.978(-1)
P(10)	18625.534(20)	18615.029(-3)		18579.786(-8)
P(11)	18624.213(10)	18613.646(-10)		18578.512(-18)
R(0)				18588.320(16)
R(2)			18597.950(-8)	
R(3)			18598.032(-17)	18588.917(-16)
R(4)			18597.981(14)	18588.917(4)
R(5)	18635.032(-12)	18624.548(12)		18588.857(0)
R(6)	18634.874(-1)	18624.354(8)	18597.679(-4)	
R(7)	18634.648(-10)	18624.090(-19)	18597.359(17)	18588.477(-2)
R(8)	18634.332(-15)	18623.688(-2)		18588.156(2)
R(9)	18633.901(8)	18623.200(7)		18587.746(11)
R(10)	18633.428(-14)	18622.636(0)		18587.253(18)
Fitted Spectroscopic Constants[b]				
ν_0 (cm^{-1})	18634.0778(54)	18623.7868(54)	18597.1642(56)	18587.9792(60)
B_8' (cm^{-1})	0.187154(72)	0.181201(66)	0.176245(102)	0.178406(94)
r_8' (Å)	1.88957(36)	1.90911(35)	1.91418(55)	1.89240(50)
B_0'' (cm^{-1})	0.230619(56)	0.227903(41)	0.222829(51)	0.220525(56)
r_0'' (Å)	1.70222(21)	1.70230(15)	1.70238(19)	1.70212(22)

[a] Residuals in the fit of the rotational lines are provided in parentheses following each line, in units of 0.001 cm^{-1}. All of the observed bands originated from the $v''=0$ level of the $X\ ^1\Sigma^+$ ground state. Unless stated otherwise, all bands were used in a combined it to extract the most accurate values of the spectroscopic constants. A pair of interacting states was found in the $^{48}Ti^{56}Fe$ isotopic modification, see Table D.16.

[b] Errors (1σ) are provided for all fitted spectroscopic constants in parentheses following the reported value, in units of the last digit quoted.

Table D.16

Rotational Lines of the Interacting 18605 and 18616 bands of $^{48}Ti^{56}Fe$[a]

Line	Lower Energy Band	Higher Energy Band	J′	E(J′) lower state	E(J′) higher state
P(1)	18604.478	18615.956	0	18604.928	18616.406
P(2)	18603.888	18615.311	1	18605.238	18616.661
P(3)	18603.210	18614.602	2	18605.910	18617.297
P(4)	18602.361	18613.791	3	18606.856	18618.292
P(5)	18601.429	18612.804	4	18608.190	18619.548
P(6)	18600.365	18611.801	5	18609.822	18621.235
P(7)	18599.160	18610.565	6	18611.778	18623.166
P(8)	18597.826	18609.270	7	18614.024	18625.475
P(9)	18596.329	18607.889	8	18616.568	18628.146
P(10)	18594.681	18606.389	9	18619.414	18631.148
P(11)	18592.929	18604.839	10	18622.618	18634.541
P(12)		18603.210	11		18638.304
P(13)		18601.437			
R(1)		18616.842			
R(2)	18605.501	18616.943			
R(3)	18605.501	18616.842			
R(4)	18605.331	18616.720			
R(5)	18605.048	18616.418			
R(6)	18604.574	18616.032			
R(7)	18603.960	18615.555			
R(8)	18603.201	18614.961			
R(9)	18602.361	18614.298			
R(10)		18613.556			

[a] Because there was nothing to be gained by performing a deperturbation analysis of these bands, this analysis was not attempted.

Table D.17

Fit of B_v' values for levels belonging to the [15.9]1 state of TiFe[a]

Vibrational Level	B_v' ($^{46}Ti^{56}Fe$)	B_v' ($^{47}Ti^{56}Fe$)	B_v' ($^{48}Ti^{56}Fe$)	B_v' ($^{49}Ti^{56}Fe$)	B_v' ($^{50}Ti^{56}Fe$)
1	0.18772(21)	0.18399(-38)	0.18248(-5)	0.18246(-1)	0.17496[b]
2		0.18436(50)	0.18214(20)	0.18026(1)	0.178323(20)
3	0.18549(-32)	0.18352(17)	0.18125(-10)	0.17801(-1)	0.177405(-41)
4	0.18474(-21)	0.18255(-30)	0.18056(-20)		0.176610(20)
5	0.18442(32)	0.18236(2)	0.18033(15)	0.17816[b]	0.17917[b]
			Fitted spectroscopic constants		
B_e' (cm^{-1})	0.18878(58)	0.18513(55)	0.18341(26)	0.18581(3)	0.18044(14)
r_e' (Å)	1.8970(29)	1.8887(28)	1.8868(13)	1.8643(2)	1.8817(7)
α_e' (cm^{-1})	0.000850(282)	0.000508(276)	0.000589(132)	0.002226(18)	0.000856(75)
α_e' (Pekeris)[c]	0.001829	0.001733	0.001713	0.001747	0.001662

[a] Residuals in the fit of the B_v' values are provided in parentheses following each entry, in units of 0.00001 cm^{-1}. Error limits (1σ) for the resulting fitted spectroscopic constants are provided in units of the last digit quoted.

[b] Omitted from the fit, because the B_v' value showed evidence of perturbations.

[c] The value of α_e calculated from the Pekeris relationship, $\alpha_e = [6(\omega_e x_e B_e^3)^{1/2} - 6B_e^2]/\omega_e$, should be close to the fitted value if the bands are unperturbed and follow a Morse potential reasonably closely. The failure of the calculated values to match the fitted values shows that despite the good fit of the vibronic levels to the anharmonic form and the good fit of the B_v values to the form $B_v = B_e - (v+1/2)\,\alpha_e$ for several of the isotopes, the levels are either perturbed or follow a potential that differs significantly from the Morse potential.

Table D.18

Fit of B_v' values for levels belonging to the $[16.2]0^+$ state of TiFe[a]

Vibrational Level	B_v' ($^{46}Ti^{56}Fe$)	B_v' ($^{48}Ti^{54}Fe$)	B_v' ($^{47}Ti^{56}Fe$)	B_v' ($^{48}Ti^{56}Fe$)	B_v' ($^{49}Ti^{56}Fe$)	B_v' ($^{50}Ti^{56}Fe$)
1	0.18716(9)	0.18615(0)	0.18499(0)	0.18261(-9)	0.18078(9)	0.17885(6)
2	0.18630(-10)	0.18533(0)	0.18412(-2)	0.18183(18)	0.17998(-14)	0.17819(-10)
3	0.18569(-6)	0.18451(0)	0.18329(1)	0.18050(-9)		
4	0.18516(8)	0.18453[b]	0.18309[b]	0.18108[b]	0.17901(4)	0.17732(3)
5	0.18588[b]	0.18439[b]	0.18364[b]	0.18144[b]	0.17948[b]	0.17756[b]
6	0.18702[b]	0.18701[b]	0.18481[b]	0.18254[b]	0.18051[b]	0.17862[b]
7	0.18354[b]	0.18488[b]	0.18417[b]	0.18283[b]	0.18162[b]	0.17967[b]
8	0.18715[b]		0.18120[b]		0.17624[b]	0.17841[b]
			Fitted spectroscopic constants			
B_e' (cm^{-1})	0.18806(20)	0.18739(0)	0.18625(4)	0.18429(48)	0.18155(28)	0.17954(19)
r_e' (Å)	1.8850(2)	1.8826(0)	1.8831(2)	1.8823(25)	1.8860(15)	1.8864(10)
α_e' (cm^{-1})	0.000660(107)	0.000822(4)	0.000847(27)	0.001056(292)	0.000576(154)	0.000499(108)
α_e' (Pekeris)[c]	0.002611	0.002538	0.002560	0.002433	0.002539	0.002452

[a] Residuals in the fit of the B_v' values are provided in parentheses following each entry, in units of 0.00001 cm^{-1}. Error limits (1σ) for the resulting fitted spectroscopic constants are provided in units of the last digit quoted.

[b] Omitted from the fit, because the B_v' value showed evidence of perturbations, specifically, a failure of the B_v' values to decrease with increasing v′.

[c] The value of α_e calculated from the Pekeris relationship, $\alpha_e = [6(\omega_e x_e B_e^3)^{1/2} - 6B_e^2]/\omega_e$, should be close to the fitted value if the bands are unperturbed and follow a Morse potential reasonably closely. The failure of the calculated values to match the fitted values shows that the levels are either perturbed or follow a potential that differs significantly from the Morse potential.